N-body dynamical modelling of the Milky Way Disc for the *Gaia* era.

Jason Alexander Sergio Hunt

Thesis submitted for the degree of

Doctor of Philosophy (PhD)

of

University College London

Mullard Space Science Laboratory

Department of Space and Climate Physics

University College London

May 2015

I, Jason Hunt, confirm that the work presented in this thesis is my own. Where information has been derived from other sources, I confirm that this has been indicated in the thesis.

_____

_____

Abstract

We present a new dynamical modelling code, called PRIMAL, designed to reveal the structure of the Galactic disc from the upcoming observational data of the European Space Agency's *Gaia* mission. PRIMAL is based on the Made-to-Measure method, where a particle based galaxy model is adjusted to match observational constraints. In PRIMAL, observables of the target system are compared with those of an N-body model at the position of the target stars. The masses of the N-body model particles are changed to reproduce the observables of the target system and the gravitational potential is adjusted self-consistently. First, we show that the algorithm can recreate an axisymmetric disc system created by N-body simulations in a known dark matter halo with no error in the observables. We then adapt the algorithm to include likelihood based velocity constraints, which can take into account observational error of individual stars, and demonstrate that PRIMAL can recreate disc systems with a bar, including recovery of the pattern speed of the bar. Finally, we apply PRIMAL to mock observational data generated from an N-body barred disc simulation by replacing each N-body particle with a single M0 giant star and applying the dust extinction and expected *Gaia* errors. We show that PRIMAL can reproduce the structure and kinematics of the target system, despite the Galactic extinction and the observational errors in the mock target data. In addition, we present a population synthesis code, called SNAPDRAGONS, which can generate a *Gaia*-like mock star catalogue from N-body simulations, taking into account stellar populations, dust extinction and *Gaia* errors. By examining *Gaia* mock data generated from our N-body simulation, we find that the peculiar kinematics around the co-rotating spiral arms commonly seen in N-body simulations is visible in the mock *Gaia* data.

Acknowledgements

First and foremost I'd like to thank my supervisor Dr. Daisuke Kawata for his constant encouragement, help and support during my PhD. Daisuke's limitless optimism and constant belief in me have made a world of difference over the years and I couldn't have asked for a better supervisor. I'd like to extend that to the rest of the astrophysics group, whose expertise and enthusiasm have made this a fantastic environment in which to do a PhD. I'd like to thank all the students at MSSL for making my time here more enjoyable, and especially those I've lived with during the PhD. My time in the 'geographically challenged' student flats was thoroughly enjoyable, so thank you Ailsa, Ali, Gemma, King Jamie, Kirthika and Missagh. A special thanks go to Ailsa & Kirthika who've been stuck with me throughout the PhD, it won't be the same without you two around. I'm especially going to miss the constant supply of cake, and the ability to convince Kirthika of almost anything, no matter how ridiculous. Thanks to the MSSL badminton and football clubs for many hours of fun and for helping me to stay in shape, and thanks to all who've been part of the countless trips to various local pubs which have had the opposite effect. I'd like to thank Megan and Tom for proof reading the thesis and GREAT-ITN for paying to include me in many workshops and conferences even though technically I'm not GREAT. Thanks to Mark and Graziella for a positive experience in the Viva and for a positive outcome as well. Finally, I'd like to thank my parents Jan & Trevor for setting me on this path. The childhood indoctrination to all things space related, and strong start in life have enabled me to be where I am today. Their investment of time and money is something I'll never be able to repay, but I hope I can continue to make them proud.

Contents

List of Figures

List of Tables

Chapter 1

Introduction

1.1 Historical mapping of the Milky Way

1.1.1 The Great Debate

Almost a century has passed since the 'great debate' of Harlow Shapley and Heber Curtis (e.g. Shapley & Curtis 1921), when it was still uncertain whether the Milky Way was the entire extent of our physical Universe, or merely one of many such galaxies. Shapley argued that the structures which we now know to be galaxies outside the Milky Way were in fact nebulae within the confines of the Milky Way, which itself was the total extent of the universe. Curtis argued that these 'Spiral Nebulae' were actually 'Island Universes' similar to our own Galaxy, observed at vast distances. Although the answer to this has been clear to us for many decades, the data which they had available to them back in 1921 made it very difficult to determine the truth at the time.

Shapley's argument consisted of three key points. Firstly, he discusses the relative size-distance of the Milky Way compared to the external galaxies. For example, if Andromeda (M31) was a similar size as the Milky Way, then its distance must be of the order of $10^5 - 10^7$ light years to appear with its observed diameter in the sky. This was considered by many to be an infeasibly large distance. Secondly, van Maanen (1916) claims to observe the Pinwheel Galaxy (M101) rotating. This put a firm constraint on the distance to M101, because if it was an external galaxy the rotation would violate the speed of light. Curtis responded by saying that if these observations were correct, then he would be wrong about these Spiral Nebulae being Island Universes. Thirdly, there

was the observation of a nova in M31 which outshone the galactic nucleus (Beesley 1985) and would have to be substantially brighter than any other known novae to place M31 as an extragalactic object. This was later revealed to be a supernova, a phenomenon which was unknown at the time. It is also the first observed extra-galactic supernova and the only one to date in M31.

Curtis' argument also contained novae as one of its components. However, instead of citing a specific nova, he showed that there were more novae in M31 than in the rest of the Milky Way, with no apparent cause. He also showed that these novae were substantially dimmer than would be expected if M31 were a spiral nebula within the confines of the Milky Way. Curtis also states that the spectrum of the spiral matches the expectation of the spectrum of a galaxy of stars, and that the 'dust lanes' observed in M31 appear similar to those found in the Milky Way. The doppler shifts of these 'spiral nebulae' give large velocities ($\sim 1,200$ km s^{-1}) which are different from other known galactic objects and are easier explained for extra-galactic objects.

Hubble finally settled the debate (e.g. Hubble 1926) by observing Cepheid variable stars (which can be used as standard candles) in M31 and other spirals. This discovery changed our view of the Universe and paved the way for later work in galactic astronomy and cosmology, including Hubble's own theory of an expanding Universe. Although Curtis was right about the spirals being extragalactic, Shapley was closer on where we are within the Milky Way and the currently estimated mass of the Milky Way is in between their estimates.

The 'great debate' highlights the importance of measuring the size and mass distribution of the Milky Way, which is a fundamental theme of astronomy. This thesis describes the development of a method to help constrain the structure of the Milky Way. It takes advantage of the unprecedented volume and accuracy of upcoming observational data as well as the powerful computational facilities and algorithms we will have access to.

1.1.2 Mapping the Milky Way

Humanity has always been enticed by the stars, and the practice of attempting to map their positions and motions can be traced back to at least ~ 300 BC (for a review, see Newton 1974), although we will never know who tried it first.

Regardless of where the practice truly originated, Hipparchus (c. 190−120 B.C.) assembled the first recorded star catalogue from a combination of his predecessors work and his own observations. He is often credited with the discovery of the Earth's precession, although other candidates for this include Eratosthenes (276−194 B.C.) and Aristarcus (c. 310−230 B.C.). Ptolemy (c. 90−168 A.D.) carried on Hipparchus' work and expanded his catalogue into what is known as Ptolemy's Almagest, which still survives today (e.g. Ptolemy & Manitius 1995).

After Ptolemy, many observers have continued to make additions and improvements to the catalogue of known stars. A few catalogues stand out above the others as providing notable increases in either size or accuracy, e.g. Ulugh Beg's (1394−1449), Tycho Brahe's (1546−1601), Johannes Hevelius' (1611−1687) and John Flamsteed's (1646−1719) catalogues (for a review, see Perryman 2012). As well as the positions on the sky, right-ascension (α) and declination (δ), the distance to the star is needed to complete the positional information for a star. The first distance to a star is generally considered to have been measured in 1838 (for a review, see Perryman 2012). This was a parallax measurement of 10.3 light years to the star 61 Cygni, performed by Friedrich Bessel.

Parallax is a technique used to determine distances to nearby stars based upon simple triangulation. This is possible because of the Earth's orbit around the Sun. The difference in perspective provided by the difference in position every half year means that nearby stars appear to move around in the sky, compared to 'fixed' background stars, over an annual cycle. The left panel of Fig. 1.1 (Figure 1 in Perryman 2012) demonstrates this, although with drastically exaggerated angles. Unfortunately, in reality the change in angle is tiny. For example, Alpha and Proxima Centauri (the closest stars) have a parallax shift of ~ 1 arcsecond, and the further the star the smaller the angle. There is a limit on how far we can measure distances with parallax because of the dependence on the accuracy of the measurements of positions on the sky. The 'fixed' background stars, which can also be external galaxies or quasars, are of course not really fixed but merely have a change in angle too small to

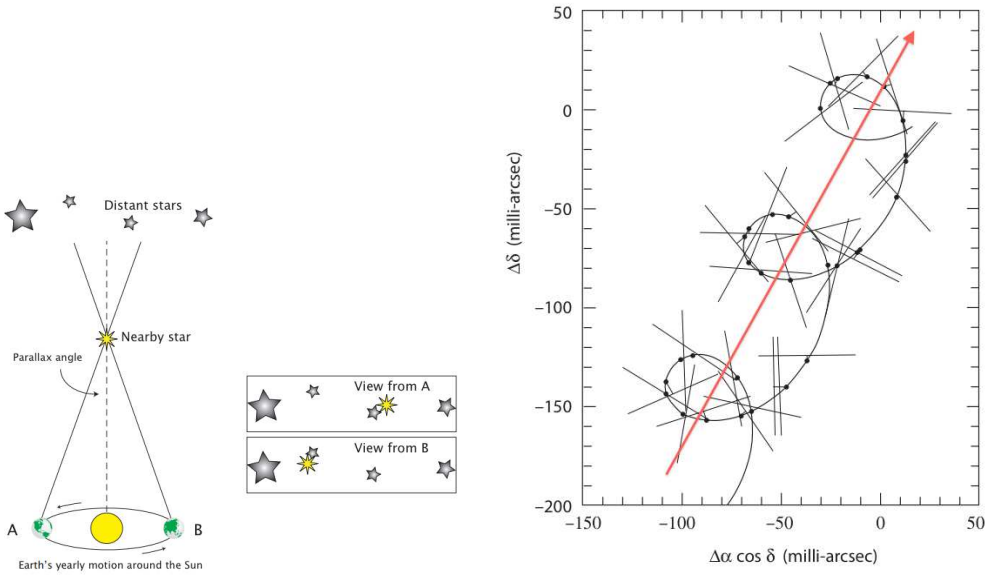

Fig. 1.1: Diagram of parallax determination (left). The angles in this diagram are greatly exaggerated. Path on the sky of a star from the *Hipparcos* catalogue (right), the lines represent the measurements, and the curve is fitted to them. The dots represent the inferred positions, with the short line joining it to the line being the residual (from Perryman 2012).

be detected.

However, despite continuing improvements in observing technology, from the naked eye, to telescopes, to photographic plates, to Charge-Coupled Device (CCD)s, atmospheric effects were always present. Finally, during the 20^{th} century, this started to enforce strict limits on the accuracy of the measurements that we could make from the ground at the wavelength of visible light. This heralded the advance of surveys using different parts of the electromagnetic spectrum (see Section 1.2). In 1989 the European Space Agency (ESA) overcame the atmospheric problem by launching the first space based astrometry mission, *Hipparcos* (see Section 1.2.1), named as both an acronym for HIgh Precision PARallax COllecting Satellite and a tribute to Hipparchus. A comparison of a limited selection of star catalogues by time, size and accuracy of the measurements can be seen in Fig. 1.2.

As well as the oscillations in a star's position owing to the change in perspective, the stars also move across the sky. The right panel of Fig. 1.1 shows the path on the sky of one of the stars from the *Hipparcos* catalogue

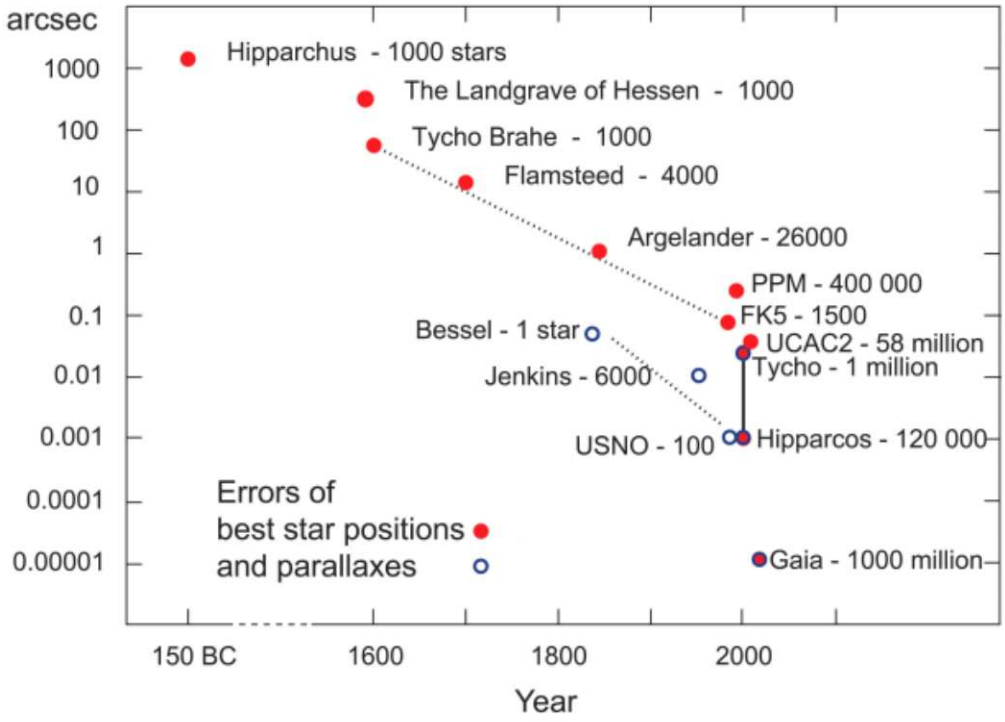

Fig. 1.2: Improvements in astrometric accuracy from Hipparchus to *Gaia* (From the *Gaia* Astrometric Accuracy Assessment, ESA).

across three years of observations. The curve is fitted to the measurements and the amplitude of the oscillations is used to calculate the parallax, π. The arrow indicates the linear component of movement, representing the star's proper motion, which is often described with the change in the position along the direction of right-ascension, μ_α, and declination, μ_δ, over time.

The proper motions only provide velocities in two dimensions. The final piece of the puzzle is the radial velocity of the stars, v_r, which is a measurement of the speed of the stars moving towards or away from us. In 1842, Christian Doppler theorised that light should be 'blue shifted' when moving towards us and 'red shifted' when moving away, just like the pitch of sound. In 1848, Hippolyte Louis Fizeau theorised that the spectral lines of different elements in an observed star would be shifted to different wavelengths. Twenty years later Sir William Huggins used this technique to obtain the first radial velocity measurements for a number of bright stars (Menzel 1972).

Combining the kinematic information with the positional informa-

tion gives us the full 6 dimensional phase space information of the stars $(\alpha, \delta, \pi, \mu_\alpha, \mu_\delta, v_\mathrm{r})$, which are the fundamental building blocks of a living view of the Milky Way.

1.2 Milky Way Surveys

1.2.1 *Hipparcos*

For the last two decades Galactic astronomy has been relying on *Hipparcos* data. *Hipparcos* was a major ESA mission (1989−1993) which returned parallaxes and proper motions for approximately 118,000 stars up to a magnitude of $Hp = 12.4$ mag (where Hp is the apparent magnitude in the *Hipparcos* photometric system) consisting of two main sample groups, reaching accuracies of about one milli-arcsecond. The first sample is a whole sky survey of 52,000 stars brighter than $V \leq 7.9+1.1\sin(b)$ mag for blue stars with $B-V<0.8$, and brighter than $V \leq 7.3+1.1\sin(b)$ mag for red stars with $B-V \geq 0.8$ (where b is the galactic latitude). The second sample is 66,000 objects selected for scientific interest, e.g. systems of multiple stars, fainter than the brightness limit for the main catalogue (e.g. Eyer et al. 2012; Dommanget & Lampens 1993). The results from *Hipparcos* were formed into an extensive online catalogue (Perryman & ESA 1997) which has undergone more reduction by van Leeuwen (2007) to reduce the systematic errors for bright stars.

Along with the main *Hipparcos* catalogue, the Tycho catalogue was compiled from the satellite's star mapper system. Although this comes with a lower accuracy in the astrometry, it includes 2 colour photometry and contains $\sim 10^6$ stars (ESA 1997). Although the *Hipparcos* survey observed known stars, the Tycho catalogue covered the whole sky. The Tycho catalogue was superseded by the Tycho-2 catalogue. This was constructed using end-of-mission satellite attitude and calibration data to allow measurements down to a fainter signal to noise level. The Tycho-2 catalogue contains $\sim 2.5 \times 10^6$ stars and is 99% complete to $V \leq 11$ mag (Perryman 2011).

Hipparcos made great improvements in multiple astronomical fields (for a review, see Perryman 2011). For example, *Hipparcos* provided a drastic increase in the accuracy of distance estimates of stars, which in turn helped

determine absolute magnitudes. *Hipparcos* also improved the measurements of stellar proper motions, which, when coupled with the improvements in distance measurements, has provided substantial increases in our understanding of the kinematic and dynamical structure of the solar neighbourhood. The *Hipparcos* data provides a reference frame which has allowed re-reduction of older astrometric measurements, such as Schmidt plate surveys (e.g. Reid 1990), and provided a common reference system for contemporary surveys such as the Sloan Digital Sky Survey (see Section 1.2.3).

Galactic astronomy is now entering a golden age. Despite *Hipparcos*' significant improvement over prior catalogues, todays technology is more than capable of improving this once more. The successor to *Hipparcos*, *Gaia*, is currently collecting data, but ground based surveys are also a vital source of information about our Galaxy. We shall discuss some of them in the next section. However, this is not an exhaustive listing.

1.2.2 Past ground based surveys

The Two Micron All Sky Survey (2MASS, Skrutskie et al. 2006) was a near infra-red survey performed on two 1.3-m telescopes, one at Mount Hopkins, Arizona, USA, and the other one at the Cerro Tololo Inter-American Observatory (CTIO), Chile. 2MASS observed simultaneously in the J, H and K_s bands (1.25, 1.65 and 2.16 μm respectively). 2MASS provided $\sim 4.1 \times 10^6$ images of the sky, a catalogue of $\sim 1.6 \times 10^6$ extended sources, and positional and photometric information for $\sim 4.7 \times 10^8$ point sources with 99.5% sky coverage down to $J < 15.8$ mag, $H < 15.1$ mag and $K_s < 14.3$ mag at signal to noise ratio $S/N = 10$.

The Geneva-Copenhagen Survey (GCS, Nordström et al. 2004) was a spectroscopic survey which observed 16,682 nearby F and G dwarfs and measured metallicities and radial velocities. The GCS provided radial velocities for around 13,500 stars within a few hundred parsecs, which, when combined with *Hipparcos* parallaxes and Tycho-2 proper motions, completed the 6 dimensional phase space information $(\alpha, \delta, \pi, \mu_\alpha, \mu_\delta, v_\mathrm{r})$ for these stars. The majority of the radial velocity measurements were performed by the photoelectric cross-correlation spectrometers, CORAVEL (e.g. Baranne et al. 1979), operated at

the Swiss 1-m telescope at Observatoire de Haute-Provence, France and the Danish 1.5-m telescope at ESO, La Silla, which cover the whole sky between them. Several hundred stars rotating too rapidly for CORAVEL were observed with digital spectrographs from the Harvard-Smithsonian Center for Astrophysics.

1.2.3 Ongoing ground based surveys

The Sloan Digital Sky Survey (SDSS, York et al. 2000) was a photometric and spectroscopic survey performed on a 2.5-m telescope at the Apache Point Observatory (APO), Sunspot, New Mexico, USA. The photometric survey operated in the magnitude range $15 \leq g \leq 23$ mag, and the spectroscopic survey obtained spectra for around 10^6 galaxies and 10^5 quasars which were identified in the photometric survey. This photometric view of faint objects has helped build a global picture of the stellar distribution (Jurić et al. 2008) and has been particularly useful in identifying stellar streams in the Milky Way's halo (Belokurov et al. 2006) and ultra-faint satellite galaxies. Although the original SDSS finished in 2005, the success of SDSS led to an extension of the survey, SDSS-II, containing three subprojects. One subproject is the SDSS Legacy Survey, a well calibrated photometric and spectroscopic map of 7,500 degrees in the north and three stripes in the south, one with ultra-deep imaging. Another subproject is the SDSS Supernova survey, a repeated survey of the same stripe of sky, which detected $\sim$ 500 type Ia and 80 type Ib/c supernovae over three years. A third subproject is the Sloan Extension for Galactic Understanding and Exploration (SEGUE), which will be discussed in more detail below.

SEGUE (Yanny et al. 2009) was a spectroscopic survey of $\sim 230,000$ stars with $14 \leq g \leq 20.3$ mag, at spectral resolution of $R \sim 2,000$. SEGUE has proved useful for isolating stellar substructure, for example, identifying the stellar halo. SEGUE's success led to a follow-up survey, SEGUE-2, which is part of SDSS-III. Using the existing SDSS spectrographs, SEGUE-2 obtained spectra with $R = 2,000$ of an additional $\sim 119,000$ stars in selected fields, up to a magnitude of $\sim$19.5 (Rockosi et al. 2009). Combining SEGUE and SEGUE-2 provides a sample of $\sim 350,000$ stars beyond the solar neighbour-

hood.

SDSS-III also contains the Baryon Oscillation Spectroscopic Survey (BOSS), the Multi-object APO Radial Velocity Exoplanet Large-area Survey (MARVELS) and the Apache Point Galactic Evolution Experiment (APOGEE). BOSS is designed to detect the imprint of baryon acoustic oscillations in the early universe by mapping luminous red galaxies and quasars. MARVELS is designed to detect exoplanets by measuring the radial velocity of $\sim 11,000$ stars.

APOGEE (Allende Prieto et al. 2008) is a high resolution ($R = 23,500$) near infra-red spectroscopic survey of $\sim 150,000$ giant stars in the Milky Way. APOGEE operates in the H band ($1.51\ \mu\text{m} < \lambda < 1.70\ \mu\text{m}$), which experiences around one-sixth of the extinction in the V band, allowing APOGEE to penetrate the dust that obscures the inner galaxy down to $H = 12.2$ mag. The majority of spectra are taken in the range $\mid b \mid < 10^{\text{o}}$ surveying giant stars within the Galactic bulge, bar, disc and halo. APOGEE measures radial velocities to an accuracy of $\lesssim 100$ m s^{-1}, atmospheric parameters and individual elemental abundances to an accuracy of ~ 0.1 dex. Together, SEGUE-2 and APOGEE provide a new level of detail to the current picture of the Milky Way.

SDSS-III finished in June 2014, and SDSS-IV is now in progress[1]. Like its predecessors, SDSS-IV contains multiple surveys. Firstly, APOGEE-2 is a stellar survey of the Milky Way with two major components, a northern survey at APO, and a complementary southern survey at the 2.5-m du Pont Telescope at Las Campanas observatory. This southern component increases APOGEE-2's potential observable coverage to all sky (although only certain fields are selected), and will include more bulge fields and the Magellanic Clouds. APOGEE-2 will survey around 3×10^5 stars with radial velocity accuracies of $\lesssim 100$ m s^{-1} and an accuracy of abundance measurements to ~ 0.1 dex for 15 elements. Secondly, Mapping Nearby Galaxies at APO (MaNGA), which is an Integral Field Unit (IFU) spectroscopic survey across the face of $\sim 10,000$ galaxies. Thirdly, the extended Baryon Oscillation Spectroscopic

[1] http://www.sdss3.org/future/

Survey (eBOSS) is a cosmological survey of quasars and galaxies, which itself contains two subprograms. The Time-Domain Spectroscopic Survey (TDSS) is a spectroscopic survey of variable sources, and the SPectroscopic IDentification of ERosita Sources (SPIDERS) is a survey of X-ray sources detected by eROSITA, the primary instrument on the *Spectrum-Roentgen-Gamma* satellite due to be launched in 2016.

The Panoramic Survey Telescope And Rapid Response System (Pan-STARRS, Kaiser et al. 2010) is a wide-field time-domain imaging survey covering around 75% of the sky ($\delta > -30^{o}$) down to $V \leq 24$ mag. Pan-STARRS operates in the wavelength range of 400−1,000 nm, and is operated on a 4-m telecope on Halekala, Maui. There are two Pan-STARRS telescopes, PS1 and PS2. PS1 has been active for over 3 years and it has observed the full visible area multiple times in 5 bands ($grizy$). PS1 has performed 4 different surveys. One survey is the 3π survey covering 3π steradians of the sky. Another survey is the medium-deep survey (MDS), which covers 10 selected regions and is designed to observe supernovae. Another survey is designed to detect potential Earth-impacting asteroids, and observes near the ecliptic plane. Finally, the PAndromeda survey is designed to look for variable stars in the Andromeda galaxy and microlensing events in its halo. PS2 has been commissioned and has recently started operations (e.g. Morgan et al. 2014).

The VISTA Variables in the Via Lactea survey[2] (VVV, Minniti et al. 2010) is a public ESO near infra-red variability survey on the 4-m Visible and Infrared Survey Telescope for Astronomy (VISTA) at ESO's Cerro Paranal Observatory in Chile. VVV has a survey area of 562 square degrees, and operates in the wavelength range of 0.9−2.5 μm. The survey will run from 2010−2016 covering 10^9 point sources in the Milky Way. VVV will produce a catalogue of over 10^6 variable sources in two regions. The first one is the region of the bulge, with $-10^{o} < l < 10^{o}$ and $-10^{o} < b < 5^{o}$. The second one is the region of the disc plane with $-65^{o} < l < -10^{o}$ and $-2^{o} < b < 2^{o}$.

The RAdial Velocity Experiment (RAVE, Steinmetz et al. 2006) is a multi-fibre spectroscopic survey covering the southern hemisphere. RAVE

[2]http://vvvsurvey.drupalgardens.com/

measures radial velocities with an accuracy of ≤ 2 km s^{-1}, effective temperature with an accuracy of ~ 200 K, metallicity with an accuracy of 0.5 dex and surface gravity with an accuracy of 0.3 dex, for $483,330$ stars using the Six Degree Field spectrograph on the 1.2-m UK Schmidt Telescope of the Anglo-Australian Observatory. RAVE operates between 8,400−8,800 Å and observes stars whose magnitude range is $9 \lesssim I \lesssim 12$ mag.

The GALactic Archaeology with HERMES (GALAH, De Silva et al. 2015) survey is a spectroscopic survey on the Anglo-Australian Telescope using the High Efficiency and Resolution Multi-Element Spectrograph (HERMES, Wylie-de Boer & Freeman 2010). HERMES provides high resolution ($R \sim 28,000$) spectra for ~ 400 stars simultaneously within a 2 square degree field of view, covering four passbands, $4,713 \leq \lambda \leq 4,903$ Å to $B \leq 14.2$ mag, $5,643 \leq \lambda \leq 5,873$ Å to $V \leq 13.8$ mag, $6,478 \leq \lambda \leq 6,737$ Å to $R \leq 14.0$ mag and $7,585 \leq \lambda \leq 7,887$ Å to $I \leq 14.2$ mag. The GALAH survey covers $\mid b \mid > 10^{\rm o}$ and $-80^{\rm o} < \delta < 10^{\rm o}$ and will collect spectra for $\sim 10^6$ stars with absorption lines from 29 elements. GALAH will survey dwarfs and giants in the Milky Way's thin and thick discs and the halo, and giant stars in the bulge, helping to study the Milky Way's formation history.

The LAMOST Experiment for Galactic Understanding and Exploration (LEGUE, Deng et al. 2012) is a spectroscopic survey on The Large sky Area Multi-Object fibre Spectroscopic Telescope (LAMOST), which is a Chinese national scientific research facility. LEGUE will survey 2.5×10^6 stars with $r < 19$ mag, and an additional 5×10^6 stars with $r < 17$ mag. LEGUE is divided into three parts, the spheroid, the disc and the anticentre. The spheroid survey covers $\mid b \mid > 20^{\rm o}$, the disc survey covers as much of $\mid b \mid < 20^{\rm o}$ as is visible from LAMOST (the direction of the Galactic centre is only visible during summer and will be poorly sampled) and the anticentre survey covers $\mid b \mid < 30^{\rm o}$ for $150^{\rm o} \leq l \leq 210^{\rm o}$. A single pointing has a field of view of ~ 20 square degrees and can take 4,000 spectra in a single exposure. Most stars will be observed with a resolution of $R = 1,800$. A higher resolution ($R = 5,000$) grating will be added during the survey.

The Bar and Spiral Structure Legacy (BeSSeL, Brunthaler et al. 2011)

survey is a Very Long Baseline Interferometry (VLBI) survey observing microwave amplifications by stimulated emission of radiation (maser) sources. The survey will help map the spiral structure of our galaxy and measure fundamental parameters of the Milky Way structure, such as the distance to the Galactic centre, R_0, and the circular speed at the Solar radius, Θ_0. The survey has an accuracy of ~ 0.03 mas, which is relative positional accuracy between the maser sources and background objects. The BeSSeL survey has found evidence that the IAU recommended values of R_0 and Θ_0 are likely to need some revision, with $R_0 = 8.34 \pm 0.16$ kpc and $\Theta_0 = 240 \pm 8$ km s^{-1} (Reid et al. 2014). Due to the rarity of these masers the BeSSeL survey has quite a small sample set and over the course of the mission it will measure ~ 400 sources.

The *Gaia*-ESO (European Southern Observatory) public spectrographic survey (Gilmore et al. 2012) is an ongoing survey that uses the Very Large Telescope (VLT)'s Fibre Large Array Multi Element Spectrograph (FLAMES) which feeds the GIRAFFE and UVES spectrographs. *Gaia*-ESO will collect high resolution ($R \sim 20,000$) spectra for $\sim 10^5$ stars down to $V < 19$ mag and $R \sim 47,000$ spectra for $\sim 5,000$ F, G and K stars with $J \leq 14$ mag. The scientific goals are to study the formation, evolution and disruption of open clusters, the calibration of complex physics that affects stellar evolution, to study the halo substructure, dark matter and rare stars, to study the nature of the bulge, the origin of the thick disc and the formation, evolution and structure of the thin disc, along with the kinematics in the Solar neighbourhood.

1.2.4 Upcoming ground based surveys

The Large Synoptic Survey Telescope (LSST, Ivezic et al. 2008) is planned to be an 8.4-m telescope facility on Cerre Pachón in Chile. LSST will have a 9.6 square degree field of view contained with a total observable area of 30,000 square degrees with $\delta < 34.5^{\circ}$. LSST will operate in six bands ($ugrizy$) within the wavelength range 320−1,050 nm. The main survey (90% of observing time) will cover $\sim 18,000$ square degrees over 10 years and is expected to detect $\sim 2 \times 10^{10}$ stars and $\sim 2 \times 10^{10}$ galaxies. The remaining 10% of the observing time will be used for special projects, such as a Very Deep and Fast

time domain survey (Ivezic et al. 2008). The LSST database, which will be public, will contain $\sim 32 \times 10^{12}$ observations of $\sim 4 \times 10^{10}$ objects. LSST will generate ~ 15 TB of information per night (which is roughly equivalent to the total amount of data collected with SDSS) and for the first time will create a catalogue with more objects than people on Earth.

The Subaru Measurement of Images and Redshifts (SuMIRe, Sugai et al. 2012) project, using the Prime Focus Spectrograph (PFS, e.g. Takada et al. 2014) on the 8.2-m SUBARU telescope, will target cosmology with galaxy surveys, Galactic archaeology, and studies of galaxy/AGN evolution. The PFS is an optical/NIR multi-fibre spectrograph and will be one of the main instruments when added to the Subaru telescope. It will cover the wavelength range of 380−1,260 nm in three passbands (380−650 nm, 630−970 nm and 940−1,260 nm).

The WHT Enhanced Area Velocity Explorer (WEAVE, e.g. Dalton et al. 2014) is a wide field spectrograph on the 4.2-m William Herschel Telescope (WHT) at the Observatorio de Roque de los Muchachos, La Palma. WEAVE can position up to 150 fibres individually, with each fibre observing an individual star or galaxy. WEAVE is planned to begin operations in 2017, with low and high resolution surveys. The low resolution ($R \sim 5,000$) survey will provide radial velocities for more then 10^6 stars with $17 < V < 20$ mag, with an accuracy of $\lesssim 5$ km s^{-1}. The high resolution ($R \sim 20,000$) survey will provide elemental abundances for $\sim 50,000$ giant stars with $V < 17$ mag to an accuracy of ~ 0.1 dex.

The 4-metre Multi-Object Spectroscopic Telescope (4MOST, e.g. de Jong et al. 2014) is a wide field spectroscopic survey facility under development for the VISTA telescope with operations expected to start by the end of 2020. 4MOST has a 2.5 square degree field of view with 2,400 fibres. 1,600 of which go to two spectrographs with resolution $R \gtrsim 5,000$ in the wavelength range 390−950 nm, and 800 of which go to a spectrograph with resolution $R \gtrsim 20,000$ with wavelength range 390−457 nm and 595−950 nm (e.g. Depagne 2015). 4MOST will take spectra for $\sim 2.5 \times 10^7$ objects in the southern sky.

The Multi-Object Optical and Near-infrared Spectrograph (MOONS, Cirasuolo et al. 2014) is a spectroscopic instrument for the VLT. MOONS contains $\sim 1,000$ fibres which can be arranged over a field of view of ~ 500 square arcmin. MOONS will observe $\sim 1 - 2 \times 10^6$ galaxies at redshift $z > 1$, and will provide high resolution spectra for $\sim 3 \times 10^6$ stars in the galaxy. MOONS has a medium resolution mode ($R \sim 4,000 - 6,000$) which covers the wavelength range of $0.8 - 1.8$ μm and a high resolution mode which will cover three selected sub-regions of the wavelength range, with $R \sim 9,000$ at $0.765 - 0.895$ μm and $R \sim 20,000$ at $1.177 - 1.268$ and $1.521 - 1.635$ μm.

As well as the upcoming ground based surveys, *Gaia*, a space-based successor to *Hipparcos* has recently completed its commissioning phase. We are especially interested in *Gaia*, as it will provide us with detailed positional and kinematic data for around one billion stars (Robin et al. 2012). *Gaia* will survey the whole sky several times and each object will be observed between tens and hundreds of times depending on its position on the sky (Cacciari 2009).

1.3 *Gaia*

ESA's *Gaia* satellite was launched on 19^{th} December 2013. It has an operational lifetime of 5 years, with provisions made for a possible 12−18 month extension. The start of routine operations occurred in early 2014, with the first preliminary data release scheduled for summer 2016. The data processing will be performed by numerous parts of the European scientific community, centring around the *Gaia* Data Processing and Analysis Consortium (DPAC). This includes production of the final astronomical catalogues. A large amount of preparatory software development and scenario modelling has already been occurring over the past few years (e.g. Seabroke et al. 2011; Liu et al. 2012; Allende Prieto et al. 2013).

1.3.1 Science objectives

While following on from the success of *Hipparcos*, *Gaia* has a different scientific goal. While *Hipparcos* was mainly concerned with stellar studies, *Gaia* is mainly focused on the structure, dynamics, evolution and formation history of the Milky Way. However, in addition to this, *Gaia* will also provide a large

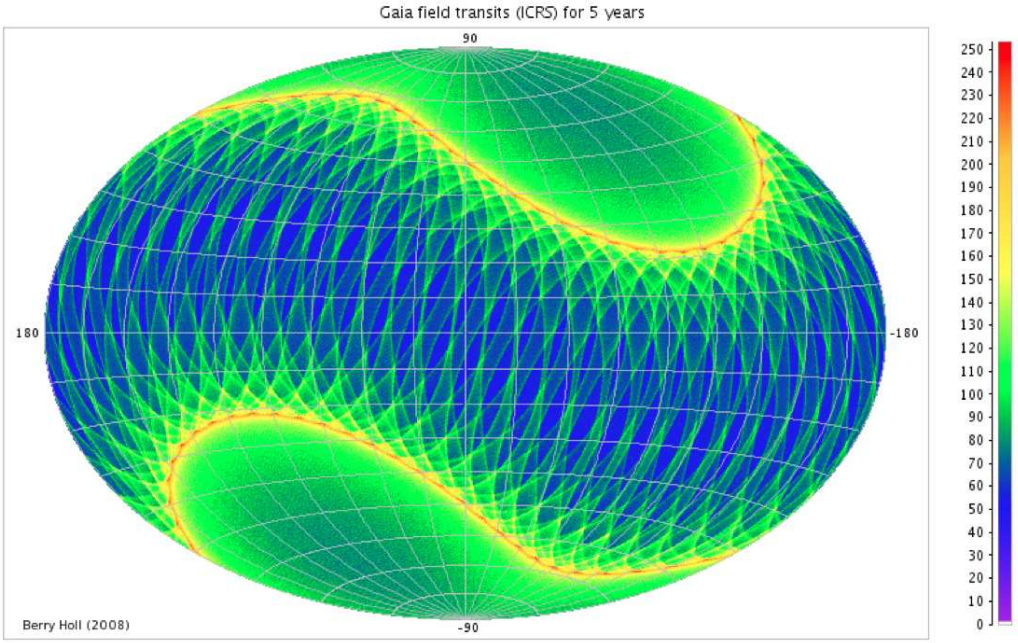

Fig. 1.3: Expected end of mission sky coverage map for *Gaia*, colour coded by the number of times *Gaia* will observe each field of view (Berry Holl 2008).

amount of data for other fields of study. These include asteroid studies (e.g. Delbo' et al. 2012), stellar astrophysics (e.g. Plez 2011), exoplanet discovery (e.g. Busonero 2011), external galaxies (e.g. Krone-Martins et al. 2013), the reference frame (e.g. Taris et al. 2013), the distance scale (e.g. Turon et al. 2012), open clusters (e.g. Alfaro Navarro et al. 2011), globular clusters (e.g Pancino et al. 2013), the transient universe (e.g Wyrzykowski et al. 2012) and fundamental physics (e.g. Eyer et al. 2012). *Gaia* will also provide alerts for transient events. It discovered its first supernova in October 2014[3] and continues to find more (e.g. Wyrzykowski et al. 2015). *Gaia* will collect astrometric and photometric data for over a billion objects up to $G \lesssim 20$ mag, along with spectroscopic data for about 150 million objects with magnitudes up to $G \lesssim 16$ mag (e.g. Katz et al. 2004; Wilkinson et al. 2005).

The sky coverage pattern for *Gaia* (see Fig. 1.3) is designed to allow homogeneous sky coverage, with all positions scanned from different angles. This is balanced against the need from an engineering standpoint to maintain a 45° angle to the Sun to maintain thermal balance (Prusti 2012). With this

[3]http://sci.esa.int/gaia/54630-gaia-discovers-its-first-supernova/

scanning law, each object will be sampled on average around 70 times across the operational period.

1.3.2 Instrumentation

The *Gaia* spacecraft contains three major modules, the payload module, the mechanical service module and the electrical service module[4]. The payload module contains the optical instruments and the electronics which are needed to manage and process the data. To facilitate this, it includes the Video Processing Unit, the Clock distribution Unit, and the Payload Data Handling Unit. The mechanical service module contains the mechanical, structural and thermal components which support the instruments and the spacecraft electronics. It also contains the micro-propulsion system, the deployable sunshield, the payload thermal tent and the Solar array and Harness. The electrical service module controls the pointing, electrical power distribution, central data management and radio communication with the Earth.

The payload module contains the two telescopes, which point in two different directions, separated by 106.5°. The light collected by the two telescopes is focused into a common focal plane and read by the three scientific instruments. Fig. 1.4 shows the arrangement of CCDs on *Gaia's* focal plane. The observed star's light crosses the plane from left to right, passing the sky mapper CCDs, the astrometric field CCDs, the Blue Photometer (BP) CCDs, the Red Photometer (RP) CCDs and the Radial Velocity Spectrometer (RVS) CCDs in that order.

The sky mapper detects objects with $G \lesssim 20$ mag which enter *Gaia*'s field of view. The data from the 14 sky mapper CCDs are used by *Gaia*'s onboard computer to identify the objects to be observed by the main astrometric and spectroscopic CCDs.

The astrometric instrument, which uses the global astrometry concept from *Hipparcos*, measures the relative separation of potentially thousands of stars present in the field of view. It operates in the G band (wavelength range 330−1,050 nm, see Fig. 1.5). It samples the field of view with 62 CCDs (light blue in Fig. 1.4) which are each read out in a time-delayed integration

[4]http://www.cosmos.esa.int/web/gaia/spacecraft-instruments

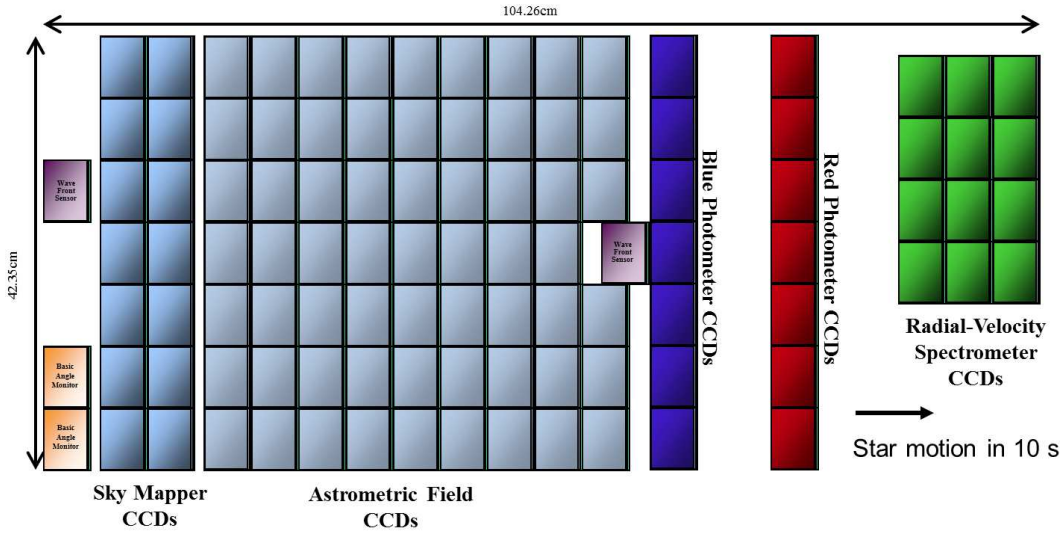

Fig. 1.4: CCD arrangement on the *Gaia* focal plane (Short & de Bruijne, ESA). This includes the basic angle monitor CCDs (orange), the wave front sensor CCDs (purple), the sky mapper CCDs (medium blue), the astrometric field CCDs (light blue), the blue photometer CCDs (dark blue), the red photometer CCDs (red) and the radial velocity spectrometer CCDs (green).

(TDI) procedure which is synchronised to the scanning law of the satellite. By combining the measurements for each star over the course of the mission, it is possible to calculate its parallax and proper motion.

The spectrophotometric instrument consists of a blue and a red photometer. The BP (dark blue in Fig. 1.4) operates in the wavelength range of 330−680 nm, and the RP (red in Fig. 1.4) operates in the wavelength range of 640−1,050 nm (see Fig. 1.5). The photometers are prisms located just before the focal plane which disperse the light entering the field of view. The prisms disperse the light onto the photometric CCDs which provide the spectral energy distribution (SED) of each star, allowing measurements of the effective temperature, surface gravity, metallicity and reddening of the stars (e.g. Jordi et al. 2010).

The RVS, which measures the radial velocity of the stars with $G \lesssim 16$ mag, is a near-infrared integral field spectrograph. The RVS operates in the wavelength range of 845−872 nm (see Fig. 1.5), with a resolution of $R \sim 11,500$. The RVS is integrated with the astrometric and photometric instruments and light coming from both viewing directions are superimposed on to the RVS

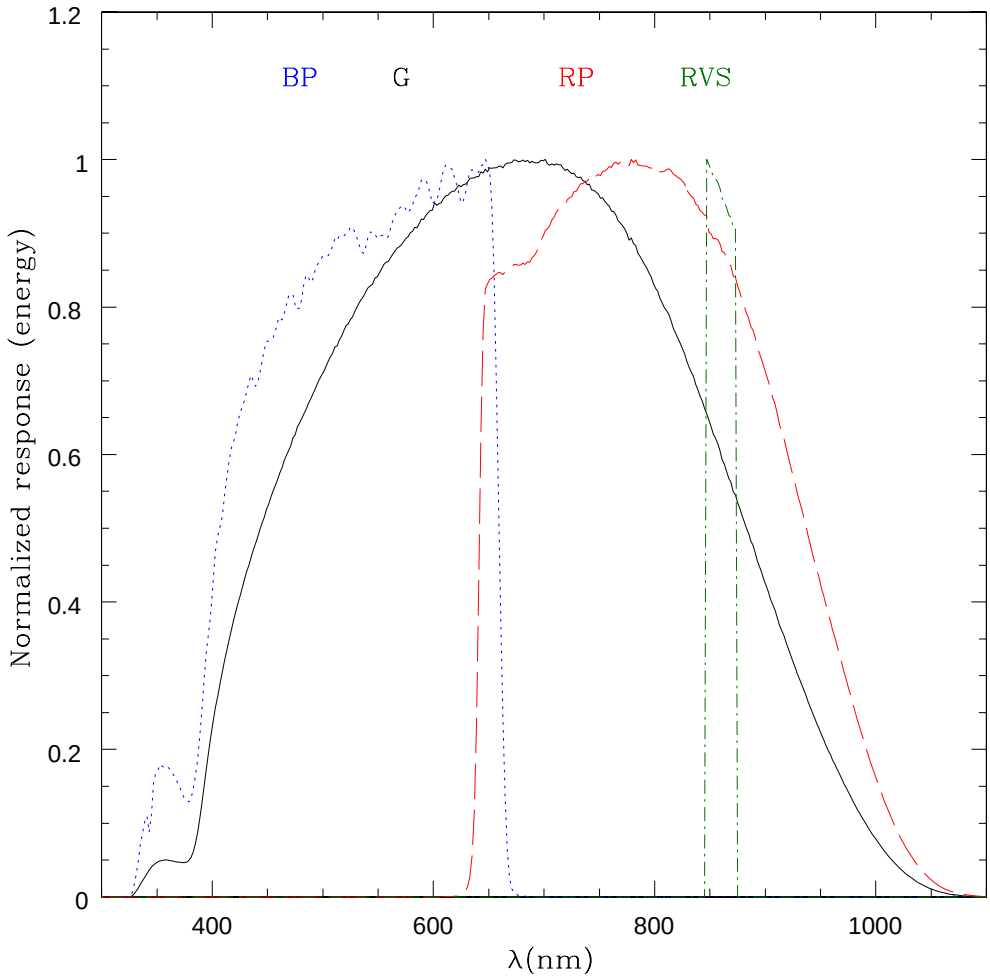

Fig. 1.5: *Gaia G* (solid black), $G_{\rm BP}$ (blue dotted), $G_{\rm RP}$ (red dashed) and $G_{\rm RVS}$ (green dash-dotted) normalised passbands (Figure 3. in Jordi et al. 2010).

CCDs which are located in the *Gaia* focal plane (3 CCD strips and 4 CCD rows, green in Fig. 1.4).

1.3.3 Pre-launch science performance

Despite the significant increase in accuracy of *Gaia* compared to *Hipparcos*, the *Gaia* survey will of course still be subject to error, due to both noise and calibration. In this section, we discuss the pre-launch science performance estimates and then in Section 1.3.4 we will discuss the updated estimates after the commissioning.

Fig. 1.6 shows the pre-launch estimated parallax error by G magnitude. The parallax will carry the heaviest error out of the astrometry, photometry

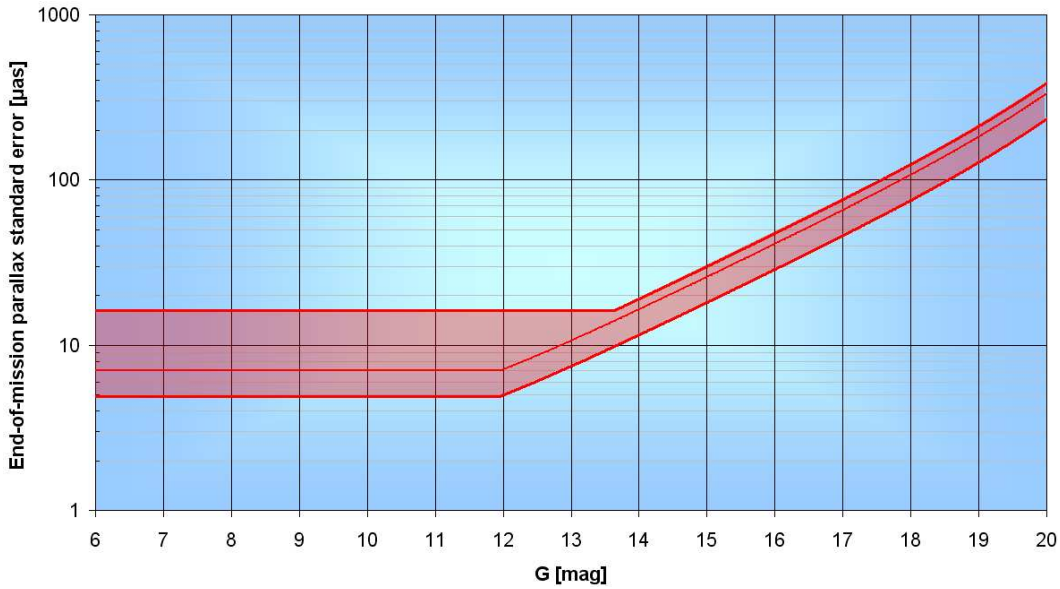

Fig. 1.6: Pre-launch expected end of mission parallax error by magnitude (Figure 10 in de Bruijne 2012).

and spectroscopy. The accuracy between $G = 12$ mag and $G = 20$ mag is limited by photon noise and background noise. Between $G = 6$ mag and $G = 12$ mag the CCDs are operating close to the saturation limit. Therefore, they are only partially exposed to avoid completely saturating the detector. Fig. 1.7 shows the pre-launch estimated photometric accuracy. The photometric accuracy is calibration dominated for sources with $G \lesssim 12$ mag. Fig. 1.8 shows the radial velocity error, which is dependent on magnitude and spectral type. With red stars, similarly to the photometric error, the error will become calibration dominated to a limit of 1 km s^{-1} for stars with $G \lesssim 14$ mag (Prusti 2012).

1.3.4 Post-launch revised science performance estimates

The *Gaia* science performance estimates have changed post launch. There are three significant issues as listed by de Bruijne et al. (2015). Firstly, the basic angle between the lines of sight of the two telescopes is more unstable than expected. Secondly, the transmission of the optics slowly degrades with time. Thirdly, there are significant levels of stray light, which periodically vary with time.

The first issue will be dealt with by using the Basic-Angle-Monitor

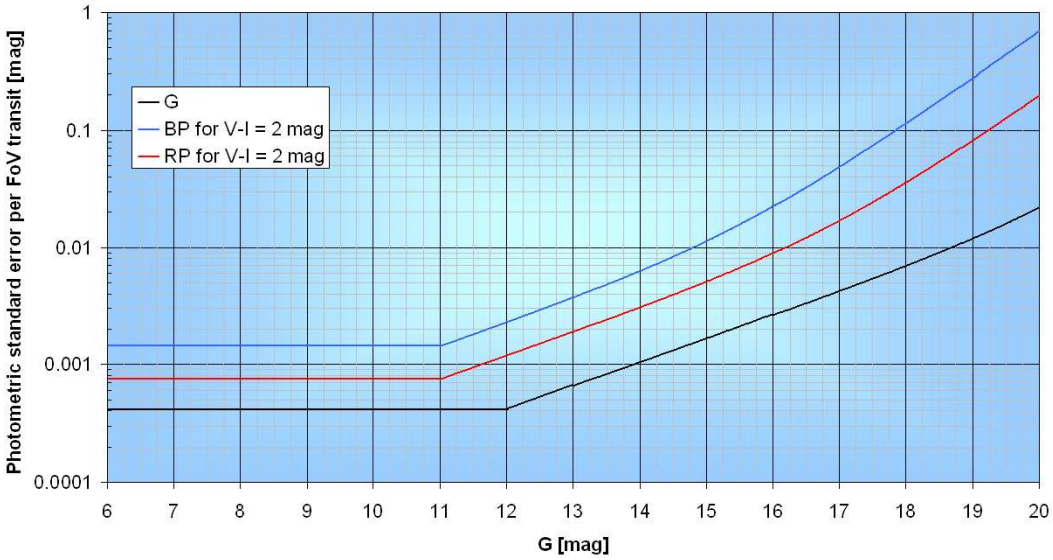

Fig. 1.7: Pre-launch expected end of mission photometric error by magnitude and color (Figure 11 in de Bruijne 2012).

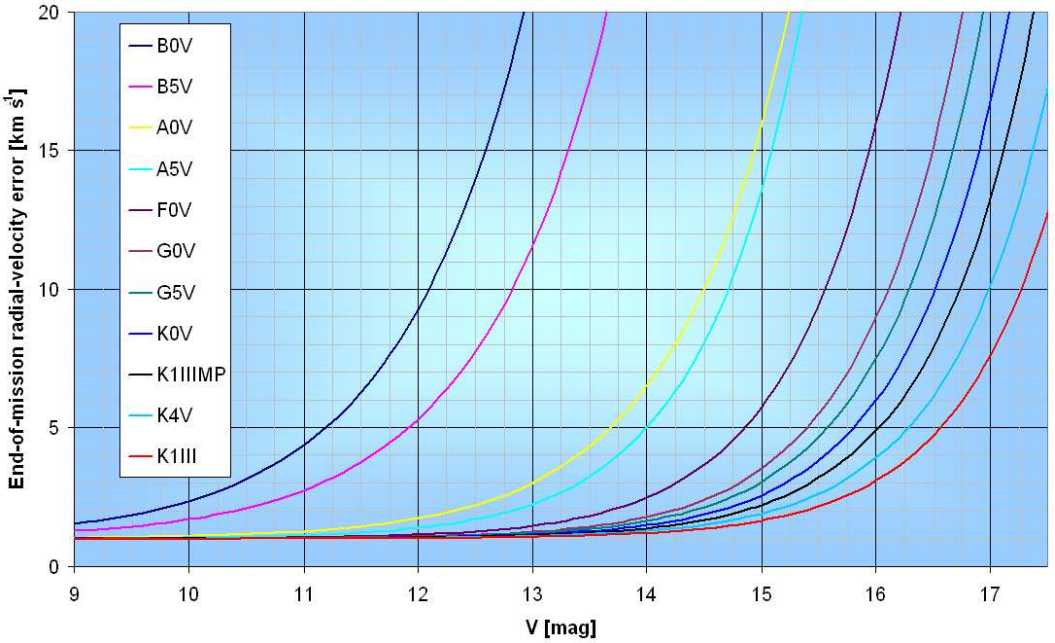

Fig. 1.8: Pre-launch expected end of mission radial velocity error by magnitude and spectral type (Figure 12 in de Bruijne 2012).

(Mora et al. 2014), which allows the measurement of the variations in the angle. Knowing the variation allows its inclusion in the astrometric global iterative solution (Lindegren et al. 2012). The second issue is considered to be caused by contamination by water ice on the mirrors in the payload module. This can be addressed by periodically heating the payload to decontaminate the optics. However, this affects the end-of-life performance by $\sim 10\%$. The third issue leads to increased noise levels, and thus has a non-trivial effect on the end-of-mission astrometric, photometric and spectroscopic standard errors (de Bruijne et al. 2015).

1.3.5 Data release scenario

The *Gaia* data will be available to the public upon release. It will be released in five major sections, with photometric science alerts and near Earth asteroid data being continually released at short notice. This section provides a summary of the current timeline for the major data releases, although this is subject to change based upon the ongoing commissioning phase. The information presented in this section is available online[5] as of 6^{th} April 2015.

The first release is scheduled for summer 2016. It consist of positions (α, δ) and G mag for single-star systems with acceptable errors. This data release will also include the Hundred Thousand Proper Motion (HTPM, de Bruijne & Eilers 2012) project catalogue, which will provide proper motions for the stars in the *Hipparcos* catalogue. Using the 23 year baseline since the *Hipparcos* measurements, the HTPM project proper motion errors will be $14-134$ μas yr^{-1} and the parallax errors will be $\sim$ 43-295 μas (Michalik et al. 2014).

The second data release is scheduled for early 2017. It will consist of five parameter astrometry $(\alpha, \delta, \pi, \mu_\alpha, \mu_\delta)$ for single-star systems. It will also include BP/RP photometry with standard errors for sources where the astrophysical parameter estimation has been verified, and mean radial velocities for sources showing no variation.

The third data release is scheduled for 2017/18. It will consist of orbital solutions, with the system radial velocity and five parameter astrometry for

[5] http://www.cosmos.esa.int/web/gaia/release

many binary systems. It will also contain a classification of the object and its stellar parameters, with BP/RP spectra and/or RVS spectra. Mean radial velocities will also be released for objects not showing variability and with available atmospheric parameter estimates.

The fourth data release is scheduled for 2018/19. It will consist of variable star classifications, released together with the epoch photometry used for the stars. It will also include solar-system results and non-single star catalogues.

The fifth and final data release is scheduled for 2022, and will consist of full astrometric, photometric and radial velocity catalogues. It will contain all available variable star and non-single star solutions and source classifications. It will also contain astrophysical parameters for stars, unresolved binaries, galaxies and quasars. Additionally, a list of exo-planets, epoch and transit data for all sources and all ground based observations will be released.

This full data set will provide an unprecedentedly large amount of data about the Galaxy we live in, and will be an ideal opportunity to improve upon our knowledge of the structure of the Milky Way and its fundamental parameters. However, despite the amount of objects which *Gaia* will detect, this is still only a fraction of the objects present in the Milky Way. Fig. 1.9 shows a face-on artist's impression of the Milky Way (upper, Churchwell et al. 2009) constrained by available data, including stellar data from the Galactic Legacy Mid-Plane Survey Extraordinaire (GLIMPSE) and an image of the Milky Way on the sky from the ESO 'GigaGalaxy Zoom' project[6] (lower). The images are overlaid with the predicted density of the stars observed by *Gaia*[7]. Fig. 1.9 shows that even with *Gaia's* impressive capabilities it will still be a long way short of observing the entirety of our Galaxy, and the structure on the far side of the Galactic centre will remain comparatively uncertain. This highlights the challenge of constructing a global picture of the Milky Way directly from the *Gaia* data.

[6] http://videos.spacetelescope.org/gigagalaxyzoom/B.html

[7] http://www.cosmos.esa.int/web/gaia/iow_20110810

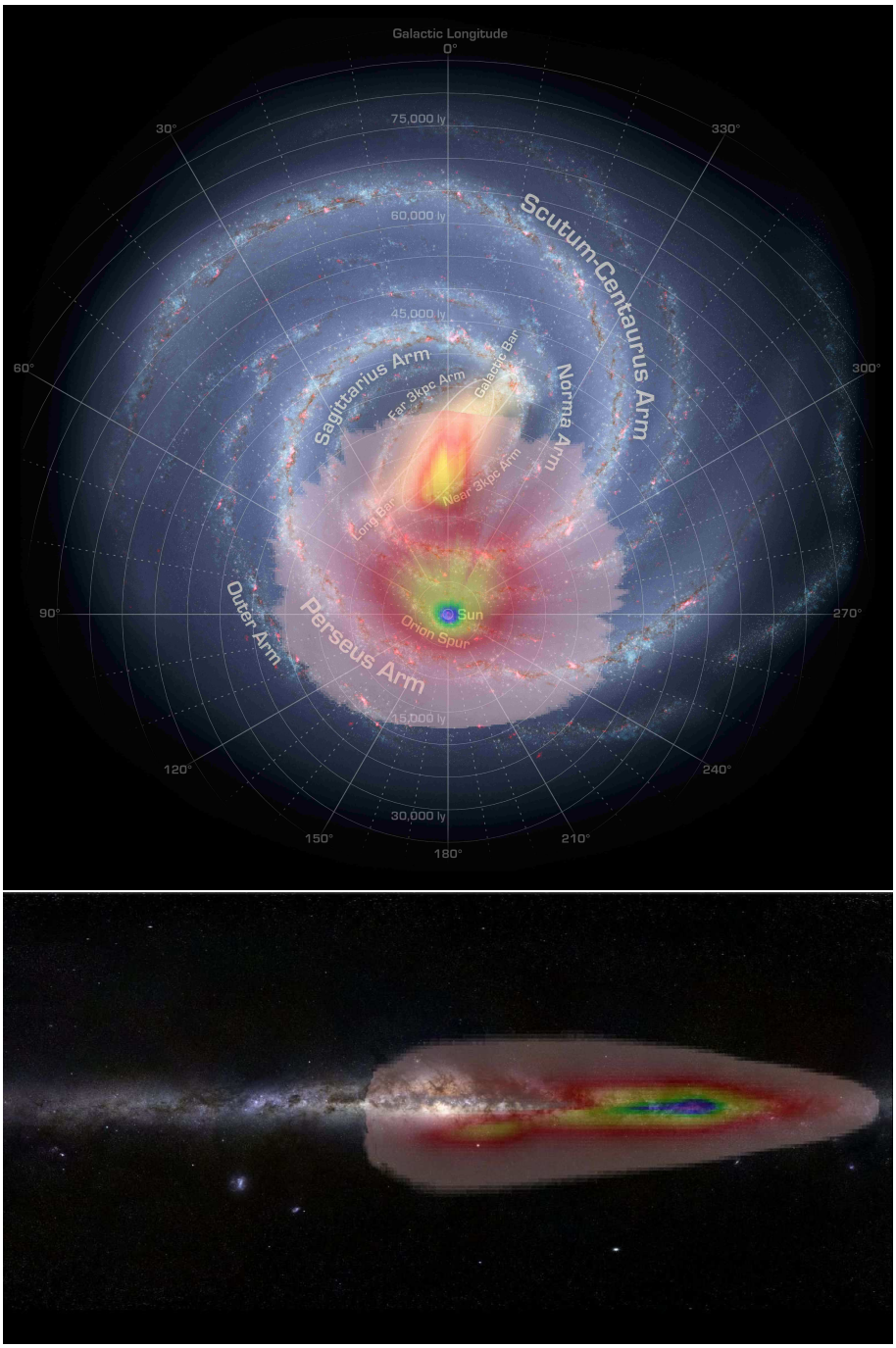

Fig. 1.9: Face-on artists impression (upper, Churchwell et al. 2009) and image on the sky (lower) of the Milky Way overlaid with colour contours of the number density of stars which *Gaia* is predicted to observe in the Milky Way. The overlay is colour coded to represent the density of stars *Gaia* will detect, with higher density regions shown in blue, and lower density regions shown in pink (credit to X. Luri & A. Robin for the overlaid image of the distribution of stars expected to be observed with *Gaia*.)

1.4 The structure of the Milky Way

Data from modern surveys have helped us to learn an enormous amount about the Milky Way, and our understanding of the Galaxy that is our home in the Universe is vastly superior than in the days of Hipparchus and Ptolemy. The Milky Way is known to be a barred spiral galaxy (e.g. Spergel & Blitz 1990; Weinberg 1992; Binney et al. 1997) which is made up of three components, the disc, the halo and the bulge/bar. This thesis focuses on the disc and the bar.

This section gives a short summary of a few of the estimated values for some of the fundamental parameters of the Milky Way. We focus on the angle between the bar and the line-of-sight to the Galactic centre, henceforth bar angle, the pattern speed of the bar, the distance from the Sun to the Galactic centre, the circular velocity at the solar radius, and the debate regarding the thin and thick disc.

1.4.1 Structure of the bar

While it is known that there is a bar in the inner region of the Milky Way, there is disagreement over whether the bar is formed of a single structure, or if it is also comprised of a short bar and a separate long flat bar with a different bar angle from that of the short bar.

The short bar, which is thick in the z direction, is visible in the data from the Cosmic Background Explorer (*COBE*, Boggess et al. 1992). For example, Dwek et al. (1995) recover an angle between the bar and the line-of-sight to the Galactic centre of $20^{\rm o} \pm 10^{\rm o}$ from data from the Diffuse Infrared Background Experiment (DIRBE) on the *COBE* satellite. The long bar, which is thin in the z direction, was observed later. Hammersley et al. (2000) present evidence for the long bar from Infra-red observations in the galactic plane for $0^{\rm o} \leq l \leq 37^{\rm o}$. They obtain a bar angle of $43^{\rm o} \pm 7^{\rm o}$, noting that it is geometrically distinct from the short thick bar. Cabrera-Lavers et al. (2007) analyse the distribution of red clump stars from the TCS-CAIN Near Infrared (NIR) survey (González-Fernández et al. 2007) at different lines of sight in the inner Galaxy. They also find two distinct bar structures. Cabrera-Lavers et al. (2007) find a short thick bar with an angle of $12.6^{\rm o} \pm 3.2^{\rm o}$, and a long thin bar

with an angle of $43^{\circ} \pm 1.8^{\circ}$. Cabrera-Lavers et al. (2008) also find two distinct bars in the UKIRT Infrared Deep Sky Survey (UKIDSS, Lawrence et al. 2007) Galactic Plane Survey data, again using red clump tracers. The short thick bar is found to have an angle of $23.6^{\circ} \pm 2.19^{\circ}$, and the long thin bar is found to have an angle of $42.44^{\circ} \pm 2.14^{\circ}$.

However, as stated in Athanassoula (2013), although around $20 - 25\%$ of barred galaxies have two bars, the ratio of the lengths of the bars measured for the Milky Way is incompatible with observations of external galaxies. The average ratio of length between the short and long (or primary and secondary) bar in external galaxies is ~ 0.12. However, the ratio of the short and long bar in the Milky Way is ~ 0.8 (Romero-Gómez et al. 2011). Thus, they conclude that it is highly unlikely that the long and short bar are separate structures. It is proposed (e.g. Romero-Gómez et al. 2011; Athanassoula 2013) that these two bars are components of a single bar with the short bar being the boxy/peanut component and the long bar being the thin outer component. Martinez-Valpuesta & Gerhard (2011) corroborate this interpretation by calculating 'observed' star counts from an N-body model with a single boxy bar. They show that observations of two separate bars with different bar angles can be reproduced from a single boxy bar, owing to interactions between spiral structure and the ends of the boxy bar.

However, the difference in estimated angles is still at odds with this interpretation. Athanassoula (2013) state that new measurements of the angle of the long bar are lower (e.g. 35°, Zasowski et al. 2012) than the initial estimations, and the shape of the bar may cause the measurements of the angles to be artificially high for the thin component. Wegg et al. (2015) analyse the distribution of red clump giant stars from UKIDSS, 2MASS, VVV and GLIMPSE. They find a continuous transition in the scale heights of the red clump giants between the thick boxy/bulge and the long bar, concluding that it is a single structure as seen in external galaxies and N-body simulations, with a bar angle of $28 - 33^{\circ}$.

1.4.2 Pattern speed of the bar

There is also still discussion of the pattern speed of the bar, $\Omega_{\rm p}$, which is a measure of the speed with which the bar rotates. For example, Binney et al. (1997) calculate a value of $\Omega_{\rm p} = 60 - 70$ km s^{-1} kpc^{-1} from a model constructed to match the *COBE*/DIRBE surface brightness map of the inner galaxy. Dehnen (2000) performs simulations of a barred disc galaxy, and analyses the velocity distribution around the Outer Lindblad Resonance (OLR). He finds that, if the OLR of the bar is close to the Solar radius and the bar angle is $10 - 70^{\rm o}$ (which easily encompasses the estimations of the bar angle of the Milky Way, see Section 1.4.1), there is a bi-modality in the radial-tangential, $(U - V)$, velocity distribution of Solar neighbourhood stars. Dehnen (2000) shows that this bi-modality is present in the *Hipparcos* data, and infers that the OLR in the Milky Way is slightly smaller than the radius of the Sun. He shows that the pattern speed of the bar in the simulations is 1.85 ± 0.15 times the local circular frequency, Ω_0. Thus, Dehnen (2000) predicts a pattern speed of the Milky Way's bar of $\Omega_{\rm p} = 53 \pm 3$ km s^{-1}kpc^{-1} using the value of $\Omega_0 \sim 28.5$ (Reid et al. 1999; Backer & Sramek 1999). This is of course providing that the bi-modality (one component of which is the Hercules stream) is caused by the OLR of the bar. However, another interpretation is that it is induced by spiral structure (e.g. Quillen et al. 2011). Debattista et al. (2002) adapt the Tremaine-Weinberg method (Tremaine & Weinberg 1984) with OH/IR stars (hydroxyl masers which are bright in IR) from the Australia Telescope Compact Array and Very Large Array (ATCA/VLA) OH 1,612 MHz survey (e.g. Sevenster et al. 1997). Assuming that the radial velocity component of the local standard of rest, $U_{\rm LSR} = 0$, $R_0 = 8$ kpc and the tangential component of the local standard of rest, $V_{\rm LSR} = 220$ km s^{-1}, they calculate $\Omega_{\rm p} = 59 \pm 5 (\pm 10$ systematic) km s^{-1}kpc^{-1}.

Gerhard (2011) provides a review of previous work, concluding a likely pattern speed for the bar of $\Omega_{\rm p} \sim 50 - 60$ km s^{-1}kpc^{-1}. However, the debate is ongoing, with more recent work finding both high and low values of $\Omega_{\rm p}$. For example, Antoja et al. (2014) analyse the kinematics of the Hercules stream-like feature in the $U - V$ velocity distribution at different Galactic radii using

the RAVE data, building on the work in Dehnen (2000). They calculate $\Omega_{\rm p} = 56 \pm 2$ km s^{-1}kpc^{-1}, a similar value to Dehnen (2000). Long et al. (2013) found $\Omega_{\rm p} \sim 40$ km s^{-1}kpc^{-1} and Portail et al. (2015) found $\Omega_{\rm p} \sim 25 - 29$ km s^{-1}kpc^{-1}, both using data from BRAVA as constraints for Made-to-Measure (M2M) modelling (see Section 1.6).

1.4.3 Position of the Sun

The distance from the Sun to the Galactic centre, R_0, also contains uncertainty, and estimations of other parameters, for example, the circular motion at R_0 and the solar proper motion, are affected by an assumed R_0. Some examples of estimations of R_0 are as follows. McMillan (2011) uses Bayesian statistics to find the probability density function (pdf) for multiple Galactic parameters, using observational kinematic data and prior parameter estimations from existing literature. He finds a best fitting value of $R_0 = 8.29 \pm 0.16$ kpc. Schönrich (2012) analyses Data Release 7 and 8 (DR7, DR8) of SDSS. He finds a value of $R_0 = 8.27 \pm 0.29$ kpc, which is in excellent agreement with the value of McMillan (2011).

Maser data can be used to constrain R_0, and the galactic spiral structure (see Section 1.4.6). Maser emission is associated with high mass star forming regions, and provide tracers for the Galactic structure. VLBI techniques can provide parallaxes and proper motions for the masers. By fitting a model of the Galaxy to data from 20 masers in 18 star forming regions, Reid et al. (2009a) find $R_0 = 8.4 \pm 0.6$ kpc. Reid et al. (2009b) calculate the parallax for masers in Sgr B2, a high mass star forming region in the Galactic centre. They find a value of $R_0 = 7.9^{+0.8}_{-0.7}$ kpc. Reid et al. (2014) repeat the analysis of Reid et al. (2009a) on a sample of 103 masers, and finds $R_0 = 8.34 \pm 0.16$ kpc. Fig. 1.10 shows the parallax derived positions for the sample of masers in Reid et al. (2014), overlaid on the artists impression of the Milky Way in Churchwell et al. (2009) also seen in Fig. 1.9.

1.4.4 Circular velocity at the solar radius

Coupled with R_0, estimation of the circular velocity at R_0, $v_{\rm circ}(R_0)$, remains uncertain. While the IAU recommended value of the local circular veloc-

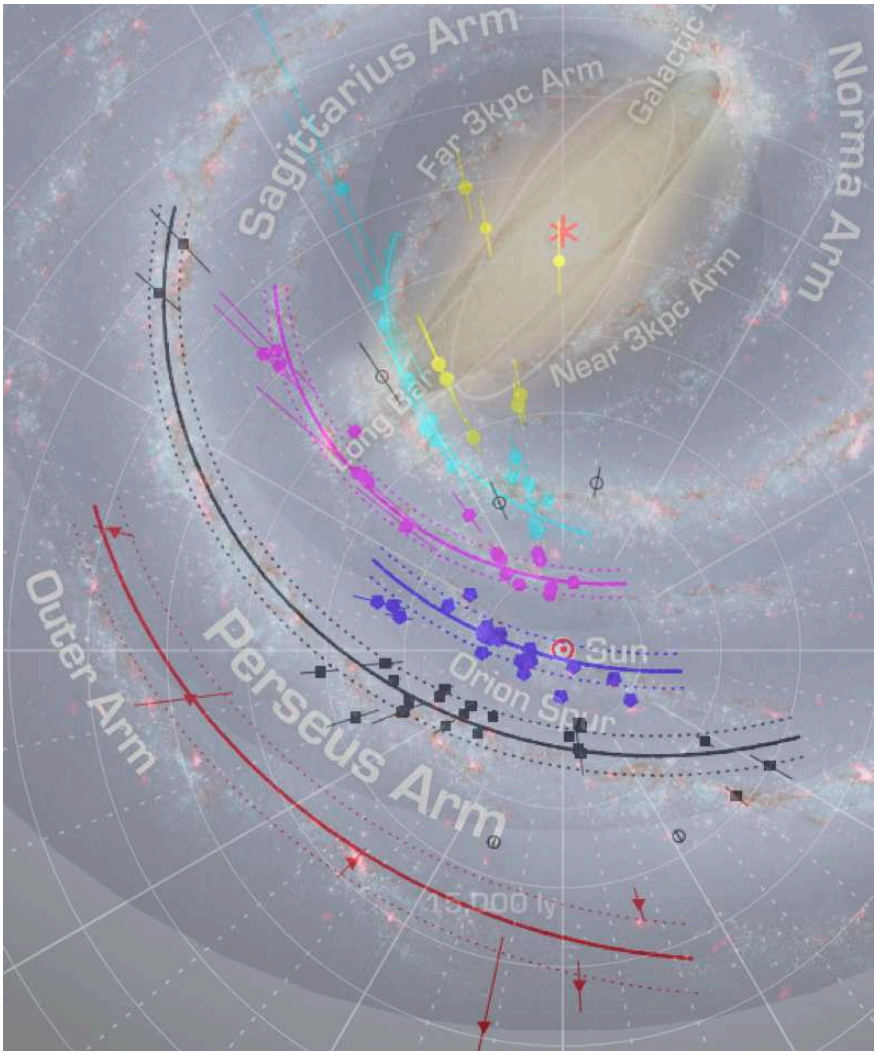

Fig. 1.10: Figure 1 of Reid et al. (2014) showing parallax derived positions for their sample of masers, overlaid on the artists impression of the Milky Way in Churchwell et al. (2009) also seen in Fig. 1.9. The different coloured points are masers associated with different spiral arms. These include the Outer arm (red triangles), Perseus arm (black squares), Local or Orion arm (blue pentagons), Sagittarius arm (pink hexagons) and Scutum-Centaurus arm (cyan octagons). The yellow circles are inner galaxy sources, and the open circles are masers for which the assignment to an arm was not clear. The solid lines show the centre of the spiral arms calculated in Reid et al. (2014).

ity remains at $v_{\rm circ}(R_0) = 220$ km s^{-1} (Kerr & Lynden-Bell 1986), there are many different estimates. For example, Reid & Brunthaler (2004) estimate $v_{\rm circ}(R_0)$ by considering the motion of the Galactic centre. They calculate the angular motion of Sgr $A^\star$ in the Galactic plane as -241 ± 15 km s^{-1}. Then, removing the Solar motion of $V_\odot = 5.25 \pm 0.62$ km s^{-1} (Dehnen & Binney 1998) gives a value of $v_{\rm circ}(R_0) = 236 \pm 15$ km s^{-1} (assuming $R_0 = 8.0 \pm 0.5$ kpc). However, assuming a different value of the Solar motion will change the measurement of $v_{\rm circ}$. For example, using the value of the Solar motion of $V_\odot = 12$ km s^{-1} (Cox 2000) reduces the measurement to $v_{\rm circ}(R_0) = 229$ km s^{-1}. Reid et al. (2014) find a value of $v_{\rm circ}(R_0) = 240 \pm 8$ km s^{-1} (assuming $R_0 = 8.34 \pm 0.16$ kpc) for their model fit to the maser data as described in Section 1.4.3. Again, this estimate is dependent on the Solar motion, which is estimated at $V_\odot = 14.6 \pm 5.0$ km s^{-1}. McMillan (2011) finds a best fitting value of $v_{\rm circ}(R_0) = 239.2 \pm 4.8$ km s^{-1} (assuming $R_0 = 8.29 \pm 0.16$ kpc). Schönrich (2012) finds $v_{\rm circ}(R_0) = 238 \pm 9$ km s^{-1} (assuming $R_0 = 8.27 \pm 0.29$ kpc) using the method described in Section 1.4.3, assuming a solar motion of $V_\odot = 12.24 \pm 0.47 (\pm 2$ systematic) km s^{-1} (Schönrich et al. 2010). Bovy et al. (2012a) analyse APOGEE data in the Galactocentric range of $4 < R < 14$ kpc. They fit an axisymmetric kinematic model to the observed line-of-sight velocities making no prior assumption of R_0 or $V_\odot$. Bovy et al. (2012a) estimate $v_{\rm circ}(R_0) = 218 \pm 6$ km s^{-1} and $v_{g,\odot}(R_0) = 242^{+10}_{-3}$ km s^{-1} from the model, resulting in a Solar motion of $V_\odot = 26 \pm 3$ km s^{-1}. Bovy et al. (2012a) state that they can strongly rule out a value of $v_{\rm circ}(R_0) > 235$ km s^{-1}.

1.4.5 Thin and thick disc

While we call the disc one of the three components of the Milky Way, it is often classified as having 'thin' and 'thick' components. In this section, we will discuss the discovery, structure, and formation theories of the thin and thick disc.

Gilmore & Reid (1983) show for the first time the separate components in our Galaxy's disc, which were previously observed in external galaxies (e.g. Tsikoudi 1979; Burstein 1979), by analysing a sample of 12,500 stars complete to $I \leq 18$ mag and $V \leq 19$ mag, from UK Schmidt Telescope plates in 18.24

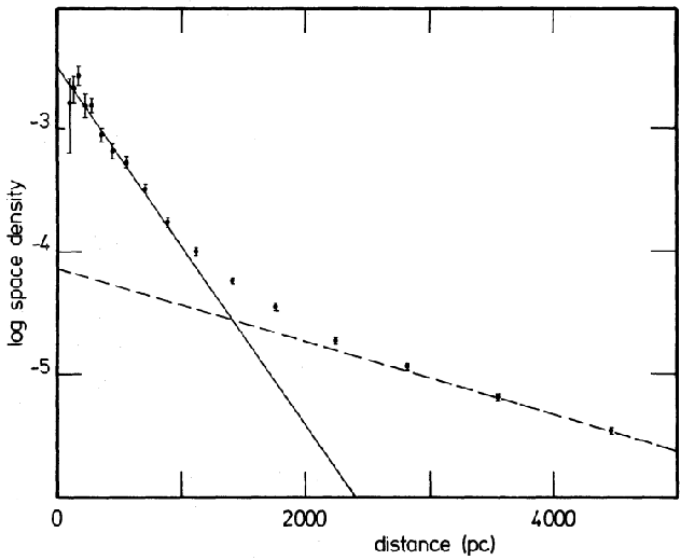

Fig. 1.11: From Figure 6a in Gilmore & Reid (1983) showing star counts against distance from the galactic plane for stars with $4 \leq M_V \leq 5$ (circles) which are fit by two exponentials for the 'thin' (solid) and 'thick' (dashed) disc components.

square degrees in the direction of the South Galactic Pole. They calculate photometric distances using an absolute magnitude-colour relation for dwarf stars. By calculating the number density distribution for different magnitude ranges, they find an 'old thin disc' which can be fit with an exponential profile with scale height $z_\mathrm{d} = 0.3$ kpc and a 'thick disc' which can be fit with an exponential profile with $z_\mathrm{d} = 1.45$ kpc. Fig. 1.11 (Figure 6a in Gilmore & Reid 1983) shows the number density of stars as a function of distance from the galactic plane for stars with $4 \leq M_V \leq 5$ mag (circles) which are fit by two exponentials for the 'thin' (solid) and 'thick' (dashed) disc components.

Table 1 in Siegel et al. (2002) provides a summary of previous estimations of the scale length and height of the thin and thick discs ($2.25 \leq R_\mathrm{d,thin} \leq 4.0$ kpc, $0.2 \leq z_\mathrm{d,thin} \leq 0.475$ kpc, $2.8 \leq R_\mathrm{d,thick} \leq 4.3$ kpc, $0.58 \leq z_\mathrm{d,thick} \leq 2.39$ kpc). Jurić et al. (2008) shows strong evidence for a two component Galactic disc in their analysis of SDSS data. They show the 3D number density distribution in the solar neighbourhood is fit well by two exponential components with $R_\mathrm{d,thin} = 2.6$ kpc, $z_\mathrm{d,thin} = 0.3$ kpc, $R_\mathrm{d,thick} = 3.6$ kpc and $z_\mathrm{d,thick} = 0.9$ kpc.

However, the formation scenario for the two disc components is not known.

Mikolaitis et al. (2014) summarise the four main categories of theory as: 1) the heating of an existing thin disc by a violent merger (e.g. Quinn et al. 1993), 2) the merger of small satellites which deposit stars into the thick disc (e.g. Abadi et al. 2003), 3) the formation of a thick disc in situ following a strong accretion of gas (e.g. Brook et al. 2004), and 4) the radial rearrangement of the disc via radial mixing (e.g. Schönrich & Binney 2009).

Sales et al. (2009) study the orbital properties of stars in a simulation based upon each of these four possible scenarios, with a view to constrain the formation mechanism based upon orbital eccentricity. They find that there are differences in eccentricity in each simulation, and the level of eccentricity of thick disc stars should help determine between formation scenarios based on in situ formation scenarios (e.g. Brook et al. 2004) which have stars with low eccentricities, and mergers (e.g. Abadi et al. 2003) which have stars with high eccentricities. However, merger driven accretion may also have stars with low eccentricities if the accretion is similar to the rotation of the disc. Sales et al. (2009) state that with the current level of kinematic data available they are unable to make a definitive distinction based on orbital eccentricities.

Bovy et al. (2012b) make the claim that the Milky Way has no distinct thick disc (see also Bovy et al. 2012c,d). They analyse the distribution of $\sim 24,000$ G-type dwarfs from SDSS/SEGUE in the [Fe/H] versus [α/Fe] distribution, and find that when weighting by mass and correcting for the uneven sampling of the underlying stellar populations, the bi-modality of the thin and thick disc populations seen in the raw data disappears. However, because of the low resolution spectroscopy of the SEGUE data, combined with the typically large uncertainties in the chemical abundance measurements, 0.1 dex for [α/Fe] and 0.2 dex for [Fe/H] (Lee et al. 2011), the small separation between thin and thick disc populations can be smoothed out.

Bensby et al. (2011) analyse a sample of 26 microlensed dwarf and subgiant stars in the Galactic bulge, with detailed stellar abundances and ages. They find a bi-modality in [Fe/H] for the microlensed stars, with peaks at [Fe/H]~ -0.6 and [Fe/H]~ 0.3. There is a distinct gap at solar metallicity. This is in contrast with a sample of 204 red giant stars in the bulge from

FLAMES-GIRAFFE spectra (Zoccali et al. 2008), which peaks around Solar metallicity. The low metallicity dwarfs are found to be old stars, with $\langle Age \rangle = 11.7 \pm 1.7$ Gyr (mean age $\pm$ dispersion), while the high metallicity dwarfs are found to have a large range of ages, with $\langle Age \rangle = 7.6 \pm 3.9$ Gyr. They cannot give a conclusive reason for the different metallicity distribution functions for the dwarf and giant stars. However, the metal poor dwarfs show similar ages, metallicities and abundances to stars in the thick disc and they speculate that the metal rich dwarfs could be from the thin disc. This is evidence that the Milky Way contains no distinct bulge component, as suggested by results from the BRAVA survey (e.g. Shen et al. 2010) and corroborated by results from the ARGOS survey (e.g. Ness et al. 2013) and N-body simulations (e.g. Di Matteo et al. 2015).

Bensby et al. (2014) analyse high resolution spectra from a sample of 714 F and G dwarfs in the solar neighbourhood. This sample of stars was chosen to cover a wide range of metallicities and are shown to be a good representation of the stars in the GCS, i.e. an unbiased sample, in terms of the metallicity-velocity relation. Bensby et al. (2014) show a chemically distinct bi-modal distribution in the sample. The bi-modality is seen in multiple abundance relations. Most abundances have an accuracy of $\lesssim 0.2$ dex. Mikolaitis et al. (2014) analyse a sample of $\sim 2,000$ F, G and K dwarfs from the Gaia-ESO survey and also find a clear bi-modality, with the most distinct separation in [Mg I/Fe]. Mikolaitis et al. (2014) find no radial metallicity gradient in the thick disc, which is consistent with other studies (e.g. Bensby et al. 2011; Cheng et al. 2012). This is in agreement with the predictions of a gas rich disc at high redshift, e.g. scenario 3, but can also be consistent with the other scenarios if mixing in the radial direction is strong (Cheng et al. 2012).

Nidever et al. (2014) analyse the metallicity and α-element abundances of $\sim 10,000$ red clump stars from APOGEE with $\sim 5\%$ distance errors (Bovy et al. 2014). There is a distinct bi-modality in the [α/Fe] versus [Fe/H] distribution for $-0.9 <$ [Fe/H] < -0.2. However, at higher metallicities ([Fe/H]$\sim$0.2) the two clear populations merge. The shape of the high [α/Fe] population in the [α/Fe] versus [Fe/H] distribution remains similar across the

observed area of the Galaxy. The low [α/Fe] population is substantially more dominant closer to the disc plane. This is a strong bi-modality, with a clear gap at intermediate levels of [α/Fe], which can be taken as a strong indication that the thin and thick discs are distinct populations.

There is currently no definitive observational evidence to determine definitively between the differing scenarios of the origin of the thick disc. It is likely that multiple mechanisms play a part in the formation of the thick and thin disc. However, it is currently not clear which mechanism is primarily responsible. Upcoming surveys, both *Gaia* and spectroscopic ground based surveys (see Section 1.2), will provide the next level of dynamical and chemical information about the stars in our Galaxy, and will help to place more constraints upon the formation history of the thin and thick discs.

1.4.6 Spiral structure

The spiral structure in the Milky Way also suffers from uncertainties, both in terms of the properties of our Galaxy's spiral structure, and also the origin from which spiral structure forms. This section will first discuss briefly the theories of spiral arms (for a comprehensive review, see Dobbs & Baba 2014) and then provide a few examples of estimates of the Milky Way's spiral structure.

It is known from observations of the almost flat rotation curve of disc galaxies that the stars in the inner region have a higher angular velocity, $\Omega = v_{\rm rot}/R$, than those in the outer region. Therefore the spiral structure should 'wind up' relatively quickly if the spiral arms rotate at the mean rotation velocity of the stars (e.g. Wilczynski 1896), which is contrary to observations of many 'grand design' spiral galaxies. This is called the 'winding dilemma', and is one of the classic problems with spiral arm theories. A proposed solution to the winding dilemma is given by spiral density wave theory (Lin & Shu 1964). This theory treats the spiral structure as a density wave which can rotate rigidly as a feature, irrespective of the rotation of the stars, with a constant pattern speed and thus be long lived.

However, no N-body simulations (see Section 1.5.6) have yet been able to reproduce these long lived stable spiral arms, despite the increase in computational power and resolution which has occurred in recent years

(e.g. Sellwood 2011; Dobbs & Baba 2014). Recent work has shown spiral modes and waves which appear to survive over multiple rotations (Quillen et al. 2011; Roškar et al. 2013; Sellwood & Carlberg 2014) when analysing spectrograms (see Grand et al. 2012a, for a caution on this technique). However, the spiral arm features in the stellar mass are short-lived but recurrent (e.g. Sellwood & Carlberg 1984; Carlberg & Freedman 1985; Bottema 2003; Fujii et al. 2011; Grand et al. 2012a,b, 2013; Baba et al. 2013; Roca-Fàbrega et al. 2013; D'Onghia et al. 2013), including in galaxies with a central bar (e.g. Grand et al. 2012b; Roca-Fàbrega et al. 2013). These results imply that the large spiral arms visible in external galaxies may only *appear* to be rigid structures extending over the disc, while in fact they are transient and reforming features.

Observationally, the number and nature of the spiral arms in the Milky Way remains unclear. Vallée (2014b) gives a summary of recent (late 2013 to mid 2014) studies of the spiral arm structure in the Milky Way, with the majority of recent studies favouring a four armed logarithmic spiral (e.g. Reid et al. 2014). However, approximately one sixth of the studies (Vallée 2014b) favour a more tightly wound two arm spiral (e.g. Francis 2013). Benjamin et al. (2005) show results from GLIMPSE, which is a catalogue of $\sim 3 \times 10^7$ sources within $\mid b \mid \leq 1^{\rm o}$. They show three regions ($26^{\rm o} \leq l \leq 28^{\rm o}, 31.5^{\rm o} \leq l \leq 34^{\rm o}, 306^{\rm o} \leq l \leq 309^{\rm o}$) where stellar counts are $\sim 20\%$ higher than what is expected from the exponential fitting function. The $l = 26^{\rm o} - 28^{\rm o}$ region may be related to the bar. The $l = 31.5^{\rm o} - 34^{\rm o}$ region may also be associated with the bar, or the inner part of the Scutum-Centaurus arm. The $l = 306^{\rm o} - 309^{\rm o}$ region could be the tangent of the Centaurus arm. No enhancement in the stellar counts is found in the direction of the Sagittarius arm.

Reid et al. (2014) use the maser data described in Section 1.4.3 to identify the location of the spiral arms. The high mass star forming regions which contain the masers can be assigned to a spiral arm by association with CO and HI emission features in the longitude-line-of-sight velocity ($l - v$) map. Fig. 1.10 shows the parallax derived positions for the sample of masers (Figure 1 in Reid et al. 2014). It is overlaid on the artists impression of the Milky

Way's bar and spiral structure in Churchwell et al. (2009) constrained by the GLIMPSE data and HI 21 cm Galactic Plane Surveys and CO surveys. The different coloured points are masers associated with different spiral arms. The solid lines show the centre of the spiral arm calculated in Reid et al. (2014). Fig. 1.10 shows that the maser data of Reid et al. (2014) are in reasonable agreement with the view of Churchwell et al. (2009). However, the maser data favours a lower pitch angle for the Perseus (Black), Sagittarius (pink), Outer (red) and Orion (or local, blue) arms, and a larger pitch angle for the Scutum (cyan) arm.

Vallée (2014a) provides a catalogue of spiral arm tracers published since the 1980s. Fig. 1.12, which is Figure 3 in Vallée (2014a), shows an estimation of the distribution of spiral arms in the Milky Way constructed from the various sets of tracers. Fig. 1.12 shows the stellar (yellow), ^{12}CO (and H_2) (blue), hot dust (red), thermal and relativistic electrons and HI atoms (green), and cold dust (orange) components of the arms. Fig. 1.12 shows an offset between the stellar and gaseous components of the Galaxy's spiral arms, which is predicted by density wave theory (Roberts 1969). However, Baba et al. (2010), find that the $l - v$ map of the Milky Way is more easily fit with a simulation with dynamic spiral arms seen in N-body simulations (see above). Pettitt et al. (2014) use Smoothed Particle Hydrodynamics (SPH) simulations to study the interstellar medium (ISM) in the Milky Way. They construct synthetic $l - v$ emission maps and compare them with observed emissions. They find that neither the two arm or four arm model fits perfectly. The two armed models cannot reproduce all the observed arm features, and the four armed models produce too high emissions in the inner galaxy.

No firm conclusion can be drawn from the current observational data. The data from *Gaia*, amongst other current and upcoming surveys, will help further constrain the nature of the Milky Way spiral structure. We will discuss this further in Chapter 5. Of course, the uncertainty in the measurements of both the spiral structure and the more general parameters of the Milky Way's structure, comes primarily from interstellar extinction. Unlike surveys of external galaxies, where the extinction can be corrected for with a function

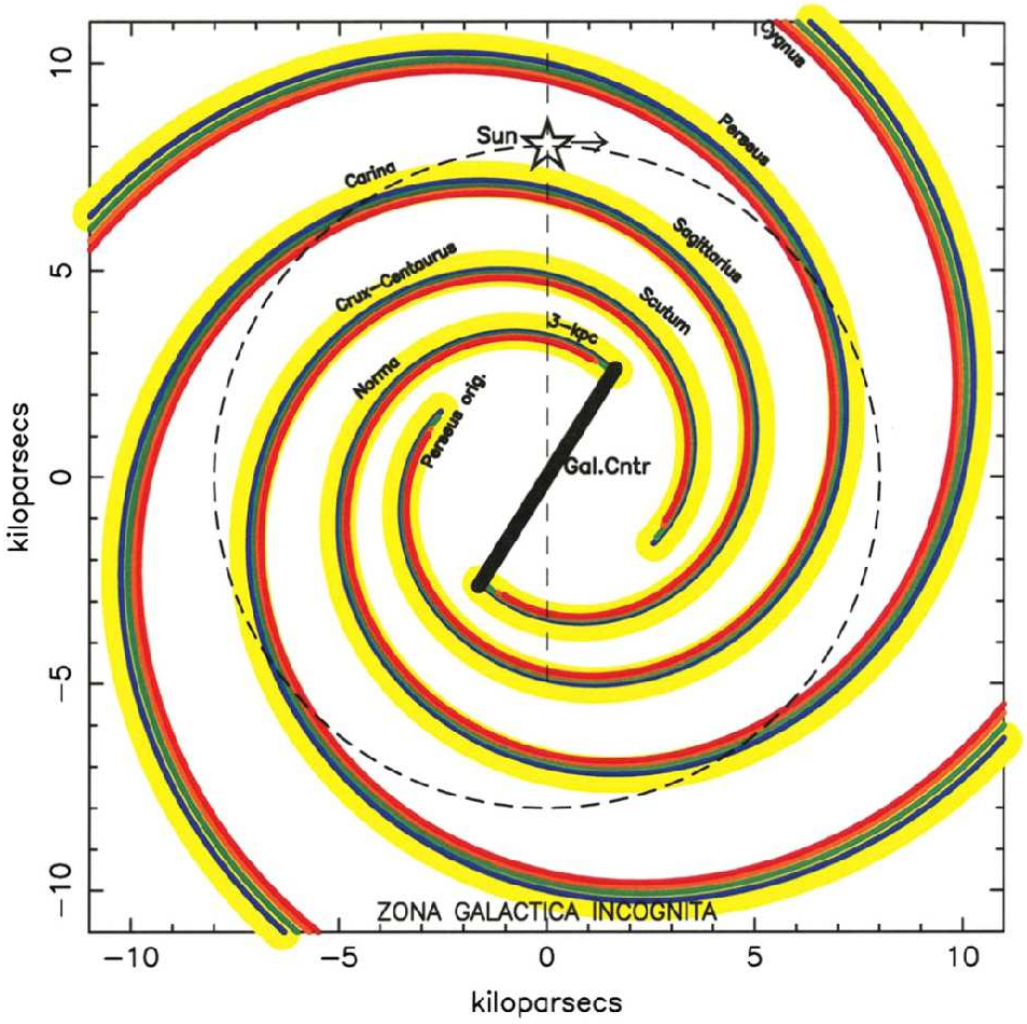

Fig. 1.12: Figure 3 in Vallée (2014a) showing the estimated spiral arm structure of the Milky Way constructed from various tracer data. The figure shows the stellar (yellow), ^{12}CO (and H_2) (blue), hot dust (red), thermal and relativistic electrons and HI atoms (green) and cold dust (orange) components of the arms.

of Galactic longitude and latitude, $A_\lambda(l, b)$ (e.g. Schlegel et al. 1998), we need three dimensional extinction maps, i.e. a function of l, b and distance, d, $A_\lambda(l, b, d)$. Galactic dust extinction of the Milky Way is discussed in more detail in Section 4.6 and Section 5.3.1.

Even with increasingly large surveys and increasingly accurate data, we will still need to infer the properties of the Milky Way from data which do not uniformly cover the Galaxy, and comes with varying levels of observational errors and a complicated observational selection function. Creating computational models of the complex structures within the Galaxy, such as the bar and

spiral arms, will enable us to compare theory with observations, and reveal the structures of the Galactic disc.

1.5 Galaxy Modelling

There are three different types of galaxy model, mass models, kinematic models and dynamical models. Mass models only describe the density distribution and the galactic potential (e.g. Klypin et al. 2002). Kinematic models specify the density and velocity distributions, but lack the constraint that the model must be in a steady state in the galactic potential. A model which also satisfies this criteria is known as a dynamical model (e.g. Widrow et al. 2008). This section will give brief examples of mass and kinematic galaxy models, and then focus on dynamical modelling methods.

One classical example of a mass model of the Milky Way is in Bahcall & Soneira (1980), who construct a mass model for the Milky Way based upon the priors of observations of the density/luminosity structure of external galaxies. For their standard model, they use an exponential disc with a de Vaucouleurs spheroidal bulge (e.g. de Vaucouleurs 1959). They use the analytical stellar luminosity function for the disc of Tremaine et al. (1975) which is fit to the data of McCuskey (1966), Luyten (1968) and Wielen (1974). They compare their 'standard' model and observed star counts and find that at lower latitudes there is an offset between star counts in the model and the observed counts of Seares et al. (1925) by approximately 0.3 mag. However, there is good agreement at high latitudes up to apparent magnitude $V \leq 22$ mag. There is an excess of stars fainter than $V = 22$ mag in the data of Tyson & Jarvis (1979) compared to the model, which they suggest may be due to stars in a separate stellar halo component, which is not included in the model. Additionally, Bahcall & Soneira (1980) show that the rotation curve of their standard model is not consistent with observations, and requires a massive dark halo component to reproduce the flat rotation curve.

Robin et al. (2003) present a kinematic Milky Way model, known as the Besançon model. Robin et al. (2003) use measurements of the luminosity function (Jahreiß & Wielen 1997), age-velocity dispersion (Gomez et al. 1997) and

local density and potential (Creze et al. 1998) from the *Hipparcos* data to constrain the model. The Besançon model contains a stellar halo, where both the Initial Mass Function (IMF) and density law are constrained by star counts at high and medium latitudes (Robin et al. 2000). Robin et al. (2012) provide a view of the Besançon galaxy model as seen by *Gaia*, taking into account dust extinction using a 3D dust distribution model of Drimmel et al. (2003). However, there is no inclusion of *Gaia*-like observational error. The *Gaia* Object Generator (GOG, Luri et al. 2014) is used to create simulated *Gaia* catalogue data from the Besançon model, adding observational errors based upon *Gaia's* science performance estimates.

Czekaj et al. (2014) present a revised version of the Besançon galaxy model with updated methodology, which treats the IMF, Star Formation Rate (SFR) and stellar evolutionary tracks as free parameters. They compare the old and new models with Tycho-2 data and find that the new model better reproduces the Tycho-2 observations. The best fit to the Tycho-2 data is found when using a decreasing SFR (Aumer & Binney 2009) and either the Kroupa-Haywood v6 (Czekaj et al. 2014) or Haywood-Robin (Robin et al. 2003) IMF. However, while the Besançon model reproduces star counts to an excellent degree, it is not guaranteed to be in a steady state within its own potential, meaning it is not a dynamical model.

There are arguably six different types of dynamical galaxy model, although sometimes where the line of distinction is drawn can be ambiguous. These are moment based models, distribution function based models, Schwarzchild models, torus models, action-angle models and N-body models.

1.5.1 Moment based methods

Moment based methods find solutions of the Jeans equation (or higher order velocity moments of the collisionless Boltzmann equation) that best fit the observed moments and minimise χ^2 (e.g. Young 1980; Łokas 2002; Cappellari 2008; Williams et al. 2009; Cappellari et al. 2009). The main drawback of this method is that there is no guarantee that there will be a distribution function with the required velocity moments. It is also usually restricted to spherically symmetric models as the symmetry allows simplifying assumptions to be made,

but may be extended to axisymmetic models under certain circumstances.

1.5.2 Distribution function based methods

Distribution function based methods fit the distribution function to the data. These methods are used in three stages of complexity. Firstly, there are methods which can be applied to only spherical, or integrable systems (e.g. Dejonghe 1984, 1986; Bishop 1987; Dejonghe & de Zeeuw 1988; Gerhard 1991; Hunter & de Zeeuw 1992; Merritt & Tremblay 1994; Carollo et al. 1995; De Bruyne et al. 2000; Kronawitter et al. 2000). Secondly, perturbation theory can be used to extend the method to near integrable potentials (e.g. Saaf 1968; Dehnen & Gerhard 1993; Matthias & Gerhard 1999). Thirdly, the method can be applied to axisymmetric models by assuming that the distribution function is only dependent on the energy, E, and the angular momentum, L_z (e.g. Hunter & Qian 1993; Dehnen & Gerhard 1994; Kuijken 1995; Qian et al. 1995; Merritt 1996). They can be more general than the moment based methods, and in principle there is no reason why they cannot be extended to the third integral of motion.

1.5.3 Schwarzschild methods

Schwarzschild's methods, also known as orbit based methods, work by computing a large number of orbits evolved over many orbital periods in a fixed potential. The orbit information is then collected into an orbit library, which is weighted to produce the best fit to the target model (e.g. Schwarzschild 1979; Richstone & Tremaine 1985; Schwarzschild 1993; van der Marel et al. 1998; Cretton et al. 1999; Gebhardt et al. 2000; Cappellari et al. 2002; Valluri et al. 2004; Thomas et al. 2005; Cappellari et al. 2006; Shapiro et al. 2006; Thomas et al. 2009; van den Bosch & de Zeeuw 2010). This method has the advantage of not requiring the distribution function or the other integrals of motion, and in certain rare circumstances, the distribution function may even be recovered (Häfner et al. 2000). Schwarzschild's method is normally considered to be the most powerful of the methods discussed so far, and in principle is not restricted by symmetry. However, due to the complexity of applying the method to complex phase space structure, it is usually only used

for axisymmetric models.

1.5.4 Torus methods

Torus methods are similar to orbit based methods (e.g. McGill & Binney 1990; Binney & Kumar 1993; Kaasalainen & Binney 1994; Binney & McMillan 2011; McMillan & Binney 2012). The key difference between torus modelling and orbit based modelling is that while in orbit based modelling the orbits are time series of phase-space points, in torus modelling these phase-space points are replaced by orbital tori. The star's position on this torus is defined by its action and angle variables. Binney & McMillan (2011) list the advantages of torus modelling over Schwarzschild modelling. For example, once the phase-space density of the orbits becomes known, it is easier to relate the weights of individual tori to the distribution function than in orbit based modelling. Torus modelling is a method to provide orbits, $(\boldsymbol{x},\boldsymbol{v})$, from the action variable, $\boldsymbol{J}$.

1.5.5 Action based methods

Action based models are similar to torus modelling, but performed in the opposite direction. While torus modelling takes the action, $\boldsymbol{J}$, and outputs an orbit, $(\boldsymbol{x},\boldsymbol{v})$, action based modelling takes the orbit, $(\boldsymbol{x},\boldsymbol{v})$, and outputs an action, $\boldsymbol{J}$ (e.g. McMillan & Binney 2008; Sanders 2012; Binney 2012a,b; Bovy & Rix 2013; Bovy 2014, 2015; Sanders & Binney 2015). McMillan & Binney (2008) propose an iterative procedure for finding actions from orbits, starting from an estimate of the action and moving towards a solution. However, this is a slow process and a solution is not guaranteed. Later works suggest using a Stäckel potential (Stäckel 1890) as an approximation either for each individual orbit (Sanders 2012) or the Galactic potential (Binney 2012a). However, the methods in Sanders (2012) and Binney (2012a) break down when the radial and/or vertical actions of an orbit are of a similar magnitude to the angular momentum (Bovy 2014).

1.5.6 N-body modelling

N-body models are based on the gravitational attraction between a collection of 'N' bodies. These form the basis for the work in this thesis and will be

discussed in more detail.

The first N-body simulation is shown in Holmberg (1941), who simulates an encounter between two galaxies using light bulbs instead of computers to simulate the gravitational attraction between N-bodies. Holmberg (1941) observes tidal features when the galaxies interact (although describing them as spiral arms), which are later explored in more depth by Toomre & Toomre (1972). The first computational N-body model is described in von Hoerner (1960), who models a star cluster with $N \leq 16$, where N is the number of stars. Aarseth (1963, 1966) then examines galaxy clusters using $25 \leq N \leq 100$. White (1976) expands upon the work of Aarseth, using a N=700 body system. In White (1976), the total mass of the model is chosen to be equivalent to the total luminosity of the Coma cluster. He finds that the luminosity profile of the model matches well the luminosity profile for the Coma cluster in Oemler (1974), implying strong levels of mass segregation. However, White (1977) shows that mass segregation in the Coma cluster is in fact weak, and thus a large fraction of the mass of the Coma cluster is not contained within the galaxies, in agreement with Rood (1965).

As shown in Dehnen & Read (2011), the increase in N has roughly doubled every two years following Moore's Law (e.g. Moore 1965), until the last decade when the development of parallel computing has sparked a rapid increase in N. Sellwood & Carlberg (1984) use 20,000 particles to model a spiral galaxy, and show the spiral arms arise and then disappear as the disc evolves. However, Fujii et al. (2011) show that N-body simulations of pure stellar discs, i.e. without gas, with low numbers of particles experience high shot noise which leads to rapid growth of spiral structure, which in turn leads to rapid heating of the disc and disrupts the spiral arms. Fujii et al. (2011) give a limit of $N \gtrsim 3 \times 10^6$ over which this numerical heating is avoided. Recent simulations easily reach this limit, for example Baba et al. (2010) use 3×10^6 star particles and 10^6 gas particles and D'Onghia et al. (2013) use 10^8 star particles.

N-body modelling can be collisional, or collisionless, with the collisional simulations being useful to model star clusters and galactic centres, and the

collisionless simulations being useful to model galaxies and large scale structure (for a review, see Dehnen & Read 2011). The key assumption of stellar dynamics in galaxies is that the stellar systems are collisionless (e.g. Binney 2013). Therefore the collisionless N-body models are good approximations for galactic dynamics, where the number densities are too small and the dynamical time is too long for stellar encounters to be important (Dehnen & Read 2011). This thesis presents a novel method to construct an N-body model of the Milky Way disc, and thus we will focus on collisionless N-body modelling.

Unlike collisional N-body systems, two body interactions in collisionless systems must be numerically suppressed in order to maintain the collisionless nature of the system. This is achieved by the introduction of softening, which reduces the gravitational force experienced when particles are very near to each other. The minimum softening length required to suppress large angle deflections in two body interactions is given by (Dehnen & Read 2011)

$$\epsilon \sim Gm/\sigma^2, \tag{1.1}$$

where m is the particle mass and σ is the typical velocity dispersion. Softening may be fixed, with the same value of the softening length parameter, ϵ, for each particle, or adaptive, where ϵ_i is based upon the local density around the i^{th} particle (e.g. Dehnen & Read 2011).

With or without the introduction of softening, calculating the gravitational force acting on an N-body particle by summing up the force acting on it from every other particle requires N^2 calculations. This becomes prohibitively expensive for large values of N. N-body codes using direct summation are useful for the modelling of star clusters, although larger systems such as galaxies require a different method of force calculation to perform high-resolution simulations in a reasonable length of time. Barnes & Hut (1986) propose a tree algorithm, which reduces the computational cost to the order of $N\log(N)$, while introducing some small errors. The tree code approximates the force of distant groups of particles using a multipole expansion around the groups centre of mass. These groups are determined by a 'tree' of cubic cells, which, if they contain more than one particle, are split into eight daughter

cells half the size of the parent cell (in a standard 'oct-tree'). These are split until no cells contain more than a single particle. Which level of these hierarchical cells the force acting on a particle is calculated from depends on the distance between the cell and the particle and the size of the cell. When the cell contains one particle, the force from that particle is calculated directly (e.g. Dehnen & Read 2011).

As an alternative, the gravitational force can be calculated using a particle-mesh based method. Particle-mesh codes calculate the potential over a grid, starting from calculating the density field and solving the associated Poisson equation (Hockney & Eastwood 1981). The computational time is of the order $N_g \log(N_g)$, where N_g is the number of grid points. However, the method is inaccurate for inhomogeneous particle distributions when the resolution of the grid is insufficient to calculate forces for regions of high particle density. Adaptive mesh codes (e.g. Berger & Oliger 1984) address this issue by constructing a finer grid in areas of higher density.

The primary issue with N-body modelling is how to tailor the model to match observational data or theoretical constraints. Owing to the chaotic nature of the evolution, it is not trivial to set up the initial conditions for an N-body simulation such that the simulated galaxy evolves into the desired form. We summarise a few examples, although a comprehensive review of N-body galaxy models will not be included here.

Fux (1997) creates 13 N-body barred models of the Milky Way by evolving bar unstable axisymmetric models containing disc, spheroid and dark halo components. He evolves the models using the particle-mesh code of Pfenniger & Friedli (1993). He then scales the models to match the line-of-sight velocity dispersion of M giants in Baade's window, $(l, b) \sim (1^{\rm o}, -4^{\rm o})$, in Sharples et al. (1990). The location of the observer in the models is constrained by $COBE$/DIRBE data, resulting in a best fitting angle of the bar of $\sim 28^{\rm o} \pm 7^{\rm o}$. The bars in the best fitting models have a pattern speed in the range of $\Omega_{\rm p} = 45 - 55$ km s^{-1} kpc^{-1}.

Widrow et al. (2008) uses a Markov chain Monte Carlo (MCMC) method to construct a series of axisymmetric Milky Way models consisting of a disc,

bulge and halo, which are fit to nine observational data sets including estimates of the rotation curves and total mass at large radii in Dehnen & Binney (1998). They compare the range of disc and bulge masses from their MCMC analysis with models from the literature and find good agreement with Bahcall et al. (1983), Kent (1992) and Klypin et al. (2002), but find significantly different values than Johnston et al. (1999), who favour a higher mass for the bulge and disc. However, the models do not well reproduce the line-of-sight velocity dispersion in the bulge found in Tremaine et al. (2002). Widrow et al. (2008) choose 25 of these models with a range of structural parameters and evolve them for 5 Gyr using the N-body tree code of Dubinski (1996). The models have 8×10^5 disc particles, 2×10^5 bulge particles and 10^6 halo particles. They find that all the N-body models produce bars, with the time of formation dependent on the parameters of the model. Widrow et al. (2008) find that the pattern speeds of the bars are initially around $\Omega_\mathrm{p} = 50$ km s^{-1} kpc^{-1}, and decline over a few Gyr to values of around $\Omega_\mathrm{p} \sim 20-30$ km s^{-1} kpc^{-1}, owing to momentum transfer to the halo. By comparing with values from the literature, for example $\Omega_\mathrm{p} = 60 - 70$ km s^{-1} kpc^{-1} (Binney et al. 1997) and $\Omega_\mathrm{p} = 53 \pm 3$ km s^{-1} kpc^{-1} (Dehnen 1999), Widrow et al. (2008) conclude that if their models are reasonable approximations to the Milky Way, then the Galaxy's bar has formed within the last 1-2 Gyr. However, as discussed in Section 1.4, the pattern speed of the Galaxy's bar is not well constrained, and lower pattern speeds are found in different studies, e.g. $\Omega_\mathrm{p} = 25 - 30$ km s^{-1} kpc^{-1} (Portail et al. 2015), which, by this argument, would imply an older bar. Using these axisymmetric models which match observations as initial conditions for N-body simulations allows construction of Milky Way-like dynamical models. However, the bar formation leads to the models reproducing the observations less well (Debattista 2009).

Shen et al. (2010) construct a N-body model of the Milky Way. The model of Shen et al. (2010) contains a boxy bar which forms self-consistently as the simulation evolves. The bar is formed as the disc buckles, which results in the bar thickening vertically. The bar resembles the peanut structure observed in the Milky Way (e.g. Wegg & Gerhard 2013, see Section 1.4.1) and external

galaxies (e.g. Burbidge & Burbidge 1959). The model is then scaled to match the radial velocity data from BRAVA. They find that the boxy bar, seen almost edge-on in the model, can reproduce the BRAVA data, and is also consistent with the radial velocities in Rangwala et al. (2009), without the need for a classical bulge formed by mergers. They find a best fitting bar angle of $\sim 20^{o}$.

The Made-to-Measure method (Syer & Tremaine 1996) provides another way to construct N-body models of a desired form, which can reproduce observational data and galactic structure. These form the basis for the work in this thesis and will be discussed in more detail in the next section.

1.6 The Made-to-Measure method

1.6.1 Theory and development

The Made-to-Measure (M2M) method, pioneered by Syer & Tremaine (1996), is a procedure for tailoring existing galaxy models to match some target data. The existing galaxy model can be a test particle simulation, or an N-body simulation, and the target data can be in the form of a distribution function, another galaxy model, or real observational data. Syer & Tremaine (1996) show that the M2M method is capable of constructing equilibrium systems similar to the target system, by changing the weights of the model particles so that the differences between the model and target data are minimised and the observable properties of the target system are reproduced. We give a brief summary of the method of Syer & Tremaine (1996) here, and a more detailed description in Chapter 2.

The M2M method is built around the prescription to change the particle weights over time. Syer & Tremaine (1996) compare some 'observable' quantity of the target,

$$Y_j = \int K_j(\mathbf{z}) f(\mathbf{z}) \mathrm{d}^6\mathbf{z}, \tag{1.2}$$

with the corresponding observable of the model,

$$y_j(t) = \sum_{i=1}^{N} w_i K_j[\mathbf{z}_i(t)], \tag{1.3}$$

where $\mathbf{z}$=($\mathbf{r}$,$\mathbf{v}$), N is the total number of model particles, i is the i^{th} model particle, w_i is the weight of the i^{th} model particle, j is the j^{th} observable, and

K_j is a known kernel. They then calculate the difference between the model observable and the target observable,

$$\Delta_j(t) = \frac{y_j(t) - Y_j}{Y_j}. \tag{1.4}$$

If $\Delta_j < 0$, they increase the weight of the i^{th} particle, w_i, and if $\Delta_j > 0$, they decrease w_i. The change in weight is controlled with the equation

$$\frac{\mathrm{d}w_i(t)}{\mathrm{d}t} = -\epsilon w_i(t) \sum_{j=1}^{J} \frac{K_j[\mathbf{z}_i(t)]}{Z_j} \Delta_j(t), \tag{1.5}$$

where ϵ is a small positive constant to control the rate of change, and Z is so far arbitrary. The kernel K_j ensures that the particle weights are only altered if the i^{th} particle contributes to the j^{th} observable, and the inclusion of w_i on the right-hand side scales the rate of change with the particle's weight.

Syer & Tremaine (1996) employ a temporal smoothing scheme (see Chapter 2), which effectively increases the resolution of the model, to help reduce statistical fluctuations in Δ_j for low resolution models. Additionally, if the number of particles is greater than the number of observables, equation (1.5) is ill conditioned. If this is the case, while the system as a whole will converge rapidly to a solution, the individual particle weights will continue to fluctuate. To address this issue, Syer & Tremaine (1996) introduce a regularisation term into equation (1.5) to remove the ill conditioning. The regularisation term forces the weights towards some prior set of values. This transforms equation (1.5) into

$$\frac{\mathrm{d}w_i(t)}{\mathrm{d}t} = \epsilon w_i(t) \left[\mu \frac{\delta S}{\delta w_i} - \sum_{j=1}^{J} \frac{K_j[\mathbf{z}_i(t)]}{Y_j} \tilde{\Delta} j(t) \right], \tag{1.6}$$

where μ is a parameter controlling the strength of the regularisation term, $\tilde{\Delta}_j$ denotes the temporally smoothed version of Δ_j, and S is the entropy, given by

$$S = -\sum_i w_i \log(w_i/\hat{w}_i), \tag{1.7}$$

where $\hat{w}_i$ is a pre-determined set of weights which we will call the prior. The prior is set as $\hat{w}_i = 1/N$ in Syer & Tremaine (1996).

Syer & Tremaine (1996) show results for five one dimensional simulations in a fixed potential, demonstrating the importance of the temporal smoothing

and the regularisation term. Syer & Tremaine (1996) use three target mass models, one spherical and two triaxial, and test their M2M algorithm's ability to reproduce each target system. For each system they start from three different initial conditions and use both a fixed analytical gravitational potential and a fixed gravitational potential calculated numerically in a grid at the beginning of the simulation. By exploring each combination, they perform twelve models, of which all except one are successful. The successful models converge to a solution which is suitably similar to the target. The unsuccessful model fails to reproduce a sufficient number of tube orbits of the target, because the initial condition is set up to be dominated by box orbits. Syer & Tremaine (1996) demonstrate the potential of the M2M method, although it has seen little use until recently.

NMAGIC, developed by de Lorenzi et al. (2007), is the first major implementation of the M2M algorithm. In Syer & Tremaine (1996), only density observables are used to constrain the model. NMAGIC improves upon the initial M2M algorithm of Syer & Tremaine (1996) by adding the ability to use velocity constraints. NMAGIC was also the first M2M algorithm to include observational errors in the constraints by replacing equation (1.4) with

$$\Delta_j(t) = \frac{y_j(t) - Y_j}{\sigma(Y_j)}, \tag{1.8}$$

and equation (1.6) with

$$\frac{\mathrm{d}w_i(t)}{\mathrm{d}t} = \epsilon w_i(t) \left[\mu \frac{\delta S}{\delta w_i} - \sum_{j=1}^{J} \frac{K_j[\mathbf{z}_i(t)]}{\sigma(Y_j)} \tilde{\Delta} j(t) \right], \tag{1.9}$$

where $\sigma(Y_j)$ is the error in the target observable Y_j. This was an important step forward, as it allowed real observational data to be used as constraints.

NMAGIC has been applied to observational data of external galaxies. For example, de Lorenzi et al. (2008) introduce the likelihood equation to enable the use of discrete Planetary Nebula (PN) velocity measurements as constraints, and apply NMAGIC to NGC 4697. They construct models with a variety of dark matter haloes which are consistent with the observations, and they state that more PN velocities at a higher distance from the centre of the Galaxy would be needed to further constrain the halo with this method.

NMAGIC has also been applied to NGC 3379 in de Lorenzi et al. (2009), where they conclude that the kinematics of NGC 3379 are consistent with a number of dark matter halo profiles, and do not well constrain the mass distribution in the galaxy. Das et al. (2011) apply NMAGIC to surface-brightness data, long-slit kinematics and PN velocities to create a dynamical model of the massive elliptical galaxy NGC 4649. They find that they cannot constrain well the circular velocity curve, when they fit only surface brightness and long-slit kinematic constraints. However, when they include PN kinematics, they find a rotation curve that is flat outside 12 kpc and which is consistent with the X-ray observations of Nagino & Matsushita (2009). de Lorenzi et al. (2013) apply NMAGIC to NGC 4244 and create initial conditions of N-body models of the galaxy to test whether the nuclear star cluster in the centre of NGC 4244 could have formed via accretion of star clusters. They find that accretion of a star cluster of more than 13 percent of the mass of the nuclear cluster is inconsistent with the vertical anisotropy.

NMAGIC has been improved recently by Morganti & Gerhard (2012), who propose a new regularisation scheme based upon a flexible prior. The Global Weight entropy Regularisation (GWR) scheme in Syer & Tremaine (1996) encourages a structure whose particle weights are similar to the global prior, typically $\hat{w}_i = 1/N$, where N is the total number of particles. This makes it difficult to recover highly anisotropic structure and strong phase space gradients unless they are already in place in the initial conditions. This was previously noticed by de Lorenzi et al. (2008) and de Lorenzi et al. (2009) who use low levels of regularisation in their models to recover strong radial anisotropies. Morganti & Gerhard (2012) suggest that instead of constant priors, the priors are modified such that particles on nearby orbits have similar priors, and particles on very different orbits have different priors. They call this Moving Prior Regularisation (MPR). Morganti & Gerhard (2012) show that MPR is beneficial to accuracy of the model when it is used in NMAGIC. They also show that the system can converge to a unique solution, independent of the choice of initial model. Morganti & Gerhard (2012) apply NMAGIC with MPR to NGC 4697 and NGC 3379, which are the galaxies previously modelled in

de Lorenzi et al. (2008) and de Lorenzi et al. (2009), respectively. For both galaxies, the models using MPR are smoother and are less dependent upon the initial particle model than the models using GWR. Morganti et al. (2013) apply the updated version of NMAGIC to NGC 4494, and find a higher dark matter fraction but less radial anisotropy in this galaxy than in NGC 4697 and NGC 3379, and a strong central concentration of baryons.

Dehnen (2009) proposes a number of improvements to the M2M methodology of Syer & Tremaine (1996), and demonstrates its application to the generation of N-body initial conditions. For example, Dehnen (2009) addresses the issue of total weight conservation, which is not guaranteed in the original algorithm. Dehnen (2009) suggests that the simplest method to achieve total weight conservation is to re-normalise the particle weights after each iteration such that their total weights equal one. He also proposes to use total weight conservation itself as a constraint. However, if the total mass of the system is unknown, e.g. in the case of the Milky Way, the total weight needs to be allowed to evolve freely according to the constraints. He also describes a particle re-sampling scheme, which is suggested in Syer & Tremaine (1996) but not implemented. A large range of weights within the model effectively reduces the resolution of the N-body model, and thus at least periodic resampling of particles is desirable.

Malvido & Sellwood (2015) also make use of the M2M method to construct self-similar Einasto N-body dark matter halos (Einasto & Haud 1989). The M2M adaptation in Malvido & Sellwood (2015) is most similar to the methodology of de Lorenzi et al. (2007), who also created triaxial halos (see also de Lorenzi et al. 2009). However, the main difference is that Malvido & Sellwood (2015) do not employ temporal smoothing, which they argue is unnecessary and counterproductive for sufficiently large values of N. Malvido & Sellwood (2015) show that the generated halo models are stable after the model has converged to its solution, which is tested by evolving the model self-consistently without the M2M algorithm. They renormalise the particle masses to conserve the total mass but do not resample the particles, which results in an uneven spread of particle masses in the final model.

It is also worth mentioning the iterative method as described in Rodionov et al. (2009), which bears some similarities to M2M, and has been used to create equilibrium N-body systems matching certain constraints. The iterative method starts with an existing dynamical model. Then, it is evolved freely for a set amount of time via a standard N-body code. Then, the parameters of the model are altered to better reproduce the desired target system. These last two steps are repeated iteratively until the model agrees with the constraints. For example, the initial model satisfies a known mass distribution but the velocities are not dynamically consistent. The model is evolved using an N-body code. The resulting velocity distribution is mapped onto the initial model, preserving the original mass distribution, but the evolved velocity distribution. After many iterations, the model is an equilibrium dynamical model with the desired mass distribution. Unfortunately, the method cannot be used when the mass distribution is not known. Because of this, it is unsuitable to be applied to the case of the Milky Way which we are interested in.

1.6.2 Application to the the Milky Way

As well as external galaxies, the M2M method has also been applied to the Milky Way. Bissantz et al. (2004) apply the M2M algorithm of Syer & Tremaine (1996) to the Milky Way for the first time, and create a stellar dynamical model of the Milky Way's barred bulge and disc. They start with a barred galaxy generated by an N-body simulation, whose initial condition is an axisymmetric bar-unstable system used in Debattista (2003). For density constraints, Bissantz et al. (2004) use the previously constructed mass model of the Milky Way of Bissantz & Gerhard (2002) based upon the $COBE$/DIRBE map in Spergel et al. (1996). They do not include kinematic constraints. However, the kinematics of the model agree well with kinematic observations towards Baade's Window ($(l, b) = (1^{\circ}, -4^{\circ})$, Sharples et al. 1990; Spaenhauer et al. 1992) and the field $(l, b) = (8^{\circ}, 7^{\circ})$ (Minniti et al. 1992), which are lines-of-sight with low extinction. Their dynamical model is also consistent with the microlensing event timescale distribution in Alcock et al. (2000).

The model in Bissantz et al. (2004) is an encouraging first attempt at M2M modelling of the Milky Way. However, the M2M algorithm has undergone significant improvements since Bissantz et al. (2004), for example the implementation of kinematic constraints in de Lorenzi et al. (2007), and much more observational data has become available, which leaves substantial room for improvement.

The next application of M2M to the Milky Way is in Long et al. (2013), the third in a series of three papers. In the first paper, Long & Mao (2010) present their adaptation of the M2M algorithm, and apply it to the dwarf spheroidal galaxy, Draco. Then, in Long & Mao (2012), they perform a direct comparison between M2M and the Schwarzchild method with regard to calculating the mass to light ratios and anisotropy of 24 elliptical and lenticular galaxies. Long & Mao (2012) find that M2M and Schwarzschild's method give similar mass to light ratios, although there is a small difference. However, there is less agreement between the methods on the anisotropy.

Long et al. (2013) apply their M2M algorithm in Long & Mao (2010, 2012) to observed radial velocity data from the Bulge RAdial Velocity Assay (BRAVA) survey (e.g. Rich et al. 2007; Kunder et al. 2012). They use density constraints from the particle mass distribution of the N-body boxy/barred Milky Way galaxy model of Shen et al. (2010) (see Section 1.5.6), which matches BRAVA data after suitable mass scaling. Then, Long et al. (2013) rotate the gravitational potential calculated from the N-body model of Shen et al. (2010) with the assumed pattern speed of the bar. They run multiple models altering the pattern speed and angle of the bar, and explore which models best fit their observables. They find that their best model recovers the bar angle and pattern speed of the Shen et al. (2010) N-body model, $\theta = 30^{\rm o}$ and $\Omega_{\rm p} = 40$ km s^{-1} kpc^{-1} respectively, and reproduces the mean radial velocity and radial velocity dispersion of the BRAVA data well.

The most recent work of the M2M method, also applied to the Milky Way, is Portail et al. (2015), who also make use of the BRAVA data as kinematic constraints. For the density constraints, they use the three dimensional number density distribution of red clump giants in the Galactic bul-

ge/bar, determined from the VISTA variables in the Vía Láctea survey (VVV, e.g. Saito et al. 2012) in Wegg & Gerhard (2013). Portail et al. (2015) apply NMAGIC to five different initial models. The models differ in the degree of maximality of the disc, which is the proportion of the stellar disc's contribution to the rotation velocity curve. Portail et al. (2015) find a similar total mass of the bulge/bar for the different models, although the stellar fraction shows significant difference dependent on the degree of maximality. They obtain bar pattern speeds of $\Omega_{\rm p} = 24.7 - 29.0$ km s^{-1} kpc^{-1}, which is a little lower than the best fit bar pattern speed determined by Long et al. (2013) of $\Omega_{\rm p} = 40$ km s^{-1} kpc^{-1} who also use the BRAVA data. Portail et al. (2015) also compare the mass to light ratios from their models with predictions from different IMFs. This is important because the conversion between the number density of red clump giants and the stellar mass density is not known. The conversion requires the assumption of the ratio between the number of red clump giants and the total stellar mass integrated over the masses of all types of star, which depends on their age and metallicity, and the IMF. They effectively rule out the Salpeter IMF (Salpeter 1955) for a bulge population with Age ≥ 10 Gyr, while the Kroupa (Kroupa 2001), Chabrier (Chabrier 2003) and Zoccali (Zoccali et al. 2000) IMFs are consistent with the red clump/mass ratio which is required to reproduce the observations with NMAGIC. Portail et al. (2015) find that the X-shape of the bulge is off-centre, which is common in external galaxies (e.g. Bureau et al. 2006). This application of M2M to the Milky Way's bulge is an up to date example of the power of the M2M method to dynamically model our Galaxy, and is encouraging for future M2M modelling of the Milky Way.

1.7 The work of this thesis

The aim of this thesis is to develop a novel M2M method for reconstructing the mass and kinematic structure of the Milky Way, in particular the disc component, from the data returned by ESA's *Gaia* mission. Previous M2M algorithms use target data in the form of a distribution function or a binned density distribution. However, the data that *Gaia* will return will be

the position and velocity of individual stars. Therefore, we have designed a particle-by-particle M2M algorithm, PRIMAL, that compares the observables at the location of each star (or the target stellar particle) with the model observables at the same locations, and adjusts the model particle masses in the same fashion as the original algorithm of Syer & Tremaine (1996). The gravitational potential of the Milky Way is not well known. Thus, in PRIMAL we calculate the model potential self-consistently from the changing particle masses, which enables us in theory to simultaneously recover the potential of the galactic disc.

Part of the challenge of constructing a realistic model of the Milky Way disc is due to our position within it. Even *Gaia* will not see the majority of the stars in our own Galaxy, owing to the magnitude limit and complex observational selection effects such as dust extinction. In this thesis, we show that PRIMAL can construct a dynamical model of a disc galaxy similar to the Milky Way, from mock observational data with a *Gaia*-like selection function and *Gaia* level errors. Although there will be no *Gaia* data releases before summer 2016, we can develop, calibrate and test PRIMAL with mock *Gaia* data from systems whose full structural information is known, to improve the resulting dynamical model. The goal of this thesis is to develop a dynamical model based on M2M, ready to be applied to the *Gaia* data.

It is an open question whether N-body models, or other dynamical models, can truly represent the Milky Way or other galaxies. However, accurate models of the Milky Way are important for allowing us to understand and compensate for observational bias, which are present in all Galactic surveys owing to complicated observational selection effects such as dust extinction.

This thesis is organised as follows. Chapter 2 describes our M2M method. Section 2.2 describes the traditional M2M method, and Section 2.3 describes our particle based adaptation. We then show our initial success recreating an axisymmetric target disc galaxy model in Section 2.4. Chapter 3 shows our recovery of structured discs. Section 3.2.1 shows the adaptations to the method since Chapter 2, and Section 3.3 shows our success recovering three disc galaxy models with non-axisymmetric structure. Chapter 4 describes the

application of PRIMAL to mock data in equatorial co-ordinates, with the errors expected in the *Gaia* data, taking into account Galactic dust extinction. Section 4.3 describes the construction of single population mock *Gaia* data and Section 4.5 shows our success in recovering the boxy-disc structure of the target galaxy from mock *Gaia* tracer data created from an N-body simulated barred disc galaxy taking into account extinction and *Gaia*-like errors. Chapter 5 describes the construction of more realistic mock *Gaia* data and an example of its use. In Section 5.3.2, we describe my population synthesis tool, SNAPDRAGONS. In Section 5.4, we use it to make predictions about the visibility in the *Gaia*-like observational data of peculiar velocity structure around spiral arms seen in our N-body simulations. In Chapter 6 we summarise our conclusions and discuss possible avenues for future work. Chapter 2 is published in Hunt & Kawata (2013), Chapter 3 is published in Hunt et al. (2013), Chapter 4 is published in Hunt & Kawata (2014b) and Chapter 5 is published in (Hunt et al. 2015).

Chapter 2

Disc galaxy modelling with a particle-by-particle method

This chapter is based on Hunt & Kawata (2013)

In this chapter, we describe the initial version of a new particle-by-particle adaptation of the made-to-measure (M2M) method, aiming to model the Galactic disc from upcoming Galactic stellar survey data. In our new particle-by-particle M2M method, the observables of the target system are compared with those of the model galaxy at the position of the target stars (i.e. particles). The masses of the model particles are changed to reproduce the observables of the target system, and the gravitational potential is automatically adjusted by changing the masses of the particles. This chapter demonstrates, as the initial work, that the particle-by-particle M2M can recreate a target disc system created by an N-body simulation in a known dark matter potential, with no error in the observables. The radial profiles of the surface density, velocity dispersion in the radial and perpendicular directions, and the rotational velocity of the target disc are all well reproduced from the initial disc model, whose scale length is different from that of the target disc. We also demonstrate that our M2M algorithm can be applied to an incomplete data set and recreate the target disc reasonably well, when the observables are restricted to a part of the disc. We discuss our calibration of the model parameters and the importance of regularisation.

2.1 Introduction

The previous M2M algorithms discussed in Section 1.6 use a distribution function or binned density distribution. However, the data that Gaia and the related surveys return will be in the form of individual stellar data. Therefore, we have designed a particle-by-particle M2M algorithm that compares the observables at the location of each star (or the target particle) with the model observables at the same locations, and adjusts the weights in the same fashion as the original algorithm of Syer & Tremaine (1996). In this chapter, we present proof of concept of the particle-by-particle M2M by recreating disc galaxies, generated with a Tree N-Body code, GCD+ (Kawata & Gibson 2003). Our algorithm uses a self-consistent gravitational potential of the model galactic disc, which evolves over time along with the particle weights. We also show a model constructed from a partial target data set, demonstrating that the observables of the target galaxy do not have to cover the whole galaxy for M2M to work. This is the first step towards the real observational data from Galactic surveys, where the information will be provided for a limited region of the sky, with a more complicated selection function due to the dust extinction, crowding and stellar populations. This chapter is organised as follows. Section 2.2 describes the traditional M2M method and Section 2.3 describes the methods behind our particle based adaptation. Section 2.4 shows the performance of the particle-by-particle M2M for recreating the target disc system. In Section 2.5, we discuss the accomplishments of this chapter, and describe the next stages of our work.

2.2 The M2M algorithm

In this section, we will give a brief description of the M2M algorithm as detailed, for example, in Syer & Tremaine (1996), de Lorenzi et al. (2007) and Long & Mao (2010), which forms the base for our work. The M2M algorithm works by calculating observable properties (observables hereafter) from the model and the target, and then adapting particle weights such that the properties of the model reproduce those of the target. The target can be in the form of a distribution function, an existing simulation, or real observational

data. The model can be a test particle simulation in an assumed fixed or adaptive potential, or a self-gravity N-body model.

As stated in Chapter 1, the observables of the target system are described by

$$Y_j = \int K_j(\mathbf{z}) f(\mathbf{z}) d^6\mathbf{z}, \tag{2.1}$$

where j represents each individual observable, $\mathbf{z} = (\mathbf{r}, \mathbf{v})$ are the phase space coordinates, $f(\mathbf{z})$ is the distribution function of the target galaxy and K_j is a known kernel. Observables can come in many forms, including surface or volume densities, surface brightness and line-of-sight kinematics. The corresponding observable for the model takes the form

$$y_j = \sum_{i=1}^{N} w_i K_j[\mathbf{z}_i(t)], \tag{2.2}$$

where w_i are the particle weights and $\mathbf{z}_i$ are the phase space coordinates of the model's i^{th} particle. We then calculate the difference in the observables of the target and the model,

$$\Delta_j = \frac{y_j(t) - Y_j}{Y_j}. \tag{2.3}$$

We then use this Δ_j to determine the so called force of change with the equation

$$\frac{\mathrm{d}}{\mathrm{d}t} w_i(t) = -\epsilon w_i(t) \sum_j \frac{K_j[\mathbf{z}_i(t)]}{Z_j} \Delta_j(t), \tag{2.4}$$

where Z_j so far is an arbitrary constant, and the factor K_i/Z_j can be thought of as the degree to which the i^{th} particle contributes to the j^{th} observable. ϵ is a parameter enabling us to control the rate of change. The linear dependence of equation (2.4) upon w_i, coupled with the provision that a small enough ϵ is used, ensures that the weights do not become negative. Syer & Tremaine (1996) show a proof of convergence for equation (2.4) providing that the system starts close to the target.

If $N{>}J$, i.e. the number of the model particles, N, greatly exceeds the quantity of available constraints, J, the differential equation (2.4) is ill-conditioned. Syer & Tremaine (1996) suggest removing this ill conditioning by introducing entropy, by maximising the function

$$F = \mu S - \frac{1}{2}\chi^2, \tag{2.5}$$

where

$$\chi^2 = \sum_j \Delta_j^2, \tag{2.6}$$

and μ is a parameter to control the regularisation. The entropy is given by

$$S = -\sum_i w_i \ln\left(\frac{w_i}{\hat{w}_i}\right), \tag{2.7}$$

where $\hat{w}_i$ are the priors, a predetermined set of weights, normally identical to each other such that $\hat{w}_i = 1/N$. The system can be normalised (de Lorenzi et al. 2007) such that

$$\sum_{i=1}^{N} w_i = 1. \tag{2.8}$$

This is useful if the total mass of the target system is one of the constraints. We do not impose this restriction as we wish to be able to create a system with a different total mass from the initial model.

Once the new entropy term is introduced to the force of change, equation (2.4) is replaced by

$$\frac{\mathrm{d}}{\mathrm{d}t}w_i(t) = -\epsilon w_i(t)\left[\sum_j \frac{K_j[\mathbf{z}_i(t)]}{Y_j}\Delta_j(t) - \mu\frac{\delta S}{\delta w_i}(t)\right], \tag{2.9}$$

or

$$\begin{aligned}\frac{\mathrm{d}}{\mathrm{d}t}w_i(t) = \; &- \; \epsilon w_i(t)\left[\sum_j \frac{K_j[\mathbf{z}_i(t)]}{Y_j}\Delta_j(t)\right. \\ &+ \left. \mu\left(\ln\left(\frac{w_i(t)}{\hat{w}_i}\right) + 1\right)\right],\end{aligned} \tag{2.10}$$

for the most complete form. Note that Z_j has been replaced by Y_j due to the maximisation of equation (2.5).

It is shown in Syer & Tremaine (1996) and de Lorenzi et al. (2007) that fluctuations in equation (2.3) may be reduced by employing temporal smoothing, effectively boosting N without drastically increasing computation time. This is achieved by replacing $\Delta_j(t)$ in equation (2.4) with $\tilde{\Delta}_j(t)$, where

$$\tilde{\Delta}_j(t) = \alpha\int_0^\infty \Delta_j(t-\tau)\mathrm{e}^{-\alpha\tau}d\tau, \tag{2.11}$$

with α being small and positive. This $\tilde{\Delta}_j(t)$ can be calculated from the differential equation

$$\frac{\mathrm{d}\tilde{\Delta}(t)}{\mathrm{d}t} = \alpha(\Delta - \tilde{\Delta}). \tag{2.12}$$

This temporal smoothing effectively increases the number of particles from N to

$$N_{\mathrm{eff}} = N\frac{t_{\frac{1}{2}}}{\Delta t}, \tag{2.13}$$

where Δt is the length of the time step and $t_{\frac{1}{2}} = (\ln 2)/\alpha$ is the half life of the ghost particles. Syer & Tremaine (1996) show that excessive temporal smoothing is undesirable, and should be limited to $\alpha \geq 2\epsilon$.

The parameters ϵ, μ and α must be determined via parameter search. We will discuss our choice of these parameters in Section 2.3.4.

2.3 Particle-by-particle M2M

This section describes our original adaptation to the M2M algorithm. The majority of the methodology remains the same as described in Section 2.2, with the most substantial difference involving the Smoothed Particle Hydrodynamics (SPH) kernel (e.g. Lucy 1977; Gingold & Monaghan 1977), which will be described in Section 2.3.1. Syer & Tremaine (1996) used a kernel where they divide the coordinate space into bins. For example, for the density at the j^{th} bin with volume V_j, the kernel, $K_j(\mathbf{r}_i)$, is set to be M_j/V_j if $\mathbf{r}_i$ is within the j^{th} bin, where M_j is the mass in the j^{th} bin and equation (2.8) is satisfied. If $\mathbf{r}_i$ is outside the j^{th} bin, $K_j(\mathbf{r}_i) = 0$. Because $K_j(\mathbf{r}_1)$ and $K_j(\mathbf{r}_2)$ are the same if $\mathbf{r}_1$ and $\mathbf{r}_2$ are in the same bin, this limits the resolution to the bin size. However, as mentioned in Section 1.7, our ultimate target is the Milky Way, and the observables are not binned data, but the position and velocity of the individual stars which are distributed rather randomly. To maximise the available constraints, we evaluate the observables at the position of each star and compare them with the N-body model, i.e. in a particle-by-particle fashion. To this end we introduce a kernel often used in SPH, $W(r, h)$, which is a spherically symmetric spline function given by

$$W(r,h) = \frac{8}{\pi h^3} \times \begin{cases} 1 - 6(r/h)^2 + 6(r/h)^3 & \text{if } 0 \leq r/h \leq 1/2, \\ 2[1-(r/h)]^3 & \text{if } 1/2 \leq r/h \leq 1, \\ 0 & \text{otherwise.} \end{cases} \tag{2.14}$$

as shown in Monaghan & Lattanzio (1985), where $r = \mid \mathbf{r}_i - \mathbf{r}_j \mid$. Note that in our particle-by-particle M2M the kernel, $W(r,h)$, does not explicitly include the total mass, $M_{\rm tot}$, because we wish to eventually apply it to the Milky Way, whose mass is unknown. Therefore, the SPH kernel in equation (2.14) is not equivalent to the M2M kernel, K_j, in Section 2.2.

Below, we describe our particle-by-particle M2M, considering that the target system is an N-body system whose particle position and velocity are known without any error. Of course in the real data of the Galaxy, there are complicated observational errors and selection functions, which often depend on stellar population and dust extinction. In this chapter, we ignore these and consider an idealised system for a target. As described in Section 1.7, the aim of this chapter is to demonstrate how our new M2M works and the potential of future application to the Galactic disc. We below assume that the target system consists of a single population, which we shall refer to as particles, and whose position and velocity are known without errors.

2.3.1 Method

We use the kernel of equation (2.14) to calculate the density at the target particle locations, $\mathbf{r}_j$, of both the target and the M2M model. Hereafter, we replace the particle weights, w_i, with their masses, m_i, due to our adoption of self-gravity in the particle-by-particle M2M. For example, the density of the target at $\mathbf{r}_j$ is evaluated by

$$\rho_{{\rm t},j} = \sum_{k=1}^{N} m_{{\rm t},k} W(r_{kj}, h_j), \tag{2.15}$$

where $m_{{\rm t},k}$ is the mass of the target particle, $r_{kj} = \mid \mathbf{r}_k - \mathbf{r}_j \mid$, and h_j is the smoothing length determined by

$$h_j = \eta \left(\frac{m_{{\rm t},j}}{\rho_{{\rm t},j}} \right)^{1/3}, \tag{2.16}$$

where η is a parameter and we have set $\eta = 3$. In SPH simulations, a value of η between 2 and 3 are often used, and we employ the relatively higher value to maximise the smoothness. This results in ~ 113 neighbouring particles being included in the smoothing, when the particles are distributed homogeneously in three-dimensional space. The solution of equation (2.16) is calculated iteratively until the relative change between two iterations is smaller than 10^{-3} (Price & Monaghan 2007). Similarly,

$$\rho_j = \sum_{i=1}^{N} m_i W(r_{ij}, h_j), \tag{2.17}$$

from the model particles. The target density, $\rho_{\mathrm{t},j}$, is calculated only once at the beginning of the M2M simulation, and the model density, ρ_j, is recalculated at every timestep.

For velocity constraints, we define the following form of the observables, using the same kernel. For example for radial velocity

$$\delta v_{\mathrm{t,r},j} = \sum_{k=1}^{N} (v_{\mathrm{t,r},k} - v_{\mathrm{t,r},j}) m_{\mathrm{t},k} W(r_{kj}, h_j), \tag{2.18}$$

where $v_{\mathrm{t,r},k}$ is the radial velocity of the k^{th} target particle and $v_{\mathrm{t},r,j} = (v_{\mathrm{t},x,j} x_{\mathrm{t},j} + v_{\mathrm{t},y,j} y_{\mathrm{t},j})/(x_{\mathrm{t},j}^2 + y_{\mathrm{t},j}^2)^{\frac{1}{2}}$ is the radial velocity of the target system. Equation (2.18) represents the weighted mean of the relative velocities of the target particles within h_j of the target particle j.

$$\delta v_{\mathrm{r},j} = \sum_{i=1}^{N} (v_{\mathrm{r},i} - v_{\mathrm{t,r},j}) m_i W(r_{ij}, h_j) \tag{2.19}$$

is similarly calculated from the model particles. The same format is applied for the vertical and rotational velocities.

We then describe the difference in the observables, i.e. equation (2.3). For density

$$\Delta_{\rho_j} = \frac{\rho_j(t) - \rho_{\mathrm{t},j}}{\rho_{\mathrm{t},j}}. \tag{2.20}$$

For velocity, we normalised them by the target density because of the density dependence introduced in equations (2.18) and (2.19), and therefore for the radial case

$$\Delta_v = \frac{\delta v_{\mathrm{r},j}(t) - \delta v_{\mathrm{t,r},j}}{\sigma_{v_\mathrm{r}} \rho_{\mathrm{t},j}}. \tag{2.21}$$

Note that σ is not an observational error, but just a normalisation constant which we have arbitrarily set to $\sigma_{v_\mathrm{r}} = \sigma_{v_z} = \sigma_{v_\mathrm{rot}} = 10$ km s^{-1} in our demonstration in Section 2.4.

Because Δ_{ρ_j} and Δ_{v_j} are normalised differently, we modified their contribution to the force of change by introducing a new parameter ζ such that for our simulations, equation (2.10) becomes, with smoothed $\tilde{\Delta}$ by equation (2.12),

$$\begin{aligned}
\tfrac{\mathrm{d}}{\mathrm{d}t} m_i(t) &= -\epsilon m_i(t) \Bigg[M \sum_j \frac{W(r_{ij}, h_j)}{\rho_{\mathrm{t},j}} \tilde{\Delta}_{j,\rho}(t) \\
&+ \zeta M \Bigg(\xi_\mathrm{r} \sum_j \frac{W(r_{ij}, h_j)}{\sigma_{v_\mathrm{r}} \rho_{\mathrm{t},j}} (v_{\mathrm{r},i} - v_{\mathrm{t,r},j}) \tilde{\Delta}_{v_{\mathrm{r},j}}(t) \\
&+ \xi_z \sum_j \frac{W(r_{ij}, h_j)}{\sigma_{v_z} \rho_{\mathrm{t},j}} (v_{z,i} - v_{\mathrm{t},z,j}) \tilde{\Delta}_{v_{z,j}}(t) \\
&+ \xi_\mathrm{rot} \sum_j \frac{W(r_{ij}, h_j)}{\sigma_{v_\mathrm{rot}} \rho_{\mathrm{t},j}} (v_{\mathrm{rot},i} - v_{\mathrm{t,rot},j}) \tilde{\Delta}_{v_{\mathrm{rot},j}}(t) \Bigg) \\
&+ \mu \left(\ln \left(\frac{m_i(t)}{\hat{m}_i} \right) + 1 \right) \Bigg], \qquad (2.22)
\end{aligned}$$

where M is an arbitrary constant mass, which we set as $M = 10^{12}$ M$_\odot$ for this chapter. Note that in equation (2.22) the corresponding M2M kernel is $K_j = MW(r, h_j)$, e.g. for density, which is inconsistent with the one used to obtain the observables in equation (2.17), where $K_j = M_{m,\mathrm{tot}} W(r, h_j)$ and $M_{m,\mathrm{tot}}$ is the total mass of the model particles. However, we accept this inconsistency to apply the method to a system whose total mass is unknown, and we allow $M_{m,\mathrm{tot}}(t) = \sum_i m_i(t)$ to freely evolve. Therefore, we introduce the arbitrary constant M in equation (2.22), and as a result the parameters, such as ϵ, μ and ζ, must be calibrated for the specific system. Fortunately, our ultimate target is only one system, the Milky Way. We hope that we can calibrate the parameters by modelling simulated data before applying the method to the real data. Hence, note that the parameters presented in this chapter are specific to the target system in this chapter. In future works, we will calibrate the parameters and refine the methods by applying more realistic simulation data.

We use the additional individual parameters $\xi_{\rm r}$, ξ_z, $\xi_{\rm rot}$ for the different velocity observables, to allow us to fine tune their contributions to the force of change even further. Similar in spirit to de Lorenzi et al. (2007), we write ϵ as $\epsilon = \epsilon'\epsilon''$ where ϵ'' is given by

$$\epsilon'' = \frac{10}{\max_i \left(M \sum_j \frac{W(r_{ij},h_j)}{\rho_{{\rm t},j}} \tilde{\Delta}_{\rho_j}(t) \right)}, \tag{2.23}$$

for the density observable only.

In the previous works (e.g. Syer & Tremaine 1996; Dehnen 2009; Long & Mao 2010; Morganti & Gerhard 2012), the M2M method is applied to a system in a known fixed potential, i.e. using test particles. de Lorenzi et al. (2007) demonstrate that M2M works with a partially self-consistent potential, in that the potential is calculated every 25 time steps, setting the particle mass $m_i = w_i M_{\rm tot}$, where w_i is in their definition, i.e. $w_i = 1/N$. However, this repeated sudden change of the potential could come with some problems that will be discussed later.

We intend to apply our algorithm to the Milky Way, whose mass distribution is poorly known (e.g. McMillan 2011), and one of the aims of applying the dynamical model is to reconstruct the mass distribution. Therefore we use a self-consistent disc potential, setting the particle weight, w_i, to the mass, m_i, allowing the disc potential to change along with the model observables and allowing us to recover simultaneously the disc potential along with the mass and velocity profiles. In this chapter, we focus on the disc. We ignore the bulge/bar and halo stars, and assume that the dark matter potential is known for this initial demonstration. Note that the previous studies are mainly focused on elliptical galaxies, i.e. systems dominated by velocity dispersion, but not strongly rotation supported. Recreating a disc galaxy with a self-consistent potential has been attempted once before by Deg (2010), who highlights some difficulties with an M2M method that employs self-gravity. He uses a grid to calculate the observables, which makes his method different from ours.

One of the problems arising from using a self-consistent potential as mentioned by Deg (2010) is that the temporal smoothing, which worked well in fixed potential M2M methods, is problematic when used with self-gravity. The

temporal smoothing reduces shot noise by averaging the Δ_j back along their orbits, which is fine with test particles in a fixed potential because the orbits are fixed. However, in a self-consistent potential, the potential and therefore particle orbits change with time, and thus the temporal smoothing breaks the self-consistency. Therefore, we should be aware that self-gravity M2M models are very sensitive to instabilities, and we see substantial disruption when the smoothing is first turned on. A way to mitigate this damage due to the temporal smoothing is described in Section 2.3.2. In light of this, we investigated the possibility of running models without temporal smoothing. However, all models had to be substantially under-regularised to recover the velocity profiles shown in Section 2.4, which leads to the continuous fluctuation of the weights, similar to the problems of the under-regularisation discussed in Section 2.4.2.

We use a standard Euler method for the integration of the weight change equation and a leapfrog time integrator for advancing the particles. We also use individual time steps for the particles, and only update the masses of particles whose position and velocity are updated within the individual timestep. The timestep for each particle is determined by

$$\mathrm{d}t_i = C_{\mathrm{dyn}} \left(\frac{0.5 h_i}{|\mathrm{d}\mathbf{v}_i/\mathrm{d}t|} \right)^{\frac{1}{2}}, \tag{2.24}$$

with $C_{\mathrm{dyn}} = 0.2$.

2.3.2 Target system setup

Our simulated target galaxy consists of a pure stellar disc with no bulge and a static dark matter halo, set up using the method described in Grand et al. (2012a). The dark matter halo density profile is taken from a truncated NFW profile (Navarro et al. 1997; Rodionov et al. 2009) and given by

$$\rho_{\mathrm{dm}} = \frac{3H_0^2}{8\pi G} \frac{\delta_{\mathrm{c}}}{cx(1+cx)^2} \mathrm{e}^{-x^2}, \tag{2.25}$$

where δ_{c} is the characteristic density described by Navarro et al. (1997). The truncation term, e^{-x^2}, is introduced in our initial condition generator for a live halo simulation. Although we use a static dark matter halo in this chapter, we used the profile of equation (2.25). Note that the truncation term leads to very little change in the dark matter density profile in the inner region focused

on in this chapter. The concentration parameter $c = r_{200}/r_s$ and $x = r/r_{200}$, where r_{200} is the radius inside which the mean density of the dark matter sphere is equal to $200\rho_{\rm crit}$ and given by

$$r_{200} = 1.63 \times 10^{-2} \left(\frac{M_{200}}{h^{-1} M_{\odot}} \right)^{\frac{1}{3}} h^{-1}{\rm kpc}. \tag{2.26}$$

We use $M_{200} = 1.75 \times 10^{12}$ M$_{\odot}$, $c = 20$ and $H_0 = 71$ km s^{-1}Mpc^{-1}.

The stellar disc is assumed to follow an exponential surface density profile

$$\rho_{\rm d} = \frac{M_{\rm d}}{4\pi z_{\rm d} R_{\rm d}^2} {\rm sech}^2 \left(\frac{z}{z_{\rm d}} \right) {\rm e}^{-R/R_{\rm d}}, \tag{2.27}$$

where $z_{\rm d}$ is the scale height of the disc and $R_{\rm d}$ is the scale length. Our target disc has $z_{\rm d} = 0.35$ kpc and $R_{\rm d} = 3.0$ kpc. The disc has a mass of $M_{\rm d} = 3.0 \times 10^{10}$ M$_{\odot}$ and consists of 10^5 particles, with each particle having a mass of 3.0×10^5 M$_{\odot}$. We use the kernel softening suggested by Price & Monaghan (2007). Although Price & Monaghan (2007) suggest using an adaptive softening length, we use a fixed softening for these simulations for simplicity. Our definition of the softening length $\varepsilon = 1.05$ kpc is about three times larger than the equivalent Plummer softening length. We also use this for the M2M modelling runs. The velocity dispersion for each three dimensional position of the disc is computed following Springel et al. (2005a) to construct an almost equilibrium condition. We use a high value of the free parameter $f_R = \sigma_R/\sigma_z = 3$, which controls the ratio between the radial and vertical velocity dispersions, to deliberately suppress structure formation and create a smooth, almost axisymmetric disc for this initial test. Our target system is a relatively smooth disc galaxy evolved over 2 Gyr, as shown in Fig. 2.1, and it is used for all models in Section 2.4.

We set up the initial conditions of the model disc with the same parameters and method, but use a different scale length from that of the target galaxy.

2.3.3 Procedure

The sudden change in potential caused by the changing particle masses induces instabilities and potentially unwanted structure formation. This effect can be reduced by dividing the modelling process into a series of stages, each with a slightly different level of M2M algorithm. This reduces the magnitude of the

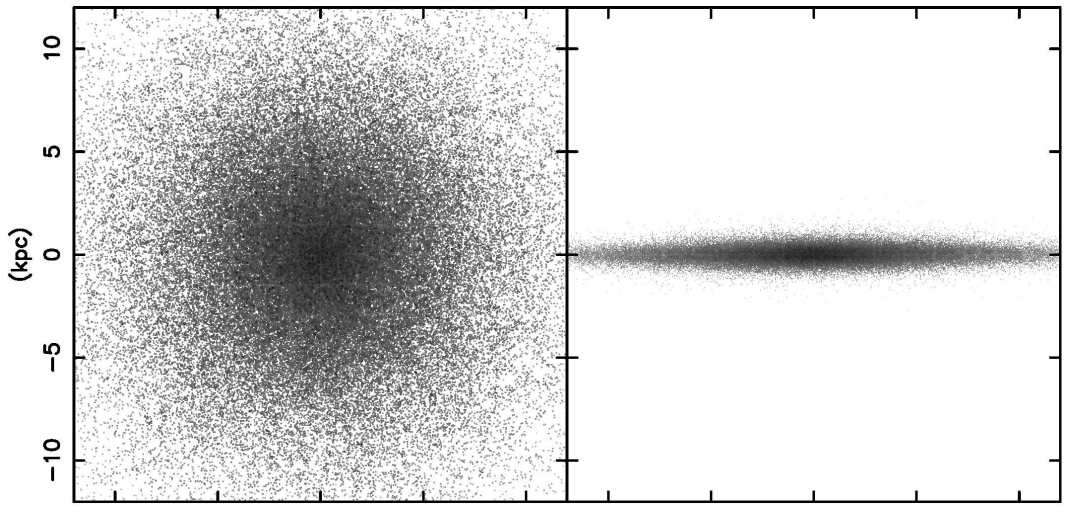

Fig. 2.1: The end result ($t = 2$ Gyr) of an N-body disc galaxy simulation. It had a scale length of 3 kpc initially. This will be used as the target system as shown in the Section 2.4. The left and right panels show the face-on and edge-on views, respectively, in a 12 kpc by 12 kpc area.

change in potential at any one time. We also set a limit on the maximum change in mass any particle can experience in one time step. We set this limit to ten percent of that particle's mass.

Initially, the model is allowed to relax in a pure self-gravity environment with no M2M constraints for 0.471 Gyr (our N-body code time unit). This relaxation period is important, as applying the M2M algorithm before the model has settled generates the aforementioned instabilities. Although our M2M algorithm was still capable of recovering the desired profile, the time scale needed was drastically increased if we turned on the M2M without the relaxation period, because the model had to smooth out again before convergence took place.

After this period of relaxation, the M2M algorithm is activated and runs without temporal smoothing for a further 1.413 Gyr, which allows the density and velocity profiles to converge quickly. During this time, the contribution of the velocity constraint is increased linearly from 0 up until our desired ζ. This allows the density profile to converge first. We found this slow increase in the velocity constraints to be important, because if the velocity constraints were introduced simultaneously at full strength, we find the large weight changes

induce the sudden potential change mentioned earlier, which is strong enough to disrupt the disc.

Then, after 1.884 Gyr, the temporal smoothing is turned on. When the M2M modelling was run with temporal smoothing from the beginning, the mass profile experienced large oscillations. The modelling then continues in this state for as long as is desired. Our M2M models are run for a period of 10 Gyr.

2.3.4 Parameter calibration

As discussed in e.g. Syer & Tremaine (1996), de Lorenzi et al. (2007), Long & Mao (2010) and Morganti & Gerhard (2012), the choice of parameters are crucial for the success of M2M modelling. In this section, we will discuss our choice of the parameters, ϵ, α, ζ and μ, and how we calibrate these values. Note that these parameters are calibrated for this specific target system. It is likely that we need different calibration for different targets. However, what we learned from the parameter search should be useful for future applications and developments of the improved version.

ϵ provides the balance between the speed of convergence, and the smoothness of the process. Note that $\epsilon = \epsilon'\epsilon''$ and ϵ'' is defined by equation (2.23). In this case, we find that when $\epsilon' > 0.1$, the weights change too rapidly, which induces the sudden potential changes and therefore more instabilities. This leads to a general decrease in the final level of accuracy of both density and velocity profiles. If $\epsilon' \leq 0.1$, convergence can be achieved and the particle weights experience a much smoother evolution. However, if ϵ' is too small, the oscillations generated by the temporal smoothing take too long to damp down, which drastically increases the length of the simulation. In the end, we have chosen $\epsilon' = 0.1$ as a balance between accuracy and simulation time. With more computing power available to us we would consider running a lower value of ϵ. However, if $\epsilon' \ll 0.1$, it is possible that the model will not show any signs of convergence as the weight change is too slow.

The choice of α, which controls the strength of the temporal smoothing, should depend upon the choice of ϵ ($\alpha \geq 2\epsilon$). We find that our modelling is not sensitive to α and we set $\alpha = 0.2$ in this chapter.

ζ (and individual ξ) controls the level of the velocity constraints. It is important to strike a balance between the density and velocity constraints, because if the level of constraints are unbalanced, one will dominate in the change of weight and the other observables will not converge. We can choose a suitable ζ (and/or $\xi_{\rm r}, \xi_z$ and $\xi_{\rm rot}$) by comparing the magnitudes of the individual terms of the right-hand-side of equation (2.22). We set ζ such that the contribution of the velocity constraint to the force of change equation is the same magnitude as, or slightly less than, the density constraints. The individual velocity components may then be fine tuned with ξ_x. For our simulations, we find that the following parameter set works well, $\zeta = 0.05$, $\xi_{\rm r} = 1$, $\xi_z = 10$ and $\xi_{\rm rot} = 1$.

μ controls the strength of the regularisation. We discuss the importance of μ in greater detail in Section 2.4.2. In our fiducial model shown in Section 2.4, we adopt $\mu = 5 \times 10^5$.

2.4 Particle-by-particle M2M results

In this section, we present the results from our modelling of a target disc galaxy. We will first show the results for our fiducial model, and then compare it with a model using only density constraints. We ran multiple M2M models with different parameters, which can be seen in Table 2.1, where $R_{\rm d,ini}$ is the initial scale length of the model disc. We only use the observables within the radius of 10 kpc.

2.4.1 Fiducial model

In this section, we present Model A, our fiducial model constructed with the parameters described in Section 2.3.4, and shown in Table 1. We start from an N-body disc with a scale length of 2 kpc, recreating the target disc ($R_{\rm d} =$ 3 kpc) with our particle-by-particle M2M, evolving the model for 10 Gyr. The left panel of Fig. 2.2 shows the radial profiles of the surface density, radial and tangential velocity dispersion, and the mean rotational velocity. The final profiles of Model A reproduce the profiles of the target system remarkably well. Note that these radial profiles are not direct constraints of the particle-by-particle M2M. Especially, it is rather surprising that the velocity dispersion

Table 2.1: M2M model parameters

Model	$R_{\rm d,ini}$ (kpc)	ϵ'	μ	α	ζ	χ^2_ρ	$\chi^2_{v_{\rm r}}$	$\chi^2_{v_z}$	$\chi^2_{v_{\rm rot}}$
A	2.0	0.1	5×10^5	0.2	0.05	0.0846	7.291	0.918	6.502
B	2.0	0.1	10^4	0.2	0	0.0831	9.599	1.074	10.873
C	2.0	0.1	10^4	0.2	0.05	0.0912	8.275	1.069	7.464
D	2.0	0.1	10^5	0.2	0.05	0.0875	7.914	1.005	7.087
E	2.0	0.1	10^6	0.2	0.05	0.0894	7.099	0.893	6.440
F	2.0	0.1	10^7	0.2	0.05	0.223	9.395	1.130	9.960
G	2.0	0.1	10^8	0.2	0.05	0.407	17.291	2.107	17.701
H	5.0	0.1	5×10^5	0.2	0.05	0.100	10.839	1.414	10.394
I	6.0	0.1	5×10^5	0.2	0.05	0.111	12.381	1.604	12.094
J	1.5	0.1	5×10^5	0.2	0.05	0.101	7.849	0.972	6.896
K	2.0	0.1	5×10^5	0.2	0.05	0.0924	7.309	0.911	6.509

profiles are recovered. We think that this is because the particle-by-particle M2M forces the model particles to follow the velocity distribution of the target particles. We also have no constraints on the total mass of the disc. Note also that the assumed velocity constant is 10 km s^{-1} in equation (2.21) yet the velocity profiles are reproduced at a level much less than 10 km s^{-1}. This is not surprising however, because we have different normalisations for density and velocity, and adjust ζ and ξ to balance their contributions in equation (2.22) making the choice of σ arbitrary. Therefore, $\sigma_{v_{\rm r},{\rm t}}$ is not indicating an error, but is merely a constant value for normalisation. In this chapter, we do not include any error. The left panel of Fig. 2.3 shows the weight evolution for a selection of particles from Model A. Weight convergence is adequate, although it is not as smooth as desired. We find that the particle weight evolution is less smooth for the case where velocity observables have been added. The right panel of Fig. 2.2 shows the χ^2 evolution for each of the observables. For all observables we use

$$\chi^2_X = \frac{\sum \Delta^2_X}{N_{\rm r}}, \tag{2.28}$$

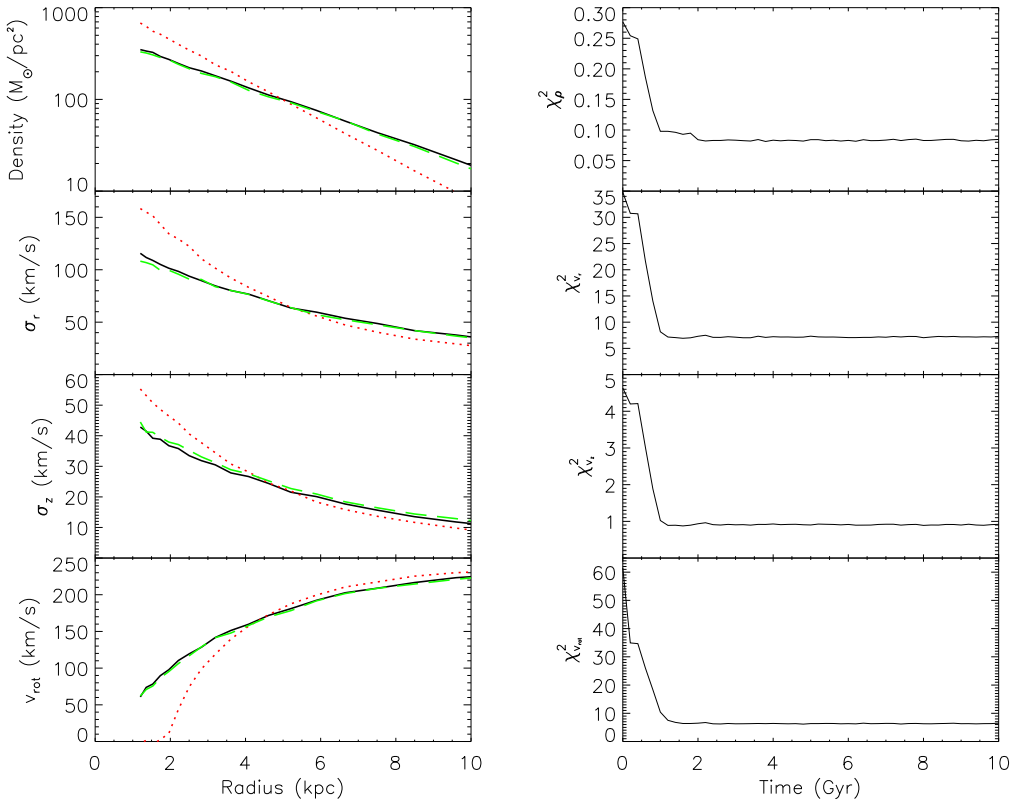

Fig. 2.2: Initial (red dotted), final (green dashed) and target (black solid), density profile (upper), radial velocity dispersion (upper middle), vertical velocity dispersion (lower middle) and rotational velocity (lower) for Model A (left). The initial model has a scale length of 2 kpc and the target model has a scale length of 3 kpc. Time evolution of χ^2 for density (upper), radial velocity (upper middle), vertical velocity (lower middle) and rotational velocity (lower) for Model A (right).

where Δ_X is equivalent to equations (2.20), i.e. $X = \rho$, and (2.21), i.e. $X = v$. This is a slightly unusual definition of χ^2 for the velocity observables. Note that we include only particles within 10 kpc and N_r is the number of target particles satisfying this criteria. In Model A, χ^2 values rapidly decrease until 2 Gyr, from which point there is almost no improvement. The final values of χ^2 are also shown in Table 1.

For comparison we show Model B, with the same initial conditions and target with the velocity constraints turned off. We find that $\mu = 5 \times 10^5$ cause over-regularisation for this case, and has to be reduced in compensation to $\mu = 10^4$. Fig. 2.4 shows the density and velocity profiles for Model B. The

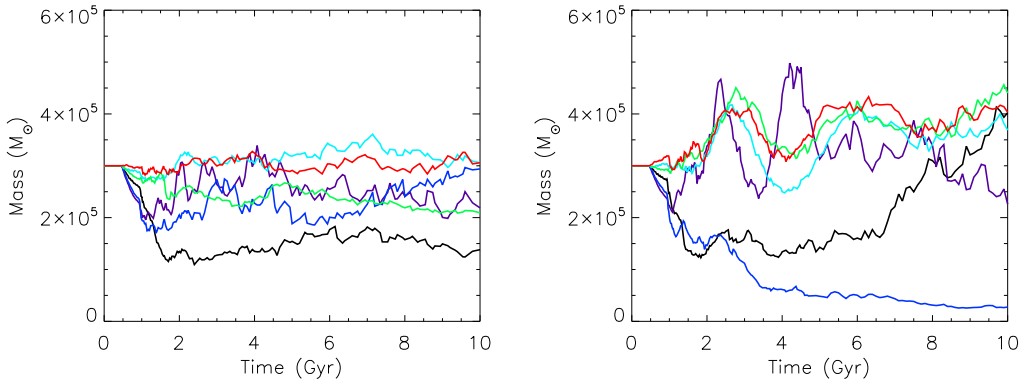

Fig. 2.3: The weight evolution for a selection of particles from Model A (left) and Model C (right).

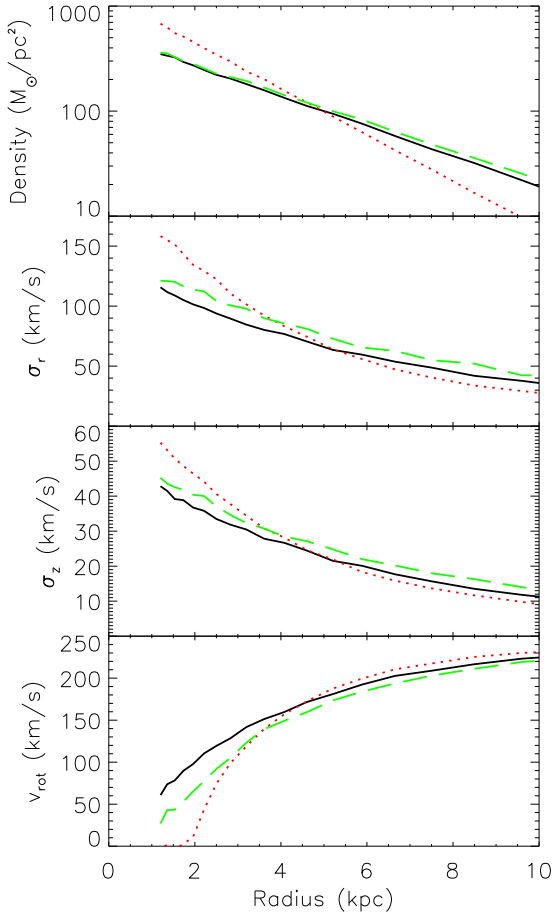

Fig. 2.4: Same as the left panel of Fig. 2.2, but for Model B which uses only the density observable as a constraint.

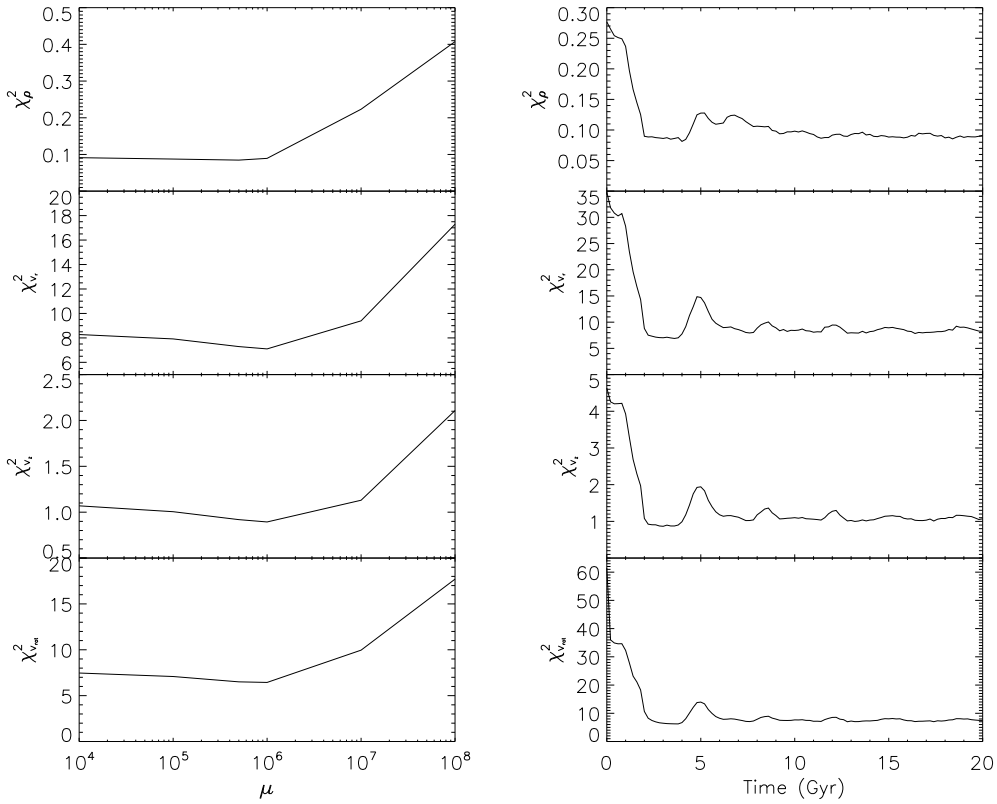

Fig. 2.5: Accuracy of our final M2M model dependent on μ as determined by χ^2 for density (upper), radial velocity (upper middle), vertical velocity (lower middle) and rotational velocity (lower) (left). Same as right panel of Fig. 2.2, but for Model C, with $\mu = 10^4$ (right).

final model-density profile resembles the target. Due to the lack of velocity constraints, while the velocity profiles do improve, they do not resemble the target. A comparison between Fig. 2.4 and the left panel of Fig. 2.2 demonstrates how the velocity constraints improve our reproduction of the dynamical properties of the target.

2.4.2 Effect of regularisation

Similar to the previous studies (e.g. Syer & Tremaine 1996; de Lorenzi et al. 2007; Long & Mao 2010), we also find that careful choice of the value of μ is key to obtain convergence to a good model, and reproduce the given observables. Therefore we discuss in this section how μ affects the modelling. We performed multiple models with the same initial conditions and parameters as Model A, except the value of μ (see Models C-G in Table 2.1). The left panel of Fig.

2.5 shows the χ^2 for the density and velocity at the final time ($t = 10$ Gyr). The figure demonstrates a slow improvement for the three velocity observables with an increasing μ up until a value of approximately $\mu = 10^6$, above which goodness of fit drops off again. The density observable benefits from a slightly lower value of μ.

Although there is not a vast difference between the final values of χ^2 for $\mu = 10^4, 10^5$ and 10^6, Model C with $\mu = 10^4$ is found to be an inappropriate model because of its poor convergence. The right panel of Fig 2.5 displays the time evolution of χ^2 in Model C which shows oscillatory behaviour. The right panel of Fig. 2.3 (Model C) shows the time evolution of the weight for the same particles selected in the left panel of Fig. 2.3 (Model A). Comparison between panels in Fig. 2.3 demonstrates that $\mu = 10^4$ is too low to suppress the large amplitude of the fluctuations in the particle weights. The weights of the particles keep changing and do not converge. Therefore, we judge that $\mu = 10^4$ is unacceptable for recreating the target system.

Fig. 2.6 displays the distribution of particle weights at the final time for Models A and C. The histogram shows a wider tail, and lower peak for the under-regularised Model C compared to our fiducial Model A. This is expected because a higher μ restricts particles from moving far from the initial mass used as a prior. As a result, Model A shows a narrower distribution and thus a higher peak close to the initial value of w_i. Fig. 2.6 also demonstrates that $\mu = 10^4$ is less favourable.

If we examine substantial over-regularisation, i.e. a higher value of μ, it is easy to see the damaging effect on the density and velocity profiles. The left panel of Fig. 2.7 shows the profiles from Model G, with $\mu = 10^8$, which shows the significant discrepancy in the density and rotational velocity profiles between the final profiles and the target profiles. The discrepancy in the other two velocity observables is not as substantial. However, it is clearly worse when compared with the left panel of Fig. 2.2.

In summary, we found that we required regularisation of around $\mu = 10^5 - 10^6$ as a compromise between the goodness of fit, and the smoothness of the χ^2 and particle weight evolution. Both $\mu = 10^7$ and $\mu = 10^8$ show over-

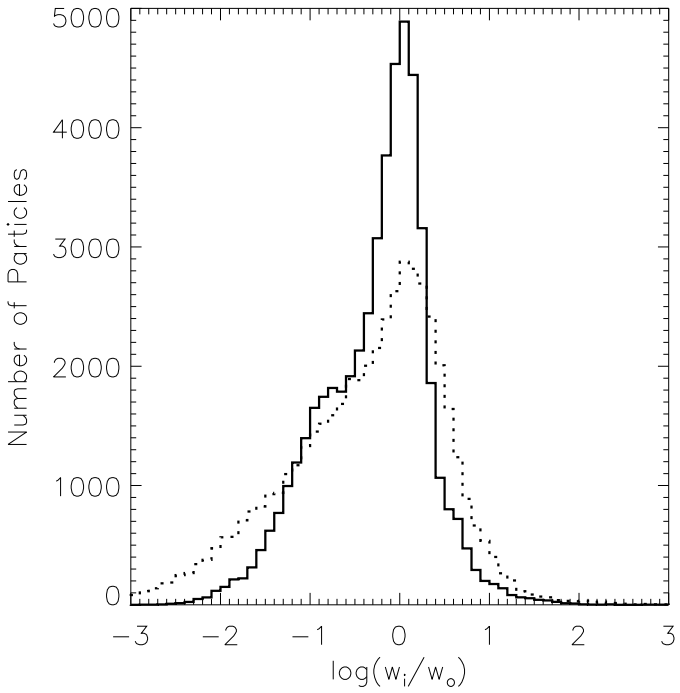

Fig. 2.6: Distribution of particle weights for Model A (solid) and Model C (dotted) at the final time, $t = 10$ Gyr. w_0 indicates the initial particle weights.

regularisation and the density profiles associated with those values converge to an incorrect profile. $\mu = 10^4$ shows large oscillations in both χ^2 and particle weights, and convergence is not reached. Anything in the range of $\mu = 10^5 - 10^6$ appears appropriate and hence our fiducial model adopts $\mu = 5 \times 10^5$. As can be seen from Table 2.1, we find under-regularisation is preferable to over-regularisation. This is also the case in previous literature (e.g. de Lorenzi et al. 2008; Morganti & Gerhard 2012) implying that this is a generic feature of M2M and not intrinsic to any specific algorithm.

2.4.3 Different initial conditions

We also tested the algorithm on the same target, using initial discs with a different scale length, but with the same parameters as Model A. We have already discussed the benefits of tailoring μ to the model. Thus, we were not expecting that these models (Models H-I in Table 2.1) would recreate their target systems to the same level as Model A. However, for demonstration purposes, we show how the parameter set in Model A works if the initial

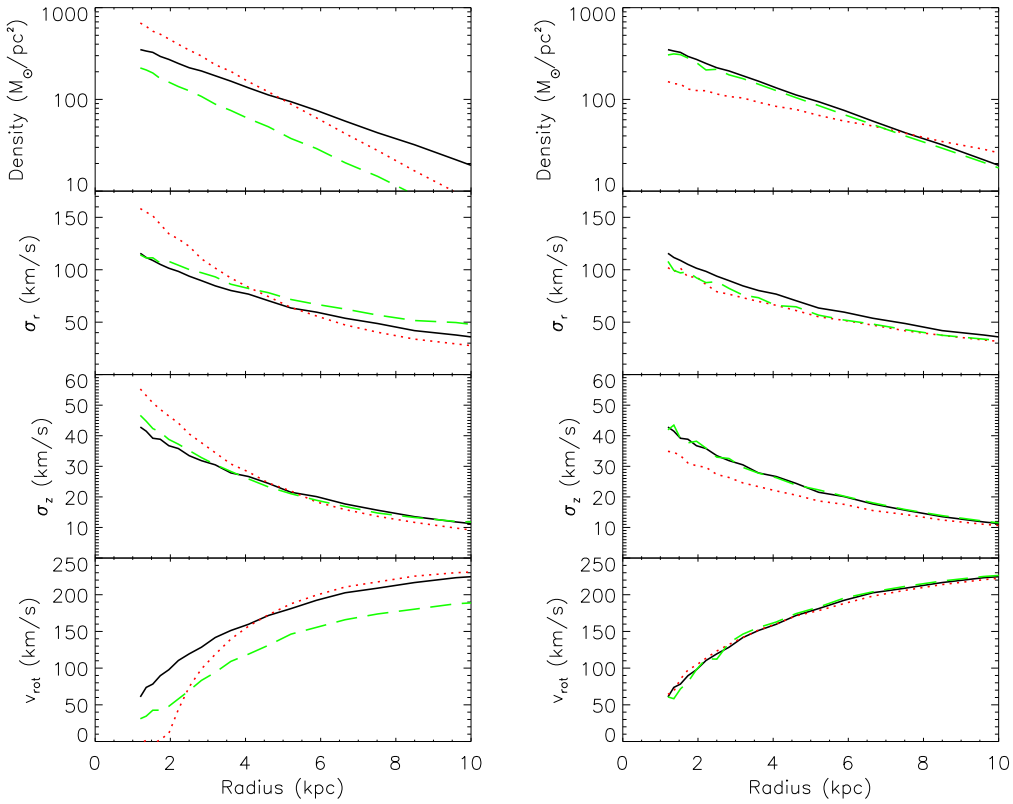

Fig. 2.7: Same as the left panel of Fig. 2.2 but for Model G, with $\mu = 10^8$ (left), and Model H (right), where $R_{\rm d,ini} = 5.0$ kpc

conditions are different. When we started from a higher initial scale length (Model H with $R_{\rm d,ini} = 5$ kpc and Model I with $R_{\rm d,ini} = 6$ kpc), we attained a reasonable reproduction of the target. However, the final χ^2 is systematically higher than Model A (see Table 1). The right panel of Fig. 2.7 shows the profiles from Model H, which slightly disagree with the targets. This seems to be due to over-regularisation, and we would need to adjust μ in order to obtain a better model. On the other hand, when we started from a lower initial scale length (Model J with $R_{\rm d,ini} = 1.5$ kpc, the profiles are shown in the left panel of Fig. 2.8), χ^2 was only fractionally worse than the fiducial case Model A (see Table 2.1). This demonstrates that it is better to set the initial disc with a smaller scale length. In the application to the real observational data of the Milky Way, we do not know the right shape of 'the target model'. However, we hope that further studies with these target galaxies would help us to understand more about how the M2M modelling behaves in different

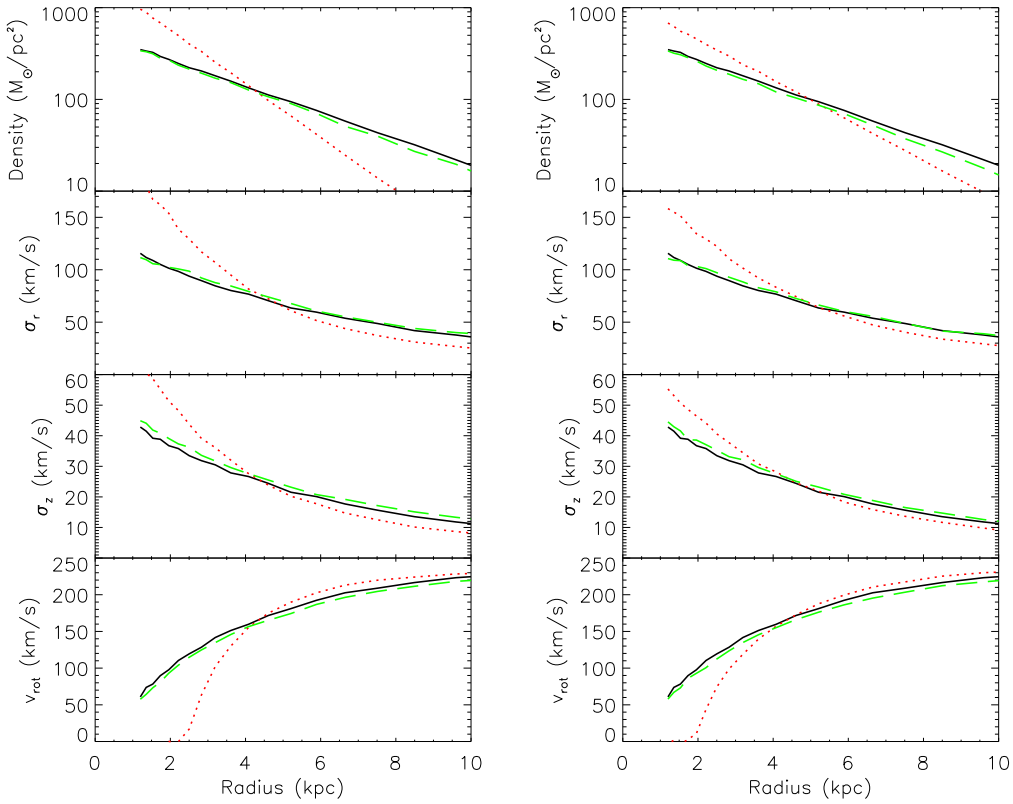

Fig. 2.8: Same as the left panel of Fig. 2.2, but for Model J , where $R_{\rm d,ini} = 1.5$ kpc (left), and Model K (right), where the observables are calculated only in a sphere of 10 kpc around a point in the plane and at 8 kpc from the galactic centre.

cases, and how we should calibrate the parameters.

2.4.4 The partial data case

Because our goal is to eventually use our method with *Gaia* data, and *Gaia* will only survey a section of the Galactic disc, it is important to test our algorithm on an incomplete data set (Model K in Table 2.1). In this chapter, a simple selection function is applied for the purpose of demonstration. Remember that our models in the previous sections have used only the data within the radius of 10 kpc from the centre. In this section, we additionally restricted the observables within a 10 kpc sphere around a point in the plane, and at 8 kpc away from the Galactic centre.

The right panel of Fig. 2.8 shows the final profiles for Model K, which reproduces the target profiles reasonably well. Compared with the left panel of Fig. 2.2, the right panel of Fig. 2.8 shows only a minor discrepancy to the

target profiles, mainly in the outer region. Worse performance in the outer region is unsurprising, as the larger the radii, the smaller percentage of the particles orbits are spent within the sampled area. Table 2.1 displays a better value of χ^2 for Model K than for over-regularised models, and similar levels of the goodness of fit to under-regularised ones, without the excessive weight oscillations. Model K demonstrates that it is possible to apply our particle-by-particle M2M to a disc galaxy with only a limited selection of data.

2.5 Chapter summary

We have developed the initial version of our new particle-by-particle M2M, where the observables are compared at the position of the target particles, and the gravitational potential is automatically adjusted by the weight change of the particles. This chapter demonstrates that the particle-by-particle M2M can recreate a target disc system in a known dark matter potential. The radial profiles of the surface density, velocity dispersion in the radial and perpendicular directions, and the mean rotational velocity of the target disc are all well reproduced from the initial disc model whose scale length is different from that of the target disc. We find that the regularisation parameter, μ, is key to obtaining a reasonable convergence to a satisfactory model. We also demonstrate that our M2M can be applied to an incomplete data set and recreate the target disc reasonably well when the observables are restricted to within a sphere of radius 10 kpc around a point in the disc plane and at 8 kpc from the centre.

Admittedly, these applications are simplified cases. Our ultimate goal is to develop the M2M to be applicable to the observational data that *Gaia* and other related Galactic surveys will provide. As discussed in Section 1.3, *Gaia* will produce an unprecedentedly large amount of data for the order of a billion stars, with many dimensions of information. The accuracy of each dimension of information could be quite inhomogeneous, depending on distance, stellar population, and location in the sky due to dust extinction, crowding etc. meaning that the observational selection function is quite complex. There are many challenges before us to develop the M2M for *Gaia* type data.

We believe that as shown in this chapter, it is a good practice for galaxy modelling to attempt to reconstruct galaxy models created by N-body simulations, where the full dimensions of the properties are known. We hope that many exercises with these mock galaxy targets created by N-body simulations will be useful to identify the uniqueness of the obtained dynamical model and possible systematic biases. Although as an initial attempt we have taken a disc without any non-axisymmetric structure, in the next chapter we will apply the method to N-body discs with spiral arms and a bar. In Chapter 4, we will add more realistic errors and selection functions, to account for dust extinction and crowding.

Chapter 3

Investigating bar structure of disc galaxies via PRIMAL: A particle-by-particle M2M algorithm

This chapter is based on Hunt et al. (2013)

We have modified our particle-by-particle adaptation of the M2M method described in Chapter 2, with the aim of modelling the Galactic disc from upcoming Galactic stellar survey data. In our new particle-by-particle M2M algorithm, PRIMAL, the observables of the target system are compared with those of the model galaxy at the position of the target stars, i.e. particles. The mass of the model particles are adjusted to reproduce the observables of the target system, and the gravitational potential is automatically adjusted by the changing mass of the particles. This chapter builds upon the initial development of the particle-by-particle M2M method described in Chapter 2, introducing likelihood-based velocity constraints in PRIMAL. In this chapter, we apply PRIMAL to barred disc galaxies created by an N-body simulation in a known dark matter potential, with no error in the observables. This chapter demonstrates that PRIMAL can recover the radial profiles of the surface density, velocity dispersion in the radial and perpendicular directions, and the mean rotational velocity of the target discs, along with the apparent bar structure and pattern speed of the bar, especially when the reference frame is adjusted

so that the bar angle of the target galaxy is aligned to that of the model galaxy at every timestep.

3.1 Introduction

In Chapter 2, we discussed the development of a particle-by-particle M2M algorithm now called PRIMAL. We apply PRIMAL to the target system of a smooth axisymmetric disc created by N-body simulations, and demonstrate that PRIMAL can reproduce the density and velocity profiles of the target system well, even when starting from a disc whose scale length is different from the target system.

In this chapter, we apply PRIMAL to barred disc galaxies again generated by N-body simulations with GCD+ (Kawata & Gibson 2003; Kawata et al. 2013). We introduce a new form of velocity observable constraints as described in de Lorenzi et al. (2008), based on the likelihood function as described in Romanowsky & Kochanek (2001). We also introduce a rotating reference frame in a similar, although not identical fashion to Long et al. (2013). We use target systems whose information is known without any error. Ultimately, we wish to apply PRIMAL to real observational data, where the information will be provided for a limited region of the sky, with a more complicated selection and error function due to the dust extinction, crowding and stellar populations. However, in the development stages it is important to test the algorithm against an ideal target. In this chapter, we demonstrate the successful application of PRIMAL to the barred galaxy targets, and this is a significant step forward to modelling the Milky Way with M2M.

This chapter is organised as follows. Sections 3.2.1 and 3.2.2 contain the alterations applied to PRIMAL from Chapter 2. Section 3.3 shows the performance of our updated method for recreating the target disc systems. In Section 3.4, we provide a summary of this work.

3.2 The M2M algorithm: PRIMAL

3.2.1 Likelihood adaptation for velocity constraints

As discussed in Chapters 1 and 2, the M2M algorithm works by calculating observable properties (observables hereafter) from the model and the target,

and then adapting particle masses such that the properties of the model reproduce those of the target. The target can be in the form of a distribution function, an existing simulation, or real observational data. The model can be a test particle simulation in an assumed fixed or adaptive potential, or a self-gravity N-body model.

In Chapter 2, we use velocity observables in the form of mean local velocity field, calculated around the target particle positions, with the kernel described in equation (2.14). However, as the Galactic stellar surveys will provide us velocity information for individual particles, instead of smoothing the velocity, we can evaluate likelihood of the actual velocity of the particle. Thus, we have converted the velocity section of our algorithm to maximise the likelihood of the velocity of the target particles as shown in de Lorenzi et al. (2008). The likelihood is calculated with the equation

$$\mathcal{L} = \sum_j \ln(\mathcal{L}_j), \tag{3.1}$$

where $\mathcal{L}_j$ is the likelihood function for a single discrete velocity. Following Romanowsky & Kochanek (2001), we calculate the likelihood for individual velocity observables, v_j, at the target particle positions, $\mathbf{r}_j$, with

$$\mathcal{L}_j(v_j, \mathbf{r}_j) = \frac{1}{\sqrt{2\pi}} \int \left(\frac{\mathrm{d}L}{\mathrm{d}v}\right)_j \mathrm{e}^{-(v_j - v)^2/2\sigma_j^2} \mathrm{d}v, \tag{3.2}$$

where σ_j is the velocity error, which we have set as $\sigma_j = 2.5$ km s^{-1} for this chapter, and $\mathrm{d}L/\mathrm{d}v$ is a velocity distribution for the model. Although we fix the velocity error, and do not discuss the effects of the errors in this chapter, an advantage of the likelihood-based velocity constraints is that we can set individual errors for each velocity component of each particle. Instead of the kernel chosen in de Lorenzi et al. (2008) we use our kernel from equation (2.14), allowing us to write $\mathrm{d}L/\mathrm{d}v$ for target particle j, from model particle i, as

$$\left(\frac{\mathrm{d}L}{\mathrm{d}v}\right)_j = \frac{1}{l_j} \sum_i W_{ij} m_i \delta(v - v_i), \tag{3.3}$$

where $\delta(x)$ is the delta function and

$$l_j = \sum_i W_{ij} m_i, \tag{3.4}$$

which is the same as equation (2.17). We can express $\mathcal{L}_j$ in equation (3.2) as

$$\mathcal{L}_j = \frac{\hat{\mathcal{L}}_j}{l_j}, \tag{3.5}$$

where

$$\hat{\mathcal{L}}_j = \frac{1}{\sqrt{2\pi}} \sum_i W_{ij} m_i \mathrm{e}^{-(v_j - v_i)^2/2\sigma_j^2}, \tag{3.6}$$

and

$$\frac{\mathrm{d}\hat{\mathcal{L}}_j}{\mathrm{d}m_i} = \frac{1}{\sqrt{2\pi}} W_{ij} \mathrm{e}^{-(v_j - v_i)^2/2\sigma_j^2}. \tag{3.7}$$

This leads us to the modified term in the particle mass change equation. Following the M2M algorithm, we maximise the likelihood of equation (3.1), using

$$\frac{\mathrm{d}m_i}{\mathrm{d}t} = \epsilon m_i M \frac{\mathrm{d}\mathcal{L}_j}{\mathrm{d}m_i}, \tag{3.8}$$

where

$$\begin{aligned} \frac{\mathrm{d}\mathcal{L}_j}{\mathrm{d}m_i} &= \frac{\mathrm{d}}{\mathrm{d}m_i} \sum_j \ln\left(\frac{\hat{\mathcal{L}}_j}{l_j}\right) \\ &= \sum_j \left[\frac{\mathrm{d}}{\mathrm{d}m_i}\ln(\hat{\mathcal{L}}_j) - \frac{\mathrm{d}}{\mathrm{d}m_i}\ln(l_j)\right] \\ &= \sum_j \left[\frac{1}{\hat{\mathcal{L}}_j}\frac{\mathrm{d}}{\mathrm{d}m_i}\hat{\mathcal{L}}_j - \frac{1}{l_j}W_{ij}\right]. \end{aligned} \tag{3.9}$$

The particle mass change equation from the velocity based likelihood constraints is calculated with

$$\frac{\mathrm{d}m_i}{\mathrm{d}t} = \epsilon m_i M \sum_j W_{ij} \left[\frac{1}{\sqrt{2\pi}} \frac{\mathrm{e}^{-(v_j - v_i)^2/2\sigma_j^2}}{\hat{\mathcal{L}}_j} - \frac{1}{l_j}\right], \tag{3.10}$$

and equation (2.22) becomes

$$\begin{aligned} \frac{\mathrm{d}}{\mathrm{d}t} m_i(t) &= -\epsilon m_i(t) \Bigg\{ M \sum_j \frac{W(r_{ij}, h_j)}{\rho_{\mathrm{t},j}} \tilde{\Delta}_j(t) \\ &- \zeta M \Bigg[\sum_j W_{ij} \left(\frac{1}{\sqrt{2\pi}} \frac{\mathrm{e}^{-(v_{\mathrm{r},j} - v_{\mathrm{r},i})^2/2\sigma_{\mathrm{r},j}^2}}{\hat{\mathcal{L}}_{\mathrm{r},j}} - \frac{1}{l_j} \right) \\ &+ \sum_j W_{ij} \left(\frac{1}{\sqrt{2\pi}} \frac{\mathrm{e}^{-(v_{z,j} - v_{z,i})^2/2\sigma_{z,j}^2}}{\hat{\mathcal{L}}_{z,j}} - \frac{1}{l_j} \right) \\ &+ \sum_j W_{ij} \left(\frac{1}{\sqrt{2\pi}} \frac{\mathrm{e}^{-(v_{\mathrm{rot},j} - v_{\mathrm{rot},i})^2/2\sigma_{\mathrm{rot},j}^2}}{\hat{\mathcal{L}}_{\mathrm{rot},j}} - \frac{1}{l_j} \right) \Bigg] \\ &+ \mu \left(\ln\left(\frac{m_i(t)}{\hat{m}_i}\right) + 1 \right) \Bigg\}, \end{aligned} \tag{3.11}$$

where $v_{\rm r}$, v_z and $v_{\rm rot}$ are the radial, vertical and rotational velocity components. The parameter, ζ, is an optional adjustable parameter for changing the significance of the velocity constraints, although we set $\zeta = 1$ in this chapter. Following de Lorenzi et al. (2008), we use temporally smoothed versions (c.f. equation 2.12) of $\hat{\mathcal{L}}$ and l.

Alongside this new mass change equation, we have also altered the time when the constraints are applied from the description in Chapter 2. We found that when using the likelihood-based velocity constraints the model requires a lower level of temporal smoothing, and thus we are able to use temporal smoothing as soon as the mass change equation is enabled. Thus, we now use the following series of stages. From $t = 0$ to 0.471 Gyr (one simulation time unit), we allow the initial model to experience relaxation, following a standard self-gravity N-body calculation without any mass change. From $t = 0.471$ Gyr to 0.942 Gyr, we used temporally smoothed density constraints only, and at $t = 0.942$ Gyr, we engage the velocity constraints as well. This sequence is substantially shorter than the method used in Chapter 2, allowing the solution to converge faster, and the overall simulation length to be halved to ~ 5 Gyr. We continue to use individual timesteps for the particles, and only update the masses of particles whose position and velocity are updated within the individual timestep. The timestep for each particle is determined by

$$\mathrm{d}t_i = C_{\rm dyn} \left(\frac{0.5 h_i}{|\mathrm{d}\mathbf{v}_i/\mathrm{d}t|} \right)^{\frac{1}{2}}, \tag{3.12}$$

with $C_{\rm dyn} = 0.2$. We also retain the limit on the maximum mass change which any particle can experience in one timestep. We set this limit to 10% of that particles mass.

We have again performed a parameter search to determine differences in the likelihood-based velocity constraints, as we did in Chapter 2. There are four important parameters, ϵ, α, ζ and μ, which must be calibrated for M2M. ϵ provides the balance between the speed of convergence, and the smoothness of the process. Note that $\epsilon = \epsilon' \epsilon''$, where ϵ'' is defined by equation (2.23). We have chosen $\epsilon' = 0.1$ as an appropriate balance between accuracy and simulation time. The choice of α, which controls the strength of the temporal

smoothing, should depend upon the choice of ϵ ($\alpha \geq 2\epsilon$). We find that our modelling is not overly sensitive to α as long as the condition $\alpha \geq 2\epsilon$ is met and we set $\alpha = 2.0$ in this chapter. We set $\zeta = 1$ as mentioned before. μ controls the strength of the regularisation and is essential in reducing the oscillation in particle masses and ensuring smooth convergence. We discuss the importance of μ in much greater detail in Chapter 2. In this chapter, we adopt $\mu = 10^5$. All different models presented in Section 3.3 use this same parameter set, and have not been individually tailored to the target or model in question. This demonstrates the robustness of the method.

3.2.2 Rotating reference frames

In Chapter 2, it was sufficient to use a fixed reference frame as we were investigating smooth axisymmetric discs. However, if the target has some non-axisymmetric structure, such as a bar, the target bar angle is fixed, but the bar of the model rotates in the fixed reference frame. For example, if there is a bar, we expect the density and kinematics to be very different at the different azimuth angles at a fixed radius. Then, if the bar of the model is not aligned with the target bar, the observables of the model are evaluated in the different dynamical states from the target observables. Hence, if the bar of the model keeps rotating in the fixed frame, the model particles receive the different constraints from the target depending on the bar angle at each timestep, and the model never settles to the solution. This is discussed in Section 3.3.

Long et al. (2013) have proposed using a reference frame with a fixed bar angle, and comparing multiple simulations with different bar angles to find the best fit. This was trivial for their model, because they used a fixed shape of the bar potential and rotating with a fixed bar pattern speed, $\Omega_{\rm p}$. However, we have not assumed any pattern speed prior to the beginning of our simulations, nor have we placed any explicit constraints on it. Instead, we start with a smooth disc as the initial condition, allowing the pattern speed to evolve with the model galaxy due to self-gravity, and compare $\Omega_{\rm p}$ for the model and target galaxies at the end of the run.

Therefore, we calculate the angle of the bar in our target, and the angle of the bar in the model at each step. Then, we rotate the model to match the bar

Table 3.1: N-body target parameters. M_{200} is the mass of the halo, $M_{\rm d}$ is the mass of the disc, c is the concentration parameter, $z_{\rm d}$ is the scale height, $\sigma_{\rm r}^2/\sigma_z^2$ is the ratio between radial and tangential velocity dispersion and $\Omega_{\rm t,p}$ is the pattern speed of the bar, measured at 2 Gyr.

Target	M_{200} ($M_\odot$)	$M_{\rm d}$ ($M_\odot$)	c	$z_{\rm d}$ (kpc)	$\sigma_{\rm r}^2/\sigma_z^2$	$\Omega_{\rm t,p}$ (km s^{-1}kpc^{-1})
I	1.75×10^{12}	3.0×10^{10}	20.0	0.35	9.0	N/A
II	2.0×10^{12}	5.0×10^{10}	9.0	0.3	2.0	27.5
III	1.5×10^{12}	5.0×10^{10}	7.0	0.3	2.0	31.7
IV	1.75×10^{12}	5.0×10^{10}	9.0	0.3	2.0	28.9

angle of the target for the purposes of calculating the observables in the same reference frame. It is our hope that this method will allow the pattern speed to be recovered along with the density and velocity profiles. When applying this to the Milky Way we will not know the exact bar angle. However, we here assume that the bar angle is known for our first step of modelling the bar. We call this reference frame change the 'rotating reference frame' hereafter. In Section 3.3, we present a comparison of our method with and without this rotating reference frame, and also present the results from cases where we have chosen an incorrect bar angle.

3.2.3 Target system setup

Similar to Chapter 2, our simulated target galaxies consist of a pure stellar disc with bar structure and a static dark matter halo, set up using the method described in Grand et al. (2012a).

We have constructed four different target galaxies whose initial conditions are listed in Table 1. The scale length of the target discs are initially set as $R_{\rm t,d} = 3$ kpc. We run N-body simulations with these initial conditions, with 10^6 particles, for 2 Gyr using a tree N-body code, GCD+ (Kawata & Gibson 2003; Kawata et al. 2013), and adopt the final output as a target. We use the kernel softening suggested by Price & Monaghan (2007). Although these authors suggest using an adaptive softening length, we use a fixed softening for these simulations for simplicity. Our softening length $\varepsilon = 0.577$ kpc is about three times larger than the equivalent Plummer softening length. We also use

Table 3.2: M2M model results at the final timestep. $\Omega_{\rm t,p}$ is the target pattern speed, $\Omega_{\rm p}$ is the model pattern speed, χ^2_ρ is a measure of accuracy of the density, $\mathcal{L}_{\rm r,z,rot}$ are the likelihood values for the radial, tangential and rotational velocity, a lower value means a more accurate model.

Model	Target	$\Omega_{\rm p}$ (km s^{-1}kpc^{-1})	χ^2_ρ	$-\mathcal{L}_{\rm r}/10^6$	$-\mathcal{L}_z/10^6$	$-\mathcal{L}_{\rm rot}/10^6$
A	I	N/A	0.123	6.06	3.61	5.27
B	II	27.9	0.254	4.72	3.62	4.43
C	III	30.4	0.235	4.96	4.40	5.28
D	IV	28.3	0.189	5.14	5.15	5.02
E	II	27.3	0.230	4.77	3.65	4.47
F	II	23.6	0.276	5.77	3.91	5.21
G	II	28.0	0.250	4.87	3.67	4.55
H	II	24.3	0.21-0.49	6.82-9.99	4.59-5.48	6.63-8.77

this softening for the M2M modelling runs.

As mentioned above, in this initial stage of development, we assume that the dark matter halo potential is known and there is no other external potential such as the bulge or stellar halo. We use the same number of particles, 10^6, and the same dark matter halo and initial disc parameters for the model and target galaxies, except for the disc scale length of $R_{\rm d} = 2$ kpc for the models and $R_{\rm t,d} = 3$ kpc for the targets.

3.3 PRIMAL results

In this section, we present the results from our eight models using PRIMAL. We will first show the results for the smooth featureless target disc previously explored in Chapter 2. Then, we apply PRIMAL to three different barred targets. We also examine how PRIMAL can reproduce the target galaxy with a partial data set of the observables, or an incorrect bar angle, or without the rotating reference frame using one of the targets. Table 3.2 shows which target the model is recreating, the bar pattern speeds, the likelihood values for radial, tangential and rotation velocity, $\mathcal{L}$, in equation (3.1) and the χ^2_ρ from equation (2.28). Note that we include only particles within 10 kpc, and

$N_{\rm r}$ in equation (2.28) is the number of particles satisfying this criterion. Note also that in the likelihood case, although we seek to maximise likelihood, the values of $-\mathcal{L}$ are shown in Table 3.2, and hence smaller values in Table 3.2 mean higher likelihood. The absolute values of $\mathcal{L}$ are not important. We cannot compare these values between models for different targets. However, the relative differences in χ^2_ρ and in $\mathcal{L}$ between models for the same target observables are meaningful and are used in Section 3.3.4.

3.3.1 Smooth disc

First, we demonstrate that the newly introduced likelihood velocity constraints can reproduce the smooth featureless disc target used in Chapter 2. Model A applies PRIMAL to Target I, which was the target used in Chapter 2, but using a larger number of particles. Note that the high value of $\sigma_{\rm r}^2/\sigma_z^2$ of Target I in Table 3.1 was used to deliberately suppress structure formation. The left panel of Fig. 3.1 shows that the radial profiles of the density, the radial velocity dispersion, the vertical velocity dispersion and the mean rotation velocity for the target galaxy, the initial galaxy and the final output after PRIMAL is applied. The figure demonstrates that PRIMAL with the likelihood-based velocity constraints equally or even more accurately reproduces the target galaxies compared to our old version of the particle-by-particle M2M in Chapter 2. However, a quantitative comparison between the old and new version is not the main focus of this thesis. As discussed above, we introduced the likelihood-based velocity constraints, because we can compare the velocity more directly and also introduce different errors for individual velocity components and individual particles. Therefore, the likelihood-based velocity constraints are a necessary update, and a comparison with the old version is not an important issue. Note that the properties shown in the left panel of Fig. 3.1 are not explicitly constrained by PRIMAL. As discussed previously in Chapter 2, it is interesting to note that although our particle-by-particle M2M uses only the first moment of the velocity components as observables, because PRIMAL tries to reproduce the velocity of individual particles, the velocity distribution becomes close to the target. Therefore, the velocity dispersion can be reproduced as well.

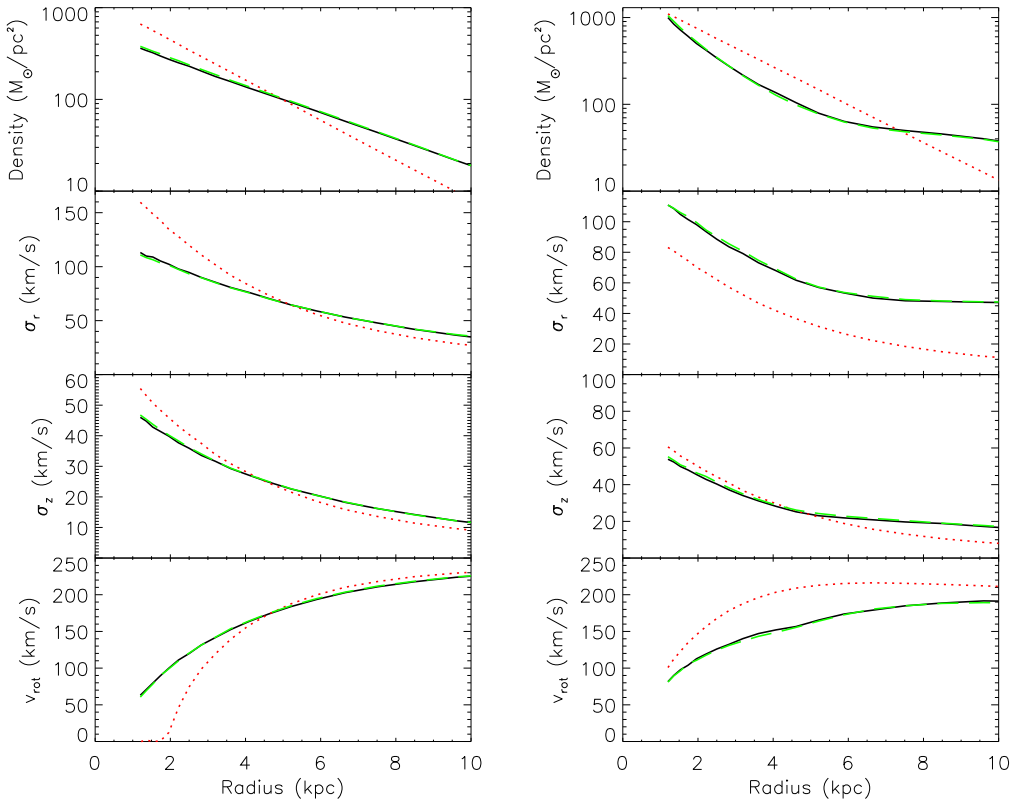

Fig. 3.1: Initial (red dotted), final (green dashed) and target (black solid) density profile (upper), radial velocity dispersion (upper middle), vertical velocity dispersion (lower middle) and rotation velocity (lower) for Model A with Target I (left), and Model B with Target II (right).

3.3.2 Barred disc models

In this section, we present the results of Models B, C and D, where we apply the same parameter set for PRIMAL to model three different target barred galaxies. Target II is a barred disc galaxy showing faint spiral structure. Fig. 3.2 shows the face-on and edge-on views of Target II (top left) and the final state of Model B (top right). The final model reproduces the bar feature very well. The observables are only constrained within 10 kpc of the galactocentric radius and hence the areas outside this radius are reproduced with less accuracy.

The right panel of Fig. 3.1 shows the radial profiles of the surface density, radial and tangential velocity dispersion, and the mean rotation velocity for the target and the final model compared to the initial model. As in Chapter 2 and Model A, these radial profiles are not directly constrained by PRIMAL,

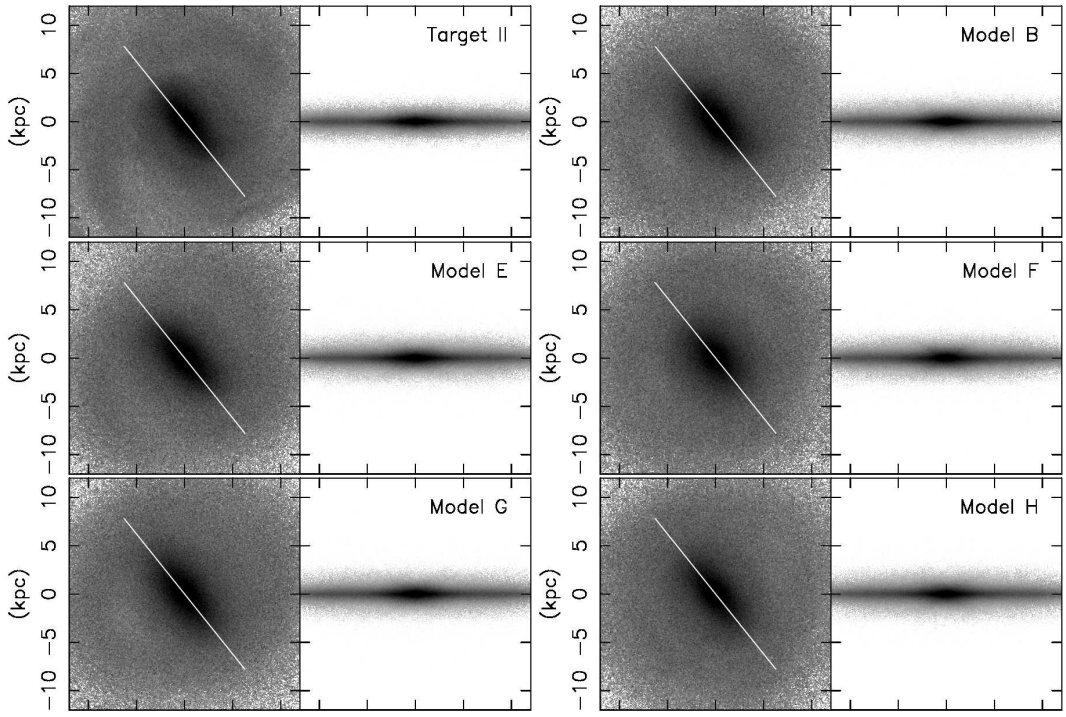

Fig. 3.2: Face-on and edge-on density maps of, Target II (top left), Model B (top right), Model E (middle left), Model F (middle right), Model G (lower left) and Model H (lower right), in a 12 kpc by 12 kpc area, plotted for comparison. The white line indicates the angle of the bar, rotated for comparison. The density scale is the same for all panels.

but are reproduced remarkably well. The right panel of Fig. 3.1 shows a substantial increase in radial velocity dispersion and a corresponding decrease in mean rotational velocity from the initial to the final model. We believe that this is due to heating from the bar which leads to an excellent agreement with the velocity dispersion of the target.

The pattern speed of the bar, $\Omega_{\rm p}$, is also reproduced very well, as shown in Tables 3.1 and 3.2. We calculate the pattern speed of the bar, $\Omega_{\rm p}$, by calculating the change in the angle of the bar between timesteps, divided by the difference in time between the steps. We take $\Omega_{\rm p}$ to be the mean value from the final 10 steps. We found that the bar pattern speed of the model is $\Omega_{\rm p} = 27.9$ km s^{-1} which is close to that of the target, $\Omega_{\rm t,p} = 27.5$ km s^{-1}. This is probably due to our self-consistent calculation of the gravitational potential, because once the mass distribution and kinematic properties of the target disc are reproduced, a bar with a similar shape and pattern speed to those of the

target is expected to develop. This is certainly helped by our use of a known, fixed dark matter halo potential. We are pleased to see a spiral arm developing in the model, which looks similar to the one seen in the target.

Model C applies PRIMAL to Target III, which is also a barred disc galaxy, but with a smaller bar than Target II, and a boxy and peanut shaped bulge (e.g. Pfenniger 1984; Athanassoula & Misiriotis 2002; Debattista et al. 2005; Bureau et al. 2006; Saito et al. 2011), as can be seen in the top left panel of Fig. 3.3. Rather surprisingly PRIMAL reproduces the boxy structure of the target as shown in the bottom left panel of Fig. 3.3. The left panel of Fig. 3.4 shows the radial profiles for Model C. We see a slight inaccuracy in the inner 2 kpc of the radial velocity dispersion, and also in the rotational velocity in the inner 4 kpc, which corresponds roughly with the length of the bar. In addition, σ_z is systematically higher than the target at all radii. As such the bar pattern speed is not as well reproduced as with Model B, with $\Omega_{\rm p} = 30.4$ km s^{-1} compared to $\Omega_{\rm t,p} = 31.7$ km s^{-1}. However, we still think that this is a reasonably good recovery of the target, and it is encouraging for further development of PRIMAL for its application to more complicated observational data.

Model D takes Target IV which is morphologically similar to Target III, with a small bar and boxy peanut feature, as can be seen in the top right panel of Fig. 3.3. We see a slightly larger bar in the model than in the target. The right panel of Fig. 3.4 shows slight inaccuracies in the recovery of the radial and vertical velocity dispersion and mean rotational velocity in the inner 3 kpc roughly consistent with the radius of the bar. However, the pattern speed is still recovered well with $\Omega_{\rm p} = 28.3$ km s^{-1} for the final model compared to the target of $\Omega_{\rm t,p} = 28.9$ km s^{-1}.

3.3.3 Working with partial data

Even with the huge amount of data returned by *Gaia* and related stellar surveys, due to our position within the Milky Way's disc, we will not even come close to having a complete data set of the disc stars. Therefore, it is important to make sure our method is still applicable when we do not have access to the complete picture of the disc. Our previous models have used all

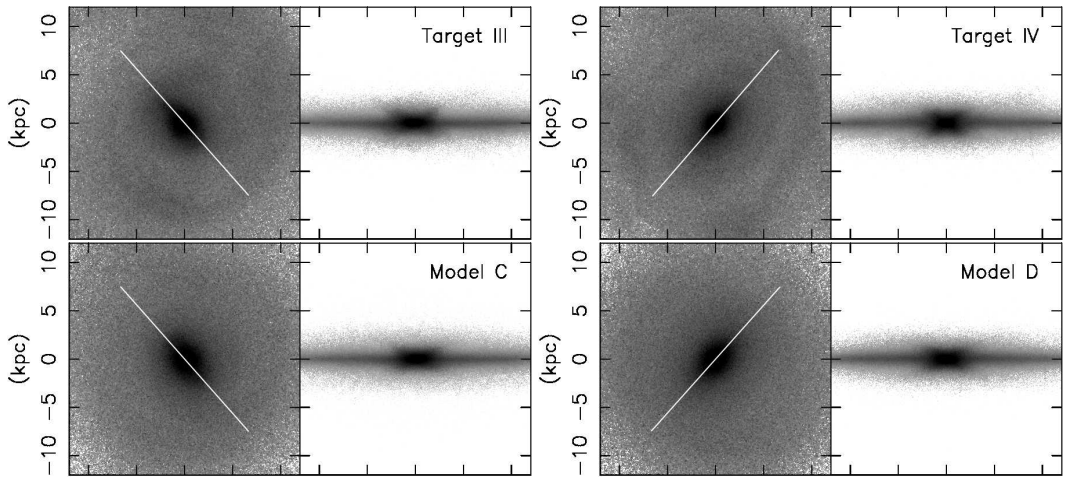

Fig. 3.3: Same as Fig. 3.2, but for Target III (upper left), Model C (lower left), Target IV (upper right) and Model D (lower right).

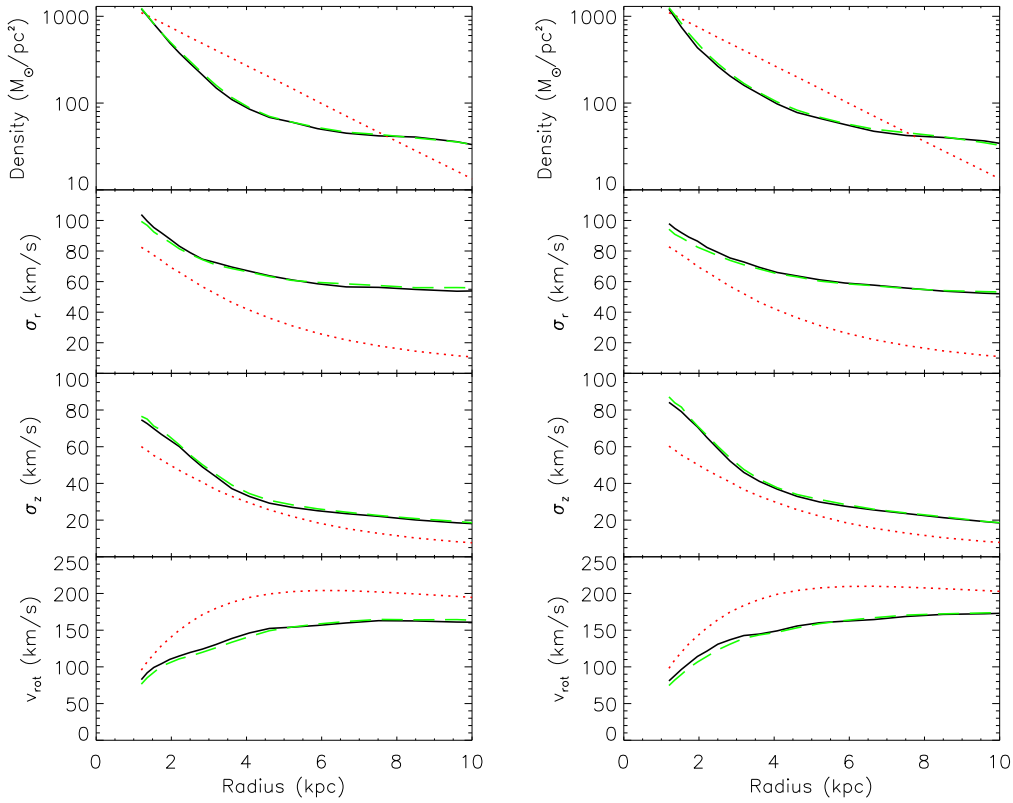

Fig. 3.4: Same as Fig. 3.1, but for Model C with Target III (left), and Model D with Target IV (right).

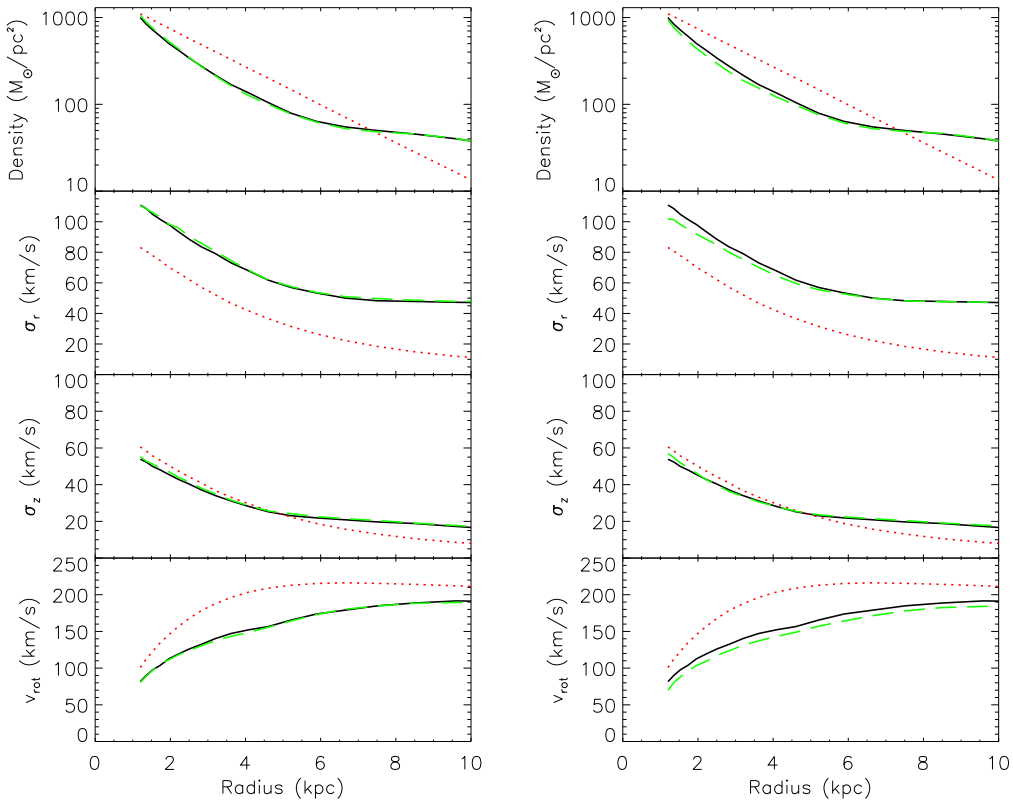

Fig. 3.5: Same as Fig. 3.1 but for Model E with Target II (left), performed with a partial data set, and Model F with Target II (right), performed with the assumed angle of the bar offset from 30° compared to the real value.

data within 10 kpc from the galactic centre. However, Model E was performed with a simple selection function restricting the observable volume to a 10 kpc sphere around a point in the plane and at 8 kpc from the galactic centre, i.e. at $(x, y, z) = (8, 0, 0)$ in Fig. 3.2, roughly emulating *Gaia's* observable area, while ignoring effects such as extinction and errors. This is merely the first step towards using PRIMAL with realistic data.

The middle left of Fig. 3.2 shows the face-on and edge-on view of Model E, which has a similar bar to the target (top left panel), with a hint of a spiral arm in the lower left quadrant matching the one visible in the target. The left panel of Fig. 3.5 shows that an excellent agreement of the final model with the target radial profiles is still obtained with the restricted data set. This is an improvement on Chapter 2, where we saw loss of accuracy when the observable field was restricted. We believe that this is helped by both the

likelihood form of velocity observable and the higher resolution with which the simulations have been carried out. The bar pattern speed is recovered very well with $\Omega_{\rm p} = 27.3$ km s^{-1} compared to the target of $\Omega_{\rm t,p} = 27.5$ km s^{-1}. This shows the ability of PRIMAL to produce reasonable results when supplied with a partial data set of the disc particles. However, we are aware that this selection function is crude and the next stage of our work will deal with more realistic selection functions and expected observational errors.

3.3.4 Working with an incorrect bar angle

As mentioned in Section 1.4.1, the bar angle of the Milky Way is still debated. Ultimately, we aim to recover the dynamical state of the Milky Way with PRIMAL from the future stellar survey data, and recovering the bar angle is also one of our targets. In the previous sections, we assumed that the bar angle of the target is known and we align the bar of the model galaxy to that of the target at every timestep to evaluate the observables. If we do not know the bar angle of the target, like with the Milky Way, we could try different bar angles and hope that the models with the lowest χ^2_ρ and/or the maximum likelihood values recover the bar angle of the target, which is the strategy taken by Long et al. (2013). In this section, we examine the effects of running PRIMAL with an incorrect bar angle. Models F and G are performed with the bar angles deliberately set to be incorrect by 30$^{\rm o}$ and 10$^{\rm o}$, respectively. In this section, we again use all data within 10 kpc from the galactic centre.

Model F has been performed while assuming that the bar angle is 30$^{\rm o}$ less than the real angle of the target. The middle right panel of Fig. 3.2 shows a poor reproduction of the target bar morphology in Model F, which is significantly shorter than that of the target (top left panel). We also see no evidence of the spiral structure seen in other cases. The right panel of Fig. 3.5 shows the radial profiles for Model F. There is a discrepancy in the inner 4 kpc of the model compared to the target in both the density profile and the radial velocity dispersion. This is in agreement with the weaker bar shown in the middle right panel of Fig. 3.2. The average rotational velocity is also lower across the disc. This is also reflected in the final pattern speed of $\Omega_{\rm p} = 23.6$ km s^{-1} compared to the target of $\Omega_{\rm t,p} = 27.5$ km s^{-1}. However, in the real

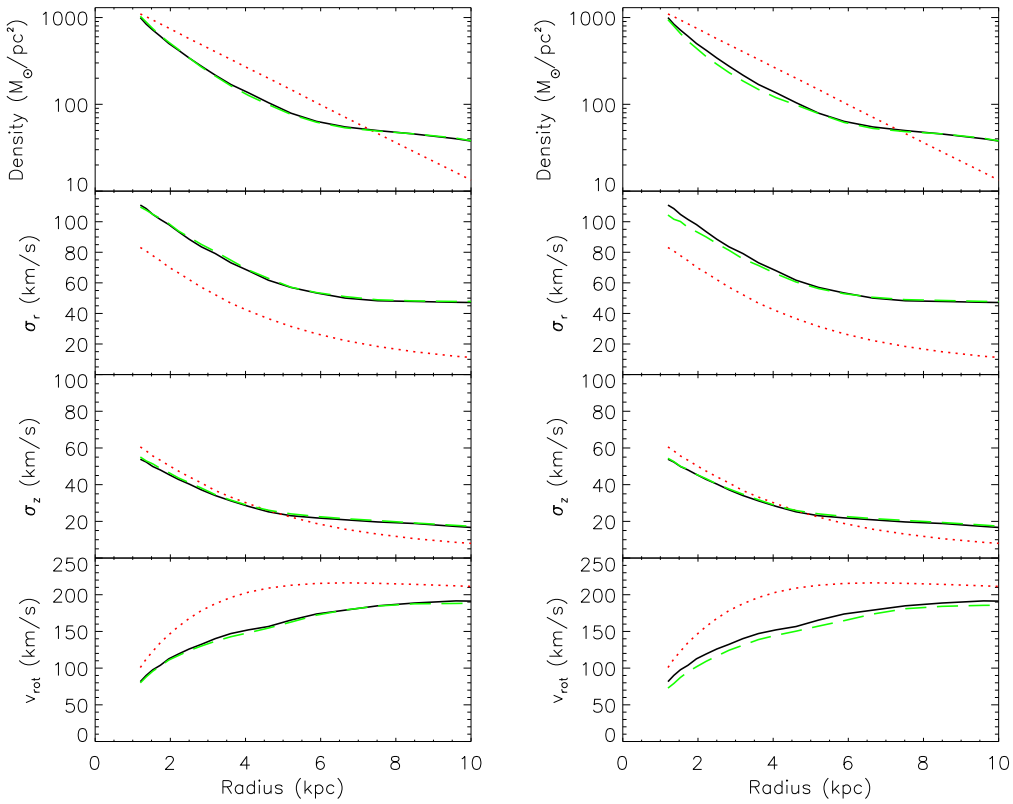

Fig. 3.6: Same as Fig. 3.1 but for Model G with Target II (left), performed with the assumed angle of the bar offset from 10° compared to the real value, and Model H with Target II (right), which is performed without the rotating reference frame.

Milky Way case, we cannot know the correct profiles or the bar pattern speed in advance. On the other hand, we can evaluate the goodness of fit by χ^2_ρ or the values of the likelihood, $\mathcal{L}_v$. In Table 3.2, Model F shows significantly worse values of χ^2_ρ and $\mathcal{L}_v$ than those of Model B which assumes the correct bar angle. Therefore, we should be able to tell easily if the bar angle is off by 30°, at least in this simple target case.

Model G has been performed while assuming that the bar angle is 10° less than the bar angle of the target. The lower left panel of Fig. 3.2 shows a barred disc which is morphologically similar to the target (top left panel). The bar is reproduced well whereas the spiral structure is barely visible. The left panel of Fig. 3.6 shows the radial profiles for Model G, which again reproduces very well those of the target. The bar pattern speed is still well recovered with $\Omega_{\rm p} = 28.0$ km s^{-1} compared to the target of $\Omega_{\rm t,p} = 27.5$ km s^{-1}. In Table 3.2, Model

G shows similar values of χ^2_ρ and $\mathcal{L}_v$ to those of Model B, although the velocity likelihood values are slightly worse. These results may indicate that PRIMAL does not have the power to determine the bar angle within 10^o accuracy, but can recover it with better than 30^o accuracy. However, our ultimate target is much more complicated than this ideal target, and at this stage we do not explore further the expected accuracy of recovering the correct bar angle for this ideal target. At least we demonstrate that with this type of exercise we can examine how accurately the dynamical model, such as PRIMAL, can recover the bar angle. In future work, we will construct more realistic mock observational data from N-body barred simulated discs and 'train' PRIMAL to recover the bar angle as accurately as possible, and finally evaluate the expected accuracy of our recovered bar angle using the comparison demonstrated in this section.

3.3.5 The importance of the rotating reference frame

In this section, we show a brief comparison between the resulting models with and without the rotating reference frame. Model H was performed under identical conditions to Model B, but without the reference frame corrections detailed in Section 3.2.2. The lower right panel of Fig. 3.2 shows that the resulting disc contains a less prominent bar, and no evidence of spiral structure in a similar fashion to Model F. The right panel of Fig. 3.6 shows the radial profiles of Model H. In the inner 4 kpc region, the radial density and radial velocity profiles are lower for the model than for the target. The average rotation velocity is lower than that of the target across the whole disc. The pattern speed is also too low with $\Omega_{\rm p} = 24.3$ km s^{-1} compared to the target of $\Omega_{\rm t,p} = 27.5$ km s^{-1}. Fig. 3.7 shows a comparison of the evolution of the χ^2_ρ of the density between Model B and Model H. The χ^2_ρ in Model H experiences periodic oscillations in time with the bar rotation which are not seen in Model B. This lack of a smooth model convergence along with the poor accuracy on the recovered radial profiles shows the importance of having a rotating reference frame.

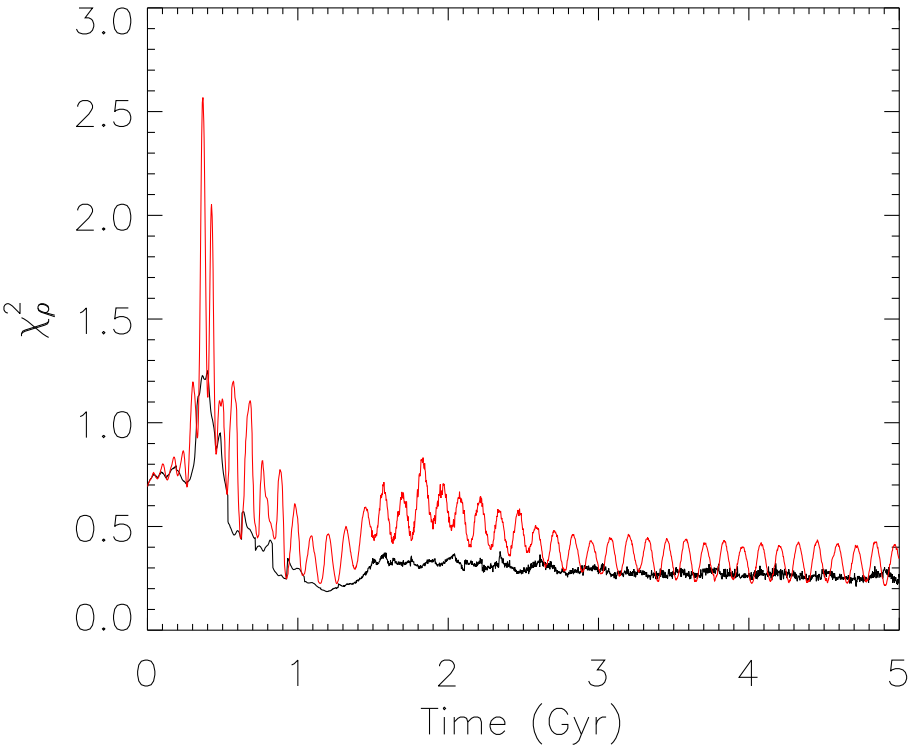

Fig. 3.7: Time evolution of χ^2_ρ for Model B (black line) compared to Model H (red line).

3.4 Chapter summary

In this chapter, we have demonstrated that our updated particle-by-particle M2M algorithm, PRIMAL, can recover a target disc system with a bar, including boxy/peanut features, in a known dark matter halo potential. In PRIMAL, the observables are compared with the model at the position of the target particles. The mass of the model particles are adjusted to reproduce the target observables, and the gravitational potential is calculated self-consistently from the model particle mass distribution. We have introduced the likelihood-based velocity constraints to PRIMAL, which allows us to compare the velocity of the target particle more directly than the smoothed velocity field used in our previous algorithm. To apply this method to a barred disc, we evaluate at every timestep the density and velocity likelihood after the reference frame of the model disc has been corrected. Hence, the bar of the model is always aligned with the bar of the target. Our fiducial model recovers the radial profiles of

the surface density, the radial and vertical velocity dispersion and the mean rotation velocity of the target system very well. In addition, because of our self-gravity implementation of M2M, we can reproduce the bar morphology and pattern speed. We have demonstrated that PRIMAL performs well even when the observables are restricted to within a sphere of radius 10 kpc around a point in the disc plane and at 8 kpc from the centre.

While promising, these applications are still simplified cases. Our ultimate goal is to further improve PRIMAL to be applicable to the future stellar survey data, including the *Gaia* data. While *Gaia* will return an unprecedentedly large amount of data, for approximately one billion stars, the accuracy of this data will be highly variable due to distance, extinction, location in the sky, and etc. In Chapter 4, we further improve PRIMAL to take extinction and *Gaia*-like observational errors into account.

Chapter 4

M2M modelling of the Galactic disc via PRIMAL: Fitting to *Gaia* error added data

This chapter is based on Hunt & Kawata (2014b)

We have adapted our M2M algorithm, PRIMAL, to use mock Milky Way like data constructed from an N-body barred galaxy with a boxy bulge in a known dark matter potential. We use M0 giant stars as tracers, with the expected error of ESA's space astrometry mission *Gaia*. We demonstrate the process of constructing mock *Gaia* data from an N-body model, including the conversion of a Galactocentric Cartesian coordinate N-body model into equatorial coordinates, and how to add error to it for a single stellar type. We then describe the modifications made to PRIMAL to work with observational error. This chapter demonstrates that PRIMAL can recover the radial profiles of the surface density, radial velocity dispersion, vertical velocity dispersion and mean rotational velocity of the target disc, along with the pattern speed of the bar, to a reasonable degree of accuracy despite the lack of accurate target data. We also construct mock data which take into account dust extinction and show that PRIMAL recovers the structure and kinematics of the disc reasonably well. In other words, the expected accuracy of the *Gaia* data is good enough for PRIMAL to recover these global properties of the disc, at least in a simplified

condition, as used in this chapter.

4.1 Introduction

In Chapters 2 and 3, we have described the development of an M2M algorithm called PRIMAL. In Chapter 2, we applied PRIMAL to the target system of a smooth axisymmetric disc created by N-body simulations and demonstrated that PRIMAL can reproduce the density and velocity profiles of the target system well, even when starting from a disc whose scale length is different from the target system. In Chapter 3, we applied an updated methodology to disc galaxies with bar structure, and demonstrated that PRIMAL can reproduce the density and velocity profiles of these more complex targets, as well as providing a good estimate of the pattern speed of the bar.

In this chapter, we first apply PRIMAL to the mock observational data of a single population of stars, M0III, which are constructed from a N-body simulated target galaxy. First, we ignore the dust extinction for simplicity and achieve a good recovery of the properties of the target system even with the *Gaia* expected errors. Then, we apply the dust extinction to the same mock target data and attain a reasonable recovery. Finally, we apply extinction to mock data using red clump stars as tracers and compare the results for these different tracers.

This chapter is organised as follows. Section 4.3 describes how we turn a target N-body galaxy model into mock observational data with *Gaia*-like errors. Section 4.4 describes the M2M methodology of PRIMAL, with a more detailed explanation shown in Chapters 2 and 3. Section 4.5 shows the performance of our updated method for recreating the target disc system from the mock *Gaia* data ignoring dust extinction to highlight the effects of the observational error. Section 4.6 describes the results for the mock data taking the dust extinction into account. In Section 4.7, we provide a summary of this work.

4.2 Target setup

We use for demonstration a single target galaxy created with an N-body simulation. We selected our Target IV from Chapter 3 as it shows boxy/peanut

structure in the central bulge, which is thought to exist in the Milky Way (e.g. Wegg & Gerhard 2013, see Section 1.4.1). It is set up using the method described in Grand et al. (2012a), with the equations presented in Chapter 2.

The initial conditions for the target galaxy for this chapter are constructed using the parameters, $M_{200} = 1.75 \times 10^{12} M_{\odot}$, $M_{\rm d} = 5.0 \times 10^{10} M_{\odot}$, $c = 9.0$, $z_{\rm d} = 0.3$ kpc, $\sigma_{\rm r}^2/\sigma_z^2 = 2.0$ and the scale length of the target disc is initially set as $R_{\rm t,d} = 3$ kpc as described in Chapter 3. Our simulated target galaxy consists initially of a pure stellar disc with an exponential profile with no bulge and a static dark matter halo with the profile of Navarro et al. (1997). We run an N-body simulation with this initial condition, with 10^6 particles, for 2 Gyr using a tree N-body code, GCD+ (Kawata & Gibson 2003; Kawata et al. 2013), and adopt the final output as a target, shown in the top panel of Fig. 4.1.

For the model setup, as mentioned above, in this initial stage of development, we assume that the dark matter halo potential is known and there is no other external potential such as the bulge or stellar halo. We use the same number of particles, 10^6, and the same dark matter halo and disc structure parameters for the model and target galaxies, except for the initial disc scale length of $R_{\rm d} = 2$ kpc for the models which is different from $R_{\rm t,d} = 3$ kpc for the targets. We then evolve the model galaxy gravitationally while simultaneously adjusting it with PRIMAL.

4.3 Generating *Gaia* mock data

Our target data are in Galactocentric Cartesian coordinates and hence must be converted into equatorial coordinates before we can add error based upon the *Gaia* science performance estimates.

First, we shift the centre to the solar position, with the orientation of the axes remaining unchanged. Then, we change the orientation of the axes so that the x axis points in the direction of right ascension $\alpha = 0^{\rm o}$ and declination $\delta = 0^{\rm o}$, the y axis points in the direction of $(\alpha, \delta) = (90^{\rm o}, 0^{\rm o})$ and the z axis is aligned with the Earth's North Pole using the transformation matrix, $\mathcal{T}$. We call these equatorial Cartesian coordinates. $\mathcal{T}$ is given by the inverse of

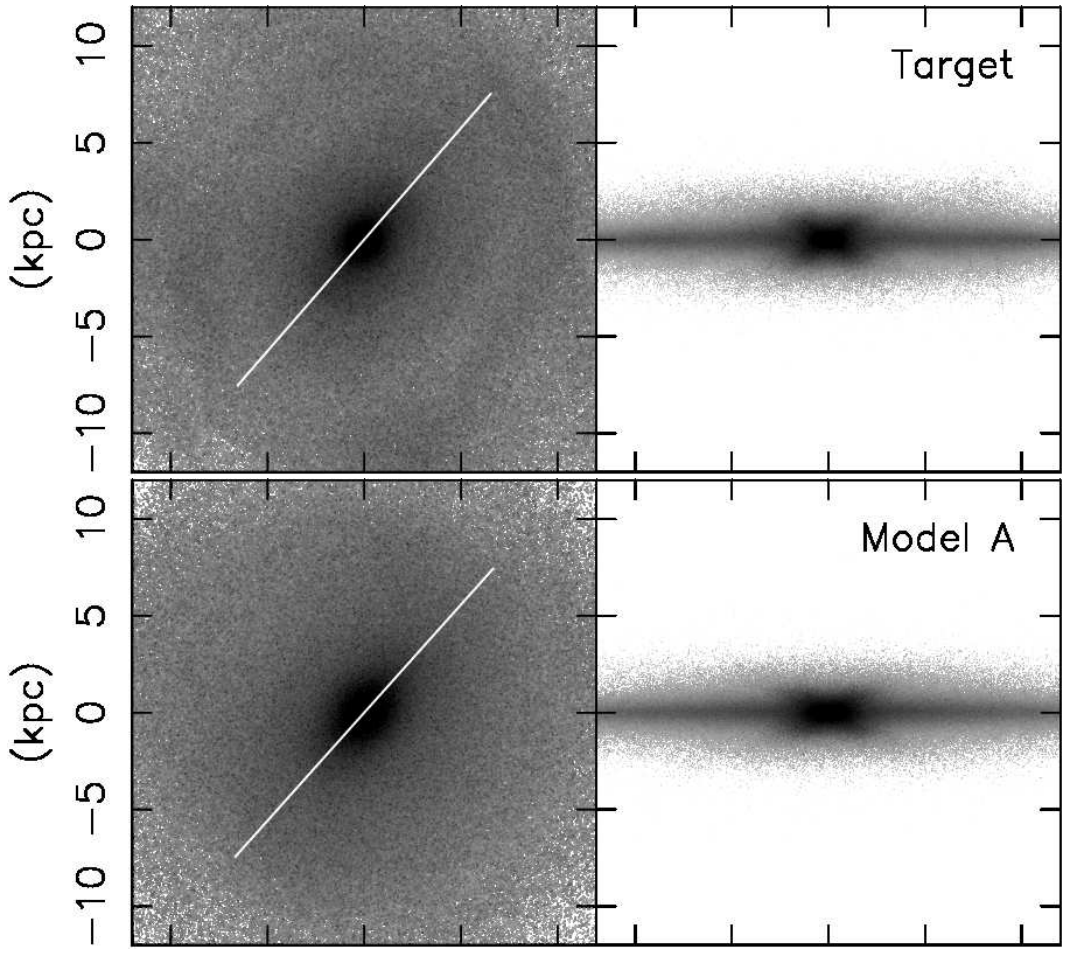

Fig. 4.1: Face-on (left) and edge-on (right) density map of the Target (top) and Model A (bottom), in a 12 kpc by 12 kpc area.

the product of three rotation matrices, $\mathcal{T} = \mathcal{T}_1\mathcal{T}_2\mathcal{T}_3$, as shown in Pasetto et al. (2003).

$\mathcal{T}_1$ provides a rotation around the position angle of the North Celestial Pole with respect to the semi-circle passing through the North Galactic Pole and the zero Galactic longitude,

$$\mathcal{T}_1 = \begin{bmatrix} \cos\theta_0 & \sin\theta_0 & 0 \\ \sin\theta_0 & -\cos\theta_0 & 0 \\ 0 & 0 & 1 \end{bmatrix}. \tag{4.1}$$

$\mathcal{T}_2$ and $\mathcal{T}_3$ provide rotations around the equatorial position angles of the North

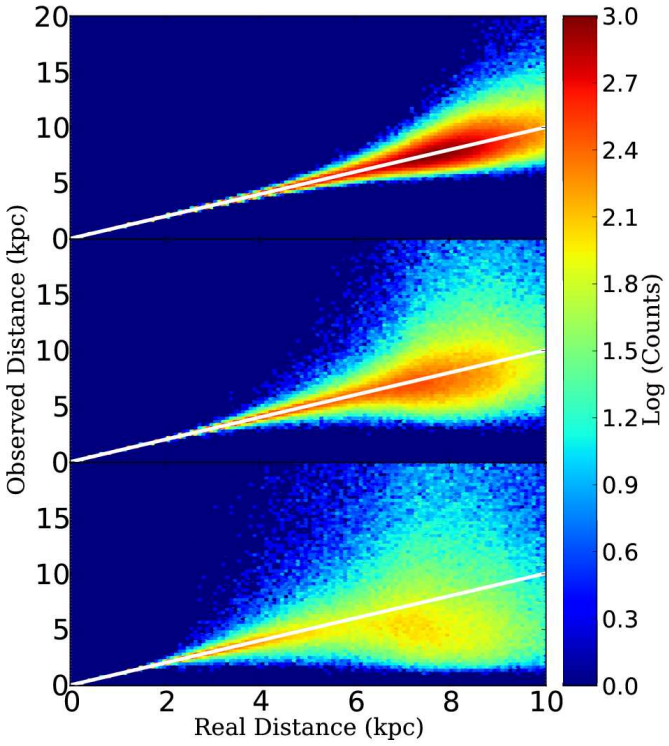

Fig. 4.2: Real distance ($1/\pi$), compared to observed distance ($1/\pi_{\rm obs}$), based on the *Gaia* science performance estimates of the parallax for M0III stars without extinction (upper), M0III stars with extinction (middle) and red clump stars with extinction (lower). The white lines lie along the 1:1 relation to guide the eye.

Galactic Pole

$$\mathcal{T}_2 = \begin{bmatrix} -\sin\delta_{\rm NGP} & 0 & \cos\delta_{\rm NGP} \\ 0 & -1 & 0 \\ \cos\delta_{\rm NGP} & 0 & \sin\delta_{\rm NGP} \end{bmatrix}, \tag{4.2}$$

and

$$\mathcal{T}_3 = \begin{bmatrix} \cos\alpha_{\rm NGP} & \sin\alpha_{\rm NGP} & 0 \\ \sin\alpha_{\rm NGP} & -\cos\alpha_{\rm NGP} & 0 \\ 0 & 0 & 1 \end{bmatrix}. \tag{4.3}$$

We use the values of $\theta_0 = 122.7^{\rm o}$, $\delta_{\rm NGP} = 27^{\rm o}27'$ and $\alpha_{\rm NGP} = 192^{\rm o}49'30''$ for

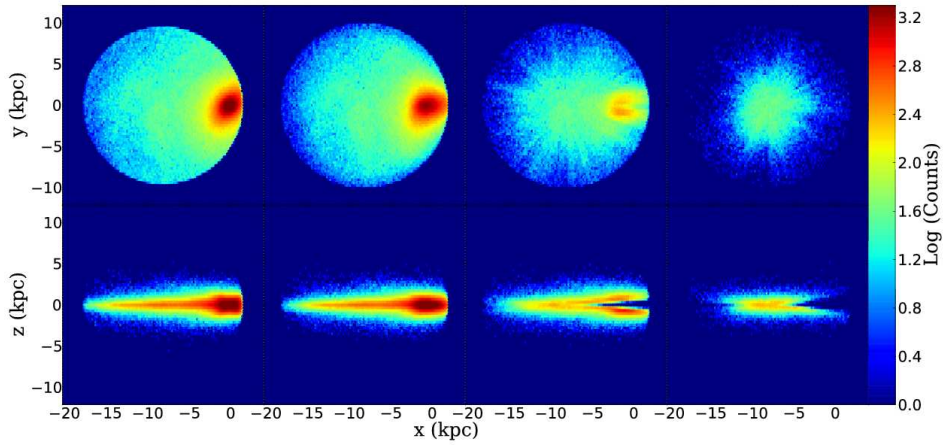

Fig. 4.3: Face-on (upper) and edge-on (lower) logarithmic number counts of observed stars for M0III stars with no error (left) with $V \leq 14.5$ mag, M0III stars with error but no extinction (middle left) with $V \leq 14.5$ mag and $d_{\rm obs} \leq 10$ kpc, M0III stars with extinction (middle right) with $V \leq 16.5$ mag and $d_{\rm obs} \leq 10$ kpc and red clump stars with extinction (right) with $V \leq 16.5$ mag and $d_{\rm obs} \leq 10$ kpc.

these angles, giving us

$$\mathcal{T} = \begin{bmatrix} -0.0549 & -0.8734 & -0.4838 \\ 0.4941 & -0.4448 & 0.7470 \\ -0.8677 & -0.1981 & 0.4560 \end{bmatrix}. \tag{4.4}$$

The coordinate matrix, $\mathcal{A}$, for conversion from equatorial Cartesian coordinates to equatorial coordinates is given by

$$\mathcal{A} = \begin{bmatrix} \cos(\alpha)\cos(\delta) & -\sin(\alpha) & -\cos(\alpha)\sin(\delta) \\ \sin(\alpha)\cos(\delta) & \cos(\alpha) & -\sin(\alpha)\sin(\delta) \\ \sin(\delta) & 0 & \cos(\delta) \end{bmatrix}, \tag{4.5}$$

such that

$$\begin{bmatrix} v_{\rm r} \\ \frac{k\mu_\alpha}{\pi} \\ \frac{k\mu_\delta}{\pi} \end{bmatrix} = \mathcal{A}^{-1}\mathcal{T}^{-1} \begin{bmatrix} U \\ V \\ W \end{bmatrix}, \tag{4.6}$$

where $k = 4.74$ is a unit conversion factor between the velocity of the star with respect to the Sun, (U, V, W), in km s^{-1} and the proper motions of the star (μ_α, μ_δ) in arcsec yr^{-1}.

We treat the N-body particles as a single stellar population, which we will then add error to. We have chosen to use M0 giant (M0III) stars, with assumed $M_V = -0.4$ and $V - I_c = 1.78$, for our tracers as these bright red giant stars will carry the least error in the estimation of their parallax and radial velocity. We assume each N-body particle (with $m_i = 5 \times 10^4 M_\odot$) corresponds to one M0III star. Thus, there exists one M0 giant for every star cluster with mass of $5 \times 10^4 M_\odot$. This is a very simple assumption and does not follow a stellar population model or use a particular IMF. In reality, calculating the stellar mass density from the observed stars will be one of the biggest unknowns, because it is sensitive to their age, metallicity, IMF and evolutionary track. However, in this chapter, we simply assume the conversion from M0III star number density to stellar mass density is known without any error, as a first step towards more realistic data. We will relax this strong assumption in future work.

We also assume that we know the position and motion of the Sun. We locate the observer at $(-8, 0, 0)$ kpc in Fig. 4.1, and the motion of the Sun is assumed to be 228.14 km s^{-1}. Additionally, in this chapter, we generate error added data for any particle with *Gaia* magnitude $G \leq 20$ mag and $G_{\rm RVS} \leq 16.5$ mag. The relations to convert V and $(V - I_c)$ to G and $G_{\rm RVS}$ (Jordi et al. 2010) are

$$\begin{aligned} G = \; & V \quad -0.0257 - 0.0924(V - I_c) \\ & - \quad 0.1623(V - I_c)^2 + 0.0090(V - I_c)^3, \end{aligned} \tag{4.7}$$

and

$$\begin{aligned} G_{\rm RVS} = \; & V \quad -0.0119 - 1.2092(V - I_c) \\ & + \quad 0.0188(V - I_c)^2 + 0.0005(V - I_c)^3. \end{aligned} \tag{4.8}$$

We then add error to our target based upon the *Gaia* performance estimates listed on the *Gaia* website.[1] Note that in this chapter we are using the

[1] http://www.cosmos.esa.int/web/Gaia/science-performance

pre-launch error models. A simple performance model, based upon the *Gaia* Mission Critical Design Review, gives the equation for the end of mission parallax standard error, σ_π, as

$$\begin{aligned}\sigma_\pi &= (9.3 + 658.1z + 4.568z^2)^{1/2} \\ &\quad \times (0.986 + (1 - 0.986)(V - I_c)),\end{aligned} \tag{4.9}$$

where

$$z = \max\left(10^{0.4(12-15)}, 10^{0.4(G-15)}\right), \tag{4.10}$$

and where $6 \leq G \leq 20$ mag.

For $6 \leq G \leq 12$ mag, shorter integration times will be used to avoid saturating the CCDs. The end of mission performance will depend on the exact scheme used to avoid saturation. Thus, for the moment, equation (4.10) allows us to ignore this uncertainty and returns a constant $\sigma_\pi = 7$ μas for stars with $6 \leq G \leq 12$ mag. We assume this same error for $G < 6$ mag. Although *Gaia* will not return data for $G < 6$ mag, information on these very bright stars will be readily available from other surveys. Additionally, the area covered by $G < 6$ mag M0III stars will be covered by intrinsically fainter stars when using multiple populations. With M0III stars, $G = 6$ mag corresponds to the apparent magnitude of stars at $d_{\rm obs} \sim 0.25$ kpc. Therefore, only a small fraction of the mock data will be affected by this simplification.

The position and proper motion errors can be determined from a relationship with σ_π, which varies over the sky, and as such are derived from scanning law simulations. A table[2] on the *Gaia* Science Performance website shows the ecliptic longitude averaged numerical factor with which to multiply with σ_π, to return the appropriate value of σ_{α^*}, σ_δ, σ_π, $\sigma_{\mu_{\alpha^*}}$ or σ_{μ_δ}. This table[2] also takes into account the variation of the number of transits over the sky.

Note that σ_{α^*} denotes the error in true arc, and may be converted to the standard right ascension with

$$\sigma_{\alpha^*} = \sigma_\alpha \cos(\delta), \tag{4.11}$$

and similarly

$$\mu_{\alpha^*} = \mu_\alpha \cos(\delta). \tag{4.12}$$

[2]http://www.cosmos.esa.int/web/Gaia/table-6

We then convert the proper motions to velocities in km s^{-1} in the direction of α and δ with

$$v_\alpha = 4.74(\mu_\alpha/\pi)\cos(\delta) \tag{4.13}$$

and

$$v_\delta = 4.74(\mu_\delta/\pi). \tag{4.14}$$

However, because the error in the proper motions is also dependent on the error in the parallax, the errors must be convolved before they may be used in PRIMAL. We use the approximations

$$\sigma_{v_\alpha} = 4.74\sqrt{\frac{1}{\pi^2}\left(\sigma^2_{\mu_{\alpha^*}} + \frac{\mu^2_{\alpha^*}}{\pi^2}\sigma^2_\pi\right)}. \tag{4.15}$$

and

$$\sigma_{v_\delta} = 4.74\sqrt{\frac{1}{\pi^2}\left(\sigma^2_{\mu_\delta} + \frac{\mu^2_\delta}{\pi^2}\sigma^2_\pi\right)}. \tag{4.16}$$

to convolve the errors and also to convert the errors in μ_{α^*} and μ_δ to errors in v_α and v_δ.

A simple performance model for the end of mission radial velocity error, σ_{v_r}, is given by

$$\sigma_{v_r} = 1 + b\mathrm{e}^{a(V-14)}, \tag{4.17}$$

where a and b are constants dependent on the spectral type of the star. Some examples are given in a table[3] on the *Gaia* science performance website. This performance model is valid for $G_{\mathrm{RVS}} \leq 16.1$ mag, where the fit error is 0.07 mag (Jordi et al. 2010). The a and b values are estimated by linear interpolation as a function of $V - I_c$ using the table. We then apply these errors to the data from our M0III N-body target and displace the measured parallax, proper motion and radial velocity from the true values using random sampling.

Now that our data contain error, we need to strike a balance between the quantity of data available and the quality of the data, as stars with very large parallax errors provide incorrect information in the observables of our model. As such, we do not use all the available particles as points around which to calculate the observables, but merely those whose magnitude is within a predetermined limit.

[3] http://www.cosmos.esa.int/web/Gaia/table-5

Fig. 4.2 shows the real distance from the observer compared to the observed distance for particles within 10 kpc for M0III stars (top). We first discuss a simplified case where the dust extinction effects are ignored. The effects of the dust extinction will be discussed in Section 4.6. The observed distance, $d_{\rm obs}$, in Fig. 4.2 is the error added distance from the observer. $d_{\rm obs}$ is calculated from the randomly displaced parallax measurement, $\pi_{\rm obs}$, following the expected parallax errors. The top panel of Fig. 4.2 shows that the accuracy of the distance measurement is excellent within 4 kpc, but starts to diverge quickly at higher distances. It also shows that while the difference between the observed and correct positions for the majority of stars remain within $\sim$ 2 kpc even up to $d = 10$ kpc, a significant fraction have errors of more than 50%. For this chapter, we have set the limit for the selection of the data to be $d_{\rm obs} < 10$ kpc. We also add the selection limit of $V \leq 14.5$ mag for obtaining accurate radial velocities. Note that this estimate of distance error uses only parallax distance estimates, whereas from the real *Gaia* data it is also possible to measure photometric distances which may help to reduce the error.

Fig. 4.3 shows the face-on (upper panels) and edge-on (lower panels) distribution of generated M0III stars which meet our selection criteria ($V \leq 14.5$ mag and $d_{\rm obs} \leq 10$ kpc). The left-hand panels show the true distribution of the selected stars and the second column shows the distribution of the stars after the error has been added, i.e. the position of the stars after the random displacements in parallax. Fig. 4.3 shows the target data reach the centre of the galaxy. However, the observed shape of the bar differs between the true distribution and the error added data. With the addition of error, the boxy structure of the bar is much weaker and the angle of the bar becomes less apparent.

4.4 The M2M algorithm: PRIMAL

We have presented a full description of both the original M2M and our particle-by-particle M2M in Chapters 2 and 3. In this section, we describe the modifications made to PRIMAL from the previous chapters.

In a change from Chapters 2 and 3, we have converted the algorithm to take target data in equatorial coordinates, e.g. right ascension, α, declination, δ, parallax, π, radial velocity from the position of the Sun, $v_{\rm r}$, and proper motions, v_α and v_δ. We make this change as this is the form in which *Gaia* will return its data. We maintain six dimensional phase space information, and as such no accuracy should be lost at this stage.

We again convert our Galactocentric Cartesian model data into equatorial coordinates to compare the radial velocity and proper motion observables constructed from the *Gaia* data via the process shown in Section 4.3. We then calculate the velocity likelihood observables in equatorial coordinates, using the equations derived in Chapter 3, e.g. for v_α, the likelihood is given by

$$\hat{\mathcal{L}}_{v_{\alpha,j}} = \frac{1}{\sqrt{2\pi}} \sum_i W_{ij} m_i \mathrm{e}^{-(v_{\alpha,j}-v_{\alpha,i})^2/2\sigma^2_{v_{\alpha,j}}}, \tag{4.18}$$

for model particle i and target particle j.

We also convert the target particle positions into Cartesian coordinates to allow the same form of density observable as Chapters 2 and 3, using the equation

$$\begin{bmatrix} x \\ y \\ z \end{bmatrix} = \mathcal{T} \begin{bmatrix} \cos(\alpha)\cos(\delta)/\pi \\ \sin(\alpha)\cos(\delta)/\pi \\ \sin(\delta)/\pi \end{bmatrix}, \tag{4.19}$$

using the observed parallax, $\pi_{\rm obs}$, as discussed in Section 4.3. We then use the same density observable as Chapters 2 and 3 for both the target and the model.

Note that the positions of the target stars are displaced due to the parallax errors, and the target density observables, $\rho_{{\rm t},j}$, do not correctly represent the density of the target system. Our target stars are selected with $V \leq 14.5$ mag, and the observed distance $d_{\rm obs} \leq 10$ kpc, as mentioned in Section 4.3. However, we do include particles with $V > 14.5$ mag and $d_{\rm obs} > 10$ kpc in the calculation of the density observables themselves. This helps to compensate for the underestimation of the density of the target stars just inside of the magnitude cut, for which there are significant number of stars fainter than the magnitude cut, but within the smoothing length. However, this also counts

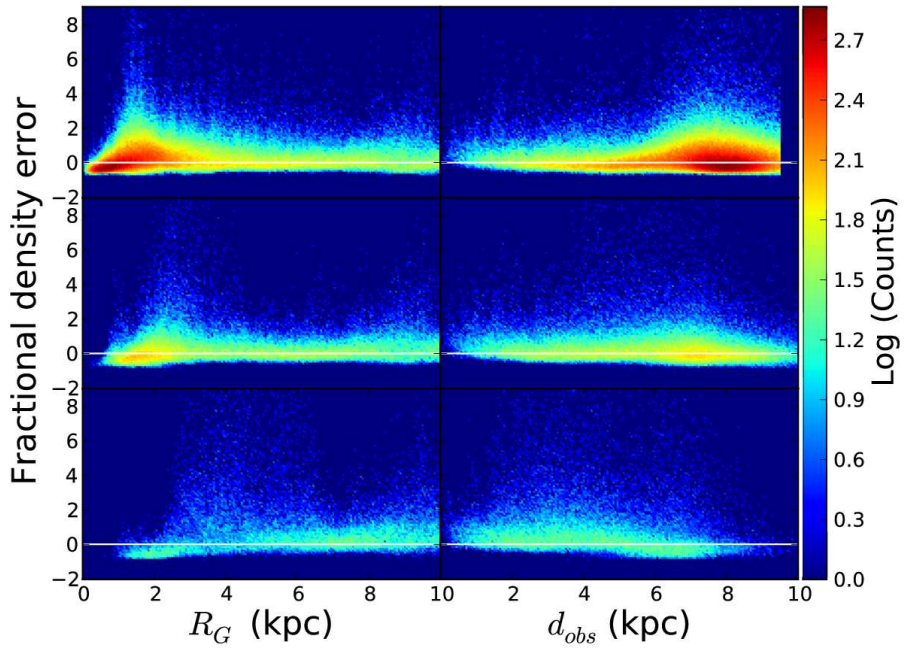

Fig. 4.4: Fractional density error $(\rho_{\rm obs} - \rho_{\rm true})/\rho_{\rm true}$ as a function of observed Galactocentric radius, $R_{\rm G}$ (left) and observed distance from the Sun, $d_{\rm obs}$ (right), for M0III stars without extinction (upper), M0III stars with dust extinction (middle) and red clump stars with dust extinction (lower), coloured by logarithmic number density of the stars. The white line lies along zero to guide the eye.

fainter stars whose observed distance is much smaller than the real distance owing to the error, which can result in overestimation of the local density.

Fig. 4.4 shows the fractional density error of the mock data against Galactocentric radius for M0III stars (upper left). The upper-left panel of Fig. 4.4 shows density tends to be overestimated when using this simplistic calculation of the density. Most notably the panel shows a substantial overestimation between 1 and 2 kpc from the Galactic centre. This overestimation can be understood from the face-on view of the distribution of stars shown in the upper panels of Fig. 4.3. In the data with the true particle positions (left), the bar is clearly shown. On the other hand, in the error added data (2nd column) the bar shown is more diffuse, and the apparent angle of the bar looks different. Therefore, for example, while (x,y)=$(-2, 0)$ is the edge of the bar in the true distribution, because of the large errors in parallax, the observed distance of

many stars in the bar are randomly displaced from the true bar location, which makes the bar appear more diffuse. As a result, the density at $(x, y) = (-2, 0)$ increases, which leads to the overestimation seen at $R_{\rm G} \sim 2$ kpc in Fig. 4.4. Fig. 4.4 also shows an underestimation in the inner 0.5 kpc region. This is also understandable from Fig. 4.3, for the same reason, because the observed central concentration is more diffuse due to the large parallax error at the centre, the very centre of the galaxy appears less dense. In this chapter, we simply take the measured density. However, because of our particle-by-particle M2M algorithm, we have many target stars, and demonstrate that PRIMAL works reasonably well even with this simple density measurement.

Fig. 4.4 shows the fractional density error of the mock data against observed distance for M0III stars without extinction (upper right). There is a general trend of overestimation matching that which is seen in the upper-left panel. The cut-off of the data at $d_{\rm obs} \sim 9.55$ kpc is due to the magnitude limit of $V \leq 14.5$ mag for the data selection.

Having converted the observables into their appropriate coordinates, we then compare these observables with the same method as Chapter 3, resulting in the change of mass equation

$$\begin{aligned}
\frac{\mathrm{d}}{\mathrm{d}t}m_i(t) &= -\epsilon m_i(t)\Bigg\{ M\sum_j \frac{W(r_{ij},h_j)}{\rho_{\mathrm{t},j}}\tilde{\Delta}_{\rho_j}(t) \\
&- \zeta M\Bigg[\sum_j W_{ij}\left(\frac{1}{\sqrt{2\pi}}\frac{\mathrm{e}^{-(v_{\mathrm{r},j}-v_{\mathrm{r},i})^2/2\sigma^2_{v_{\mathrm{r}},j}}}{\hat{\mathcal{L}}_{v_{\mathrm{r}},j}}-\frac{1}{\rho_j(t)}\right) \\
&+ \sum_j W_{ij}\left(\frac{1}{\sqrt{2\pi}}\frac{\mathrm{e}^{-(v_{\alpha,j}-v_{\alpha,i})^2/2\sigma^2_{v_{\alpha},j}}}{\hat{\mathcal{L}}_{v_{\alpha},j}}-\frac{1}{\rho_j(t)}\right) \\
&+ \sum_j W_{ij}\left(\frac{1}{\sqrt{2\pi}}\frac{\mathrm{e}^{-(v_{\delta,j}-v_{\delta,i})^2/2\sigma^2_{v_{\delta},j}}}{\hat{\mathcal{L}}_{v_{\delta},j}}-\frac{1}{\rho_j(t)}\right)\Bigg] \\
&+ \mu\left(\ln\left(\frac{m_i(t)}{\hat{m}_i}\right)+1\right)\Bigg\}, \qquad (4.20)
\end{aligned}$$

where $\hat{m}_i$ is the prior and M is an arbitrary constant mass, which we set as $M = 10^{12} M_\odot$. We set the prior $\hat{m}_i = M_{\rm tot,ini}/N$, where $M_{\rm tot,ini}$ is the initial total mass of the model system, and N is the number of particles in the model.

As with Chapters 2 and 3, we write $\epsilon = \epsilon'\epsilon''$, where

$$\epsilon'' = \frac{10}{\max_i \left(M \sum_j \frac{W(r_{ij},h_j)}{\rho_{\mathrm{t},j}} \tilde{\Delta}_{\rho_j}(t) \right)}. \tag{4.21}$$

Following de Lorenzi et al. (2008), we use temporally smoothed versions of Δ_{ρ_j}, $\hat{\mathcal{L}}$ and ρ_j. As opposed to the fixed values of the velocity error, $\sigma_{x,j}$, which were used in Chapter 3, we now use values based on *Gaia*'s performance estimates as discussed in Section 4.3. In other words, we take into account the difference in errors among different velocity components for different target stars.

We have again performed a parameter search for the optional parameters as demonstrated in Chapter 2. These parameters are ϵ', which controls the balance between speed and smoothness, μ, which controls the level of regularisation, α, which controls the degree of temporal smoothing and ζ, which controls the magnitude of the velocity observables contribution to the force of change. We have determined these values as $\epsilon' = 0.1$, $\alpha = 2.0$, $\zeta = 1$ and $\mu = 10^5$, these are in agreement with Chapter 3.

We calculate the angle of the bar in the model at each step. Then, we rotate the model to match the bar angle of the target, assuming the bar angle is known, for the purposes of calculating the observables in the same reference frame. Chapter 3 demonstrates that this method will allow the pattern speed to be recovered along with the density and velocity profiles. When applying this to the Milky Way we will not know the exact bar angle. However, here we assume that the bar angle is known for simplicity.

4.5 Results

In this section, we present the results from our models using PRIMAL. We will first show the results for the unconstrained model explained below, and then for a model where we apply PRIMAL to ideal data, i.e. the position and velocities are measured with no error. Then, we show our fiducial model where PRIMAL is applied to the error added data ignoring dust extinction. Then, we demonstrate the importance of using all three dimensions of the velocity constraints, and the importance of calculating density using stars

Table 4.1: M2M model results at the final timestep. Ω_p is the model pattern speed, with a target of 28.9 km s^{-1}kpc^{-1}, χ^2_ρ is a measure of accuracy of the density, $-\mathcal{L}_{\mathrm{r},v_\alpha,v_\delta}$ are the likelihood values for the radial velocity and proper motions.

Model	Ω_p (km s^{-1}kpc^{-1})	χ^2_ρ	$-\mathcal{L}_{v_\mathrm{r}}/10^6$	$-\mathcal{L}_{v_\alpha}/10^6$	$-\mathcal{L}_{v_\delta}/10^6$
i	34.3	0.370	7.831	8.2112	8.2012
A	28.5	0.100	5.832	5.8898	5.8288
B	28.6	0.137	7.067	2.6357	2.6315
C	26.1	0.126	6.836	2.6365	2.6322
D	25.0	0.130	6.926	2.6363	2.6322
E	33.8	0.130	6.939	2.6356	2.6314
F	22.5	0.196	6.885	2.6364	2.6332
G	25.9	0.196	8.815	2.6362	2.6327
G_i	23.9	0.274	8.898	2.6373	2.6360
H	25.6	0.167	7.548	2.6375	2.6332
H_i	44.4	3.624	10.99	4.0241	4.0203
I	27.7	0.249	1.666	0.8222	0.8211
J	27.3	1.593	0.442	0.2399	0.2396

with $V > 14.5$ mag. We then show models with different initial conditions. Table 4.1 shows a summary of the models including the bar pattern speeds, the likelihood values $\mathcal{L}_{v_\mathrm{r}}$, $\mathcal{L}_{v_\alpha}$ and $\mathcal{L}_{v_\delta}$, where

$$\mathcal{L} = \sum_j \ln\left(\frac{\hat{\mathcal{L}}_j}{\rho_j}\right), \tag{4.22}$$

and the χ^2_ρ for the density, as given in Equation (2.28). Note that we include only target particles with $V \leq 14.5$ mag and $d_\mathrm{obs} \leq 10$ kpc, and N_r is the number of particles satisfying this criteria. Note that although we seek to maximise likelihood, the values in Table 4.1 are $-\mathcal{L}$, and hence smaller values mean higher likelihood. Note that as discussed in Section 4.4, we do not take into account the error in density. Especially for distant target stars, the density tends to be overestimated, because of the larger errors in the distance. Therefore, χ^2_ρ is unlikely to be a fair measurement of the goodness of fit.

4.5.1 Unconstrained model

Firstly we show Model i, where all the constraints from M2M modelling have been turned off and the system is merely allowed to evolve within its own self-gravity and the fixed potential of the dark matter halo. Model i is for reference and comparison with the other models with M2M modelling, as the known dark matter halo and the similar initial condition of the model to the target initial condition will contribute partially to the similar mass distribution and kinematics of the final model system to those of the target system.

Fig. 4.5 shows the radial profiles of the surface density, Σ, the radial, σ_r, and vertical, σ_z, velocity dispersion and the mean rotational velocity, v_rot, for the target (black solid) and Model i (green dash) compared to the initial model (blue dot). The unconstrained model does not well reproduce the target in most areas. The Σ profile shows an overestimation of the density within 9 kpc. This is unsurprising due to the lower scale length of the initial model disc. The σ_r and σ_z profiles match poorly within 5 kpc of the centre. However, they are reproduced nicely in the outer regions, without the help of PRIMAL. The v_rot profile is overestimated across the entire disc because of the higher surface density in the inner region. The left panel of Fig. 4.6 shows the fractional difference between the target and Model i (green dash) in the radial profiles for

comparison with the other models. The fractional surface density difference is given by

$$\Delta\Sigma = (\Sigma - \Sigma_{\rm t})/\Sigma_{\rm t}, \tag{4.23}$$

where $\Sigma_{\rm t}$ is the true surface density of the target, and a similar equation is used for evaluating the fractional velocity differences in the left panel of Fig 4.6.

The top middle panel of Fig. 4.7 shows the fractional surface density difference between the target (top left panel) and Model i in a face-on view. The fractional difference in the surface density map of the model and the target are calculated using the cloud in cell method on a 240 by 240 grid. Fig. 4.7 shows a substantial overdensity in the model within $R_{\rm G} \sim 6$ kpc. This is to be expected because, without constraints from PRIMAL, the model disc remains more centrally concentrated than the target due to the initial smaller scale length of 2 kpc.

We have measured the pattern speed of the bar of the target galaxy by measuring the difference in the bar angle at different epochs. The bar pattern speed measured is $\Omega_{\rm t,p} = 28.9$ km s^{-1}kpc^{-1} for the target galaxy. The pattern speed of the bar for Model i is overestimated significantly with $\Omega_{\rm p} = 34.3$ km s^{-1}kpc^{-1} for Model i.

4.5.2 Ideal data

In this section, we show Model A which contains no error in the target data for reference. This is similar to Model D from Chapter 3, which uses the same target galaxy and initial conditions for the model. In this chapter, we use a more realistic selection of the target data, i.e. $V \leq 14.5$ mag (corresponding to $d_{\rm obs} \sim 9.55$ kpc for M0III stars), compared with $R_{\rm G} \leq 10$ kpc used in Chapter 3, and utilise observables in equatorial coordinates as discussed in Section 4.3. A more detailed study of PRIMAL when applied to data with no error is the subject of Chapter 3.

Fig. 4.5 shows the radial profiles of the surface density, Σ, the radial, $\sigma_{\rm r}$, and vertical, σ_z, velocity dispersion and the mean rotational velocity, $v_{\rm rot}$, for

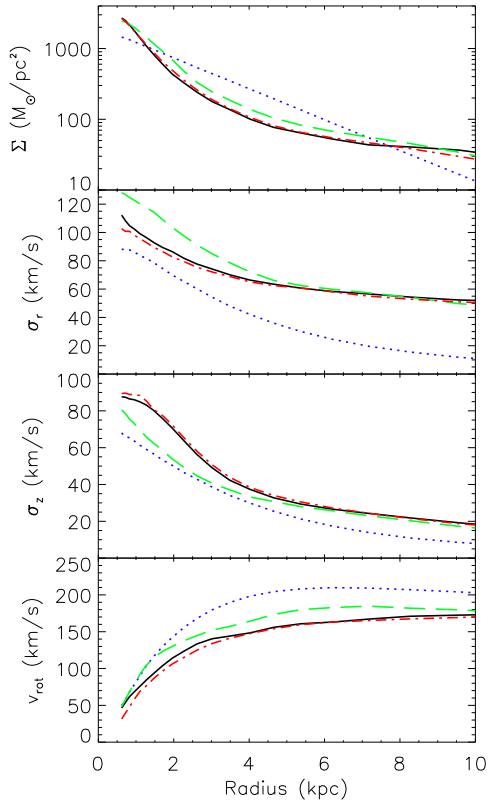

Fig. 4.5: Surface density profile (upper), radial velocity dispersion (upper middle), vertical velocity dispersion (lower middle) and rotation velocity (lower) for the Initial model (blue dot), target (black solid), Model A (red dash-dot) and Model i (green dash).

the target (black solid) and Model A (red dash-dot) compared to the initial model (blue dot). As in Chapters 2 and 3, these radially binned profiles are not directly constrained by PRIMAL, but are reproduced remarkably well, especially if compared with the unconstrained model, Model i. Fig. 4.5 shows a substantial increase in the radial velocity dispersion and a corresponding decrease in the mean rotational velocity from the initial to the final model, leading to an excellent agreement with the target profiles in all areas apart from the inner 3 kpc of $\sigma_{\rm r}$ and $v_{\rm rot}$ which are slightly underestimated, corresponding to the boxy structure. The left panel of Fig. 4.6 shows the fractional difference between the radial profiles of the target and Models i and A. Model A (red dash-dotted) shows less than ten percent error in all areas apart from the outer edge of the density profile and the inner 1 kpc in the rotation velocity profile.

The top right panel of Fig. 4.7 shows an excellent recovery of the face-

on view of the surface density distribution in the middle region of Model A. However, the recovery is still flawed, including a ring of underdensity around $r = 10$ kpc, which is due to the failure to recover the spiral/ring structure, which is seen in the target galaxy in the top left panel (see also Fig. 4.1). However, the pattern speed of the bar is recovered extremely well with $\Omega_{\rm p} = 28.5$ km s^{-1}kpc^{-1} for the final model compared to the target of $\Omega_{\rm t,p} = 28.9$ km s^{-1}kpc^{-1} (see Table 4.1). Additionally, Fig. 4.1 shows the morphology of Model A reproduces well the boxy morphology of the Target's central bulge. The values of χ^2, $\mathcal{L}_{v_{\rm r}}$, $\mathcal{L}_{v_\alpha}$ and $\mathcal{L}_{v_\delta}$ from Model A (shown in Table 4.1) are all better than those for Model i, the unconstrained model. They cannot be directly compared to the results for subsequent models, because the positions of the tracers will have changed and different tracers may have been selected for use by the $d \leq 10$ kpc and $V \leq 14.5$ mag selection criteria.

4.5.3 Fiducial model

In this section, we present Model B, our model which best reproduces the target galaxy described in Section 4.3, when working with the error added observables. The right panel of Fig. 4.6 shows the fractional difference in the radial profiles for Model B (black solid) compared with the target galaxy. The final profiles reproduce the target profiles reasonably well, considering the parallax errors present in the observational data. However, there is a noticeable decrease in accuracy when compared with Model A (red dash-dotted). There is an overestimation of the density between $R_{\rm G} \sim 2$ and 4 kpc, and an underestimation within 1 kpc. There is also an underestimation in the inner regions of the $\sigma_{\rm r}$, σ_z and $v_{\rm rot}$ profiles. This drop in accuracy is to be expected due to the addition of observational error. The inaccuracy in the surface density profile is believed to be due to systematic error in the density estimate of the target galaxy as we see in Fig. 4.4. The error in the density estimate is discussed further in Section 4.5.5.

The left panel of the second row of Fig. 4.7 shows that there is increased overestimation of the density except in the bar region in Model B when compared with Model A (top right). This matches what is seen in the right panel of Fig. 4.6, with the overestimation greatest between $R_{\rm G} \sim 2$ and 4 kpc, and

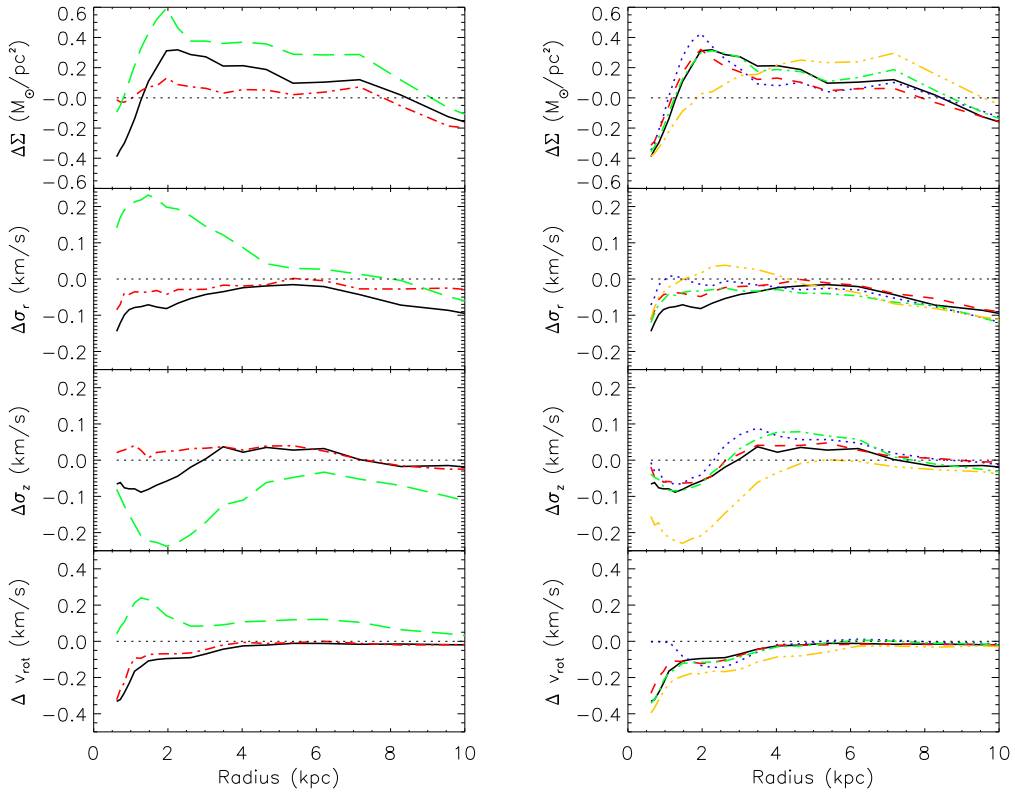

Fig. 4.6: Fractional difference between models and target in the radial profile of the surface density (upper), radial velocity dispersion (upper middle), vertical velocity dispersion (lower middle) and rotation velocity (lower) for Model i (green dash), A (red dash-dot) and B (black solid) (left). Same as left, but for Model B (black solid), Models C (blue dot), D (red short-dash) and E (green dash-dot) which use only the density, or specific velocities as constraints and Model F (yellow triple-dot-dash) which only calculates density from stars with $V < 14.5$ mag.

an underestimation present in the central 1 kpc.

Table 4.1 shows a pattern speed of the bar of $\Omega_{\rm p} = 28.6$ km s^{-1}kpc^{-1} for Model B, compared to $\Omega_{\rm t,p} = 28.9$ km s^{-1}kpc^{-1} for the target. This is a remarkably good recovery considering the less accurate constraints in the inner region of the target galaxy and considering our naive application of PRIMAL to the error added data, and is encouraging for further development.

4.5.4 Limited velocity constraints

In this section, we show the importance of using velocity constraints, as opposed to merely density constraints. We also show the importance of using

three dimensional velocity constraints, as using either $v_{\rm r}$ or $v_{\alpha,\delta}$ alone results in an inferior model.

The right panel of Fig. 4.6 shows the fractional difference in the radial profiles for Model C (blue dot), performed using only the density observables as constraints. Because the density is directly linked to the positions of the target stars, the error in the density observables can become quite high as you get further from the Sun, as shown in the top right panel of Fig. 4.4. The top left panel of Fig. 4.4 shows that the density in the inner region of the target galaxy is overestimated. As a result, the recovery of the density around 2 kpc is worse than the fiducial model, Model B (black solid). The right panel of Fig. 4.6 also shows the σ_z profile is a better match to the target in the inner 2 kpc but worse around 4 kpc when compared to the fiducial model. The $v_{\rm rot}$ profile is better reproduced at 0.5 kpc, but is worse around 2.5 kpc. This is unsurprising as there are no constraints upon the velocity. Interestingly, we find an improvement in the $\sigma_{\rm r}$ profile in the central part of the galaxy. However, we believe that this is a coincidence and higher $\sigma_{\rm r}$ is driven by overestimated density constraints.

The area of overestimated density can be clearly seen in Fig. 4.7, which shows the fractional surface density difference map. The middle panel in the 2nd row of Fig. 4.7 shows two patches of substantial overestimation either side of the bar in Model C. This is because Model C contains a substantial bulge but a weak bar. The pattern speed of the bar recovered is worse than in Model B with $\Omega_{\rm p} = 26.1$ km s^{-1}kpc^{-1} for Model C, compared to the target of $\Omega_{\rm t,p} = 28.9$ km s^{-1}kpc^{-1}.

The right panel of Fig. 4.6 shows the fractional difference in the radial profiles for Model D (red dash), performed using density and radial velocity observables as constraints. When comparing Model D with Model C (blue dot), we see an improvement in the Σ profile and the velocity profiles, apart from the inner 2 kpc of the $\sigma_{\rm r}$ and $v_{\rm rot}$ profiles. Fig. 4.7 shows the fractional surface density difference map for Model D (2nd row right), which when compared with Model C (2nd row middle) shows very little difference. However, the pattern speed of the bar for Model D has become worse when compared

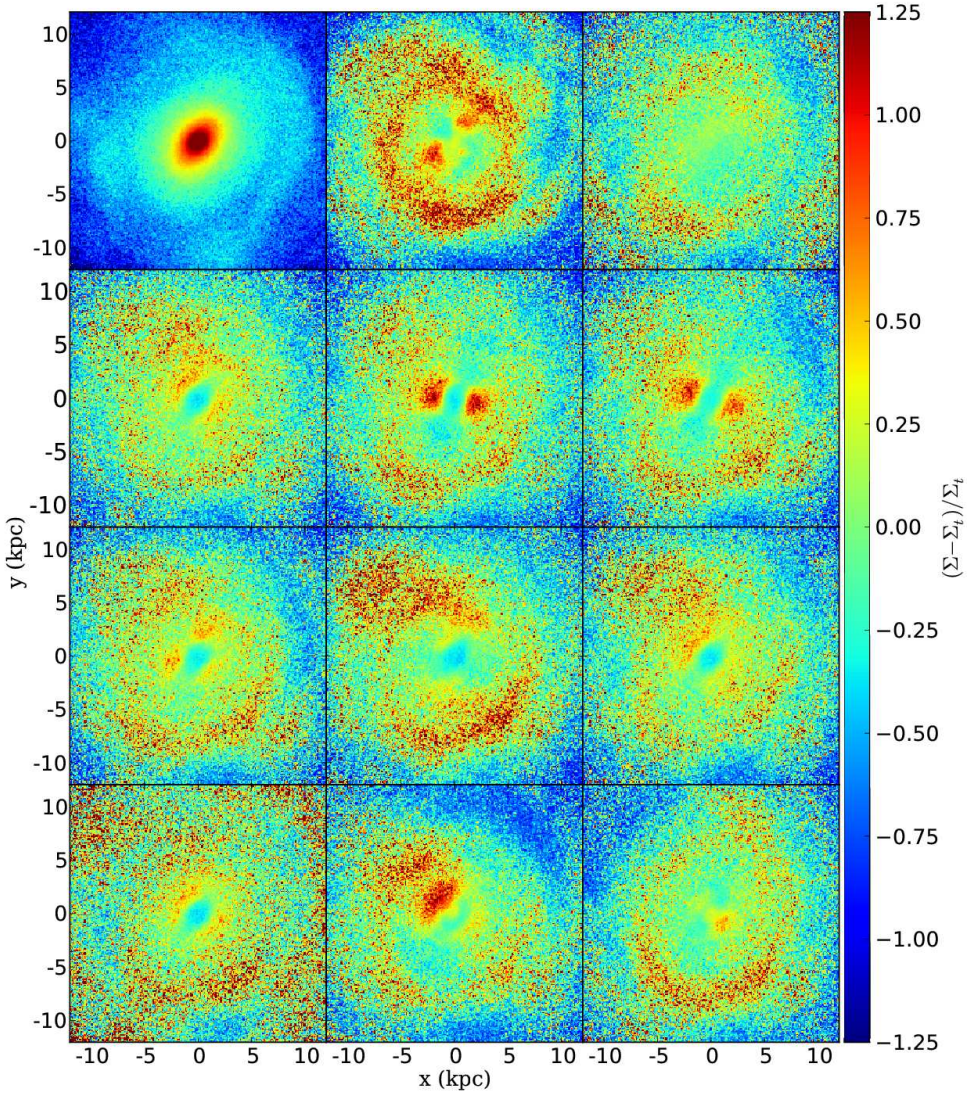

Fig. 4.7: Face-on surface density map of the target (top left) and the face-on fractional projected surface density difference maps ($\Delta\Sigma = (\Sigma - \Sigma_t)/\Sigma_t$,) calculated with a cloud-in-cell method on a 240×240 grid, for Models *i* (top middle), A (top right), B (2nd row left), C (2nd row middle), D (2nd row right), E (3rd row left), F (3rd row middle), G (3rd row right), H (bottom left), I, (bottom middle) and J (bottom right) plotted for comparison. The difference maps use the same scale as given by the colour bar. Red shows an overdensity in the model, and blue is an underdensity in the model. The surface density of the target (top left) uses its own logarithmic colour scale.

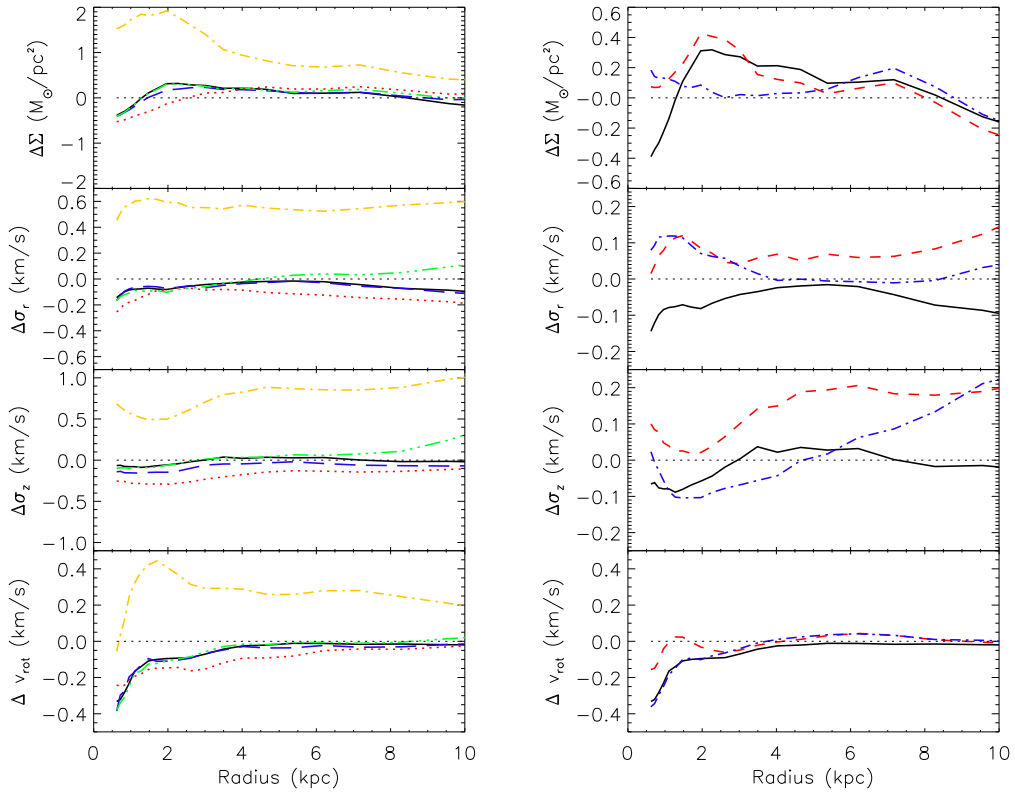

Fig. 4.8: Same as Fig. 4.6, but for Model B (black solid), Model G (blue dash) which has $R_{\rm d,ini} = 4.0$ kpc, G$_i$ (red dot) which is Model G without constraints, Model H (green triple-dot-dash) which has $M_{\rm d,ini} = 10^{11} M_{\odot}$ and H$_i$ (yellow dash-dot) which is Model G without constraints (left). Note the scale for this figure is different to that of both panels of Fig. 4.6 and the right panel of this figure. Same as the left panel, but for Model B (black solid), Model I (red dash) which uses M0III tracers with extinction added and Model J (blue dash-dot) which uses red clump tracers with extinction added.

with Model C, with $\Omega_{\rm p} = 25.0$ km s^{-1}kpc^{-1} for Model D, compared to the target of $\Omega_{\rm t,p} = 28.9$ km s^{-1}kpc^{-1}. Therefore, we think that it is important to include observed proper motions as constraints.

The right panel of Fig. 4.6 also shows the fractional difference in the radial profiles for Model E (green dash-dot), performed using density and proper motion observables as constraints. When comparing Model E and Model B (black solid), we see that using the proper motion constraints only, rather than the full velocity constraints has improved the recovery of the $\sigma_{\rm r}$ profile within 3 kpc. However, it has resulted in a worse recovery of the σ_z profile. The $v_{\rm rot}$ and Σ profiles in general remain similar.

The left panel of the 3rd column of Fig. 4.7 shows the fractional surface density difference map for Model E, which when compared with Model C (2nd row middle) shows a noticeable improvement. The areas of overdensity on either side of the bar have been removed, and the recovery is more similar to Model B (2nd row left). However, the pattern speed of the bar for Model E is worse when compared with Models B or C (see Table 4.1), with $\Omega_{\rm p} = 33.8$ km s^{-1}kpc^{-1} for Model E, compared to the target of $\Omega_{\rm t,p} = 28.9$ km s^{-1}kpc^{-1}.

When we compare Models C, D and E with Model B, we find Model B to be superior, especially when aspiring for an accurate recovery of the pattern speed of the bar, leading us to conclude that the three dimensional velocity information is an important constraint to use when it is available. This agrees with our findings in Chapter 2, where this test was performed on data without errors. Table 4.1 shows the χ^2, $\mathcal{L}_{v_{\rm r}}$, $\mathcal{L}_{v_\alpha}$ and $\mathcal{L}_{v_\delta}$ for Models B, C, D and E. We see very little difference in $\mathcal{L}_{v_\alpha}$ and $\mathcal{L}_{v_\delta}$. However, the values of $\mathcal{L}_{v_{\rm r}}$ show the best recovery of the radial velocities is actually found by Model C, the model which only uses the density constraint. We find this odd, but it matches what we observe in the right panel of Fig. 4.6, and as we discussed above, this is a coincidence owing to the overestimation of the density.

4.5.5 The importance of the data selection

As discussed in Section 4.3, we use only part of the data available to us as constraints to avoid using the observables with too large error. In this chapter, we use target M0III stars with $V \leq 14.5$ mag and $d_{\rm obs} \leq 10$ kpc around which to calculate the observables. However, because *Gaia* will observe stars with $G \lesssim 20$ mag, we include the stars with $G \lesssim 20$ mag in the calculation of the density for the observables if they lie within the smoothing length h. Model F is constructed using the target density measured only using M0III stars with $V \leq 14.5$ mag and $d_{\rm obs} \leq 10$ kpc. This leads to a reduced estimate of density for observables close to the selection limit, because approximately half of their selection kernel will be outside the limit and contain no stars.

The right panel of Fig. 4.6 shows the fractional difference in the radial profiles for Model F (yellow triple-dot-dash). When comparing Model F with

the other models, we see the overestimation of the density at $R_{\rm G} = 2$ kpc present in the other models in the right panel of Fig. 4.6, has been removed. However, the Σ profile is worse in all other areas. The three velocity profiles have all deteriorated, with the σ_z profile being particularly poor in the inner 4 kpc and it is barely an improvement over the unconstrained case (left panel of Fig. 4.6, green dash). Fig. 4.7 shows the fractional surface density difference in the face-on view for Model F (3rd row middle), which when compared with Model B (2nd row left), shows a substantially worse recovery with two large patches of overdensity either side of the bar. The pattern speed of the bar for Model F is the worst recovery of any of the models presented, with $\Omega_{\rm p} = 22.5$ km s^{-1}kpc^{-1} for Model E, compared to the target of $\Omega_{\rm t,p} = 28.9$ km s^{-1}kpc^{-1}. This demonstrates the importance of the density measurements including faint stars. Because the density observables are different in Model F, the value of χ^2 may not be directly compared to the preceding models, but the likelihoods may. The velocity likelihoods are again all very similar.

4.5.6 Different initial conditions

In this section, we show Models G and H, which are performed in the same fashion as the fiducial model, Model B, but starting from different initial conditions for the model. We also show Models G$_i$ and H$_i$ which are Models G and H performed with the constraints from M2M modelling turned off.

Model G uses an initial disc with scale length $R_{\rm d,ini} = 4$ kpc, compared with the previous models which use $R_{\rm d,ini} = 2$ kpc. The left panel of Fig. 4.8 shows the fractional difference in the radial profiles for Model G (blue dash). When comparing Model G with the fiducial model, Model B (black solid), we see very similar $\sigma_{\rm r}$ and $v_{\rm rot}$ profiles. However, the σ_z profile is underestimated. The Σ profile is in general superior to the fiducial model, but not by a large amount.

The right panel of the 3rd row of Fig. 4.7 shows the fractional surface density difference map for Model G, which, when compared with Model B (2nd row left), shows almost no difference. The pattern speed of the bar for Model G is lower than the target, but still a reasonable recovery with

$\Omega_{\rm p} = 25.9$ km s^{-1}kpc^{-1}, compared to the target of $\Omega_{\rm t,p} = 28.9$ km s^{-1}kpc^{-1}. The values of χ^2 and $\mathcal{L}_{v_{\rm r}}$ are slightly worse than Model B. However, the values of $\mathcal{L}_{v_\alpha}$ and $\mathcal{L}_{v_\delta}$ are very similar to that of the fiducial model.

Model G$_i$ is Model G with the constraints from M2M modelling turned off. This is the same as with Model i, but starting from an initial disc with $R_{\rm d,ini} = 4.0$ kpc. The left panel of Fig. 4.8 shows the fractional difference in the radial profiles for Model G$_i$ (red dot), which when compared with Model G (blue dash) shows a worse match to the target for all the radial profiles, apart from the Σ profile at $R \sim 2.5$ kpc, which is due to the change between the underestimation in the inner region, and overestimation in the outer region. The pattern speed of the bar for Model G$_i$ is worse than for Model G, with $\Omega_{\rm p} = 23.9$ km s^{-1}kpc^{-1}, compared to the target of $\Omega_{\rm t,p} = 28.9$ km s^{-1}kpc^{-1}. The values of χ^2, $\mathcal{L}_{v_{\rm r}}$, $\mathcal{L}_{v_\alpha}$ and $\mathcal{L}_{v_\delta}$ are all worse than those of Model G.

Model H uses an initial disc with mass $M_{\rm d,ini} = 10^{11} M_\odot$, compared to the other models which start from a disc with $M_{\rm d,ini} = 5 \times 10^{10} M_\odot$. The left panel of Fig. 4.8 shows the fractional error in the radial profiles for Model H (green triple-dot-dash). When comparing Model H with Model B (black solid), we find that the result is very similar in all profiles within 5 kpc from the centre. However, the fractional difference in the outer section of the profiles is significantly larger for all profiles, especially in the $\sigma_{\rm r}$ and σ_z profiles. The bottom left panel of Fig. 4.7 shows the fractional surface density difference map for Model H, which when compared with Model B (2nd row left) shows a generally heavier disc, with overdensities present especially at large radii. This is unsurprising considering the heavier initial Model disc mass. The pattern speed of the bar for Model H is lower than the target, but still a reasonable recovery with $\Omega_{\rm p} = 25.6$ km s^{-1}kpc^{-1} for Model H, compared to the target of $\Omega_{\rm t,p} = 28.9$ km s^{-1}kpc^{-1}. Similarly to Model G, The values of χ^2 and $\mathcal{L}_{v_{\rm r}}$ are slightly worse than Model B. However, the values of $\mathcal{L}_{v_\alpha}$ and $\mathcal{L}_{v_\delta}$ are very similar to that of the fiducial Model.

Model H$_i$ is Model H with the constraints from M2M modelling turned off. This is the same as with model i but starting from an initial disc with $M_{\rm d,ini} = 10^{11} M_\odot$. The left panel of Fig. 4.8 shows the fractional difference in the radial

profiles for Model H_i (yellow dash-dot), which when compared with Model H (green triple-dot-dash) shows a very poor recovery of all the radial profiles. The pattern speed of the bar for Model H_i is substantially overestimated with $\Omega_{\rm p} = 44.4$ km s^{-1}kpc^{-1}, compared to the target of $\Omega_{\rm t,p} = 28.9$ km s^{-1}kpc^{-1}. The values of χ^2, $\mathcal{L}_{v_{\rm r}}$, $\mathcal{L}_{v_\alpha}$ and $\mathcal{L}_{v_\delta}$ are all significantly worse than those of Model H.

Models G and H show that the results from PRIMAL are not heavily dependent on the initial conditions of the model. As with most modelling methods, it is easier to recover the target properties if the initial model is close to the target. In the final application, we can iteratively change the initial condition, and find a suitable one. Comparing Models G and H with Models G_i and H_i show that PRIMAL is able to recover the properties of the target galaxy from initial discs which would otherwise not evolve into a galaxy which resembles the target. In particular the comparison between Model H and Model H_i shows the power of PRIMAL to recover the properties of the target galaxy from a model which is initially very different from the desired solution.

4.6 Dust extinction

In previous sections, we applied PRIMAL to the mock data constructed without the dust extinction for simplicity, and to highlight the effect of the observational errors on the modelling of the Galactic disc. However, in the real Galaxy, there is the dust extinction which changes the brightness and the colours of the stars, and can block their light completely depending on their distance and the position in the sky.

Interstellar extinction is a major problem that must be addressed before a convincing model of the Milky Way can be produced. Unlike surveys of external galaxies, where the Galactic extinction can be corrected for with a function $A_\lambda(l, b)$ (e.g. Schlegel et al. 1998), we need three dimensional extinction models, e.g. a function $A_\lambda(l, b, d)$, where d is the distance from the Sun. While there are three dimensional extinction maps, they do not cover the entire sky. For example, the map by Drimmel & Spergel (2001), fitted to the far-infrared (FIR) and NIR data from the *COBE*/DIRBE instrument, is for

Galactic latitudes $\mid b \mid \leq 30^{o}$ and $\mid l \mid \leq 20^{o}$. Another example is shown in Marshall et al. (2006), for $\mid l \mid \leq 100^{o}$ and $\mid b \mid \leq 10^{o}$. However, a continuous estimate of $A_{\lambda}(l, b, d)$ has not yet been constructed (Rix & Bovy 2013). However, ways to constrain the extinction on any one star can be determined using a Bayesian method (e.g. Bailer-Jones 2011), and a method using the 2MASS near infra-red (NIR) and *Spitzer*-IRAC mid infra-red (MIR) photometry called the Rayleigh-Jeans Colour Excess (RJCE) method (Majewski et al. 2011). The RJCE method works by comparing changes in stellar NIR−MIR colours due to interstellar reddening which can be calculated as stars are all essentially the same colour in the Rayleigh-Jeans part of the spectral energy distribution. Nidever et al. (2012) have used the RJCE method to produce a 2D map of extinction in the Galactic mid-plane for $256^{o} < l < 65^{o}$ and $\mid b \mid \leq 1^{o} - 1.5^{o}$ (with $\mid b \mid \leq 4^{o}$ for certain longitudes), up to $d \sim 8$ kpc.

To add extinction to our target tracers, we use the extinction map of the Milky Way taken from GALAXIA (Sharma et al. 2011). The publicly available population synthesis code, GALAXIA, generates stellar populations from a galaxy model. GALAXIA uses a 3D polar logarithmic grid of the dust extinction which is constructed from the method described by Bland-Hawthorn et al. (2010) and using the dust maps of Schlegel et al. (1998). We calculate extinction values for our target for each individual M0III tracer. We then modify the magnitudes and colours of the tracers based upon the extinction and apply the *Gaia* expected error as shown in Section 4.3.

In this section, we demonstrate how PRIMAL performs when applied to the mock data considering the dust extinction. We first show Model I, which uses the M0III tracers used in the preceding models, with dust extinction added to our mock data. Then, we show Model J, which uses red clump stars with assumed $M_V = 1.27$ mag and $V - I_c = 1.0$ as tracers, with dust extinction added in the same fashion.

Fig. 4.2 shows real versus observed distance for M0III stars with extinction (middle) and red clump stars with extinction (lower). The middle panel of Fig 4.2 shows that the accuracy within 4 kpc remains excellent even with the addition of extinction to our M0III tracers. However, there is a large drop

in accuracy at larger distances. However, it is encouraging that the highest concentration of particles remains centred around the 1:1 line. The bottom panel of Fig. 4.2 shows a large spread of accuracies for the fainter red clump tracers. In this first investigation we set a selection limit of $V \leq 16.5$ mag and $d_{\rm obs} \leq 10$ kpc for the models with extinction to increase the number of sampled stars, deferring an extensive investigation into the selection criteria to following work.

Fig. 4.3 shows the face-on (upper panels) and edge-on (lower panels) distribution of M0III stars with error but without extinction (2nd column), M0III stars with extinction (3rd column) and red clump stars with extinction (right). A comparison of the 2nd and 3rd column panels of Fig. 4.3 shows that the addition of extinction has a substantial effect on the amount of data available at the Galactic centre, with the data in the plane being lost from $d_{\rm obs} \sim 3$ kpc towards the Galactic centre. The right panels of Fig. 4.3 show that for the red clump tracers, the $V \leq 16.5$ mag limit leaves only a small amount of target data available to use as constraints. There is no evidence of an overdensity from the Galactic centre, and a large amount of data has been lost from the Galactic plane.

Fig. 4.4 shows the fractional density error of the mock data against observed Galactocentric radius (left) and observed distance from the Sun (right) for M0III stars without extinction (upper), M0III stars with extinction (middle) and red clump stars with extinction (lower). The middle left panel of Fig. 4.4 shows a similar trend to the case without extinction (upper left). However, the worst overestimation of the density is now spread between $R_{\rm G} \sim 2$ and 4 kpc. The lower panels of Fig. 4.4 show an even larger spread of the overestimation between $R_{\rm G} \sim 3$ and 7 kpc, and the density for stars whose observed distance is more than 6 kpc is mostly underestimated.

The right panel of Fig. 4.8 shows the fractional difference in the radial profiles for Model I (red dash) which uses M0III tracers with dust extinction and observational error. Model I shows a substantial overestimation of the density around 2 kpc, a general overestimation of the $\sigma_{\rm r}$ and σ_z profiles, but a better recovery in the inner region of the $v_{\rm rot}$ profile. The bottom middle panel of Fig.

4.7 shows the fractional surface density difference map for Model I, which when compared with Model B (2nd row left) shows a substantially worse recovery. There is an overdensity near the centre, which is not present in the fiducial model, and a large underdensity in the top right of the plot. However, the pattern speed of the bar is again recovered well with $\Omega_{\rm p} = 27.7$ km s^{-1}kpc^{-1} for Model I, compared to the target of $\Omega_{\rm t,p} = 28.9$ km s^{-1}kpc^{-1}. The density overestimation in the inner part of the Σ profile and in Fig. 4.7 is concerning. However, it is not surprising considering the overestimation shown at $R_{\rm G} \sim 2$-3 kpc in the middle left panel of Fig. 4.4. Due to the extinction, the number of target stars selected has decreased dramatically from 517,527 to 173,821 (see Table 4.1) and the location of the remaining observables will have moved. Therefore, in Model I the values of χ^2, $\mathcal{L}_{v_{\rm r}}$, $\mathcal{L}_{v_\alpha}$ and $\mathcal{L}_{v_\delta}$ may not be directly compared to the preceding models.

The right panel of Fig. 4.8 shows the fractional difference in the radial profiles for Model J (blue dash-dot) which uses red clump tracers with dust extinction and error added to the target data. Model J shows a good recovery of the Σ profile. Model J is also better than model B (black solid) between $R_{\rm G} = 2$ and 6 kpc, which is very encouraging. Model J is similar to Model I in the inner 2 kpc of the $\sigma_{\rm r}$ profile, and is a substantially better reproduction of the rest of the profile, again superior to Model B. The σ_z profile for model J is odd, with a substantial underestimation in the inner region, and a substantial overestimation in the outer region. The $v_{\rm rot}$ profile is similar to that of Model B.

The bottom right panel of Fig. 4.7 shows the fractional surface density difference map for Model J, which when compared with Model I (bottom middle) shows a better recovery, although it is still noticeably worse than Model B (2nd row left). The pattern speed of the bar is again recovered well, with $\Omega_{\rm p} = 27.3$ km s^{-1}kpc^{-1} for Model J, compared to the target of $\Omega_{\rm t,p} = 28.9$ km s^{-1}kpc^{-1}. We find the accuracy of Model J to be very encouraging for our future exploration of more realistic mock data containing multiple populations. Due to the use of red clump tracers the number of selected tracers in Model J (52,111) has again decreased. Thus, the values of χ^2, $\mathcal{L}_{v_{\rm r}}$,

$\mathcal{L}_{v_\alpha}$ and $\mathcal{L}_{v_\delta}$ may not be directly compared to the preceding models.

The level of accuracy of Models I and J is still encouraging, considering the amount of information which is lost due to extinction. However, we find it surprising that the red clump tracers lead to a more accurate model. However, self-gravity leads to a stable model in a non-linear way, and different constraints sometimes act counter-intuitively. We stress the need for further testing of selection criteria with mock data. What we can conclude for the time being from this initial trial is that the accuracy of the recovery is difficult to control for M2M modelling, and a careful balance must be reached between the quantity and quality of data which are used for observables. The data selection criteria will need to be different depending on the type of star. We do not consider it useful to do extensive testing on the selection criteria at this stage, as PRIMAL must be modified to use more realistic mock data before such tests become meaningful.

4.7 Chapter summary

We have demonstrated that PRIMAL can recover to a reasonable degree the properties of a target disc system with a bar/boxy structure in a known dark matter halo potential despite the presence of error in the observational data. To allow us to do this, we have modified PRIMAL to use equatorial coordinates which is the form of data *Gaia* will provide. In this chapter, the error added observables are compared with the model at the observed position of the target particles. We have demonstrated that PRIMAL can recover the pattern speed of the bar to an excellent degree under these conditions.

This chapter is a first attempt at dynamical modelling taking into account the *Gaia* error, and is used as a demonstration of how we can and will deal with this, not a statement of the final capability or accuracy of the algorithm. However, it is encouraging that the *Gaia* errors are good enough to recover galactic structure, at least with this simple model, and is worth further exploration of this methodology. However, we are aware that this is still a simplified case containing many assumptions. In a forthcoming work, we will modify PRIMAL to work with more realistic mock observational data

which will consist of multiple stellar populations. In Chapter 5, we describe a novel way of creating this mock data from a known N-body simulation. A strong assumption made at this stage is that we assume the relationship between cluster mass and the number density of M0III stars is known. This is of course not the case, and will have to be addressed in further works. Additionally, the work in this thesis assumes a known dark matter halo potential for simplicity, whereas in reality the dark matter distribution of the halo remains very much unknown. However, the halo does have a significant effect on the dynamics of the galaxy. Thus, we intend to explore different dark matter halo density profiles in future work, including the possibility of using a live dark matter halo. This is discussed in Section 6.2.

Chapter 5

The stellar kinematics of co-rotating spiral arms in *Gaia* mock observations

This chapter is based on Hunt et al. (2015)

We have observed an N-body/SPH simulation of a Milky Way-like barred spiral galaxy. We present a simple method that samples stars from N-body model particles. We use it to generate mock *Gaia* stellar observations, taking into account stellar populations, dust extinction and *Gaia's* science performance estimates. We examine the kinematics of stars with $V \leq 16$ mag around a nearby spiral arm at a similar position to the Perseus arm at three lines of sight in the disc plane $(l, b) = (90^{\rm o}, 0^{\rm o}), (120^{\rm o}, 0^{\rm o})$ and $(150^{\rm o}, 0^{\rm o})$. We find that the structure of the peculiar kinematics around the co-rotating spiral arm, which is found in Kawata et al. (2014b), is still visible in the observational data expected to be produced by *Gaia*, despite the dust extinction and expected observational errors of *Gaia*. These observable kinematic signatures will enable testing whether the Perseus arm of the Milky Way is similar to the co-rotating spiral arms commonly seen in N-body simulations.

5.1 Introduction

The spiral features visible in many galaxies have long been the subject of debate. As mentioned in Section 1.4.6, the mechanisms which generate them are still uncertain. The spiral density wave theory (Lin & Shu

1964) which treats the spiral structure as a density wave, and can thus be long-lived, solves the winding dilemma. However, no N-body simulations have yet been able to reproduce these long-lived stable spiral arms, despite the increase in computational power and resolution which has occurred in recent years (e.g. Sellwood 2011; Dobbs & Baba 2014). Recent work has shown spiral modes and waves which survive over multiple rotations (Quillen et al. 2011; Roškar et al. 2013; Sellwood & Carlberg 2014), while the spiral arm features in the stellar mass are short-lived but recurrent (e.g. Sellwood & Carlberg 1984; Carlberg & Freedman 1985; Bottema 2003; Fujii et al. 2011; Grand et al. 2012a,b, 2013; Baba et al. 2013; D'Onghia et al. 2013; Roca-Fàbrega et al. 2013), including in galaxies with a central bar (e.g. Grand et al. 2012b). These results imply that the large spiral arms visible in external galaxies may only *appear* to be rigid structures extending over the disc, while in fact being made of transient reforming features.

The interpretation of the transient and recurrent spiral arm features observed in N-body simulations is still in debate. For example, Minchev et al. (2012) show for the first time (by studying the time evolution of the disc power spectrum) that spiral wave modes in N-body simulations can last for as long as 1 Gyr, which can justify treating the wave modes as quasi-stationary structure, and the transient and recurrent spiral arm features can be explained by the superposition of different modes with different pattern speeds (see also Roškar et al. 2012; Sellwood & Carlberg 2014). On the other hand, Grand et al. (2012a), D'Onghia et al. (2013) and Baba et al. (2013) demonstrate non-linear growth of the spiral arm features due to similar but different (in terms of evolution) mechanisms from swing amplification (Toomre 1981), which could be difficult to explain with the linear superposition of the wave modes.

Our position within the Milky Way gives us a unique view of these spiral structures seen in external galaxies, but it comes with its own set of problems which we must overcome when studying them. The location and kinematics of the gaseous component of the arms may be determined from HI and CO observations (e.g. Dame et al. 2001; Nakanishi & Sofue 2003; Kalberla & Kerp

2009). However, to observe the kinematics of the stellar component in and around the spiral arms, we must look through the disc plane, which carries the heaviest levels of dust and gas, and thus high levels of extinction.

Dust extinction has long been a problem for Milky Way model construction. As discussed in Section 4.6, although there are reasonably reliable extinction maps for extragalactic sources whose extinction by the interstellar medium of the Milky Way can be corrected as a function $A_\lambda(l, b)$ (e.g. Schlegel et al. 1998), three-dimensional extinction mapping for sources within the Milky Way i.e. $A_\lambda(l, b, d)$ is more challenging. There are three-dimensional extinction maps for individual sections of the sky (e.g. Drimmel & Spergel 2001; Marshall et al. 2006; Hanson & Bailer-Jones 2014; Sale & Magorrian 2014) and two-dimensional maps have been extended to three dimensions (e.g. Drimmel et al. 2003). However, a truly Galactic 3D extinction map does not yet exist (Rix & Bovy 2013). ESA's *Gaia* mission will help us map the stellar structure and kinematics of the Milky Way, and help constrain extinction at the same time (Bailer-Jones et al. 2013).

Gaia, which was launched on the 19th December 2013, will provide detailed astrometric (e.g. Lindegren et al. 2012), spectroscopic (e.g. Katz et al. 2011) and photometric (e.g. Jordi et al. 2010) information for around one billion stars in the Milky Way. Detailed information on *Gaia* scientific accuracies is available in, for example, de Bruijne (2012). Synthetic *Gaia* mock data have already been used to demonstrate different applications of the real *Gaia* data set. For example, Abedi et al. (2014) used three tracer populations (OB, A and red clump stars) with the *Gaia* selection function, errors and dust extinction, and demonstrated that the *Gaia* mock data can recover the parameters of the Galactic warp. Romero-Gómez et al. (2015) examine the Galactic bar in the *Gaia* observable space using red clump tracers with the *Gaia* selection function, errors and dust extinction. In Chapter 4, we show that we can recover the large scale structure of the Galactic disc with our made-to-measure Galaxy modelling code, PRIMAL (Chapters 2, 3 and 4), and make a good estimation of the pattern speed of the bar, using tracer populations of M0III and red clump stars with the *Gaia* selection function, errors and dust extinction.

There exist full mock catalogues of *Gaia* stars, e.g. the *Gaia* Universe Model Snapshot (GUMS) which provides a view of the Besançon Galaxy model as seen from *Gaia* (Robin et al. 2012), taking into account dust extinction while assuming there are no observational errors. This detailed prediction of *Gaia* observations gives an excellent indication of the volume and quality of data which will become available from *Gaia*, predicting 1.1 billion observable stars, almost 10,000 times more than from its predecessor, *Hipparcos*. GUMS can be extended through the *Gaia* Object Generator (GOG, Luri et al. 2014) to simulate intermediate and final catalogue data, including the introduction of realistic astrometric, photometric and spectroscopic observational errors to the catalogue based upon *Gaia* science performance estimates. While these mock data provide an excellent example of the capabilities of *Gaia*, the Besançon galaxy model is an axisymmetric model and a kinematic model not a dynamical model. Although *Gaia* will not provide accelerations, the kinematics which *Gaia* will provide are from a dynamical system, the Milky Way. Thus, it is important for our purpose to generate catalogues from fully dynamical models with non-axisymmetric structures, such as spiral arms and a bar, which for example N-body disc galaxy models can provide.

Therefore, in this chapter, we propose to create mock *Gaia* observations from an N-body model using a population synthesis code, such as GALAXIA (Sharma et al. 2011), or the methodology presented in Pasetto et al. (2012) or Lowing et al. (2015). GALAXIA is a flexible population synthesis code for generating a synthetic stellar catalogue from an N-body or an analytical galaxy model over wide sections of the sky, with a sampling scheme which generates a smoothly distributed sample of stars. Synthetic catalogues generated from dynamical Galaxy models are essential for preparing to exploit the real *Gaia* catalogue and can be used to determine whether certain features within the Milky Way will be visible to *Gaia*.

In Kawata et al. (2014b), we examined the kinematics of both the stellar and gas components around a transient, co-rotating spiral arm in a simulated barred spiral galaxy similar in size to the Milky Way. Although this arm is transient, similar arms recur during the evolution of the galaxy. We made

predictions of observable kinematic signatures that may be visible in the Milky Way's Perseus arm, if it is also a transient, recurrent and co-rotating spiral arm. We then compared our simulation with data from APOGEE and the maser sources in Reid et al. (2014) measured by the BeSSeL survey and the Japanese VLBI Exploration of Radio Astronomy, finding tentative agreement between our simulation and the observations. Owing to the low number of maser sources and the lack of distance information for the APOGEE stars, no firm conclusions could be drawn. However, it is encouraging to see similar features in both, including the possible signatures of a co-rotating spiral arm.

In this chapter, we build upon the previous work of Kawata et al. (2014b) by generating a stellar sample with different populations from the simulation data in Kawata et al. (2014b) and making mock observations of these stars taking into account the expected *Gaia* science performance estimates. The aim is not to make further predictions about the kinematics of transient, recurrent and co-rotating spiral arms, but rather to examine whether these signatures remain visible in the *Gaia* data if they exist in the Milky Way.

5.2 Simulation

We use the simulated galaxy which is presented in Kawata et al. (2014b) and Grand et al. (2015). The details of the numerical simulation code, and the galaxy model are described in Kawata et al. (2014b). We briefly describe the galaxy model in this section. The galaxy is set up in isolated conditions, and consists of a gas and stellar disc but no bulge component. The discs are embedded in a static dark matter halo potential (Rahimi & Kawata 2012; Kawata et al. 2014b). The dark matter halo mass is $M_{\rm dm} = 2.5 \times 10^{12}$ M$_\odot$, and the dark matter density follows the density profile in Navarro et al. (1997), with a concentration parameter of $c = 10$. The stellar disc is assumed to follow an exponential surface density profile with the initial mass of $M_{\rm d,*} = 4.0 \times 10^{10}$ M$_\odot$, a radial scale length of $R_{\rm d,*} = 2.5$ kpc and a scale height of $z_{\rm d,*} = 350$ pc. The gas disc is set up following the method of Springel et al. (2005b), and has an exponential surface density profile with the scale length of $R_{\rm d,g} = 8.0$ kpc. The total mass of the gas is 10^{10} M$_\odot$. The simulation comprises 10^6 gas

particles and 4×10^6 star particles. Therefore, each particle has a mass of 10^4 $M_\odot$. The resolution is sufficient to minimise numerical heating from Poisson noise (Fujii et al. 2011; Sellwood 2013). We employ a minimum softening length of 158 pc (equivalent to a Plummer softening length of 53 pc) with the spline softening and variable softening length for gas particles as suggested by Price & Monaghan (2007).

The radial profile of the mean metallicity of stars and gas is initially set by $[\mathrm{Fe/H}](R) = 0.2 - 0.05(R/1\ \mathrm{kpc})$, and the metallicity distribution function at each radius is centred on the mean metallicity value with the dispersion set to a Gaussian distribution of 0.05 dex for the gas and 0.2 dex for the stars. The stellar ages are set randomly between 0 and 10 Gyr for stars present at the beginning of the simulation.

The simulation was run for 1 Gyr from the initial conditions with the N-body smoothed particle hydrodynamics (SPH) code, GCD+ (e.g. Kawata & Gibson 2003; Rahimi & Kawata 2012; Barnes et al. 2012; Kawata et al. 2013, 2014a) without the inclusion of any continuous external inflow of gas for simplicity. In this chapter, we use the same snapshot of the galaxy as used in Kawata et al. (2014b) which is taken at $t = 0.925$ Gyr, as this snapshot shows a spiral arm at a similar location to the Perseus arm of the Milky Way in the Galactic longitude range of $l = 90 - 150^\mathrm{o}$ (see Fig. 5.1). We assume that the position and velocity of the Sun is known. We locate the observer at (−8,0,0) kpc as shown in Fig. 5.1, and the motion of the Sun is assumed to be the same as the circular velocity at 228 km s^{-1}.

The velocity dispersion for the N-body particles in the simulated galaxy at the Galactic radius, $7.5 \leq R_\mathrm{G} \leq 8.5$, is comparable to that for the stars in the Solar neighbourhood. We calculate the radial (σ_U), azimuthal (σ_V) and vertical (σ_W) velocity dispersion for the young and old particles at the Solar radius of the simulation, which is defined with the Galactic radius, $7.5 \leq R_\mathrm{G} \leq 8.5$ and $\mid z \mid \leq 0.5$ kpc. We define the young stars as the star particles with an age less than 0.5 Gyr, which are the star particles formed after the bar formation. As stated above, the simulation is only run for 0.925 Gyr and the particles older than 0.925 Gyr were created in the initial conditions. Thus, the

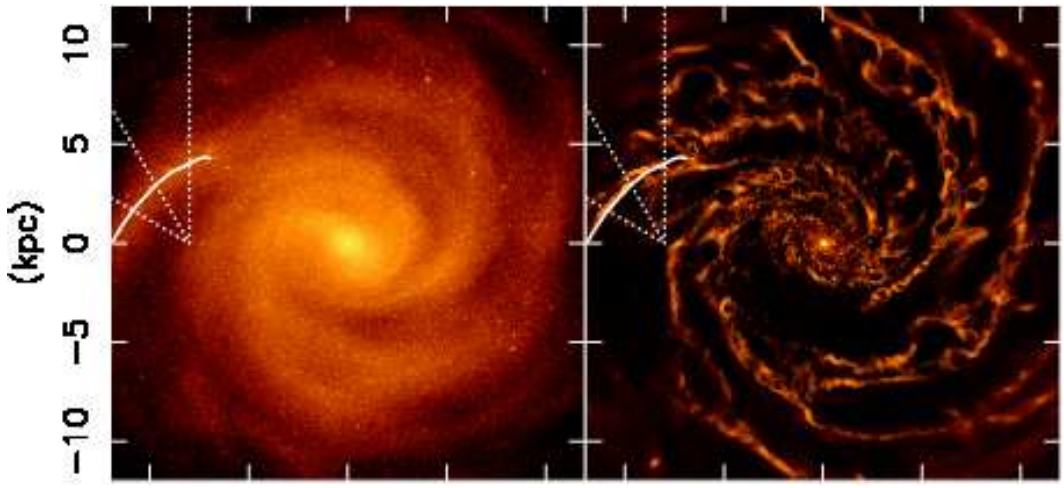

Fig. 5.1: Snapshot of the simulated galaxy in Kawata et al. (2014b) which is also used in this chapter. Face-on view of the star (left) and gas (right) particle distribution within a 12 kpc by 12 kpc area. The solid line indicates the position of the spiral arm identified. The observer is assumed to be located at $(x, y) = (-8, 0)$ kpc. Three line-of-sight directions ($l_{\rm LOS} = 90^{\rm o}, 120^{\rm o}$ and $150^{\rm o}$) are highlighted with the dotted lines. The galaxy is rotating clockwise.

old stars are defined as the particles with ages between 1 and 10 Gyr, which were created in the initial conditions with their age set randomly between 0 and 10 Gyr, and have since been kinematically heated by the formation of the bar. The analysed velocity dispersions are listed in Table 1. We compare the velocity dispersion from the simulation with the observed velocity dispersion in Holmberg et al. (2009), which shows the velocity dispersion for stars older than 1 Gyr. The velocity dispersion in Holmberg et al. (2009) increases continuously with age. We list the velocity dispersion of the second youngest bin in Figure 7 of Holmberg et al. (2009), which approximately corresponds to the age of 1.5 Gyr, and the range of the velocity dispersion for the stars with an age of 2-10 Gyr, to compare respectively with the velocity dispersion of the young and old stars in the simulated galaxy. Although the radial and azimuthal velocity dispersion of the young star particles in the simulation are higher, the velocity dispersion of the old star particles in the simulation is well within the range given in Holmberg et al. (2009) for the observed velocity dispersions for the solar neighbourhood stars.

However, we note that the aim of this chapter is to test if the *Gaia* data

Table 5.1: Radial (σ_U), azimuthal (σ_V) and vertical (σ_W) velocity dispersion of the simulation and observed values for the Milky Way (Holmberg et al. 2009).

	Simulation		Holmberg et al. (2009)	
Age	≤ 0.5 Gyr	1-10 Gyr	~ 1.5 Gyr	2-10 Gyr
σ_U	30	39	~ 26	$\sim 23 - 50$
σ_V	21	29	~ 15	$\sim 15 - 30$
σ_W	8	20	~ 10	$\sim 10 - 30$

can identify the peculiar motion around the co-rotating spiral arm found in Kawata et al. (2014b). As in Kawata et al. (2014b), the simulation is not intended to reproduce the whole structure of the Milky Way. The pitch angle of the spiral arm in the simulation is 39°, which is much larger than the estimated pitch angle for the Perseus arm, e.g. $9.4^{\circ} \pm 1.4^{\circ}$ (Reid et al. 2014).

It is worth discussing the strength of the simulated spiral arm, compared to the strength of the Perseus arm. Figure 2 in Kawata et al. (2014b) shows the simulated arm has an amplitude of ~ 0.12 in the $m = 2$ Fourier mode (normalised to the $m = 0$ mode). A pitch angle of 39° and amplitude of 0.12 is within the scatter of the pitch angle/amplitude relation explored in Figure 8 in Grosbøl et al. (2004). The local density enhancement of the Milky Way's Perseus arm is not currently well constrained. However, Benjamin et al. (2005) estimated the stellar density enhancement of the Centaurus arm is about 20% using data from GLIMPSE.

As discussed in Kawata et al. (2014b), we measured the strength of the bar using a gravitational field method (e.g. Buta et al. 2005) described in Grand et al. (2012b), and obtained the bar strength $Q_{\rm b} = 0.15$, which is consistent with the lower end of the estimates of the Milky Way's bar strength, which is between $Q_{\rm b} = 0.17$ and 0.83 in Table 1 of Romero-Gómez et al. (2011).

5.3 *Gaia* mock catalogue

In Kawata et al. (2014b), the kinematics of the spiral arm shown in Fig. 5.1 are examined at three lines of sight $l_{\rm LOS} = 90^{\circ}, 120^{\circ}$ and 150°, with $b_{\rm LOS} = 0^{\circ}$.

We do not include $l_{\rm LOS} = 180^{\rm o}$, because the distance to the spiral arm in our simulation is much further than the Perseus arm owing to the large pitch angle of the simulated galaxy. Predictions are made of the observational signatures of co-rotating spiral arms notably the difference in kinematic structure between the trailing near side and leading far side of the spiral arm. In general, in Kawata et al. (2014b, as also shown in Grand et al. 2014a), the stars in the trailing near side rotate slower because they tend to be at the apocentre and migrate outwards, and the stars in the leading far side rotate faster as they tend to be at the pericentre and migrate inwards. However, there are some stars which follow the opposite trend, leading to multiple populations seen in the rotational velocity in the leading far side, one faster and one slower than the single population in the trailing near side. These features which will be discussed later may be caused by the corotation resonance of the spiral arm, and are visible at different galactic longitudes, because the spiral arm in the simulation corotates at all the examined radial range. However, in Kawata et al. (2014b), the spiral arm kinematics are examined using the full, error and extinction free N-body data and thus such trends, when present, are easy to identify.

In this section, we describe how we generate a sample of stars from the N-body model of Kawata et al. (2014b) to produce a mock *Gaia* catalogue. It is worth noting that the population synthesis code, GALAXIA (Sharma et al. 2011) provides a tool to generate stellar populations from N-body simulation data. However, because we plan to combine such a tool with our made-to-measure Galaxy modelling code, PRIMAL, we have developed our own simplified version of GALAXIA, a population synthesis code called SNAPDRAGONS (Stellar Numbers And Parameters Determined Routinely And Generated Observing N-body Systems). SNAPDRAGONS uses the same isochrones and extinction map as GALAXIA, but uses a different and simpler process to generate the stellar catalogue which is described in Section 5.3.2. SNAPDRAGONS allows us to add the expected *Gaia* errors more easily, and enables us to track the link between sampled stars and their parent N-body particle for our future studies, e.g. PRIMAL modelling of the Galactic disc (see Chapters 2−4) by

fitting tracers from multiple stellar populations (see Section 6.2), and identifying radially migrating stars and non-migrating stars trapped by the spiral arm (Grand et al. 2014).

5.3.1 Extinction

We use the extinction map of the Milky Way taken from GALAXIA (Sharma et al. 2011), which is a 3D polar logarithmic grid of the dust extinction constructed using the method presented in Bland-Hawthorn et al. (2010) and the dust maps of Schlegel et al. (1998), which we call the 3D Schlegel map. The same method to apply extinction is used in Chapter 4 and more detail is given there. In an update from Chapter 4, we follow the reduction to the Schlegel E_{B-V} suggested in Sharma et al. (2014), such that

$$E_{B-V} = E_{B-V}\left(0.6 + 0.2\left(1 - \tanh\left(\frac{E_{B-V} - 0.15}{0.1}\right)\right)\right). \tag{5.1}$$

This reduction is made, because it has been suggested (e.g. Arce & Goodman 1999; Yasuda et al. 2007) that the reddening is overestimated by the maps of Schlegel et al. (1998) by ∼1.3-1.5 in regions with high extinction with $A_V > 0.5$ ($E_{B-V} > 0.15$). This reduces extinction by $\sim 40\%$ for low-latitude high-extinction regions but has minimal effect on high-latitude low-extinction regions. In Fig. 5.2, we compared the 3D Schlegel map with and without this reduction term with the 3D extinction map of Sale et al. (2014) which is based upon photometry from the INT Photometric Hα Survey of the Northern Galactic Plane (IPHAS). Fig. 5.2 shows the comparison of extinction, A_V, for the 3D Schlegel map without the reduction of Equation (5.1) (red dashed), the 3D Schlegel map with the reduction (green solid) and the 3D extinction map from Sale et al. (2014, blue dotted) for the lines of sight of the Galactic longitudes of $l = 90^o$ (left column), $l = 120^o$ (middle column), $l = 150^o$ (right column) and latitudes of $b = 5^o$ (top row), $b = 0^o$ (middle row) and $b = -5^o$ (bottom row). The values of A_0 in Sale et al. (2014) were used to calculate A_V at the nearest voxel to each line-of-sight using the approximation

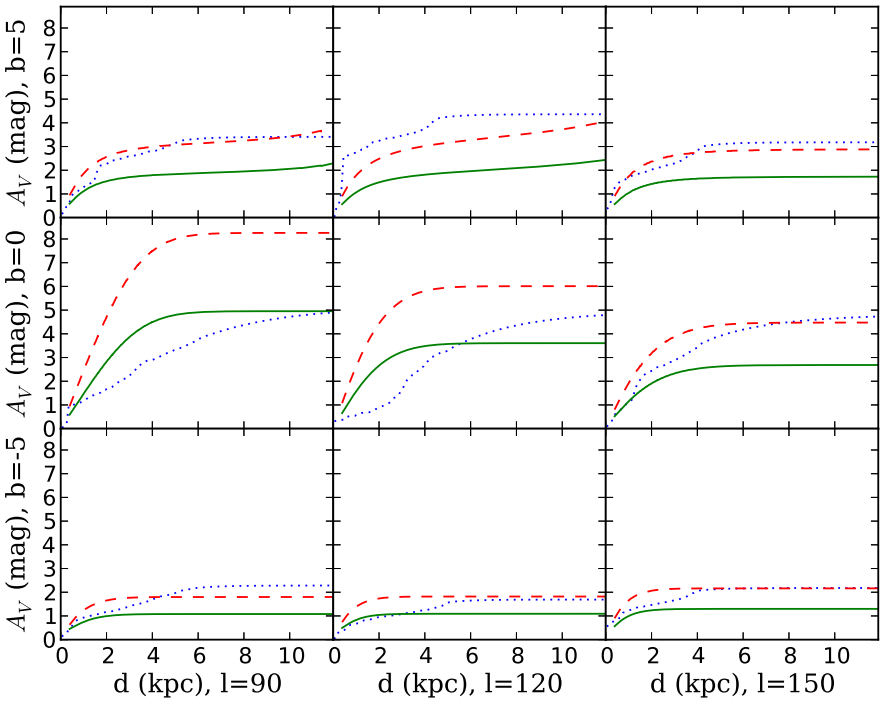

Fig. 5.2: Extinction, A_V, for the 3D Schlegel map without the reduction in the extinction by equation (5.1) (red dashed), the 3D Schlegel map with the reduction (green solid) and the 3D extinction map from Sale et al. (2014, blue dotted) for the lines of sight of the Galactic longitudes of $l = 90^{\rm o}$ (left column), $l = 120^{\rm o}$ (middle column), $l = 150^{\rm o}$ (right column) and latitudes of $b = 5^{\rm o}$ (top row), $b = 0^{\rm o}$ (middle row), and $b = -5^{\rm o}$ (bottom row).

in Bailer-Jones (2011),

$$\begin{aligned} A_V \simeq A_0 \quad &- \quad 5.376 + 2.884(\log(T_{\rm eff})) - 0.4217 A_0 \\ &- \quad 0.3865(\log(T_{\rm eff}))^2 - 0.00374 A_0^2 \\ &+ \quad 0.1072(\log(T_{\rm eff}))A_0, \end{aligned} \tag{5.2}$$

assuming $\log(T_{\rm eff}) = 4,750$ K, an average temperature for red clump stars (e.g. Puzeras et al. 2010; Bovy et al. 2014).

Fig. 5.2 demonstrates the uncertainties of the extinction at low Galactic latitudes, and the reduction term of equation (5.1) underestimates the extinction in some lines of sight compared with Sale et al. (2014). Therefore, we will present results with and without the reduction in the extinction by equation (5.1).

5.3.2 Population synthesis: SNAPDRAGONS

The goal of this population synthesis code is to split each N-body particle from the galaxy simulation into an appropriate number of stellar particles creating a mock catalogue of observable stars from our N-body model. We must choose an IMF and a set of isochrones with which to work. We choose a Salpeter IMF (Salpeter 1955) where the IMF, $\Phi(m)$, is defined in each mass interval dm as

$$\Phi(m)\mathrm{d}m = Am^{-(x+1)}\mathrm{d}m, \tag{5.3}$$

where $x = 1.35$ is the Salpeter index, and A is a constant for normalization in the desired mass range. We set this constant as

$$A_i = m_i\left(\int_{m_{\star,\min}}^{m_{\star,i,\max}} m^{-x}\mathrm{d}m\right)^{-1}, \tag{5.4}$$

where m_i is the N-body particle mass, $m_{\star,i,\max}$ is the maximum initial mass of any surviving star and $m_{\star,\min}$ is the minimum stellar mass to be considered. We make use of the Padova isochrones (e.g. Bertelli et al. 1994; Marigo et al. 2008), although the choice of isochrones (and IMF) may be substituted with others with no change to the methodology.

It is worth noting that the Padova isochrones are available only for stellar masses above 0.15 $M_\odot$. GALAXIA, for example, uses the isochrones of Chabrier et al. (2000) to extend the mass limit down to 0.07 $M_\odot$, which is the hydrogen mass-burning limit. We set our lower limit on stellar mass as $m_{\star,\min} = 0.1\ M_\odot$ to correspond with the simulation of Kawata et al. (2014b) and extrapolate from the Padova isochrones for $0.1 \leq M_\odot \leq 0.15$. It is relatively safe to do this because all such stars lie on the main sequence. Additionally, these exceedingly faint stars will not be visible at the distance of the spiral arms which are the focus of this work.

As discussed in Section 5.2, each N-body star particle in the simulated galaxy has been assigned an age and metallicity within the chemodynamical code, GCD+, then it is made to evolve. When we examine the snapshot, each particle is matched to its nearest isochrone in both metallicity and age from the grid of isochrones which are extracted from GALAXIA. Once an isochrone is selected, we identify $m_{\star,i,\max}$ from the isochrone. We then determine how

many stars to sample from the N-body particle by integrating the IMF over the desired mass range using

$$N_{\rm s} = A \int_{m_{\star,i,<V_{\rm lim}}}^{m_{\star,i,\rm max}} m^{-(x+1)} {\rm d}m, \tag{5.5}$$

where $m_{\star,i,<V_{\rm lim}}$ is minimum mass required for the star to be brighter than our apparent magnitude selection limit, $V_{\rm lim}$, taking into account the extinction value at the position of the parent particle. Stars smaller than $m_{\star,i,<V_{\rm lim}}$ are not used in the subsequent analysis, to save on computational time.

We then randomly sample stellar masses from the section of the isochrone $N_{\rm s}$ times. We have weighted the random selection by the IMF using the equation

$$m_\star = (R m_{\star,i,\rm max}^{-x} + (1-R) m_{\star,i,<V_{\rm lim}}^{-x})^{\frac{1}{-x}}, \tag{5.6}$$

where R is a random number between 0 and 1. The isochrones are comprised of discrete stellar data. Therefore, we interpolate within the nearest isochrone values of M_V and $V-I_c$ to determine $M_{V,\star}$ and $(V-I_c)_\star$ for the generated $m_\star$.

The number of stars sampled from each particle has to be an integer value. However, $N_{\rm s}$ calculated in equation (5.5) is not an integer value. Therefore, we compare the decimal component of $N_{\rm s}$ with another random number between 0 and 1, and if the random number is smaller than the decimal component of $N_{\rm s}$ we round up, otherwise we round down.

We calculate the exact stellar mass that is expected to be generated from a group of N-body star particles using the assumed IMF as

$$M_{\rm exp} = \sum_i A_i \int_{m_{\star,i,<V_{\rm lim}}}^{m_{\star,i,\rm max}} m^{-x} {\rm d}m, \tag{5.7}$$

where i represents an N-body star particle in the selected group. We also calculate the total mass of the stars which are generated from these particles

$$M_{\rm gen} = \sum_i \sum_j^{N_{\rm s}} m_{\star,j}. \tag{5.8}$$

Fig. 5.3 compares the generated stellar mass, $M_{\rm gen}$, and the exact stellar mass, $M_{\rm exp}$, within a square region of $\pm 5^{\rm o}$ around $(l,b) = (90^{\rm o}, 0^{\rm o})$ at different distance bins. Fig. 5.3 shows the mean and one standard deviation of $M_{\rm gen}/M_{\rm exp}$

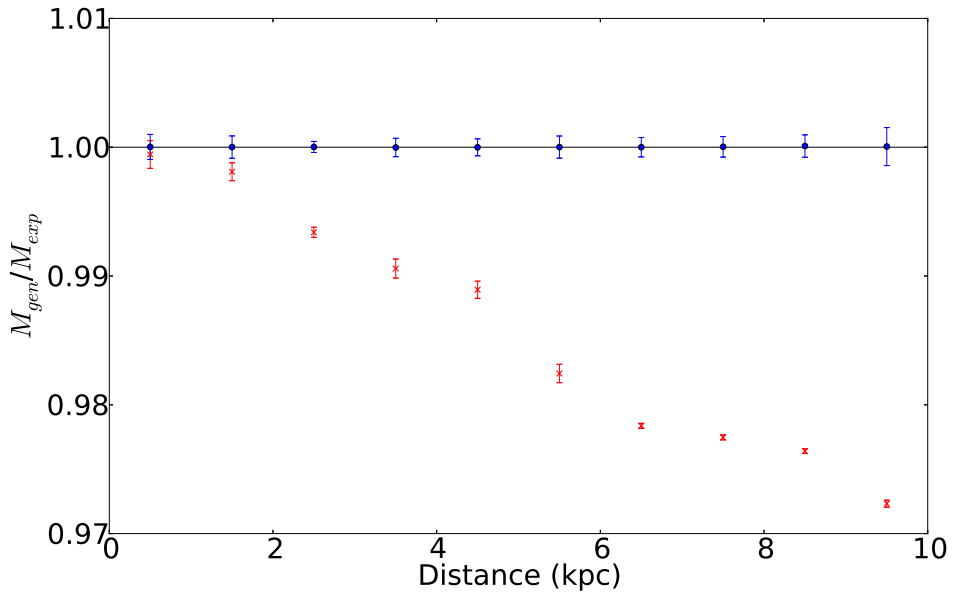

Fig. 5.3: Mean difference between expected mass, $M_{\rm exp}$, and generated mass, $M_{\rm gen}$, with one standard deviation calculated using 100 different sequences of independently generated random numbers. Blue circles show the results for the methodology presented in Section 5.3.2. Red crosses show, for comparison, the results when considering only the integer component of $N_{\rm s}$ in equation (5.5).

calculated using 100 different sequences of independently generated random numbers. Blue circles show the results of the methodology described above, which shows an excellent agreement between $M_{\rm gen}$ and $M_{\rm exp}$. For comparison, if we only round $N_{\rm s}$ down (red crosses), $M_{\rm gen}$ becomes systematically lower than $M_{\rm exp}$ at larger distances where only a few bright stars are sampled from each particle. Therefore, it is important to statistically sample the decimal component of $N_{\rm s}$.

The generated stars have the same position and velocity as their parent N-body particles. This method suffers from the discrete distribution of stars. However, if the selected volume is sufficiently sampled by enough N-body particles to resolve the structures of interest, the discreteness is not an issue. The region of the spiral arm focused on in this chapter and the peculiar velocity structures within are well sampled by the N-body particles. Therefore, we do not think that this method of sampling affects the results in this work. However, in the case of phase-space structures which are poorly sam-

pled by N-body particles e.g. in low density regions or even in high density regions, if the volume sampled is too small, the discreteness of the distribution becomes an issue. A more sophisticated method to smoothly distribute the generated stars in the phase space is applied in Lowing et al. (2015) based on the entropy-based binary decomposition (ENBID) code in Sharma & Steinmetz (2006). This is a powerful method to describe the phase-space distribution of stars from simulations that do not well resolve the targeted phase-space structure. This method could be included in the future version of SNAPDRAGONS.

5.3.3 Observational errors

Having generated the visible stellar catalogue, we then add observational errors based upon the *Gaia* Science Performance estimates[1]. We use the post launch error estimates approximated from the estimates in pre-launch performance by Mercè Romero-Gómez (e.g. Romero-Gómez et al. 2015), provided through the *Gaia* Challenge collaboration[2]. For this work, while generating the stellar catalogue we produced stars only brighter than $V_{\rm lim} \leq 16$ mag, which is well within *Gaia's* $G \leq 20$ mag magnitude limit for the astrometry. However, because we are interested in the Galactic radial and rotation velocity for the stars, which requires the full 6D phase-space information, we chose the lower magnitude limit where the *Gaia* RVS can produce the reasonably accurate line-of-sight velocity. Note that the errors are added to the parallax, proper motion and line-of-sight velocities.

A full description of the method to add the pre-launch *Gaia* error is available in Chapter 4. However, the *Gaia* science performance estimates have been revised after launch, and as such a correction must be made. The error in parallax has increased, and although it has little effect for stars with $V \leq 16$ mag with which we work in this chapter, the coefficients within equation (4.9) which describes the pre-launch parallax performance provided by Kazi, Antoja & de Bruijne (Oct. 2014), by fitting to the new estimations on the *Gaia*

[1] http://www.cosmos.esa.int/web/Gaia/science-performance
[2] http://astrowiki.ph.surrey.ac.uk/dokuwiki/doku.php

science performance web page, are revised to

$$\begin{aligned}\sigma_\pi &= (-11.5 + 706.1z + 32.6z^2)^{1/2} \\ &\quad \times (0.986 + (1 - 0.986)(V - I_c)),\end{aligned} \tag{5.9}$$

where

$$z = \max(10^{0.4(12-15)}, 10^{0.4(G-15)}). \tag{5.10}$$

Additionally, because of the loss of spectroscopic accuracy by ~ 1.5 mag in the RVS post-launch performance, we also apply a correction to the error function for the end of mission radial velocity. We change the table[3] of values a and b, again determined by fitting the revised performance estimates on the *Gaia* science performance web page, for the equation

$$\sigma_{v_\mathrm{r}} = 1 + b\mathrm{e}^{a(V-14)}, \tag{5.11}$$

where a and b are constants dependant on the spectral type of the star. The new table along with the code to add the *Gaia* error is available online[4].

5.4 Results

As discussed in Section 5.3, it was shown in Kawata et al. (2014b) that in general the stars in the trailing near side of the spiral arm rotate slower than average because they tend to be at the apocentre, and the stars in the leading far side of the spiral arm rotate faster than average as they tend to be at the pericentre. However, there are groups of stars which follow different trends leading to multiple populations which will be discussed later. It is important to determine whether such features will still be visible in the *Gaia* catalogue, not just the error and extinction-free N-body model. In this section, we show the result of sampling these N-body data into stellar data, first looking at the properties of the resulting mock stellar catalogue, and then examining the spiral arm kinematics with the stellar data taking into account dust extinction and *Gaia* science performance estimates.

[3] http://www.cosmos.esa.int/web/Gaia/table-5

[4] https://github.com/mromerog/Gaia-errors

5.4.1 Population synthesis

In this section, we describe the stellar catalogue produced by SNAPDRAGONS, and show the resulting intrinsic colour-magnitude diagram (CMD) varying the area of the sky coverage. Fig. 5.4 shows the CMD for stars generated by SNAPDRAGONS from particles within a square region of $\pm 2^{\rm o}$ (upper) and $\pm 5^{\rm o}$ (lower) around $(l, b) = (90^{\rm o}, 0^{\rm o})$. The upper panel of Fig. 5.4 shows clearly the individual stellar isochrones, because there are only a small number of N-body particles in the selected region, and each particle has only one age and metallicity. These problems are resolved when smoothing is applied in the phase-space distribution and age-metallicity distribution (e.g. Sharma et al. 2011). However, as discussed in Section 5.3.2, we deliberately avoid this smoothing to maintain the clear particle-star relation. The lower panel of Fig. 5.4 shows no such discrete structure, as there are sufficiently many particles to cover a broad range of stellar ages and metallicities in the CMD. Therefore, care is required with the resolution of the N-body simulation and the selection function, if we discuss in detail the stellar population distribution in the CMD. However, this is unlikely to affect the study in this chapter.

We compared the star counts within a circular region of radius of $5^{\rm o}$ around $(l, b) = (90^{\rm o}, 0^{\rm o})$ for SNAPDRAGONS applied to our N-body simulation and GALAXIA using a version of the Besançon model. SNAPDRAGONS generated 205,621 stars with $V \leq 16$ mag, and GALAXIA generated 251,880 stars with $V \leq 16$ mag. The difference is caused by the structure in the underlying galaxy model. SNAPDRAGONS generates far fewer stars near to the observer owing to the low density inter-arm region close to the observer in the lines of sight. The Besançon model assumes axisymmetric stellar distribution, i.e. no azimuthal density contrasts (such as spiral arms and interarm regions) are applied. Therefore, GALAXIA+Besançon generates substantially more stars at low distances.

5.4.2 Observable spiral arm kinematics

In this section, we examine if the possible kinematic signatures of co-rotating transient and recurrent spiral arms identified in Kawata et al. (2014b) will be visible in the *Gaia* data, even given the dust extinction in the disc and *Gaia's*

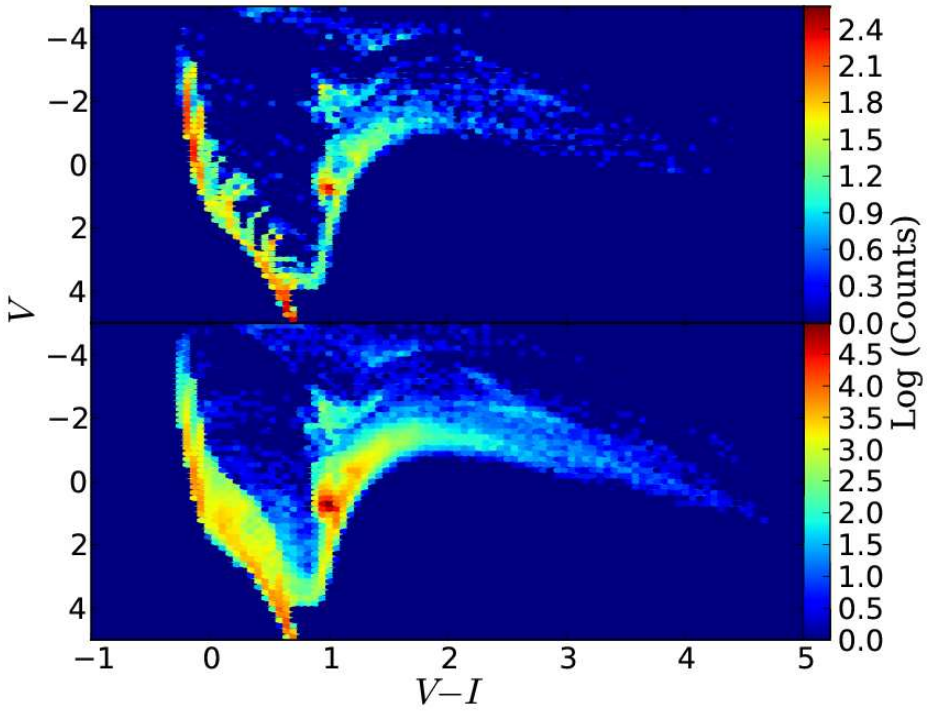

Fig. 5.4: Intrinsic CMD for stars generated by SNAPDRAGONS from particles within a square region of $\pm 2^{\circ}$ (upper) and $\pm 5^{\circ}$ (lower) around $(l, b) = (90^{\circ}, 0^{\circ})$. Stars with apparent magnitude of $V \leq 16$ mag only are included.

science performance accuracy. A detailed analysis of the kinematics themselves was the focus of Kawata et al. (2014b), while this work is concerned with the visibility of this kinematic structure in the *Gaia* data. We examine the rotational velocities of the stars in the catalogue for different distances, because in Kawata et al. (2014b) we found that the rotation velocity is most affected by the transient co-rotating spiral arm. Then, we calculated the probability density function (PDF) of the rotation velocity of stars behind and in front of the spiral arm using Kernel Density Estimation (KDE), which we are using as a desirable alternative to histograms (e.g. Wasserman 2006).

Fig. 5.5 shows a smoothed contour plot of the Galactocentric rotational velocity against observed heliocentric distance for particles and stars within a square region of $\pm 5^{\circ}$ around $(l, b) = (90^{\circ}, 0^{\circ})$ (left), $(l, b) = (120^{\circ}, 0^{\circ})$ (middle) and $(l, b) = (150^{\circ}, 0^{\circ})$ (right). This compares the kinematics of the underlying N-body model (upper) with the stellar catalogue generated with SNAPDRAG-

ons, before (middle) and after (lower) the addition of the errors from the *Gaia* science performance estimates. Owing to the high percentage of low-mass and luminosity stellar types which would dominate the selected region and saturate the plot at small distances, we have made cuts to our sample to visualise the underlying kinematic structure from the stellar catalogue. We have first cut the sample of stars in all three lines of sight with absolute magnitude, $M_V \leq -1$ mag, calculated from the apparent magnitude V and observed distance $d_{\rm obs}$, assuming the dust extinction is known. We then cut with $\sigma_{v_{\rm los}}/(v_{\rm los} \times d_{\rm obs}) \leq 0.015$ kpc^{-1} to select the stars with lower error in the line-of-sight velocities at a smaller distance to generate similar quantities of data at different distance scales. This selection function selects bright stars which are a mix of young blue stars and old red stars. The number of stars selected are 11,903 for $(l, b) = (90, 0)$, 12,989 for $(l, b) = (120, 0)$ and 5,794 for $(l, b) = (150, 0)$. This is purely for illustration purposes and we are not suggesting that this is a desirable selection function with which to analyse the kinematics. The upper panels of Fig. 5.5 show the different kinematic structure in the N-body model at the different lines of sight. These are the same data as those shown in the top panels of Figure 4 in Kawata et al. (2014b). Note that the density colour scale for the N-body data is different from the stellar data in the middle and lower panels.

The middle row of panels of Fig. 5.5 show the velocities of the selected stars, which appear slightly different from those of the N-body data owing to the selection function. While the generated stars have the same position and velocities as their parent N-body particles, the dust extinction, the magnitude cut of $V \leq 16$ mag and the above mentioned selection of bright stars with the velocity error limit are applied. Therefore, the middle panels are different from the top panels. Especially, owing to the strong extinction in the plane, not all the N-body data in the top panel are 'visible' in the selected stars in the middle panel. While the general shape of the distribution has been recovered, at $(l, b) = (90^{\rm o}, 0^{\rm o})$ (middle left), the fast rotating stars within the arm dominate the density scale and wash out the rest of the plot slightly. At $(l, b) = (120^{\rm o}, 0^{\rm o})$ (middle), although there is some saturation around 220

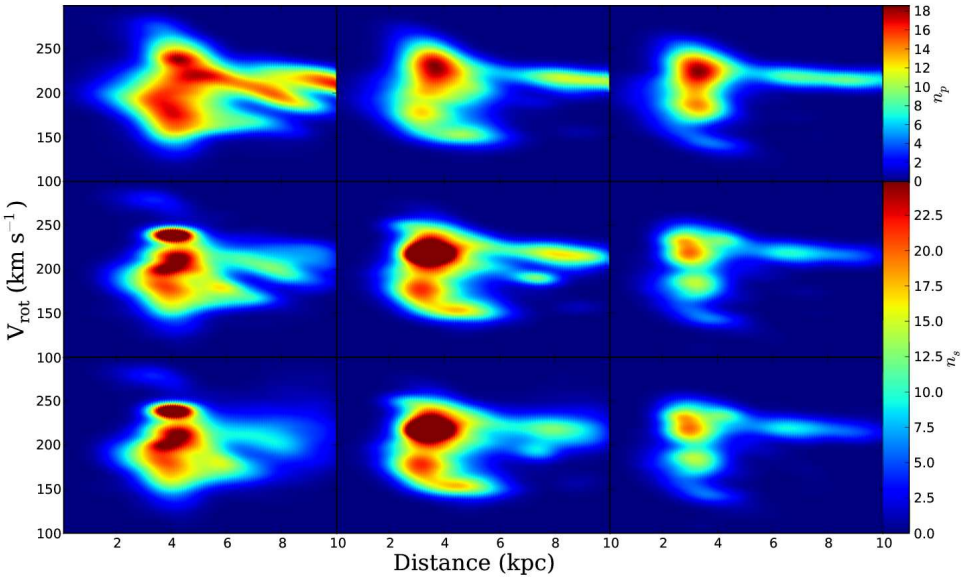

Fig. 5.5: Smoothed linear scale contour plot of heliocentric distance against Galactocentric rotation velocity of simulation particles (upper), selected SNAPDRAGONS stars (middle) and selected SNAPDRAGONS stars observed with *Gaia* error (lower) within a square region of $\pm 5^{\circ}$ around $(l, b) = (90^{\circ}, 0^{\circ})$ (left), $(l, b) = (120^{\circ}, 0^{\circ})$ (middle) and $(l, b) = (150^{\circ}, 0^{\circ})$ (right). For the SNAPDRAGONS stars (middle and lower panels), a limited selection of $M_V \leq -1$ mag calculated using V and $d_{\rm obs}$ and assuming a known extinction, along with $\sigma_{v_{\rm r}}/(v_{\rm r} \times d_{\rm obs}) \leq 0.15$ is shown to avoid overly dense populations of fainter stars at smaller distances. This is to visualise the data set, and these faint stars contribute to the subsequent analysis. The colour scale shows number density of N-body particles (upper) and SNAPDRAGONS stars (middle and lower) in arbitrary units.

km s^{-1}, the kinematic structure is clearly visible and is a good match to the particle data. Similarly at $(l, b) = (150^{\circ}, 0^{\circ})$ (middle right), despite the lower number of counts, the kinematic structure is clearly shown.

The lower panels of Fig. 5.5 show the error affected rotation velocity and distance for the selected stars taking *Gaia* science performance estimates into account. The rotation velocity is calculated from the observed parallax, proper motion and line-of-sight velocities. At $(l, b) = (90^{\circ}, 0^{\circ})$ (lower left), the shape of the distribution remains relatively unchanged, with the main loss in accuracy occurring around $d_{\rm obs} \sim 7 - 10$ kpc. The recovery of the kinematic structure around the spiral arm around $d_{\rm obs} \sim 4$ kpc remains almost identical

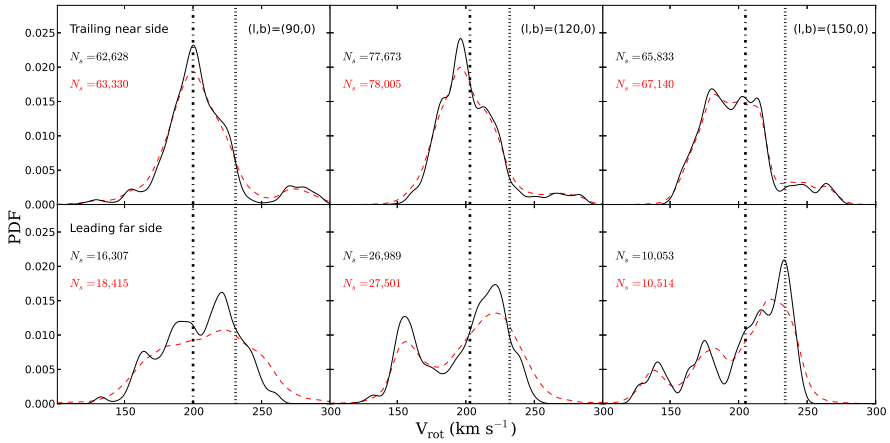

Fig. 5.6: Comparison of the distribution of Galactocentric rotational velocities for the stars generated by SNAPDRAGONS within a square region of $\pm 5^{\circ}$ around $(l, b) = (90^{\circ}, 0^{\circ})$ (left), $(l, b) = (120^{\circ}, 0^{\circ})$ (middle) and $(l, b) = (150^{\circ}, 0^{\circ})$ (right) in the trailing near side (upper) and leading far side (lower) of the spiral arm which meet the $V \leq 16$ mag selection limit when applying the reduction in the extinction with equation (5.1). The black solid curve shows the true velocities, and the red dashed curve shows the distribution once the *Gaia* errors have been applied. The number of stars, $N_{\rm s}$, used to construct the PDFs is given in each panel for the velocities without (black) and with (red) the inclusion of error. The vertical lines show the circular velocity (dotted) and the mean rotation velocity (dash-dotted) at the radius of the spiral arm.

to the case without observational errors. At $(l, b) = (120^{\circ}, 0^{\circ})$ (lower middle), the visible loss of accuracy is again in the outer region of $d_{\rm obs} \sim 7 - 10$ kpc, with the region containing the spiral arm remaining very similar to that of the error-free case. At $(l, b) = (150^{\circ}, 0^{\circ})$ (lower right), the entire distribution remains very similar to the middle right panel, the case without *Gaia*-like observational errors.

Fig. 5.6 shows the PDFs, with a KDE bandwidth of 4 km s^{-1}, for the rotational velocity of the stars in the catalogue within a square region of $\pm 5^{\circ}$ around $(l, b) = (90^{\circ}, 0^{\circ})$ (left), $(l, b) = (120^{\circ}, 0^{\circ})$ (middle) and $(l, b) = (150^{\circ}, 0^{\circ})$ (right) in the trailing near side, between 1 and 2 kpc closer than the centre of the arm (upper) and leading far side between 1 and 2 kpc further than the centre of the arm (lower) using the 3D Schlegel map with the extinction reduced with equation (5.1). These heliocentric observed distance bins were

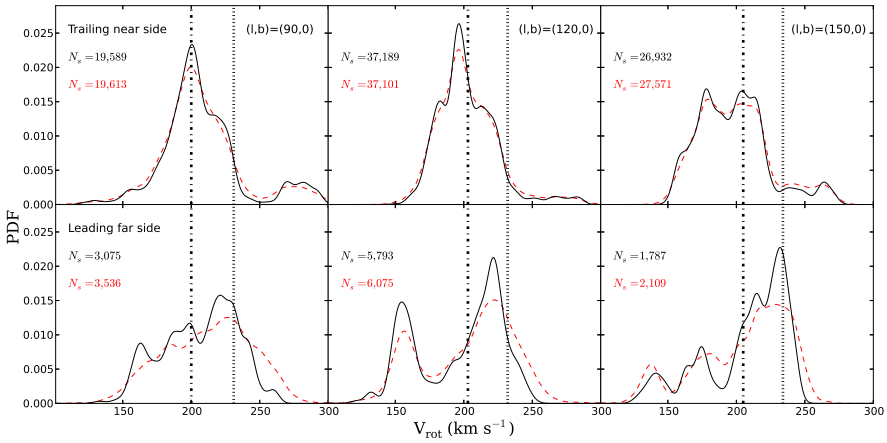

Fig. 5.7: Same as Fig. 5.6, but for the results using the 3D Schlegel map without the reduction in the extinction given by equation (5.1).

chosen as they show the discussed structure most clearly. We also performed the analysis on bins which are closer to the centre of the arm. The same features are present, but they are less clear. The number of stars, $N_{\rm s}$, used to construct the PDFs is given in each panel of Fig. 5.6 for the velocities without (black) and with (red) the inclusion of error. The centre of the arm was determined to be at $d = 4.0$ kpc at $(l, b) = (90^{\rm o}, 0^{\rm o})$, $d = 3.4$ kpc at $(l, b) = (120^{\rm o}, 0^{\rm o})$ and $d = 3.3$ kpc at $(l, b) = (150^{\rm o}, 0^{\rm o})$. Note that Fig. 5.6 uses all the stars with $V \leq 16$ mag, not applying the selection function used for illustration purposes in Fig. 5.5. At all three lines of sight, Fig. 5.6 shows a clear difference in the distribution of velocities for the 'true' data (black solid) when comparing the different observed distances, as shown in Kawata et al. (2014b). This is a positive outcome considering the loss of data from the dust extinction. When comparing the 'true' (black solid) stellar catalogue data with the stellar data taking into account dust extinction and *Gaia*'s expected errors (red dashed), a general smoothing out of the structure is evident in the 'observed' data. The upper panels of Fig. 5.6 showing the trailing near side of the arm show very similar PDFs when comparing the true and observed stellar data, whereas the lower panels showing the leading far side show an information loss, especially at $(l, b) = (90^{\rm o}, 0^{\rm o})$, where the three peaks are no longer resolved. This is to be expected because of the higher distances, and

therefore additional extinction. However, at $(l, b) = (120^{\circ}, 0^{\circ})$ and $(150^{\circ}, 0^{\circ})$ even on the far side of the spiral arm the structure within the distribution is still clearly visible.

Fig. 5.7 shows the same as Fig. 5.6, using the higher extinction values of the 3D Schlegel map without the reduction term of equation (5.1). The features in Fig. 5.7 remain very similar to Fig. 5.6 despite the difference in extinction. There is a significant reduction in the number of observed stars for the 3D Schlegel map without the reduction in extinction. Therefore, it is important to note that the assumed extinction model will have a large effect on the mock catalogue. However, it is encouraging for the interpretation of the *Gaia* data that the same peculiar kinematic features are visible with this higher extinction estimate. Owing to the similarity between Figs. 5.6 and 5.7, the subsequent discussion will focus on Fig. 5.6.

When comparing the 'observed' data in Fig. 5.6 in front and behind the spiral arms, we see a clear difference in the PDF at all three lines of sight. In each case, the PDF in the trailing near side of the spiral arm forms a single central peak similar to the mean rotation velocity, with a small tail towards faster rotation velocities, whereas the leading far side of the spiral arm shows a broader distribution of velocities with a peak velocity faster than the peak for the trailing near side. The difference is particularly apparent at $(l, b) = (120^{\circ}, 0^{\circ})$ where the leading far side shows two clear peaks, one faster and one slower than the single peak in the trailing near side. This bi-modal distribution can also be seen in the lower middle panel of Fig. 5.5 between 4.39 and 5.39 kpc (although note that Fig. 5.5 uses a different selection function). Also at $(l, b) = (150^{\circ}, 0^{\circ})$, the single broad peak in the trailing near side is easily distinguishable from the leading far side which shows three peaks. These three peaks are also partially visible in the lower right panel of Fig. 5.5 between 4.29 and 5.29 kpc. These features all match those observed in Kawata et al. (2014b) despite the addition of dust extinction and observational errors to the data.

In general, as shown in Grand et al. (2014), the stars in the leading side rotate faster as they tend to be at pericentre phase and migrating inwards, and

stars in the trailing side rotate slower as they tend to be at apocentre phase and migrating outwards. This explains the single large peak in the trailing side, and the largest peak on the leading side which has a higher rotational velocity than the single peak on the trailing side as shown in Fig. 5.6. However, when the transient spiral arm starts forming, stars which are close to the arm on the trailing side and are close to the pericentre phase are accelerated towards the arm, passing through and then slowing down as they reach the apocentre on the leading side as discussed in Kawata et al. (2014b). These stars correspond to the 'slower' peaks visible in the lower panels of Fig. 5.6. Similarly, the stars which are close to the arm and close to the apocentre phase on the leading side are decelerated by the arm, and are overtaken by the arm. Then they are accelerated again by the arm once they are on the trailing side at pericentre phase, which corresponds to the small tail present at high velocities in the upper panels of Fig. 5.6. The difference in the rotation velocity distribution between the leading and trailing side of the spiral arm seen in Figs. 5.5 and 5.6 is that the latter population is smaller than the former. It appears that it is easier for stars to escape from the arm on the leading side than the trailing side. From our analysis of N-body simulations, this appears to be a common feature of transient and co-rotating spiral arms.

Comparetta & Quillen (2012) propose that the radial overlap of multiple longer lived patterns moving at different pattern speeds can reproduce the transient spiral features, which when strong enough can lead to radial migration away from the corotation radius associated with co-rotating spiral arms as seen, for example in Grand et al. (2012a,b). In such a scenario, the spiral arm features are co-rotating, which may give rise to the coexistence of many inner and outer Lindblad resonances in a range of radii and lead to the features visible in Figs. 5.5−5.7. However, further analysis of the spiral arms in N-body simulations is required before drawing firm conclusions on the mechanism that generates such kinematic signatures. We will address this in future studies.

From Figs. 5.5−5.7, we find that *Gaia's* scientific accuracy ought to be sufficient to examine the kinematic structure of the nearby spiral arms in the Milky Way, even on the far side of the arm. Figs. 5.6 and 5.7 both show clear

differences in the kinematics in the leading and trailing sides of the spiral arm, notably the difference in the number and locations of the peaks, and the small high-velocity tail present in the trailing near side. The comparison between the middle and lower panels of Fig. 5.5 shows little difference, implying that the observational error from *Gaia* will have limited effect on our ability to study the kinematics of the spiral arms. Further examination of galaxy models constructed using the different theories of spiral arm formation will be essential to determine the distinct kinematic signatures of each theory.

5.5 Summary

We observed our N-body/SPH simulation of a Milky Way-like barred spiral galaxy to create a mock *Gaia* stellar catalogue, with particular interest in the stellar kinematics in and around the spiral arms. We focused on the same three lines of sight in the disc plane as Kawata et al. (2014b), $(l, b) = (90^{\rm o}, 0^{\rm o}), (120^{\rm o}, 0^{\rm o})$ and $(150^{\rm o}, 0^{\rm o})$ and analysed the galactocentric rotational velocities of the selected stars as a function of the distance from the observer. In agreement with existing literature on N-body spiral galaxy simulations, the spiral arm features seen in the stellar mass in our model are transient, recurrent and co-rotating, i.e. the spiral arm is rotating at the circular velocity of the stars at the selected lines of sight.

We show that the structure in the kinematics identified in Kawata et al. (2014b) remains visible after the inclusion of dust extinction and observational errors based upon *Gaia* science performance estimates. Although the inclusion of these observational effects makes the trends less clear, they are still observable in the mock *Gaia* data in front of and behind the spiral arm. The structure on the trailing near side is relatively unchanged, whereas the structure on the leading far side is, naturally, more affected, although the bi-modal (or more) and broader distribution of the rotation velocities is still clearly visible. Because we believe that these kinematic signatures are indications of transient and co-rotating spiral arms owing to the corotation resonance at all radii, we predict they should be visible in the *Gaia* data at different longitudes if the Milky Way's Perseus arm is also a transient and co-rotating spiral arm.

Encouraged by the success of this study, we intend to repeat the analysis with simulated galaxies which use different theories of spiral structure formation, for example test particle simulations (e.g. Minchev & Quillen 2008; Minchev et al. 2010; Minchev & Famaey 2010; Faure et al. 2014; Antoja et al. 2014) and N-body simulations with a fixed spiral arm potential (e.g. Wada et al. 2011). From these analyses, we expect to make predictions of the kinematic signatures of different spiral arm theories, which can be tested by the *Gaia* stellar catalogue (see Section 6.2).

Chapter 6

Conclusions & further work

6.1 Thesis conclusions

This thesis describes a novel M2M algorithm, PRIMAL, designed to create a dynamical model of the Milky Way from *Gaia*-like observational data. Traditional M2M algorithms work in a fixed potential, and alter particle weights during the modelling. PRIMAL applies the M2M method to a live N-body model, altering the particle masses and the potential which is calculated self-consistently. This naturally leads to structure formation, allowing us to reproduce non-axisymmetric structure such as a bar and spiral arms. Previous M2M algorithms bin the target data, lowering the effective resolution of the observations, whereas PRIMAL compares the N-body model with the observables at the position of each target star. By retaining individual stellar observables as constraints, we can reproduce small-scale phase-space structure and are not restricted by the bin size. This, for example, allows us to study the structure and velocity field of the spiral arms and bar. Additionally, we can take into account the observational errors of individual stars. Previous studies (e.g. de Lorenzi et al. 2007) applied the mean error, which is valid for extragalactic observations, but is not suitable for the Galactic data where the error of each star depends on its stellar type, magnitude and position on the sky.

In Chapter 2, we describe the proof of concept for PRIMAL. We detail the M2M equations and the new particle-by-particle adaptation of the M2M method, which is designed to work with *Gaia* (and other upcoming stellar survey) data. This initial version contained two important innovations over

existing M2M algorithms. Firstly, while previous algorithms used fixed bins to calculate the 'observables', we use a spline kernel often used in smooth particle hydrodynamics (SPH) to compare individual stellar data. This effectively increases the resolution of our constraints from the number of bins times the number of constrained parameters to the number of observed stars times the number of constrained parameters. Secondly, we apply our algorithm to a self-gravitating N-body system, whereas previous algorithms use test particle simulations under a fixed potential. In a test particle M2M, they cannot change orbits, and thus, if the initial model orbits are not representative of the target, they cannot well reproduce the target data. This is not the case for an N-body system, which allows orbits to change and has the additional advantage of naturally leading to non-axisymmetric structure formation. Additionally, because the potential is calculated self-consistently, once the system has reached its final state the disc potential can in theory be recovered along with the structure and dynamics.

In Chapter 2, we show that our initial M2M algorithm can recreate a featureless axisymmetric disc system created by an N-body simulation in a known dark matter halo potential, with no error in the observables, starting from an initial disc model with a different scale length. We also demonstrate that our algorithm can be applied to data sets only using observables at the target particles within a $R = 10$ kpc sphere from the assumed position of the observer, which is located at $R_{\rm G} = 8$ kpc from the galactic centre, with a good degree of success.

In Chapter 3, we show that PRIMAL can be applied to non-axisymmetric systems by rotating the reference frame of the model galaxy to match the target at each timestep. We introduce the maximum likelihood method for the velocity constraints, as shown in de Lorenzi et al. (2008), which allows us to take into account individual errors for different stars and then apply PRIMAL to four different target N-body simulated galaxies. We recreate the size and shape of the bar of the target galaxy, along with its pattern speed, to a good degree of accuracy. For example, for our fiducial case the target galaxy has a pattern speed of the bar of $\Omega_{\rm t,p} = 27.5$ km s^{-1}kpc^{-1} and our M2M

model results in a pattern speed of $\Omega_{\rm p} = 27.9$ km s^{-1}kpc^{-1}. We also explore the effects of assuming a different bar angle for the model galaxy from the bar angle of the target galaxy, and we find minimal effect, at least in our simplified case. This is a little concerning, as currently PRIMAL does not appear well suited to constrain the bar angle of the Milky Way. However, as stated in Chapter 3, testing with more realistic mock data is needed before we can fully asses the ability of PRIMAL to constrain the angle of the bar in the case of the Milky Way. If we determine that PRIMAL can not be used to determine the bar angle, then we can use an assumed angle from different studies and study more global structures of the Galactic disc, including the pattern speed of the bar.

In Chapter 4, we modify PRIMAL to recreate a target galaxy by comparing the target and model in *Gaia* observable space $(\alpha, \delta, \pi, \mu_\alpha, \mu_\delta, v_{\rm r})$. We create mock *Gaia* observations of tracer populations of M0 giant stars and red clump stars from our N-body target galaxy, taking into account the dust extinction in the Milky Way and the expected *Gaia* errors. In Chapter 4, we assume for the moment that each N-body target particle is represented by one tracer star, and then calculate the extinction upon it from the 3D galactic extinction map from GALAXIA (Sharma et al. 2011). We then modify the apparent magnitude of the tracer by the extinction value and then calculate a *Gaia*-like error on the parallax and velocity components using the code to estimate the *Gaia* error as a function of brightness, colour and sky position. The code to estimate *Gaia* errors is provided by Mercè Romero-Gómez (e.g. Romero-Gómez et al. 2015). We show that PRIMAL can recreate a target N-body galaxy to a reasonable degree of accuracy, despite the lack of accurate target data. Again there is an excellent recovery of the pattern speed of the bar. For our fiducial case, the target galaxy has a pattern speed of $\Omega_{\rm t,p} = 28.9$ km s^{-1}kpc^{-1} and our M2M model creates a bar with $\Omega_{\rm p} = 28.6$ km s^{-1}kpc^{-1}.

In Chapter 5, we generate a more realistic mock *Gaia* stellar catalogue from N-body simulated disc galaxies. We have developed a population synthesis code, called SNAPDRAGONS, which samples a stellar catalogue from $N-$body particles. SNAPDRAGONS takes into account the age and metallicity

of the particles and generates a *Gaia* mock stellar catalogue with errors based upon *Gaia's* science performance estimates. Mock *Gaia* data generated from known galaxy models by SNAPDRAGONS enables us to test whether particular features of the known model will be visible in the *Gaia* stellar catalogue. For example, there is still disagreement on how spiral arms form and evolve. It is in debate whether they are one of the variations of density wave theory (e.g. Lin & Shu 1964) or if they are material arms (e.g. Grand et al. 2012a). Observations of the Milky Way's spiral arms from *Gaia* may help us to resolve this debate, owing to the large area of the disc traced by the observable stars and the unprecedented accuracy of *Gaia's* astrometric measurements. In Chapter 5, we use SNAPDRAGONS to make mock *Gaia* observations from an N-body/SPH model of a barred disc galaxy similar in size to the Milky Way used in Kawata et al. (2014b). We examine the kinematics around a nearby spiral arm in a similar position to the Milky Way's Perseus arm at three lines of sight in the disc plane, $(l, b) = (90^{\rm o}, 0^{\rm o}), (120^{\rm o}, 0^{\rm o})$ and $(150^{\rm o}, 0^{\rm o})$. In Kawata et al. (2014b), we show that there are peculiar velocity features associated with co-rotating spiral arms which have the corotation resonance at every radii, because N-body simulations have co-rotating, transient spiral arms (e.g. Grand et al. 2012a,b). We determine that the kinematic signatures identified in Kawata et al. (2014b) are still visible in the *Gaia* data despite the observational error and dust extinction, and thus if the Milky Way's Perseus arm contains the signatures of co-rotating spiral arms identified in Kawata et al. (2014b), they should be visible in the *Gaia* data around the Galactic longitude $90^{\rm o} < l < 150^{\rm o}$ at least. This emphasises the usefulness of the comparison of *Gaia* data with predictions from mock data generated from N-body simulations.

In summary, in this thesis we have shown the development of a new M2M algorithm called PRIMAL, which is able to recreate a target disc galaxy model from mock observations of a single stellar population, taking into account extinction and *Gaia* level errors. We have shown that PRIMAL can recover non-axisymmetric structure including a boxy/barred bulge, and is particularly effective in recovering the pattern speed of the bar even with the in-

complete data set. Further work is needed to train PRIMAL on more realistic mock *Gaia* data in order to fully assess its capabilities. We have developed a populations synthesis code, SNAPDRAGONS, which creates a *Gaia* mock stellar catalogue of stars brighter than a chosen magnitude from N-body simulations. By analysing a *Gaia* mock catalogue generated from a N-body galaxy with co-rotating transient spiral arms, we show that the peculiar kinematic signatures of the co-rotating spiral arms will be visible in the *Gaia* data, if the Perseus arm is also a co-rotating spiral arm.

Models created by PRIMAL and mock data created by SNAPDRAGONS can also be useful for other researchers and studies beyond our own research. For example, the 'Gaia Challenge' collaboration[1], a modelling technique comparison project aimed mainly at being prepared for the *Gaia* data, has used N-body simulation data presented in this thesis (e.g. Chemin 2014). Comparing dynamical models by PRIMAL with other dynamical modelling techniques by other research groups, such as action based methods or Jeans modelling, will provide valuable insight into the strengths and weaknesses of different methods. The Gaia Challenge is an important community effort to understand the characteristics of different modelling techniques, and mock *Gaia* catalogues created by SNAPDRAGONS could be used as test data in future workshops.

6.2 Further work

The work in this thesis has opportunity for further study in multiple directions. Both PRIMAL and SNAPDRAGONS are useful tools to help study the Galactic structure and dynamics from the *Gaia* data. PRIMAL is ready to be applied to the *Gaia* data, if we can select M0III (or red clump) stars as tracers. This requires us to either assume the ratio between mass and the percentage of M0III stars, or leave it as a free parameter as done in Portail et al. (2015). PRIMAL should be further improved to be applied to the successive *Gaia* data releases (see Section 1.3.5), and will culminate in a next generation dynamical model of the Milky Way, which will be constructed from the final catalogue.

In Section 6.2.1, we discuss the future development and application of PRI-

[1] http://astrowiki.ph.surrey.ac.uk/dokuwiki/doku.php

MAL, and in Section 6.2.2, we discuss the future development and application of SNAPDRAGONS.

6.2.1 Future development of PRIMAL

As shown in Hunt & Kawata (2014a), we have introduced the resampling of N-body model particles whose masses drift too far from the mean particle mass and we are currently testing this further. We set a limit on how large or small these particle masses can become. We then delete any particle whose mass becomes lower than the lower limit, $m_{\rm min}$, to save on computational time, and split any particle whose mass becomes higher than the upper limit, $m_{\rm max}$, to prevent a single massive particle dominating local dynamics. The particles with $m_i > m_{\rm max}$ are split into the appropriate number of particles to keep their mass close to the mean particle mass, $\bar{m}$. The parent particle is retained with decreased mass, and generated particles are spaced randomly within the smoothing length of the kernel. All generated particles share all other properties with the parent particle including its velocity. This maintains a more even mass distribution around $\bar{m}$. We may replace the prior, $\hat{m}$, in the weight entropy regularisation term in the M2M method with $\bar{m}$, resulting in regularisation around a flexible prior, similar to the Moving Prior Regularisation described in Morganti & Gerhard (2012, see Section 1.6). Interestingly, we find that we can remove the weight entropy regularisation term and regularise the model with the resampling alone. This resampling scheme is currently undergoing testing, and we have yet to explore which parameters and method of regularisation work best with the resampling scheme.

An essential step in the development of PRIMAL, is to utilise multiple populations of stars simultaneously as constraints for PRIMAL, instead of the single tracer populations used in Chapter 4. Mock stellar data generated by SNAPDRAGONS from known N-body systems will be used as a more realistic set of target galaxy observational data to validate PRIMAL. Initially, it will be tested using distinct known tracer populations, e.g. F, G, K dwarfs and K, M giants, and then stars of each stellar population will be selected from the full SNAPDRAGONS catalogue. For example, the sample may be divided into dwarfs and giants in the Hertzsprung-Russell diagram (or the $T_{\rm eff} - \log_g$ plane)

via the methodology presented in Ciardi et al. (2011). The tracer populations will be selected by examining which stellar types are more clearly identified from $T_{\rm eff}$ and $\log_g$ measured by *Gaia's* spectrophotometer data, and which stellar populations effectively provide constraints for PRIMAL to model the Galactic disc. Once PRIMAL has the ability to use observable data from multiple stellar populations, it can be used to reproduce the distribution of stellar populations within the Milky Way. Along the same lines, it may be possible to use the metallicity of the target stars (e.g. [Fe/H]) as an observable using the likelihood equation. Therefore, PRIMAL is potentially able to reproduce the age-metallicity distribution at different regions in the Milky Way disc. This result will be a key piece of chemodynamical information to unravel the formation history of our Galaxy.

Additionally, the current SPH kernel used to calculate each individual star's contribution to the observables is not an ideal choice owing to its spherically symmetric nature. In actuality, the distance error in the line-of-sight owing to the parallax error (σ_π) can be large, whereas there is almost no error in the position ($\sigma_\alpha, \sigma_\delta$). Therefore, an ellipsoidal kernel elongated along the line-of-sight when the distance error is larger than the resolution of the model particles may yield superior estimates of the observables than the current kernel.

It is also important to explore the effect the dark matter halo on the recovery of the target data. The use of a known fixed halo is a major assumption in the current model which must be relaxed. Initially, the profiles of fixed dark matter haloes will be varied to determine their contribution to the fit, and how much degeneracy will be present in the recovery of the target galaxy, when an incorrect halo is assumed. The use of a live dark matter halo where the dark matter halo is described with N-body particles will also be explored, which, through momentum exchange with the stellar disc, may have a significant effect on the model. It is possible, although currently unexplored, that the dark matter halo may be modified directly during the modelling by changing the mass of the dark matter particles with additional observational constraints, e.g. the HI rotation curve and the motion of stars in the halo and streams.

If this is possible, then it would allow us to derive the best fit structure of the dark matter halo simultaneously with the structure of the Galactic disc. Altering the dark matter halo simultaneously is an ambitious task, and to our knowledge has yet to be attempted in M2M.

6.2.2 Further applications of SNAPDRAGONS

Chapter 5 shows the initial development of SNAPDRAGONS and one example of how mock *Gaia* data can be used to test theories of spiral arms. The exploration of co-rotating spiral arms shown in Chapter 5 is continuing with a comparison of the observable signatures of different theories of spiral arm structure. For example, in Kawata et al. (2015), we compare the stellar motion around the spiral arms in the *Gaia*-data-like mock catalogue generated in Chapter 5 with a mock catalogue generated from the test particle simulation in Faure et al. (2014) which models density-wave like spiral arms by considering a rigidly rotating spiral arm potential. Kawata et al. (2015) show a clear difference between the two theories. Fig. 6.1 (Figure 1 in Kawata et al. 2015) shows the Galactic rotation velocity distribution for stars with $V \leq 16$ mag generated with SNAPDRAGONS in the range of $85^{\rm o} \leq l \leq 95^{\rm o}$ and $-5^{\rm o} \leq b \leq 5^{\rm o}$ for the N-body simulation analysed in Chapter 5 (left) and the test particle simulation of Faure et al. (2014) (right). The blue lines show the velocity distribution in front of the spiral arm, and the red lines show the velocity distribution behind the spiral arm, both taking into account dust extinction and *Gaia*-level observational errors as described in Chapter 5. Fig. 6.1 shows a clear difference between the co-rotating spiral arms in the N-body model (left) and the density wave like spiral arms in the test particle simulation (right). The difference in front of the spiral arms is particularly strong between the two theories. This shows the value of such a comparison and more galaxy models will be examined in such a way. We will make predictions from simulations with different underlying theories of spiral arm formation, and determine the differences which will be visible in the *Gaia* data, allowing us to constrain the true nature of the Milky Way's spiral arms.

In closing, studies as described in this thesis are important preparation for the upcoming *Gaia* data. In this thesis we have shown the potential of

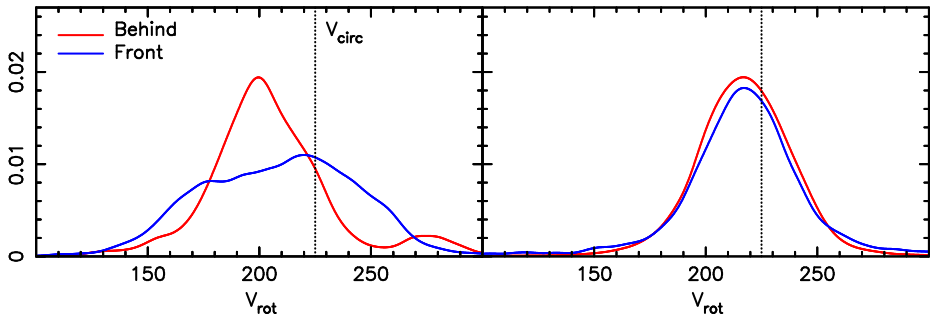

Fig. 6.1: Galactic rotation velocity distribution for stars with $V \leq 16$ mag generated with SNAPDRAGONS in front of (blue) and behind (red) a spiral arm in an N-body simulation (left) and a test particle simulation (right) taking into account dust extinction and *Gaia*-like errors (from Figure 1 in Kawata et al. 2015).

developing modelling techniques designed for the *Gaia* data. We still have over a year before the first *Gaia* data release, and seven years before the final full data release. This gives us ample opportunity to maximise the potential of PRIMAL and SNAPDRAGONS, and develop additional new modelling techniques to fully exploit the *Gaia* data. Modelling techniques developed for *Gaia* will likely be applicable to future survey data (e.g. LSST). We are entering a golden age of Milky Way science, and *Gaia* is only the beginning.

Bibliography

Aarseth S. J., 1963, MNRAS, 126, 223

Aarseth S. J., 1966, MNRAS, 132, 35

Abadi M. G., Navarro J. F., Steinmetz M., Eke V. R., 2003, ApJ, 597, 21

Abedi H., Mateu C., Aguilar L. A., Figueras F., Romero-Gómez M., 2014, MNRAS, 442, 3627

Alcock C. et al., 2000, ApJ, 541, 734

Alfaro Navarro E. J., Gallego Calvente A. T., Zapatero Osorio M. R., 2011, in Stellar Clusters and Associations: A RIA Workshop on Gaia, p. 0

Allende Prieto C., Koesterke L., Ludwig H.-G., Freytag B., Caffau E., 2013, A&A, 550, A103

Allende Prieto C. et al., 2008, Astronomische Nachrichten, 329, 1018

Antoja T. et al., 2014, A&A, 563, A60

Arce H. G., Goodman A. A., 1999, ApJL, 512, L135

Athanassoula E., 2013, Bars and secular evolution in disk galaxies: Theoretical input, Falcón-Barroso J., Knapen J. H., eds., p. 305

Athanassoula E., Misiriotis A., 2002, MNRAS, 330, 35

Aumer M., Binney J. J., 2009, MNRAS, 397, 1286

Baba J., Saitoh T. R., Wada K., 2010, PASJ, 62, 1413

Baba J., Saitoh T. R., Wada K., 2013, ApJ, 763, 46

Backer D. C., Sramek R. A., 1999, ApJ, 524, 805

Bahcall J. N., Soneira R. M., 1980, ApJS, 44, 73

Bahcall J. N., Soneira R. M., Schmidt M., 1983, ApJ, 265, 730

Bailer-Jones C. A. L., 2011, MNRAS, 411, 435

Bailer-Jones C. A. L. et al., 2013, A&A, 559, A74

Baranne A., Mayor M., Poncet J. L., 1979, Vistas in Astronomy, 23, 279

Barnes D. J., Kawata D., Wu K., 2012, MNRAS, 420, 3195

Barnes J., Hut P., 1986, Nature, 324, 446

Beesley D. E., 1985, Irish Astronomical Journal, 17, 98

Belokurov V. et al., 2006, ApJL, 642, L137

Benjamin R. A. et al., 2005, ApJL, 630, L149

Bensby T. et al., 2011, A&A, 533, A134

Bensby T., Feltzing S., Oey M. S., 2014, A&A, 562, A71

Berger M. J., Oliger J., 1984, Journal of Computational Physics, 53, 484

Bertelli G., Bressan A., Chiosi C., Fagotto F., Nasi E., 1994, A&AS, 106, 275

Binney J., 2012a, ArXiv e-prints: 1207.4910

Binney J., 2012b, MNRAS, 426, 1328

Binney J., 2013, Dynamics of secular evolution, Falcón-Barroso J., Knapen J. H., eds., p. 259

Binney J., Gerhard O., Spergel D., 1997, MNRAS, 288, 365

Binney J., Kumar S., 1993, MNRAS, 261, 584

Binney J., McMillan P., 2011, MNRAS, 413, 1889

Bishop J. L., 1987, ApJ, 322, 618

Bissantz N., Debattista V. P., Gerhard O., 2004, ApJL, 601, L155

Bissantz N., Gerhard O., 2002, MNRAS, 330, 591

Bland-Hawthorn J., Krumholz M. R., Freeman K., 2010, ApJ, 713, 166

Boggess N. W. et al., 1992, ApJ, 397, 420

Bottema R., 2003, MNRAS, 344, 358

Bovy J., 2014, ApJ, 795, 95

Bovy J., 2015, ApJS, 216, 29

Bovy J. et al., 2012a, ApJ, 759, 131

Bovy J. et al., 2014, ApJ, 790, 127

Bovy J., Rix H.-W., 2013, ApJ, 779, 115

Bovy J., Rix H.-W., Hogg D. W., 2012b, ApJ, 751, 131

Bovy J., Rix H.-W., Hogg D. W., Beers T. C., Lee Y. S., Zhang L., 2012c, ApJ, 755, 115

Bovy J., Rix H.-W., Liu C., Hogg D. W., Beers T. C., Lee Y. S., 2012d, ApJ, 753, 148

Brook C. B., Kawata D., Gibson B. K., Freeman K. C., 2004, ApJ, 612, 894

Brunthaler A. et al., 2011, Astronomische Nachrichten, 332, 461

Burbidge E. M., Burbidge G. R., 1959, ApJ, 130, 20

Bureau M., Aronica G., Athanassoula E., Dettmar R.-J., Bosma A., Freeman K. C., 2006, MNRAS, 370, 753

Burstein D., 1979, ApJ, 234, 829

Busonero D., 2011, in IAU Symposium, Vol. 276, IAU Symposium, Sozzetti A., Lattanzi M. G., Boss A. P., eds., pp. 371–375

Buta R., Vasylyev S., Salo H., Laurikainen E., 2005, AJ, 130, 506

Cabrera-Lavers A., González-Fernández C., Garzón F., Hammersley P. L., López-Corredoira M., 2008, A&A, 491, 781

Cabrera-Lavers A., Hammersley P. L., González-Fernández C., López-Corredoira M., Garzón F., Mahoney T. J., 2007, A&A, 465, 825

Cacciari C., 2009, Mem. Soc. Astron. Italiana, 80, 97

Cappellari M., 2008, MNRAS, 390, 71

Cappellari M. et al., 2006, MNRAS, 366, 1126

Cappellari M. et al., 2009, ApJL, 704, L34

Cappellari M., Verolme E. K., van der Marel R. P., Verdoes Kleijn G. A., Illingworth G. D., Franx M., Carollo C. M., de Zeeuw P. T., 2002, ApJ, 578, 787

Carlberg R. G., Freedman W. L., 1985, ApJ, 298, 486

Carollo C. M., de Zeeuw P. T., van der Marel R. P., 1995, MNRAS, 276, 1131

Chabrier G., 2003, ApJL, 586, L133

Chabrier G., Baraffe I., Allard F., Hauschildt P., 2000, ApJ, 542, 464

Chemin L., 2014, in SF2A-2014: Proceedings of the Annual meeting of the French Society of Astronomy and Astrophysics, Ballet J., Martins F., Bournaud F., Monier R., Reylé C., eds., pp. 405–409

Cheng J. Y. et al., 2012, ApJ, 746, 149

Churchwell E. et al., 2009, PASP, 121, 213

Ciardi D. R. et al., 2011, AJ, 141, 108

Cirasuolo M. et al., 2014, in Society of Photo-Optical Instrumentation Engineers (SPIE) Conference Series, Vol. 9147, Society of Photo-Optical Instrumentation Engineers (SPIE) Conference Series, p. 0

Comparetta J., Quillen A. C., 2012, ArXiv e-prints

Cox A. N., 2000, Allen's astrophysical quantities

Cretton N., de Zeeuw P. T., van der Marel R. P., Rix H.-W., 1999, ApJS, 124, 383

Creze M., Chereul E., Bienayme O., Pichon C., 1998, A&A, 329, 920

Czekaj M. A., Robin A. C., Figueras F., Luri X., Haywood M., 2014, A&A, 564, A102

Dalton G. et al., 2014, in Society of Photo-Optical Instrumentation Engineers (SPIE) Conference Series, Vol. 9147, Society of Photo-Optical Instrumentation Engineers (SPIE) Conference Series, p. 0

Dame T. M., Hartmann D., Thaddeus P., 2001, ApJ, 547, 792

Das P., Gerhard O., Mendez R. H., Teodorescu A. M., de Lorenzi F., 2011, MNRAS, 415, 1244

de Bruijne J. H. J., 2012, Ap&SS, 341, 31

de Bruijne J. H. J., Eilers A.-C., 2012, A&A, 546, A61

de Bruijne J. H. J., Rygl K. L. J., Antoja T., 2015, ArXiv e-prints

De Bruyne V., Leeuwin F., Dejonghe H., 2000, MNRAS, 311, 297

de Jong R. S. et al., 2014, in Society of Photo-Optical Instrumentation Engineers (SPIE) Conference Series, Vol. 9147, Society of Photo-Optical Instrumentation Engineers (SPIE) Conference Series, p. 0

de Lorenzi F., Debattista V. P., Gerhard O., Sambhus N., 2007, MNRAS, 376, 71

de Lorenzi F. et al., 2009, MNRAS, 395, 76

de Lorenzi F., Gerhard O., Saglia R. P., Sambhus N., Debattista V. P., Pannella M., Méndez R. H., 2008, MNRAS, 385, 1729

de Lorenzi F., Hartmann M., Debattista V. P., Seth A. C., Gerhard O., 2013, MNRAS, 429, 2974

De Silva G. M. et al., 2015, MNRAS, 449, 2604

de Vaucouleurs G., 1959, Handbuch der Physik, 53, 311

Debattista V. P., 2003, MNRAS, 342, 1194

Debattista V. P., 2009, in Proceedings of the International Astronomical Union, Vol. 5, Highlights of Astronomy, pp. 196–197

Debattista V. P., Carollo C. M., Mayer L., Moore B., 2005, ApJ, 628, 678

Debattista V. P., Gerhard O., Sevenster M. N., 2002, MNRAS, 334, 355

Deg N. J., 2010, Master's thesis, Queen's University (Canada)

Dehnen W., 1999, ApJL, 524, L35

Dehnen W., 2000, AJ, 119, 800

Dehnen W., 2009, MNRAS, 395, 1079

Dehnen W., Binney J., 1998, MNRAS, 294, 429

Dehnen W., Gerhard O. E., 1993, MNRAS, 261, 311

Dehnen W., Gerhard O. E., 1994, MNRAS, 268, 1019

Dehnen W., Read J. I., 2011, European Physical Journal Plus, 126, 55

Dejonghe H., 1984, A&A, 133, 225

Dejonghe H., 1986, Phys. Rep., 133, 217

Dejonghe H., de Zeeuw T., 1988, ApJ, 333, 90

Delbo' M., Gayon-Markt J., Busso G., Brown A., Galluccio L., Ordenovic C., Bendjoya P., Tanga P., 2012, Planet. Space Sci., 73, 86

Deng L.-C. et al., 2012, Research in Astronomy and Astrophysics, 12, 735

Depagne É., 2015, Astrophysics and Space Science Proceedings, 39, 147

Di Matteo P. et al., 2015, A&A, 577, A1

Dobbs C., Baba J., 2014, PASA, 31, 35

Dommanget J., Lampens P., 1993, Ap&SS, 200, 221

D'Onghia E., Vogelsberger M., Hernquist L., 2013, ApJ, 766, 34

Drimmel R., Cabrera-Lavers A., López-Corredoira M., 2003, A&A, 409, 205

Drimmel R., Spergel D. N., 2001, ApJ, 556, 181

Dubinski J., 1996, New A, 1, 133

Dwek E. et al., 1995, ApJ, 445, 716

Einasto J., Haud U., 1989, A&A, 223, 89

ESA, ed., 1997, ESA Special Publication, Vol. 1200, The HIPPARCOS and TYCHO catalogues. Astrometric and photometric star catalogues derived from the ESA HIPPARCOS Space Astrometry Mission

Eyer L., Dubath P., Saesen S., Evans D. W., Wyrzykowski L., Hodgkin S., Mowlavi N., 2012, in IAU Symposium, Vol. 285, IAU Symposium, pp. 153–157

Faure C., Siebert A., Famaey B., 2014, MNRAS, 440, 2564

Francis C., 2013, MNRAS, 436, 1343

Fujii M. S., Baba J., Saitoh T. R., Makino J., Kokubo E., Wada K., 2011, ApJ, 730, 109

Fux R., 1997, A&A, 327, 983

Gebhardt K. et al., 2000, AJ, 119, 1157

Gerhard O., 2011, Memorie della Societa Astronomica Italiana Supplementi, 18, 185

Gerhard O. E., 1991, MNRAS, 250, 812

Gilmore G. et al., 2012, The Messenger, 147, 25

Gilmore G., Reid N., 1983, MNRAS, 202, 1025

Gingold R. A., Monaghan J. J., 1977, MNRAS, 181, 375

Gomez A. E., Grenier S., Udry S., Haywood M., Meillon L., Sabas V., Sellier A., Morin D., 1997, in ESA Special Publication, Vol. 402, Hipparcos - Venice '97, Bonnet R. M., Høg E., Bernacca P. L., Emiliani L., Blaauw A., Turon C., Kovalevsky J., Lindegren L., Hassan H., Bouffard M., Strim B., Heger D., Perryman M. A. C., Woltjer L., eds., pp. 621–624

González-Fernández C., Cabrera-Lavers A., Garzón F., Hammersley P. L., López-Corredoira M., Vicente B., 2007, in IAU Symposium, Vol. 242, IAU Symposium, Chapman J. M., Baan W. A., eds., pp. 376–377

Grand R. J. J., Kawata D., Cropper M., 2012a, MNRAS, 421, 1529

Grand R. J. J., Kawata D., Cropper M., 2012b, MNRAS, 426, 167

Grand R. J. J., Kawata D., Cropper M., 2013, A&A, 553, A77

Grand R. J. J., Kawata D., Cropper M., 2014, MNRAS, 439, 623

Grand R. J. J., Kawata D., Cropper M., 2015, MNRAS, 447, 4018

Grosbøl P., Patsis P. A., Pompei E., 2004, A&A, 423, 849

Häfner R., Evans N. W., Dehnen W., Binney J., 2000, MNRAS, 314, 433

Hammersley P. L., Garzón F., Mahoney T. J., López-Corredoira M., Torres M. A. P., 2000, MNRAS, 317, L45

Hanson R. J., Bailer-Jones C. A. L., 2014, MNRAS, 438, 2938

Hockney R. W., Eastwood J. W., 1981, Computer Simulation Using Particles

Holmberg E., 1941, ApJ, 94, 385

Holmberg J., Nordström B., Andersen J., 2009, A&A, 501, 941

Hubble E. P., 1926, ApJ, 63, 236

Hunt J. A. S., Kawata D., 2013, MNRAS, 430, 1928

Hunt J. A. S., Kawata D., 2014a, in EAS Publications Series, Vol. 67, EAS Publications Series, pp. 83–86

Hunt J. A. S., Kawata D., 2014b, MNRAS, 443, 2112

Hunt J. A. S., Kawata D., Grand R. J. J., Minchev I., Pasetto S., Cropper M., 2015, MNRAS, 450, 2132

Hunt J. A. S., Kawata D., Martel H., 2013, MNRAS, 432, 3062

Hunter C., de Zeeuw P. T., 1992, ApJ, 389, 79

Hunter C., Qian E., 1993, MNRAS, 262, 401

Ivezic Z. et al., 2008, ArXiv e-prints

Jahreiß H., Wielen R., 1997, in ESA Special Publication, Vol. 402, Hipparcos - Venice '97, Bonnet R. M., Høg E., Bernacca P. L., Emiliani L., Blaauw A., Turon C., Kovalevsky J., Lindegren L., Hassan H., Bouffard M., Strim B., Heger D., Perryman M. A. C., Woltjer L., eds., pp. 675–680

Johnston K. V., Majewski S. R., Siegel M. H., Reid I. N., Kunkel W. E., 1999, AJ, 118, 1719

Jordi C. et al., 2010, A&A, 523, A48

Jurić M. et al., 2008, ApJ, 673, 864

Kaasalainen M., Binney J., 1994, MNRAS, 268, 1033

Kaiser N. et al., 2010, in Society of Photo-Optical Instrumentation Engineers (SPIE) Conference Series, Vol. 7733, Society of Photo-Optical Instrumentation Engineers (SPIE) Conference Series

Kalberla P. M. W., Kerp J., 2009, ARA&A, 47, 27

Katz D. et al., 2011, in EAS Publications Series, Vol. 45, EAS Publications Series, pp. 189–194

Katz D. et al., 2004, MNRAS, 354, 1223

Kawata D., Gibson B. K., 2003, MNRAS, 340, 908

Kawata D., Gibson B. K., Barnes D. J., Grand R. J. J., Rahimi A., 2014a, MNRAS, 438, 1208

Kawata D., Hunt J. A. S., Grand R. J. J., Pasetto S., Cropper M., 2014b, MNRAS, 443, 2757

Kawata D., Hunt J. A. S., Grand R. J. J., Siebert A., Pasetto S., Cropper M., 2015, ArXiv e-prints

Kawata D., Okamoto T., Gibson B. K., Barnes D. J., Cen R., 2013, MNRAS, 428, 1968

Kent S. M., 1992, ApJ, 387, 181

Kerr F. J., Lynden-Bell D., 1986, MNRAS, 221, 1023

Klypin A., Zhao H., Somerville R. S., 2002, ApJ, 573, 597

Kronawitter A., Saglia R. P., Gerhard O., Bender R., 2000, A&AS, 144, 53

Krone-Martins A. et al., 2013, A&A, 556, A102

Kroupa P., 2001, MNRAS, 322, 231

Kuijken K., 1995, ApJ, 446, 194

Kunder A. et al., 2012, AJ, 143, 57

Lawrence A. et al., 2007, MNRAS, 379, 1599

Lee Y. S. et al., 2011, AJ, 141, 90

Lin C. C., Shu F. H., 1964, ApJ, 140, 646

Lindegren L., Lammers U., Hobbs D., O'Mullane W., Bastian U., Hernández J., 2012, A&A, 538, A78

Liu C., Bailer-Jones C. A. L., Sordo R., Vallenari A., Borrachero R., Luri X., Sartoretti P., 2012, MNRAS, 426, 2463

Łokas E. L., 2002, MNRAS, 333, 697

Long R. J., Mao S., 2010, MNRAS, 405, 301

Long R. J., Mao S., 2012, MNRAS, 421, 2580

Long R. J., Mao S., Shen J., Wang Y., 2013, MNRAS, 428, 3478

Lowing B., Wang W., Cooper A., Kennedy R., Helly J., Cole S., Frenk C., 2015, MNRAS, 446, 2274

Lucy L. B., 1977, AJ, 82, 1013

Luri X. et al., 2014, A&A, 566, A119

Luyten W. J., 1968, MNRAS, 139, 221

Majewski S. R., Zasowski G., Nidever D. L., 2011, ApJ, 739, 25

Malvido J. C., Sellwood J. A., 2015, MNRAS, 449, 2553

Marigo P., Girardi L., Bressan A., Groenewegen M. A. T., Silva L., Granato G. L., 2008, A&A, 482, 883

Marshall D. J., Robin A. C., Reylé C., Schultheis M., Picaud S., 2006, A&A, 453, 635

Martinez-Valpuesta I., Gerhard O., 2011, ApJL, 734, L20

Matthias M., Gerhard O., 1999, MNRAS, 310, 879

McCuskey S. W., 1966, Vistas in Astronomy, 7, 141

McGill C., Binney J., 1990, MNRAS, 244, 634

McMillan P. J., 2011, MNRAS, 414, 2446

McMillan P. J., Binney J., 2012, MNRAS, 419, 2251

McMillan P. J., Binney J. J., 2008, MNRAS, 390, 429

Menzel D. H., 1972, Annals of the New York Academy of Sciences, 198, 225

Merritt D., 1996, AJ, 112, 1085

Merritt D., Tremblay B., 1994, AJ, 108, 514

Michalik D., Lindegren L., Hobbs D., Lammers U., 2014, A&A, 571, A85

Mikolaitis Š. et al., 2014, A&A, 572, A33

Minchev I., Boily C., Siebert A., Bienayme O., 2010, MNRAS, 407, 2122

Minchev I., Famaey B., 2010, ApJ, 722, 112

Minchev I., Famaey B., Quillen A. C., Di Matteo P., Combes F., Vlajić M., Erwin P., Bland-Hawthorn J., 2012, A&A, 548, A126

Minchev I., Quillen A. C., 2008, MNRAS, 386, 1579

Minniti D. et al., 2010, New A, 15, 433

Minniti D., White S. D. M., Olszewski E. W., Hill J. M., 1992, ApJL, 393, L47

Monaghan J. J., Lattanzio J. C., 1985, A&A, 149, 135

Moore G. E., 1965, Electronics, 38, 114

Mora A. et al., 2014, in Society of Photo-Optical Instrumentation Engineers (SPIE) Conference Series, Vol. 9143, Society of Photo-Optical Instrumentation Engineers (SPIE) Conference Series, p. 0

Morgan J. S., Burgett W., Onaka P., 2014, in Society of Photo-Optical Instrumentation Engineers (SPIE) Conference Series, Vol. 9145, Society of Photo-Optical Instrumentation Engineers (SPIE) Conference Series, p. 0

Morganti L., Gerhard O., 2012, MNRAS, 2607

Morganti L., Gerhard O., Coccato L., Martinez-Valpuesta I., Arnaboldi M., 2013, MNRAS, 431, 3570

Nagino R., Matsushita K., 2009, A&A, 501, 157

Nakanishi H., Sofue Y., 2003, PASJ, 55, 191

Navarro J. F., Frenk C. S., White S. D. M., 1997, ApJ, 490, 493

Ness M. et al., 2013, MNRAS, 432, 2092

Newton R. R., 1974, MNRAS, 169, 331

Nidever D. L. et al., 2014, ApJ, 796, 38

Nidever D. L., Zasowski G., Majewski S. R., 2012, ApJS, 201, 35

Nordström B. et al., 2004, A&A, 418, 989

Oemler A., 1974, PhD thesis, California Institute of Technology

Pancino E., Bellazzini M., Marinoni S., 2013, Mem. Soc. Astron. Italiana, 84, 83

Pasetto S., Chiosi C., Carraro G., 2003, A&A, 405, 931

Pasetto S., Chiosi C., Kawata D., 2012, A&A, 545, A14

Perryman M., 2011, A&A Rev., 19, 45

Perryman M., 2012, European Physical Journal H, 37, 745

Perryman M. A. C., ESA, eds., 1997, ESA Special Publication, Vol. 1200, The HIPPARCOS and TYCHO catalogues. Astrometric and photometric star catalogues derived from the ESA HIPPARCOS Space Astrometry Mission

Pettitt A. R., Dobbs C. L., Acreman D. M., Price D. J., 2014, MNRAS, 444, 919

Pfenniger D., 1984, A&A, 134, 373

Pfenniger D., Friedli D., 1993, A&A, 270, 561

Plez B., 2011, in SF2A-2011: Proceedings of the Annual meeting of the French Society of Astronomy and Astrophysics, Alecian G., Belkacem K., Samadi R., Valls-Gabaud D., eds., pp. 47–52

Portail M., Wegg C., Gerhard O., Martinez-Valpuesta I., 2015, MNRAS, 448, 713

Price D. J., Monaghan J. J., 2007, MNRAS, 374, 1347

Prusti T., 2012, Astronomische Nachrichten, 333, 453

Ptolemy C., Manitius K., 1995, VizieR Online Data Catalog, 5061, 0

Puzeras E., Tautvaišienė G., Cohen J. G., Gray D. F., Adelman S. J., Ilyin I., Chrniy Y., 2010, MNRAS, 408, 1225

Qian E. E., de Zeeuw P. T., van der Marel R. P., Hunter C., 1995, MNRAS, 274, 602

Quillen A. C., Dougherty J., Bagley M. B., Minchev I., Comparetta J., 2011, MNRAS, 417, 762

Quinn P. J., Hernquist L., Fullagar D. P., 1993, ApJ, 403, 74

Rahimi A., Kawata D., 2012, MNRAS, 422, 2609

Rangwala N., Williams T. B., Stanek K. Z., 2009, ApJ, 691, 1387

Reid M. J., Brunthaler A., 2004, ApJ, 616, 872

Reid M. J. et al., 2014, ApJ, 783, 130

Reid M. J. et al., 2009a, ApJ, 700, 137

Reid M. J., Menten K. M., Zheng X. W., Brunthaler A., Xu Y., 2009b, ApJ, 705, 1548

Reid M. J., Readhead A. C. S., Vermeulen R. C., Treuhaft R. N., 1999, ApJ, 524, 816

Reid N., 1990, MNRAS, 247, 70

Rich R. M., Reitzel D. B., Howard C. D., Zhao H., 2007, ApJL, 658, L29

Richstone D. O., Tremaine S., 1985, ApJ, 296, 370

Rix H.-W., Bovy J., 2013, A&A Rev., 21, 61

Roberts W. W., 1969, ApJ, 158, 123

Robin A. C. et al., 2012, A&A, 543, A100

Robin A. C., Reylé C., Crézé M., 2000, A&A, 359, 103

Robin A. C., Reylé C., Derrière S., Picaud S., 2003, A&A, 409, 523

Roca-Fàbrega S., Valenzuela O., Figueras F., Romero-Gómez M., Velázquez H., Antoja T., Pichardo B., 2013, MNRAS, 432, 2878

Rockosi C., Beers T. C., Majewski S., Schiavon R., Eisenstein D., 2009, in ArXiv Astrophysics e-prints: 0902.3484, Vol. 2010, astro2010: The Astronomy and Astrophysics Decadal Survey, p. 14

Rodionov S. A., Athanassoula E., Sotnikova N. Y., 2009, MNRAS, 392, 904

Romanowsky A. J., Kochanek C. S., 2001, ApJ, 553, 722

Romero-Gómez M., Athanassoula E., Antoja T., Figueras F., 2011, MNRAS, 418, 1176

Romero-Gómez M., Figueras F., Antoja T., Abedi H., Aguilar L., 2015, MNRAS, 447, 218

Rood H. J., 1965, PhD thesis, The University of Michigan

Roškar R., Debattista V. P., Loebman S. R., 2013, MNRAS, 433, 976

Roškar R., Debattista V. P., Quinn T. R., Wadsley J., 2012, MNRAS, 426, 2089

Saaf A. F., 1968, ApJ, 154, 483

Saito R. K. et al., 2012, A&A, 537, A107

Saito R. K., Zoccali M., McWilliam A., Minniti D., Gonzalez O. A., Hill V., 2011, AJ, 142, 76

Sale S. E. et al., 2014, MNRAS, 443, 2907

Sale S. E., Magorrian J., 2014, MNRAS, 445, 256

Sales L. V. et al., 2009, MNRAS, 400, L61

Salpeter E. E., 1955, ApJ, 121, 161

Sanders J., 2012, MNRAS, 426, 128

Sanders J. L., Binney J., 2015, MNRAS, 447, 2479

Schlegel D. J., Finkbeiner D. P., Davis M., 1998, ApJ, 500, 525

Schönrich R., 2012, MNRAS, 427, 274

Schönrich R., Binney J., 2009, MNRAS, 399, 1145

Schönrich R., Binney J., Dehnen W., 2010, MNRAS, 403, 1829

Schwarzschild M., 1979, ApJ, 232, 236

Schwarzschild M., 1993, ApJ, 409, 563

Seabroke G. M., Prod'Homme T., Hopkinson G., Burt D., Robbins M., Holland A., 2011, in EAS Publications Series, Vol. 45, EAS Publications Series, pp. 433–436

Seares F. H., van Rhijn P. J., Joyner M. C., Richmond M. L., 1925, ApJ, 62, 320

Sellwood J. A., 2011, MNRAS, 410, 1637

Sellwood J. A., 2013, ApJL, 769, L24

Sellwood J. A., Carlberg R. G., 1984, ApJ, 282, 61

Sellwood J. A., Carlberg R. G., 2014, ApJ, 785, 137

Sevenster M. N., Chapman J. M., Habing H. J., Killeen N. E. B., Lindqvist M., 1997, A&AS, 122, 79

Shapiro K. L., Cappellari M., de Zeeuw T., McDermid R. M., Gebhardt K., van den Bosch R. C. E., Statler T. S., 2006, MNRAS, 370, 559

Shapley H., Curtis H. D., 1921, Bulletin of the National Research Council, Volume 2, Part 3, 11, 171

Sharma S. et al., 2014, ApJ, 793, 51

Sharma S., Bland-Hawthorn J., Johnston K. V., Binney J., 2011, ApJ, 730, 3

Sharma S., Steinmetz M., 2006, MNRAS, 373, 1293

Sharples R., Walker A., Cropper M., 1990, MNRAS, 246, 54

Shen J., Rich R. M., Kormendy J., Howard C. D., De Propris R., Kunder A., 2010, ApJL, 720, L72

Siegel M. H., Majewski S. R., Reid I. N., Thompson I. B., 2002, ApJ, 578, 151

Skrutskie M. F. et al., 2006, AJ, 131, 1163

Spaenhauer A., Jones B. F., Whitford A. E., 1992, AJ, 103, 297

Spergel D. N., Blitz L., 1990, in Bulletin of the American Astronomical Society, Vol. 22, Bulletin of the American Astronomical Society, p. 1340

Spergel D. N., Malhotra S., Blitz L., 1996, in Spiral Galaxies in the Near-IR, Minniti D., Rix H.-W., eds., p. 128

Springel V., Di Matteo T., Hernquist L., 2005a, MNRAS, 361, 776

Springel V., Di Matteo T., Hernquist L., 2005b, MNRAS, 361, 776

Stäckel P., 1890, Math. Ann. XXXV. 91-103

Steinmetz M. et al., 2006, AJ, 132, 1645

Sugai H. et al., 2012, in Society of Photo-Optical Instrumentation Engineers (SPIE) Conference Series, Vol. 8446, Society of Photo-Optical Instrumentation Engineers (SPIE) Conference Series

Syer D., Tremaine S., 1996, MNRAS, 282, 223

Takada M. et al., 2014, PASJ, 66, 1

Taris F. et al., 2013, A&A, 552, A98

Thomas J. et al., 2009, MNRAS, 393, 641

Thomas J., Saglia R. P., Bender R., Thomas D., Gebhardt K., Magorrian J., Corsini E. M., Wegner G., 2005, MNRAS, 360, 1355

Toomre A., 1981, in Structure and Evolution of Normal Galaxies, Fall S. M., Lynden-Bell D., eds., pp. 111–136

Toomre A., Toomre J., 1972, ApJ, 178, 623

Tremaine S. et al., 2002, ApJ, 574, 740

Tremaine S., Weinberg M. D., 1984, ApJL, 282, L5

Tremaine S. D., Ostriker J. P., Spitzer, Jr. L., 1975, ApJ, 196, 407

Tsikoudi V., 1979, ApJ, 234, 842

Turon C., Luri X., Masana E., 2012, Ap&SS, 341, 15

Tyson J. A., Jarvis J. F., 1979, ApJL, 230, L153

Vallée J. P., 2014a, ApJS, 215, 1

Vallée J. P., 2014b, MNRAS, 442, 2993

Valluri M., Merritt D., Emsellem E., 2004, ApJ, 602, 66

van den Bosch R. C. E., de Zeeuw P. T., 2010, MNRAS, 401, 1770

van der Marel R. P., Cretton N., de Zeeuw P. T., Rix H.-W., 1998, ApJ, 493, 613

van Leeuwen F., ed., 2007, Astrophysics and Space Science Library, Vol. 350, Hipparcos, the New Reduction of the Raw Data

van Maanen A., 1916, ApJ, 44, 210

von Hoerner S., 1960, ZAp, 50, 184

Wada K., Baba J., Saitoh T. R., 2011, ApJ, 735, 1

Wasserman L., 2006, All of Nonparametric Statistics (Springer Texts in Statistics). Springer-Verlag New York, Inc., Secaucus, NJ, USA

Wegg C., Gerhard O., 2013, MNRAS, 435, 1874

Wegg C., Gerhard O., Portail M., 2015, ArXiv e-prints

Weinberg M. D., 1992, ApJ, 384, 81

White S. D. M., 1976, MNRAS, 177, 717

White S. D. M., 1977, MNRAS, 179, 33

Widrow L. M., Pym B., Dubinski J., 2008, ApJ, 679, 1239

Wielen R., 1974, Highlights of Astronomy, 3, 395

Wilczynski E. J., 1896, ApJ, 4, 97

Wilkinson M. I. et al., 2005, MNRAS, 359, 1306

Williams M. J., Bureau M., Cappellari M., 2009, MNRAS, 400, 1665

Wylie-de Boer E., Freeman K., 2010, in IAU Symposium, Vol. 262, IAU Symposium, Bruzual G., Charlot S., eds., pp. 448–449

Wyrzykowski L., Hodgkin S., Blogorodnova N., Koposov S., Burgon R., 2012, ArXiv e-prints

Wyrzykowski L. et al., 2015, The Astronomer's Telegram, 7014, 1

Yanny B. et al., 2009, AJ, 137, 4377

Yasuda N., Fukugita M., Schneider D. P., 2007, AJ, 134, 698

York D. G. et al., 2000, AJ, 120, 1579

Young P., 1980, ApJ, 242, 1232

Zasowski G., Benjamin R. A., Majewski S. R., 2012, in European Physical Journal Web of Conferences, Vol. 19, European Physical Journal Web of Conferences, p. 6006

Zoccali M., Cassisi S., Frogel J. A., Gould A., Ortolani S., Renzini A., Rich R. M., Stephens A. W., 2000, ApJ, 530, 418

Zoccali M., Hill V., Lecureur A., Barbuy B., Renzini A., Minniti D., Gómez A., Ortolani S., 2008, A&A, 486, 177